RATE-DEPENDENT COHESIVE-ZONE MODELS FOR FRACTURE AND FATIGUE

A thesis submitted to the University of Manchester for the degree of
Doctor of Philosophy
In the Faculty of Science and Engineering

2018

SARMED A. SALIH

School of Mechanical, Aerospace and Civil Engineering

Table of contents

Word count: 44493

List of figures

List of tables

Nomenclature

Latin symbols

A_d	Damaged area
A_e	Undamaged reference area
B	Parameter representing the rate dependency of the cohesive material
B_1	Parameter representing the rate dependency of the cohesive material
B'_1	Parameter representing the rate dependency of the cohesive material
C	Material parameter that captures the cyclic plasticity
C_R	Rayleigh surface wave speed
$D_{(\delta)}$	Damage
D_c	Cyclic damage
D_s	Static damage
E	Elastic modulus
E^{p}	Plastic modulus
f	Loading frequency
G_{c}	Total dissipated energy per unit area
G^{p}	Plastic dissipated energy in the cohesive-zone per unit area
$G^{p_{rate}}$	Rate-dependent plastic dissipated energy in the cohesive-zone per unit area
G_{fr}	Critical fracture energy
K	Stress-intensity factor
K_I	Mode I stress-intensity factor
K_{II}	Mode II stress-intensity factor
K_{III}	Mode III stress-intensity factor

K_C	Critical stress-intensity factor
K_{IC}	Mode I critical stress-intensity factor
K_{coh}	Cohesive stiffness
ΔK	Stress-intensity factor range
N	Number of cycles
ΔN	Number of cycles in the load envelope
N_u	Number of required damage updates
r	The distance from the crack tip
R	load ratio
u	Displacement in x-direction
v	Displacement in y-direction
W^{e}	Elastic strain energy per unit area
W^{Γ}	Dissipated energy per unit area due to the fracture process
W^{p}	Dissipated energy per unit area due to plastic deformation in the bulk material
W^{d}	Total work done per unit area by the external load
W^{D}	Dissipated energy per unit area in the dashpot
$W_{limit}^{\Gamma_{\mathrm{rate}}}$	Upper limit on the rate-dependent fracture energy

Greek symbols

Γ_o	Critical cohesive energy
Γ_{rate}	Rate-dependent cohesive energy
δ_{fc}	Rate-independent critical separation
δ_c^{rate}	Rate-dependent critical separation
δ_o	Instantaneous applied displacement

δ_1	Shape parameter for the linear and trapezoidal model
δ_2	Second shape parameter of the trapezoidal model
δ^{p}	Plastic separation
δ^{e}	Elastic separation
δ_f	Final separation at fracture
δ^{coh}	Separation in the cohesive element
$\dot{\delta}$	Separation rate
$\dot{\delta}^D$	Separation rate at the dashpot
δ^{cyc}	Cyclic displacement
$\delta_{(N)}^{cyc_{(max)}}$	Maximum displacement reached at the loading cycle
δ_{max}	The separation at the onset of unloading
δ	Applied separation (plastic separation plus the cyclic displacement)
$\varepsilon^{\mathrm{coh}}$	Strain at the cohesive-zone
ε^{e}	Elastic strain
η	Material viscosity
θ	The angle between *r* and the crack plain
λ	Fixed crack extension length
σ	Cohesive stress
σ_Y	Yield stress
$\sigma_1, \sigma_2, \sigma_3$	Principal stresses for plane stress and plane strain
σ^D	Stress at the dashpot
σ_c	Rate-independent critical cohesive stress
σ_c^{rate}	Rate-dependent critical stress
σ_{max}	The stress at the onset of unloading

σ_{limit}	Upper limit on the rate-dependent critical stress
$\sigma_{(f)}^{Crate}$	Frequency-dependent critical cohesive stress
ϑ	Poisson's ratio
ϕ	Mode-mixture ratio

Abbreviation

BCZM	Bilinear cohesive-zone model
CE	Cohesive element
CT	Compact tension
CTOD	Crack tip opening displacement
CZ	Cohesive-zone
CZM	Cohesive-zone model
EDM	Electrical discharge machine
FEM	Finite element method
FDCZM	Frequency-dependent cohesive-zone model
HCF	High-cycle fatigue
IP	Integration point
LEFM	Linear elastic fracture mechanics
LCE	Linear cohesive element
EPFM	Elastic-plastic fracture mechanics
PMMA	Pre-strained brittle Polymethyl methacrylate
TCZM	Trapezoidal cohesive-zone model
TSL	Traction-separation Law
UMAT	User-defined material

Abstract

Rate-Dependent Cohesive-Zone Models for Fracture and Fatigue
Sarmed Abdalrasoul Salih, 2017
Doctor of Philosophy, The University of Manchester

Despite the phenomena of fracture and fatigue having been the focus of academic research for more than 150 years, it remains in effect an empirical science lacking a complete and comprehensive set of predictive solutions. In this regard, the focus of the research in this thesis is on the development of new cohesive-zone models for fracture and fatigue that are afforded an ability to capture strain-rate effects.

For the case of monotonic fracture in ductile material, different combinations of material response are examined with rate effects appearing either in the bulk material or localised to the cohesive-zone or in both. The development of a new rate-dependent CZM required first an analysis of two existing methods for incorporating rate dependency, i.e.either via a temporal critical stress or a temporal critical separation. The analysis revealed unrealistic crack behaviour at high loading rates. The new rate-dependent cohesive model introduced in the thesis couples the temporal responses of critical stress and critical separation and is shown to provide a stable and realistic solution to dynamic fracture.

For the case of fatigue, a new frequency-dependent cohesive-zone model (FDCZM) has been developed for the simulation of both high and low-cycle fatigue-crack growth in elasto-plastic material. The developed model provides an alternative approach that delivers the accuracy of the loading-unloading hysteresis damage model along with the computational efficiency of the equally well-established envelope load-damage model by incorporating a fast-track feature. With the fast-track procedure, a particular damage state for one loading cycle is "frozen in" over a predefined number of cycles. Stress and strain states are subsequently updated followed by an update on the damage state in the representative loading cycle which again is "frozen in" and applied over the same number of cycles. The process is repeated up to failure. The technique is shown to be highly efficient in terms of time and cost and is particularly effective when a large number of frozen cycles can be applied without significant loss of accuracy.

To demonstrate the practical worth of the approach, the effect that the frequency has on fatigue crack growth in austenitic stainless-steel 304 is analysed. It is found that the crack growth rate (da/dN) decreases with increasing frequency up to a frequency of 5 Hz after which it levels off. The behaviour, which can be linked to martensitic phase transformation, is shown to be accurately captured by the new FDCZM.

Declaration

No portion of the work referred to in this thesis has been submitted in support of an application for another degree or qualification of this or any other university or institute of learning.

Copyright Statement

Acknowledgements

First and foremost, I wish to express my sincere gratitude to my supervisors, Dr Keith Davey and Dr Zhenmin Zou, for their valuable guidance, encouragement and great support during my PhD research. It has been an honour to work under their supervision.

I would also like to express my sincere thanks to the Higher Committee for Education Development in Iraq HCED and the University of Babylon for the financial support that made my PhD work possible.

I would like to acknowledge the assistance given by IT Services and services provided by the Computational Shared Facility at The University of Manchester.

Many thanks also go to the technical staff at the School of Mechanical, Aerospace and Civil Engineering, University of Manchester for their help throughout my PhD research.

I would like to thank all my friend Mohammed A. Msekh for his help and support.

I would like to thank all my friends and colleagues at The University of Manchester who supported me during my PhD research

I wish to offer my regards to all my friends here in Manchester who supported me during my research and made my life here in Manchester enjoyable.

Dedication

I dedicate this work to

Mum *and* ***Dad*** *for their sacrifices and their support to help me get the best education possible;*

Brothers *and* ***sister*** *for their support and encouragement;*

Beloved ***wife*** *and* ***kids*** *for their love, support, encouragement and for giving me the motivation to work hard during my research*

Chapter 1: Introduction

1.1 Historical review

Engineering structures such as bridges, power plants, aeroplanes, trains, cars and others have played an important role in human life since the beginning of the industrial revolution. However, these structures can suffer from mechanical failures caused by crack propagation leading to catastrophic events, which could result in a great loss of human life and significant financial cost. Cracks in engineering structures can form as a result of material defects, manufacturing defects, design flaws or as a product of cyclic loading. The potential cracks will then propagate under the applied load (monotonic or cyclic), ultimately leading to failure.

Fatigue and fracture phenomena have been the subject of research for more than 150 years. However, complete solutions for these issues have not yet been discovered [1]. In the 1900s, many failures were recorded. Since then, many researchers have started to investigate these problems such as Wohler, who found that metallic parts could work for a very long time if they were subjected to a constant load below the yield point of their material, but that they could fail if subjected to cyclic loading, even if it was below the yield point of the material. At that time, fatigue was considered a puzzling phenomenon because the researchers could not see the damage, and the only indicator of the problem was a hidden crack inside the material.

Over the past century, researchers have developed a greater understanding of the means by which fatigue develops. The process of fatigue failure can be divided into three parts: crack initiation, crack propagation, and then fast fracture, which leads to the failure [2]. The fatigue behaviour of a part could be significantly affected by different factors, which may be mechanical, microstructural or environmental. As fatigue failure can occur when the applied stress is much smaller than the yield stress of the material, it has become a point of interest for many researchers. Great effort has been made to understand and evaluate the crack growth behaviour under both monotonic and cyclic loading, and there are many mathematical and analytical models to this end in the literature. However, these models are still under development and require further research. Most of these models suffer from limitations and in some cases fail to predict the experimental evidence. One of these cases that has not yet been fully covered is when there is a rate effect. There exist many fracture and fatigue models, but they are mainly rate-independent and do not

consider the effect of the loading rate on crack growth. This aspect is therefore investigated in this study. The cohesive-zone (CZ) model is used as a vehicle to investigate the rate effect on the simulation of fracture and fatigue problems.

1.2 Conventional fracture mechanics methods

The conventional failure criteria, based on the yield stress and the ultimate tensile strength, failed to explain the catastrophic fracture failures which occurred in the cargo ships and tankers after the Second World War. Therefore, it was established that a new design philosophy was needed; this led to the invention of a new discipline known as fracture mechanics. Fracture mechanics theories are based on the concept that all engineering structures contain initial defects. These defects will propagate when a certain load is applied, leading to the final failure of the structure. The main goal of the new design strategy is firstly to determine the maximum crack length that the stracture can safely sustain; then to understand the relationship between the crack length and the material strength; and finally, to identify the critical load that will lead to the failure of the structure with a crack of a specific length.

When the structure contains a sharp crack, the field equations fail to evaluate the stress state at the crack tip and yield an unrealistic stress singularity. In 1957, G. Irwin [3] introduced a quantity called the stress intensity factor to explain the stress state at the crack tip. This quantity has become the controlling parameter for many fracture and fatigue models. The range of the stress intensity factor has successfully been used to estimate the fatigue crack growth by Paris [4] in his model and all the modified versions of this model. However, the ability of these models to make accurate predictions is limited to linear elastic fracture mechanics (LEFM) conditions.

Recently, researchers have shown an increased interest in analysing the fracture process from a thermodynamic point of view by relating the crack driving force to the energy release rate. The most widely used model to simulate crack propagation is the so-called J-integral model, which was first presented by Rice [5]. Although this model is accurate for predicting crack initiation as well as crack growth, it can only be applied when the material is loaded, so its application is limited to monotonic loading and it fails to simulate fatigue crack propagation.

1.3 Cohesive-zone model methods

The limitations of the aforementioned models have increased the need for a cohesive-zone model (CZM) which is applicable to crack initiation as well as crack growth for any type of loading. The original idea of the cohesive-zone model comes from the concept that the stress singularity at the crack tip is unrealistic [6]. The original concept of the CZM was introduced by Dugdale [7] and Barenblatt [8]. They considered the fracture process zone as a small area ahead of the crack tip, where the normal stress perpendicular to the crack direction of travel is constant and equal to the yield stress according to Dugdale, but decreases with deformation and vanishes at separation according to Barenblatt. The CZM gained greater acceptance when Hillerborg et al. [9] numerically analysed crack growth in a brittle material using a bilinear cohesive-zone model (BCZM) together with the finite element method (FEM).

The CZM was introduced in an idealised form of the void growth and coalescence as shown in Fig. 1.1 to overcome the unrealistic stress singularity at the crack tip and to simplify the complexity of the crack growth process [10]. The CZM is founded on a traction separation law (TSL); according to this law, material damage starts when traction reaches a critical value called the critical cohesive stress σ_c. The crack propagates when the displacement jump between the surfaces of the cracked material reaches a critical value, δ_c, at which point the cohesive stress becomes zero and all the cohesive energy, Γ_o, is dissipated.

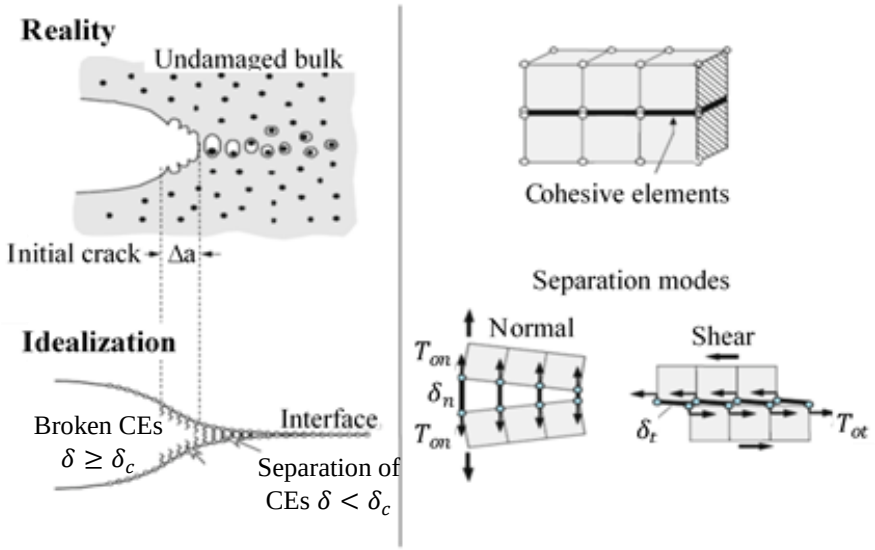

Fig. 1.1. Real and ideal representation of the crack growth process along with the cohesive-zone modelling [10].

Different types of TSLs are used in the literature, including polynomial, exponential, bilinear, and trapezoidal, as shown in Fig. 1.2. A contentious point in the literature is the importance of the shape of the traction separation curve underpinning the cohesive-zone approach. Some authors claim that the shape hardly influences the fracture simulation results [11–13], whilst other investigations demonstrate that the shape does indeed matter [14–16]. This issue is revisited in this work by contrasting the trapezoidal cohesive-zone model (TCZM) with the bilinear cohesive-zone model (BCZM).

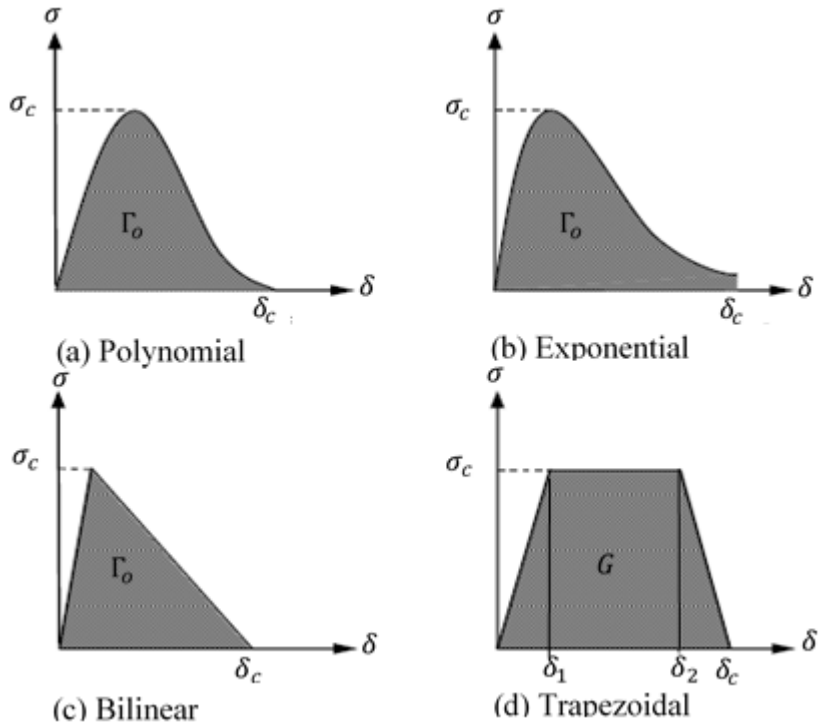

Fig. 1.2. The widely used traction separation laws: a) Polynomial, b) Exponential, c) Bilinear, d) Trapezoidal [10].

The advantage of using cohesive-zone models over the other models to simulate crack propagation is their ability to predict the initiation and the propagation of the crack. Also, it can be applied for both monotonic and cyclic loads. In addition, it requires the identification of only two of the main cohesive parameters if the shape of the traction separation law is known. It is of interest therefore to further develop the cohesive-zone model to be more applicable and reliable for investigating the rate effect on crack propagation in elasto-plastic materials both under monotonic and cyclic loads.

It is well documented that the CZM in its standard (rate-independent) forms provides an effective approach for the numerical analysis of the failure of a range of materials. This

is essentially because of the insensitivity of the crack and certain bulk materials to strain rate and crack velocity. This is not true for all materials, however, and rate sensitivity can manifest itself in a crack subjected to high strain rate since the fracture process can face greater resistance from the surrounding material, coupled with other effects such as crack branching. The standard CZM has been found to overestimate crack speeds in the case of dynamic fracture [17]. The predicted crack speed can reach the Rayleigh surface-wave speed C_R of the material, yet experimentally the maximum crack growth speed is significantly lower than C_R even for very brittle materials [18]. To achieve a better representation of the physics, it is necessary to incorporate rate dependency either in the CZM or the bulk material, or possibly both. The literature contains examples of research with rate-dependent behaviour in the bulk material combined with a rate-independent traction separation law under monotonically applied loading. Although this approach has been successfully used to represent dynamic fracture problems, as in references [19] and [20], it fails to represent experimental results in some cases, as is the case of rate-dependent crack propagation in brittle materials [17, 21–23]. Therefore, the use of a rate-dependent CZM is highly recommended [22, 24–26], where the cohesive traction σ is related not just to the crack separation δ, but also to separation rate $\dot{\delta}$, i.e. $\sigma = f(\delta, \dot{\delta})$ - a relationship first pioneered by Glennie [27]. Glennie concluded that the reason for the observed reduction in crack speed with increasing strain rate is an increase in stress levels in the vicinity of the crack tip. A negative feature of these approaches, however, is the unrealistically large values they yield for the stress in the cohesive-zone and the associated crack arrest.

A related but alternative approach to the above method is adopted for the simulation of rate-dependent behaviour, in which the critical traction is independent of rate but involves temporal changes in fracture energy along with critical separation. It is demonstrated in this work, however, that this approach can lead to unrealistic separation values and crack tearing ahead of the crack tip. A rate-dependent cohesive-zone model that overcomes the previously mentioned limitation on the available rate-dependent CZM for monotonic fracture is therefore required. Furthermore, according to the author's knowledge, there are currently no reliable CZMs for the purpose of fatigue investigation; it should also be mentioned that all existing fatigue CZMs are still under development and none have the ability to capture the rate effect. This is despite the fact that the loading rate has a

significant effect on the crack growth rate for some materials like the stainless-steel 304, as is proven experimentally in this work.

1.4 Research aim and objectives

The aim of this study is to develop a rate-dependent cohesive-zone model that can capture the strain-rate effect for the case of monotonic and cyclic crack growth in ductile material. This involves introducing a rate-dependent TCZM that captures the dynamic crack growth more accurately than the available rate-dependent CZMs for the case of monotonic loading and a frequency-dependent TCZM for fatigue crack simulation. The frequency-dependent TCZM is produced by linking a new loading-unloading hysteresis model with fast-track facility with a frequency-dependent critical cohesive stress. Although the effect of rate on crack propagation is a vitally significant problem, there are very few works concerning this topic in the literature that include an evaluation of the effect of rate on the TSL in order to estimate crack propagation.

The objectives of the work will be as follows:

- Study different 1-D Maxwell type cohesive models to find the best one that can be used to represent the problem of rate dependency.
- Investigate the benefits of using a cohesive model that captures the plasticity locally, such as the trapezoidal model, to simulate the crack growth in an elasto-plastic material.
- Derive a monotonic rate-dependent cohesive law that overcomes the limitation of the available models. This law will be used with the finite-element code ABAQUS (via a bespoke UMAT subroutine), because it is not available in any commercial finite-element solver.
- Validate the law by using it to simulate a monotonic rate-dependent problem, and contrast with the results of the simulation by using the available models in the literature.
- Experimentally test the effect of loading frequency on the fatigue behaviour of stainless-steel 304 by applying 6 different loading frequencies (0.05, 0.1, 0.5, 5, 30 and 50 Hz) at loading ratio $R = 0$ and 3 loading frequencies (0.05, 0.1 and 30 Hz) at $R = -1$.

- Derive a cohesive law for fatigue by identifying a cyclic damage mechanism within the traction separation law and validate it with the experimental results.
- Combine the new fatigue model with a new frequency-dependent critical stress to produce a frequency-dependent TCZM model that can capture the effect of frequency on fatigue simulations. This model will be implemented in the finite-element code ABAQUS (via a bespoke UMAT routine).
- The new law will be validated by simulating the experimental fatigue test procedure through finite-element simulation.

1.5 Thesis outline

After presenting a historical review and the objective of this work in the introductory chapter, the structure of the current thesis is as follows.

Chapter 2 is a review of related work in the literature to identify the limitations, gaps and strengths of existing fracture mechanics methods (stress intensity factor methods, the energy criteria, and the cohesive-zone model) in order to outline the reasons for the selection of the model adopted in this work (i.e. the cohesive-zone model) to produce a rate-dependent fracture and fatigue model.

In Chapter 3 the theoretical background of fracture and fatigue mechanisms is illustrated, presenting conventional fracture mechanics theory and the energy balance at the crack propagation. Furthermore, information about crack-tip plasticity and its calculation is shown there. Finally, the cohesive-zone models are presented and detailed information about the model used in this work is shown.

An experimental investigation of the effect of loading rate on fatigue crack growth is performed in Chapter 4. This is achieved by running fatigue tests on a notched specimen made of stainless-steel 304 at six different loading frequencies (0.05, 0.1, 0.5, 5, 30 and 50 Hz) at loading ratio $R = 0$ and three loading frequencies (0.05, 0.1 and 30 Hz) at $R = -1$.

In Chapter 5, the rate-dependent CZM is investigated by studying different combinations of one-dimensional spring, dashpot, slider and cohesive elements. A new rate-dependent model is introduced and tested. At the same time, the effect of the type of TSL and the benefits of using the trapezoidal model are illustrated.

The focus of Chapter 6 is to introduce a new loading-unloading hysteresis damage model containing a fast-track feature that can be used for the analysis of high and low-cycle fatigue crack growth.

Chapter 7 is dedicated to the derivation of the frequency-dependent CZM for fatigue and the validation of this model. This is done by combining the CZM for fatigue that is introduced in Chapter 6 with a frequency-dependent damage mechanism. The final model is validated by simulating the fatigue experiments conducted in Chapter 4.

Finally, a summary of the interesting findings of this work and recommendations for further improvement are detailed in Chapter 8.

Chapter 2: Literature review

2.1 Introduction

In the early nineteenth century, after the Industrial Revolution, a variety of machines with rotating or vibrating parts appeared in human life. With the appearance of these machines, metal failure as a result of crack propagation was recorded, revealing a significant problem that requires the attention of researchers and designers. Since then, a number of experiments have been done to understand and predict the crack growth behaviour of mechanical parts under monotonic and cyclic loading, but because experimental testing is time-consuming and costly, researchers have started to consider using analytical and numerical simulation as an alternative way to predict crack growth [2]. Many of the conventional fracture methods are based on linear elastic fracture mechanics.

2.2 Linear elastic fracture mechanics approach

The fundamentals of fracture mechanics were developed in the 1950s when Irwin investigated the crack-deriving force and the stress field at the crack tip. In 1957 Irwin introduced a parameter that represents the relationship between the nominal stress and the crack length to indicate the stress distribution in the vicinity of the crack tip. This parameter is called the stress-intensity factor, K; the crack propagates when K reaches a critical value, K_C (fracture toughness), which is a material property. The stress-intensity factor can be used to explain the crack process only if the bulk behaviour of the material is elastic and the area surrounding the crack tip in which the plastic deformation is significantly small (small-scale yielding) when compared to the crack length. This observation indicates that the problem comes under the field of linear elastic fracture mechanics (LEFM).

The relationship between the stress-intensity factor range ΔK) and the crack growth rate (da/dN) was first outlined by the pioneering work of Paris [4] through a power law, which is considered to be the most widely used fatigue model for predicting fatigue life. Although this model can match the experimental data successfully, its application is limited to specific conditions such as constant load, small-scale yielding, and large cracks [28–30]. Considerable work has been done to extend the applicability of the law. For example, as pointed out in reference [31], Gilbert et al. [32] and Wheeler [33] studied the

effect of load ratio; Drucker and Palgen [34], and Needleman [35] investigated the effect of threshold limits; Forman et al. [36] studied the crack closure effect; Willenborg et al. [37] and Xu et al. [38] added the variable amplitude effect; many other studies have followed. However, all Paris-based models are still limited to large crack growth and, in general, all the models founded on the stress-intensity factor are limited to small-scale yielding.

If the plastic zone at the crack tip is large, LEFM approaches will fail to represent the fracture process, so another approach should be adopted to describe the crack driving force. These approaches come under the field of elasto-plastic fracture mechanics (EPFM).

2.3 J -integral method for crack growth prediction

The line integral, as introduced by Rice [5, 39], is equivalent to the energy-release rate in nonlinear elastic materials. It is a path-independent integral, which could be applied to any contour starting at the lower face of the crack and ending at the upper face. A considerable amount of research has been published on the path-independency of the J-Integral; a review of a selection of these studies is reported in [40]. Riemelmoser and Pippan [41] investigated the applicability of the J-Integral method to an interface of bimaterials with different yield strengths; they found that J-Integral is path-independent within each material alone, but not at the interface. J-Integral method is considered as a very useful tool to overcome the singularity problem at a crack tip. It can also be used to characterise the crack-tip stress and strain fields in nonlinear elastic fracture mechanics problems. This has been revealed by Hutchinson [42] and Rice and Rosengren [43] (HRR) in two separate works in 1968, the existence of the HRR field was verified at the crack tip by many numerical analyses [44]. The HRR theory is an extension to the LEFM to account for large-scale yielding and related microscopic fracture mechanisms within the plastic zone such as void initiation and coalescence. In this theory the stress and displacement fields (HRR singularity) in the J-dominated region is shown by the HRR solution as

$$\sigma_{ij} = \sigma_o \left(\frac{J}{\alpha \sigma_o \varepsilon_o I_n r}\right)^{1/(n+1)} \hat{\sigma}_{ij}(\theta, n) \tag{2.1}$$

$$u_i = \alpha\varepsilon_o\gamma\left(\frac{J}{\alpha\sigma_o\varepsilon_o I_n r}\right)^{n/(n+1)}\hat{u}_i(\theta,n) \tag{2.2}$$

where J is the J-integral, σ_o, ε_o and I_n are the yield stress, strain and the integration constant. Moreover, θ and r are the coordinates from the crack tip, $\hat{\sigma}_{ij}(\theta,n)$ and $\hat{u}_i(\theta,n)$ are non-dimensional parameters that are determined by an angle θ, which is defined at the crack tip by the polar coordinate and the hardening exponent n. in addition, α is a material constant that is determined along with the hardening exponent n by a Ramberg-Osgood type relationship as

$$\frac{\varepsilon}{\varepsilon_o} = \frac{\sigma}{\sigma_o} + \alpha\left(\frac{\sigma}{\sigma_o}\right)^n \tag{2.3}$$

where σ and ε are the stress and the strain.

In order to have a stable crack growth, the HRR field concentration at the crack tip region is required to be continuous, irreversible and maintain the plastic level to an extent during the deformation. This means that the plastic fracture at the crack tip vicinity is characterised by the J-integral and the crack tip opening displacement [45].

In recent years, there has been an increasing amount of research investigating crack growth in ductile materials by using the so-called $J-$R curve or the ductile tearing resistance. However the $J-$R curve is not always a material property, and in fact, it is a geometry-dependent parameter for large-scale yielding [46–49]. As a result of this fact, the $J-$R curve cannot be transposed from one specimen to another; a detailed review regarding this problem is reported in [47]. A modified version of the $J-$R curve (or, as the author called it, the $D-$R curve) was introduced by Turner [50] to overcome the geometry dependency problem by using the total dissipated energy per unit area of the crack extension as a function of the crack extension normalised by the ligament length at the crack initiation. However, Marie and Chapuliot [46] pointed out that a test result shows that the dissipated energy rate (R) introduced by Turner cannot be transferred from one test specimen to another. Following this study, a large amount of work has been done on similar $J-$R curves, which aimed to find a relationship that could be considered as a material property, but none have provided a satisfactory result [46]. Marie and Chapuliot studied the behaviour of R and found that it has a high value at initiation, then decreases to reach a constant value (R_∞) in the steady crack-growth region. They suggest that the initiation of the crack happens at a constant initiation toughness, J_i, and the steady crack

growth can be simulated by using the stabilised value, R_∞, which they defined as the critical local energy-release rate (G_c). The model they introduce requires a fine mesh at the region near the crack tip; the authors did not discover whether or not the critical local energy G_c is a material property. Later the same authors [51] introduced a parameter which represents the critical fracture energy, G_{fr}; this parameter is related to the critical local energy, G_c, through the relation

$$G_c = \overline{\lambda} G_{fr} \tag{2.4}$$

where $\overline{\lambda}$ is the dimensionless measure of the fixed crack extension length (λ). Although they stated that G_{fr} successfully describes the crack growth and is geometry-independent as well as a material property, the model has some limitations such as the requirement for a fine mesh, restricted to fixed crack extension and the limitation to one-dimensional crack-propagation problems only. An attempt to overcome some of these limitations, especially the restriction of a fixed crack extension and the limitation to 1D problems, is reported in [49].

The models based on the J-integral are required to be applied to a loaded crack. Thus, the J-integral is considered as a powerful tool to simulate quasi-static crack-growth, but it is difficult to use in the simulation of fatigue crack propagation. However, an attempt has been made by Klingbeil [52] to use the dissipated energy rate (R) introduced by Turner to predict fatigue crack growth in ductile materials. The model that he introduced relates the fatigue crack-growth rate da/dN to the rate of change in plastic-dissipated work per cycle of load, normalised by the monotonic critical strain energy release rate. The approach introduced by Klingbeil is limited to mode I crack propagation and failed to simulate the crack-propagation data for several ductile materials [52]. Work has been done by Daily [53, 54] to add the mixed-mode effect to Klingbeil's model. Substantial research exists that is aimed at interpreting and predicting fatigue life, but even so, presently no reliable models exist to simulate fatigue crack propagation [55]. The difficulty of applying J-integral based method for fatigue investigation comes from the unloading part of the cyclic loading.

2.4 Cohesive-zone model (CZM) for fracture

Recently, a method called the cohesive-zone model has become the focus of some research in the area of fracture mechanics because it has the ability to capture crack initiation, as well as propagation. Also, this model can be used to simulate crack growth in both monotonic and cyclic load problems. The initial concept of the CZM was introduced by Dugdale [7] and Barenblatt [8]. They considered the fracture-process zone as a small area ahead of the crack tip, where the normal stress perpendicular to the direction of crack travel is constant and equal to the yield stress according to Dugdale, but decreases with deformation and vanishes at separation according to Barenblatt.

The CZM is founded on a traction-separation law (TSL); according to this law, material damage starts when traction reaches a critical value called the critical cohesive stress, σ_c. The crack propagates when the displacement jump between the cracked-material surfaces reaches a critical value, δ_c, at which point the cohesive stress becomes zero and all the cohesive energy, Γ_o, is dissipated. From this, it is evident that there are at least three parameters representing the traction-separation law. Only two of them are required if the shape of the traction-separation law is predefined. The measurement of these parameters plays a key role in the CZMs. Generally, there are two methods of determining these parameters; the first one is a direct method, in which the parameters are calculated directly by experiment, and the second one is an indirect method, in which the parameters are determined by numerical fitting of a test result. However, it is preferable to use a combination of the two methods by calculating the initial values of the parameters experimentally, then tuning them to fit test data by a numerical optimisation procedure [10, 56]. Detailed information about the evaluation of the CZM parameters can be found in reference [30]. Furthermore, the advantages and limitations of the CZM application to different materials are discussed.

The CZM gained greater acceptance when Hillerborg et al. [9] analysed crack-growth numerically in a brittle material using a bilinear cohesive-zone model (BCZM), together with the finite element method (FEM). This study was followed by the work of Needleman [57], who introduced the polynomial CZM and, subsequently, the exponential CZM [58]. Scheider [6] introduced the partly constant CZM, which is similar to Needleman's polynomial model but with a flat region in the middle. The trapezoidal cohesive-zone model (TCZM), which is of particular interest in this work, was introduced by Tvergaard and Hutchinson [13].

A bone of contention in the literature is the importance of the shape of the traction-separation curve underpinning the cohesive-zone approach. Some authors claim that the shape hardly influences fracture-simulation results [11–13], whilst other investigations demonstrate that the shape does indeed matter [14–16]. This issue is revisited in this study by contrasting the trapezoidal cohesive-zone model (TCZM) with the bilinear cohesive-zone model (BCZM). It is demonstrated that under the constraint of invariant toughness, the shape of the traction-separation curve does indeed have an effect.

In nonlinear elastic materials (elasto-plastic materials) the fracture process is more complicated than in linear elastic materials, because of the plastic deformation associated with crack growth. Tvergaard and Hutchinson [13] studied the effect of plastic deformation on crack growth (using the concept of void growth and coalescence) in an elasto-plastic material under monotonic loading by using a cohesive-zone model. They found that the energy dissipated in the fracture process could be divided into two constant values: the first one is the energy dissipated at the initiation of the crack, which is equal to the cohesive energy; the second is the energy dissipated during steady crack propagation, which is larger than the cohesive energy because it equals the dissipated energy to form the new plastic zone ahead of the crack tip plus the energy dissipated to propagate the crack (cohesive energy). They pointed out that for the trapezoidal model, the effect of energy dissipated in the plastic region, only becomes significant compared with the cohesive energy when a fully developed plastic zone is formed, which happens when the ratio of the cohesive critical stress (σ_c) to the yield strength (σ_Y) is greater than 2.5. The limitation of this method is that if σ_c exceeds the specified value for a specific hardening exponent (N), the crack will never grow. For example, if N = 0 and $\sigma_c > 2.97\sigma_Y$, then crack blunting occurs and the crack growth ceases. The model has been further developed to overcome the blunting problem by the same authors [59]; they introduced a strain-dependent cohesive-zone model by making the critical cohesive stress a function of the plastic strain. In this model, when the plastic strain reaches a critical value, the cohesive stress will start to decrease with increasing plastic strain, thus resolving the crack tip-blunting problem.

The CZM is in some way a mesh-dependent model since for accuracy a specific number of elements within the cohesive process zone are required to achieve convergence in the predicted result. In addition, the cohesive process zone length is not constant and depends on the cohesive parameters. For some materials, this zone is very small; this necessitates

a very fine mesh, making the analysis very expensive and time-consuming. Turon et al. [60] investigated the effect of mesh size on the CZM. They introduced a method to overcome the problem of the very fine mesh by reducing the value of the critical cohesive traction while keeping the cohesive energy constant. This led to an increase in the length of the process zone and helped to simulate the crack growth with a coarser mesh. They used the following equation to relate the cohesive traction to the number of elements in the process zone and the zone length

$$\sigma_c = \sqrt{\frac{9\pi E \Gamma_o}{32 N_e^0 l_e}} \tag{2.5}$$

where σ_c is the critical cohesive stress, E is the modulus of elasticity, Γ_o is the cohesive energy, N_e^0 is the number of elements within the process zone, and l_e is the length of the process zone.

This method facilitates the use of a coarser mesh with the CZM; however, it makes the value of the stresses in the vicinity of the crack tip less accurate, so care is required when changing the value of the critical traction. Further work on the use of the coarse mesh with CZM was carried out by Nguyen and Repetto [31], where they used an adaptive meshing method, in which the mesh size is a function of the radial distance from the crack tip (r). The element size was set up to be equal to $r^{3/4}$, which made the mesh coarser in the region furthest from the crack and smaller as it approached the crack, until the value of r becomes equal to the cohesive-zone length, l_{cz}.The mesh size then becomes constant (equal to $l_{cz}^{3/4}$), making the mesh size suitable for the CZM and not too small as r approaches the crack tip. Although this method helps by only requiring a fine mesh in the vicinity of the crack tip, remeshing is required to keep the fine mesh around the cohesive process zone.

2.5 Rate-dependent cohesive-zone model (CZM)

It is well documented that the CZM in its standard (rate-independent) forms provides an effective approach for the numerical analysis of the failure of a range of materials. This is essentially because of the insensitivity of the crack and certain bulk materials to strain rate and crack velocity. This is not true for all materials, however, and rate sensitivity can manifest itself in a crack at high strain rate facing greater resistance from the surrounding

material, along with other effects such as crack branching. The standard CZM has been found to overestimate crack speeds in the case of dynamic fracture [17]. The predicted crack speed can reach the Rayleigh surface wave speed, C_R, of the material, yet experimentally the maximum crack growth speed is significantly lower than C_R, even for very brittle materials [18]. As a result, it becomes necessary to incorporate a rate dependency in the CZ modelling. Two different methodologies have been used to add a rate dependency to the material-separation models: the first involves using a rate-dependent constitutive behaviour in the bulk material with a rate-independent traction-separation law. In the second method, the focus is to implement the rate-dependency in the traction separation law itself by relating cohesive traction not only to the separation but to the separation rate as well [21].

2.5.1 Rate-Independent CZM with rate-dependent bulk material

Dynamic fracture is usually associated with additional dissipated energy as a result of complicated fracture mechanisms such as crack branching. The literature contains examples of research with rate-dependent behaviour in the bulk material combined with a rate-independent traction-separation law under monotonically applied loading to account for this additional dissipated energy. For example, Ortiz and Pandolfi [61] used this approach and demonstrated good agreement with the experimental data. The researchers argued that through this approach the CZM captures the rate dependency of the failure process. Similarly, Song et al. [23] and Zhou et al. [19] successfully applied the approach to asphalt concrete and reinforced aluminium, respectively. Zhou et al. [22] pointed out, however, that the success of the study of Ortiz and Pandolfi [61] was limited to ductile materials and was successful because of the intrinsic timescale associated with ductility. The approach failed to reproduce existing experimental crack-propagation data of pre-strained brittle Polymethyl methacrylate (PMMA). Costanzo and Walton [24] asserted that the rate-independent CZM is unable to represent the experimental results from the literature, regardless of the type of traction-separation law and the fracture criterion used. A similar conclusion was reached by Langer and Lobkovsky [26] and, again, Costanzo and Walton [25].

2.5.2 Rate-dependent cohesive-zone model

It is well known that with increasing the crack speed in the case of dynamic loading, the value of the dissipated energy increases. This increase in the fracture energy is due to the dissipated energy in the surrounding area of the crack tip, caused by crack branching and other phenomena. In this case, the cohesive energy can be divided into two parts: the first represents the crack driving force, which is the same as the critical cohesive energy in the rate-independent cohesive law; the other part represents the energy dissipated in the surroundings due to crack speed. Recent investigations (see, for instance, [17, 21, 22, 24–26] and others) have pointed out that the simulation of dynamic crack growth using the standard rate-independent CZM could give unrealistic results; it is therefore highly recommended to use a rate-dependent CZM. In the rate-dependent cohesive model, the cohesive traction, σ, is related not just to the crack separation, δ, but to the separation rate, $\dot{\delta}$, as well, so $\sigma = f(\delta, \dot{\delta})$. This relation was first pioneered by Glennie [27] when he studied the sensitivity of the steel fracture toughness to the strain rate. A relation for the dynamic yield stress has been proposed in the form

$$Y = Y_o + F\dot{\varepsilon} \tag{2.6}$$

where Y is the dynamic yield stress, Y_o is the static yield stress, F is a constant, and $\dot{\varepsilon}$ is the plastic strain rate.

Glennie concluded that the reason behind the reduction in crack speed with increasing the strain rate is the increasing stress in the vicinity of the crack tip. Freund and Lee [62] reviewed Glennie's work for the dynamic fracture of a Dugdale-type problem, by considering the stress in the plastic zone ahead of the crack tip in the same way as the dynamic yield stress in the Glennie model and the static yield stress as the rate-independent critical cohesive traction, σ_c, which is equal to the material yield stress, σ_y, for the Dugdale model. They use the following relationship for the rate-dependent cohesive stress

$$\sigma_{(\dot{\delta})} = \sigma_y \left(1 + {\dot{\delta}}/{\dot{\delta}_0}\right) \tag{2.7}$$

where $\sigma_{(\dot{\delta})}$ is the rate-dependent cohesive stress, σ_y is the flow stress, $\dot{\delta}$ is the separation rate in the cohesive-zone, and $\dot{\delta}_o$ is a reference separation rate, which is a material constant.

Costanzo and Walton [25] used a similar model for mode III fracture problems to study the dynamic crack growth in elastic materials, using a viscosity coefficient, η, instead of the term $\sigma_y/\dot{\delta}_o$. It was found that the crack-tip speed is completely controlled by material viscosity; a steady-state crack-tip velocity was observed using this model. Even with a very high value of the applied load, the predicted crack speed was less than that predicted by the rate-independent model for the same load and boundary conditions.

Further development of this model was carried out by the same authors [24] by making a comparison between the result of the previous model and a model introduced by Xu et al. [63], which is in the form

$$\sigma_{(\delta,\dot{\delta})} = (\sigma_y + \eta\dot{\delta}) \times \left(1 - {}^{\delta}/_{\delta_c}\right) \tag{2.8}$$

where δ is the material separation and δ_c is the cohesive critical separation.

They concluded that the use of both models could result in a very large stress value in the cohesive-zone, which is much larger than the yield stress. Thus, this could lead to an unrealistic stress field at the crack tip and possibly unrealistic crack arrest. From this discovery, it has been concluded that a fracture criterion which can control the value of the cohesive traction of these models is crucial to obtain a satisfactory result.

Relatively similar models were used in [21, 64–67]. To overcome the problem of the unrealistic stress field and the possibility of crack arrest, Valoroso et al. [17] and Zhou et al. [22] introduced a rate-dependent CZM. In this CZM the critical traction is constant (i.e. does not change with the crack speed), while the cohesive energy and the critical separation increases with increasing the crack speed. In the former study, the rate-dependent cohesive energy was calculated using:

$$G_{Ic}^{dyn}(\dot{a}) = G_{Ic}\big(1 + H(m,\eta)\big) \tag{2.9}$$

$$H(m,\eta) = -\eta log(1-m) \tag{2.10}$$

where G_{Ic}^{dyn} is the rate-dependent critical cohesive energy, G_{Ic} is the rate-independent cohesive energy, m is equal to the crack speed divided by the Rayleigh wave speed of the material, and η is a dimensionless rate-sensitivity parameter. Conversely, in the latter the rate-dependent critical separation is calculated using

$$\delta_c = \delta_{co}\left(1 + \left(\dot{\delta}/\dot{\delta}_o\right)^n\right) \tag{2.11}$$

where δ_c is the rate-dependent critical separation, δ_{co} is the rate-independent critical separation, $\dot{\delta}$ is the separation rate, $\dot{\delta}_o$ is a reference crack-opening rate, and n is the rate-dependency index.

In this thesis, both rate-dependent CZ methodologies are investigated and compared to discover and highlight their weaknesses and to identify the best way to overcome them.

2.6 Cohesive-zone model (CZM) for fatigue

It is well known that cyclic load creates more complicated problems because of the unloading part of the load cycle and the history-dependence of the crack process. Most of the CZM applications are for monotonic crack growth prediction; for instance, all of the previously mentioned CZMs are history-independent, so can only be used for monotonic crack-propagation simulation. Therefore, to use the CZM in a fatigue crack-growth simulation, an irreversible and history-dependent cohesive law is required that can capture the damage accumulation associated with cyclic loading. This can be done by identifying an additional criterion for the development of the cohesive model's internal variables and combining it with the CZM for monotonic loading. In the literature, there are two available methods for identifying this cyclic effect; the first is the envelope-load damage model, and the other is the loading-unloading hysteresis damage model.

2.6.1 Envelope-load damage method

The maximum load of the loading cycle is the focus of the envelope-load damage model rather than a description of the complete cyclic loading behaviour. All variants founded on this particular approach formulate a damage rate, dD/dN. Although the damage rate is written here in the form of a derivative for convenience, it should be well appreciated that the damage rate is not in fact a derivative, as D is a path-dependent quantity and as such is not a function. The damage, D, is assumed to be composed of a quasi-static damage, D_s, and a cyclic damage, D_c, which are considered to be additive to provide the total damage, $D = D_s + D_c$. Thus, the damage rate is mathematically represented as

$$\frac{dD}{dN} = \frac{dD_s}{dN} + \frac{dD_c}{dN} \tag{2.12}$$

The damage accumulated, $D_{(N+\Delta N)}$, is defined via the integration of damage rate. Thus, after a specific number of cycles, $N + \Delta N$, damage is determined from the current damage, $D_{(N)}$, plus the integration of the damage rate over the interval $[N, N + \Delta N]$ and explicitly takes the form

$$D_{(N+\Delta N)} = D_{(N)} + \int_N^{N+\Delta N} (dD/dN)\, dN' \tag{2.13}$$

The integration in Eq. (2.13) is typically approximated using the 2-point Newton-Cotes quadrature; (see, for example, references [68, 69]) the approximation takes the form

$$\int_N^{N+\Delta N} (dD/dN)\, dN' \approx \frac{1}{2}((dD/dN)|_N + (dD/dN)|_{N+\Delta N})\Delta N \tag{2.14}$$

or alternatively with a 1-point Newton-Cotes quadrature, as in references [66–71], which takes the form

$$\int_N^{N+\Delta N} (dD/dN)\, dN'' \approx ((dD_s/dN)|_N + (dD_c/dN)|_N)\Delta N$$

$$\approx (dD_c/dN)|_N \Delta N \tag{2.15}$$

A source of error in Eq. (2.15) is the loss of the quasi-static damage rate, which cannot be estimated by means of the 1-point Newton-Cotes quadrature (as explained in reference [76]). Different cyclic-damage rate formulations have been adopted in the literature. The first was introduced by Robinson et al. [68] for delamination of composite laminates, where the cyclic damage rate is evaluated through the formula

$$\frac{dD_c}{dN} = \frac{C}{1-\beta} e^{\lambda D} \delta^{1+\beta} \tag{2.16}$$

where δ is equivalent mixed-mode opening, and C, β and λ are fitting parameters.

A particular drawback of this model is the number of material parameters that need to be fitted with experimental data for each loading mode and for each mode-mix ratio in the case of mixed-mode loading. A further development to the previous model is presented in reference [69] and involves the incorporation of a mode-mixture ratio, ϕ, into the damage-rate formulation in order to reduce the number of required experiments. The rate equation takes the form

$$\frac{dD_c}{dN} = C_{(\phi)} e^{D} \delta^{\beta(\phi)} \tag{2.17}$$

where ϕ is the mode-mixture ratio.

Unlike in Eq. (2.16), the parameters in Eq. (2.17) are only required to be fitted with experimental results for each loading mode and only one mixed mode. Reducing the cost required for calibrating the parameters of the previous models is achievable by linking the damage evolution to a Paris-like model of the form

$$\frac{dD_c}{dN} = \frac{1}{a'_{cz}} \frac{\left(\delta^f (1-D) + D\delta^o\right)^2}{\delta^f \delta^o} P(w_{tot}) \tag{2.18}$$

where a'_{cz} is the cohesive-zone length, and δ^f and δ^o are the equivalent mixed-mode final and onset openings, respectively [71].

Note here the implicit link between damage and the length of the cohesive-zone or some portion associated with it. Linking damage evolution to a Paris law means no additional parameters require calibration other than the standard Paris-law parameter. Simplified versions of the Turon et al. model [71] can be found in reference [72] as

$$\frac{dD_c}{dN} = \frac{1}{a_{cz}} P(\mathcal{G}) \tag{2.19}$$

and in reference [73] as

$$\frac{dD_c}{dN} = \frac{1 - D_s - D_{c,u}}{a_{fat}} P(w_{tot}) \tag{2.20}$$

where a_{fat} is the length of the fatigue part of the cohesive-zone, D_s and $D_{c,u}$ are the quasi-static damage and the cyclic damage in the quasi-static region, and $P(w_{tot})$ and $P(\mathcal{G})$ are Paris' laws as a function of w_{tot} and $\mathcal{G}$, respectively.

Damage rate in Eq. (2.19), which is assumed to be a function of a Paris law founded on energy release rate $\mathcal{G}$ (rather than w_{tot}), can be determined by the J-integral. This simplifies the process, with damage rate not depending directly on the current state of damage. The predictive accuracy of the methods used in references [70–75] is very much influenced by the integration scheme that is adopted to integrate the damage-rate equation. An additional contributing factor can be the absence of the component describing the quasi-static damage rate.

2.6.2 Loading-unloading hysteresis damage model

Unlike the envelope-load approach, the entire loading-unloading cycle is considered and represented in loading-unloading hysteresis damage models. This permits the modelling of advanced behaviour at the cohesive interface and surroundings, taking into consideration such things as friction and plasticity [76]. Loading-unloading hysteresis models are based on the reduction of the interfacial stiffness captured by a cyclic-damage variable that evolves or an internal variable that grows. The first successful attempt to use a CZM for the simulation of fatigue-crack growth is presented in reference [77], which introduces a cyclic damage factor, D, whose purpose is to quantify the amount of dissipated energy in the fracture process divided by the critical fracture energy. Variable interfacial stiffness models soon followed this work (see references [31] and [78], for example), where traction rate $\dot{T}$ is assumed to be a function of incremental stiffnesses, K^- and K^+, according to the relationship

$$\dot{T} = \begin{cases} K^-\dot{\delta}\,, & if \;\; \dot{\delta} < 0, \\ K^+\dot{\delta}\,, & if \;\; \dot{\delta} > 0, \end{cases} \tag{2.21}$$

where K^+ and K^- are the loading and unloading stiffness, respectively, and $\dot{\delta}$ is the rate of change of separation. The value of K^- is constant for each unloading part, but K^+ evolves with the number of cycles through a decay factor until complete separation of the cohesive element (CE). Alternatively, Yang et al. [78] assumed that both loading and unloading stiffness are a function of a damage parameter that evolves both during loading and unloading. A particular deficiency with these models is that crack defects are assumed to grow no matter how small they might be, which can be unrealistic. To correct for this, introduced in reference [79] are two additional parameters, σ_f and δ_Σ, which represent a fatigue stress limit (below which no crack propagation occurs) and the accumulated cohesive length, respectively. If the stress on the element ahead of the crack tip is below the fatigue stress limit, the model presents an infinite life (no crack will propagate). If, however, the stress on this element is larger than the fatigue stress limit, then material separation initiates and grows until it reaches the cohesive length, δ_o. Here δ_o represents the initiation of material separation at the critical cohesive stress, σ_c. Subsequently, damage accumulates and the critical cohesive stress reduces as a function of the damage, giving the current critical cohesive stress. Ongoing damage accumulation results in crack extension and failure of the cohesive element, which occurs when the maximum stress in

a load cycle reaches the current critical cohesive stress. This model contains all the necessary features for the description of fatigue-crack growth. However, as with all the previous models, this method remains phenomenological, requiring validation with experimental results to check accuracy and to standardise the cohesive-zone parameters. Other studies [28, 29] have considered similar approaches, in which damage does not accumulate if the stress is lower than a predefined value (the fatigue stress limit). Although the loading-unloading hysteresis damage model provides a description of fatigue behaviour over each and every time increment, it is relatively expensive in terms of the required computational time. Moreover, in practical terms it can be considered unfeasible for the simulation of high-cycle fatigue, where a large number of loading cycles is involved. To reduce the computational time required for the hysteresis damage models, an extrapolation scheme was introduced by De-Andrés [77] to approximate the damage state after a pre-defined number of cycles through a two-term Taylor expansion, of the form

$$D_{n+1} \approx D_n + (dD/dN)|_n (N_{n+1} - N_n) \tag{2.22}$$

where D_{n+1} is the new damage state at N_{n+1} cycles and D_n is the old damage state at N_n cycles, dD/dN is the damage rate.

The rate of change of D per cycle dD/dN at N_n, required for the extrapolation, is computed by a detailed step-by-step computation of a few loading cycles. A limitation of this method is the assumption that the damage rate is constant throughout the crack-propagation period. In addition, for good accuracy, the cycle increment, $N_{n+1} - N_n$, is constrained by the requirement that the damage increment, $D_{n+1} - D_n$, is relatively small. Similar methods are considered in references [80, 81].

In general, fatigue modelling using the cohesive-zone model looks promising, but is still in its infancy and requires further development, since there are no mature CZMs that can be used for industrial applications yet [76]. In this study, a loading-unloading hysteresis damage model containing a fast-track feature is introduced. The model involves an internal variable that is evaluated at one loading cycle and applied for a specific number of cycles (ΔN) to give the stress and the separation state at that specific number of cycle. For the subsequent loading cycle, this internal variable is updated to fit the current loading point; the new value is applied for the next ΔN to evaluate the material behaviour after ($N + \Delta N$) cycles. If the cohesive element happens to fail in a number of cycles fewer than

($N + \Delta N$), then a specific technique is applied within the model to ascertain the precise number of cycles at which the element failed.

2.7 Effect of frequency on fatigue behaviour in stainless-steel 304

The strength of the austenitic stainless steel is affected by the martensitic content. Martensite formation depends on the strain amplitude, temperature, grain size and the number of loading cycles [82, 83]. The dependence on strain amplitude means that the austenitic-martensitic phase transformation is significantly more sensitive in this regard to low-cycle fatigue (LCF) as opposed to high-cycle fatigue [83, 84]. However, the transformation can occur with high-cycle fatigue (HCF) as a result of plastic-strain accumulation [85, 86]. The percentage of martensite in this case however tends to be small, and typically no greater than 3% according to reference [87]. Further details on the effects of plastic-strain amplitude, temperature and chemical composition on the formation of the strain-induced martensite are available in references [83, 84, 86]. Müller-Bollenhagen et al. [87] contend that the phase transformation in austenitic stainless steel depends on the material's chemical composition and microstructure, the accumulated plastic strain and strain rate, and the temperature. The relationship between the number of fatigue cycles and the percentage of martensitic transformation has been investigated by Kalkhof et al. [88]; they found that the percentage of martensite increases linearly with the number of loading cycles, similar to the conclusion found in [85]. Through this linear relationship and the fact that the phase transformation is a function of the strain amplitude, Kalkhof et al. managed to evaluate the fatigue degradation as a function of the strain amplitude.

James [89] pointed out that at elevated temperature the crack-growth rate in the stainless steel 304 increases with decreasing frequency, as a result of additional mechanisms such as creep and oxidation, but not because of martensitic content. It is recognised that the phase transformation is inhibited at higher temperatures. It is of interest to inquire whether the loading frequency has an effect at ambient temperature, particularly if the material under consideration possesses good corrosion resistance in air and has a relatively high melting point, which makes it unlikely for corrosion and creep to occur. Related to this, Nikitin and Besel [90] investigated the effect of frequency on crack growth in AISI 304 stainless-steel at room temperature and at a fixed temperature of 25°C. They found that,

if an isothermal condition is applied at room temperature, the crack grew more slowly at a high frequency as a result of the presence of martensite. Otherwise the crack grows faster at high frequency as a consequence of self-heating (as the authors suggested). Although self-heating of the material can increase the temperature of the specimen, the authors of this work argued that cracks grow faster at high frequency because of the material self-heating. A different result is reported here, in direct contradiction with the conclusion of reference [90]. Although material temperatures can be expected to increase, this can be shown to occur gradually, and it is only when the temperature is sufficiently high that the phase transformation will be inhibited. This conclusion was drawn in references [85, 87], where it was concluded that higher strain rates occur at higher frequencies, leading to a higher plastic strain, hence a higher percentage of martensite. These studies did however find that for a fully reversed cyclic loading, the specimen temperature increases with increasing the strain amplitude and the loading frequency. Müller-Bollenhagen et al. [87] did not find any difference in the fatigue behaviour when frequencies of 90Hz and 20KHz were applied. This supports the findings of this study, as the frequencies used in [87] are relatively high and the martensitic content reaches its saturation limit for the specific temperature despite plastic strain increasing, so any changes in frequency will have little effect on crack-growth speeds.

The effect that the frequency has on fatigue-crack growth in austenitic stainless steel 304 under sinusoidal cyclic load with the stress ratio ($R = 0$ and $R = -1$) and a maximum load of 10 kN applied in an air environment at room temperature is the focus of this work. These conditions have been selected as the effect of frequency on fatigue behaviour at ambient temperature has not been fully covered in the literature.

2.8 Summary

The high cost and the time-consuming nature of experimental fracture-testing have given rise to the need to find an effective and accurate numerical method to simulate the fracture problem. The J-integral was the first successful method and remains important, and is heavily used in industry in conjunction with the finite-element method to simulate fracture problems. However, the limitations of this method in the analysis of stationary crack problems have encouraged researchers to look for alternative analysis methods that can predict crack initiation as well as crack propagation, and that can be applied to monotonic and dynamic crack problems. From the literature, it can be seen that the CZM

could be considered as the most feasible and powerful model when used with the finite-element methods to simulate fracture and fatigue problems; nevertheless, an optimum CZM that can simulate any kind of crack-growth problem remains undiscovered. Although there are a lot of CZMs in the literature that accurately represent the experimental data of monotonic crack growth, few have the ability to capture the effects of rate. The rate-dependent CZMs in the literature are not fully developed and require further investigation. In this study, these existing rate-dependent models are tested and compared to form the basis for the introduction of a new rate-dependent CZM that overcomes their particular limitations.

The application of the CZM to the simulation of fatigue-crack growth has gained researchers' interest recently, but this field is still in its infancy since very few quantitative and qualitative studies exist on the use of CZM to simulate fatigue-crack growth problems. Furthermore, existing CZMs do not account for loading rates. Mechanical parts can be subject to different loading rates in service, and consequently, cracks can behave differently for the same material under the same value of applied load. To capture this phenomenon, attention in this thesis is focused on the development of a rate-dependent trapezoidal cohesive-zone model that overcome the limitations of existing rate-dependent CZMs for monotonic crack growth and to develop a new frequency-dependent TCZM for fatigue. According to the author's knowledge, there is no or very little work on using a rate-dependent CZM to simulate fatigue-crack problems. In this work, a new CZM for fatigue-crack simulation will be introduced and linked to a frequency-dependent critical cohesive stress to give it the ability to capture the effect of frequency on fatigue-crack growth.

Chapter 3: Fracture mechanics and fatigue

3.1 Elastic fracture mechanics

3.1.1 Introduction

The main hypothesis underpinning fracture mechanics is that all material parts contain microcracks due to their production process, the presence of these cracks lead to a stress concentration, which initiates the material failure. It is well known that when load is applied to a cracked part, there will be a specific amount of plasticity in the vicinity of the crack tip. The size of this plastic zone identifies the fracture mechanics method which is adequate to deal with the problem. For example, if the size of the plastic zone is very small compared with the crack length and the part dimensions, then linear elastic fracture mechanics (LEFM) theory can be applied to find the stress distribution. Otherwise, if the plastic zone is large, the LEFM theory fails to address the stress distribution and it is required to use nonlinear theories [91].

3.1.2 Loading modes and crack tip stress field

There are three types of loading, which could be applied individually to the material or a combination of all or two of them could be applied. The first mode is the opening mode (mode I), see Fig. 3.1(a). This mode is found to be dominant in most fracture problems. The second mode is the sliding mode (mode II) called the in-plane mode, see Fig. 3.1(b). Finally, the tearing mode (mode III), the out-of-plane mode is depicted in Fig. 3.1(c).

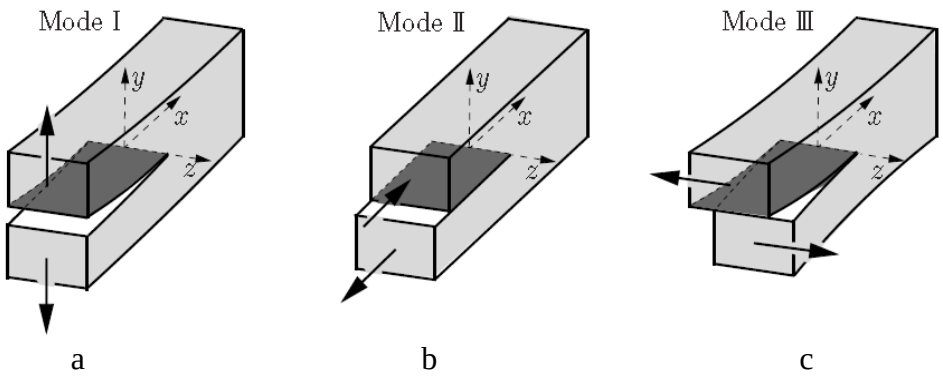

Fig. 3.1. Type of loading [112]: (a) Mode I (Opening mode), (b) Mode II (Sliding mode), (c) Mode II (Tearing mode).

The relation between stress and displacement around the crack tip is very important because it governs crack growth behaviour. The crack tip stress field is shown in Fig. 3.2, a brief description of it for each fracture mode will be presented [91].

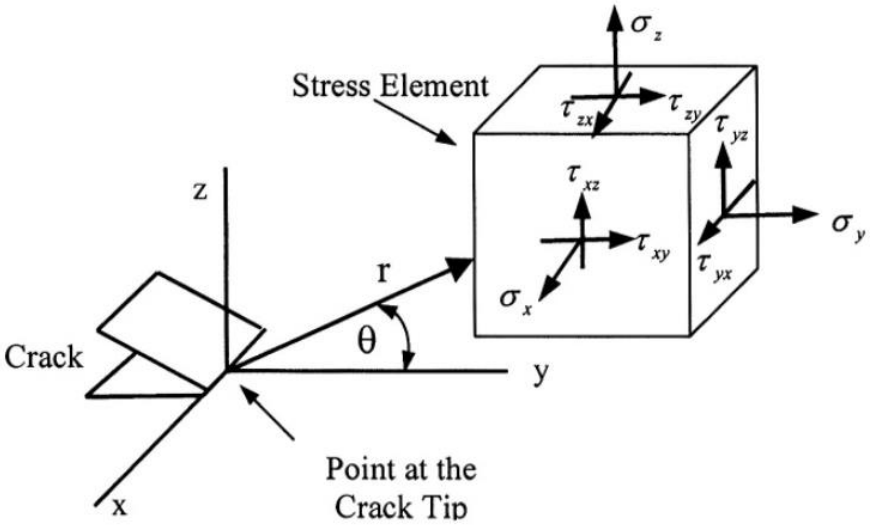

Fig. 3.2. Stresses at the vicinity of the crack tip [45].

- Mode I

In the Opening mode, the stresses and the displacements at the vicinity of the crack tip are given by the following equations for elastic behaviour:

The crack tip stress field is:

$$\sigma_{xx} \approx \frac{K_I}{\sqrt{2\pi r}} cos\frac{\theta}{2}\left(1 - sin\frac{\theta}{2} sin\frac{3\theta}{2}\right)$$

$$\sigma_{yy} \approx \frac{K_I}{\sqrt{2\pi r}} cos\frac{\theta}{2}\left(1 + sin\frac{\theta}{2} sin\frac{3\theta}{2}\right) \quad (3.1)$$

$$\tau_{xy} \approx \frac{K_I}{\sqrt{2\pi r}} cos\frac{\theta}{2} sin\frac{\theta}{2} cos\frac{3\theta}{2}$$

as $r \to 0$, where

$$K_I = \sigma\sqrt{\pi a} \quad \textit{for an infinite plate with a central crack} \quad (3.2)$$

and where K_I is mode I stress intensity factor, σ and τ are the applied normal and shear stress respectively, a is the crack length, r is the distance from the crack tip and θ is the angle.

The crack tip displacement field is υ, u

$$u \approx \frac{K_I}{2\mu}\sqrt{\frac{r}{2\pi}}cos\frac{\theta}{2}(\kappa - cos\theta)$$

$$\upsilon \approx \frac{K_I}{2\mu}\sqrt{\frac{r}{2\pi}}sin\frac{\theta}{2}(\kappa - cos\theta) \quad (3.3)$$

as $r \to 0$, where κ is equal to (3-4ϑ) for plane strain and (3-ϑ)/(1+ϑ) for plane stress.

Eqs. (3.1) and (3.3) represent the stress and displacement field for plane stress and plane strain conditions. The out-of-plane normal component of σ_{zz} for plane stress is assumed to be zero whereas for plane strain it exists and equals

$$\sigma_{zz} = \vartheta(\sigma_{xx} + \sigma_{yy}) \quad (3.4)$$

where ϑ is Poisson's ratio.

The singular principal stresses for plane stress and plane strain are

$$\sigma_1 \approx \frac{K_I}{\sqrt{2\pi r}}cos\frac{\theta}{2}\left(1 + sin\frac{\theta}{2}\right) \quad (3.5)$$

$$\sigma_2 \approx \frac{K_I}{\sqrt{2\pi r}}cos\frac{\theta}{2}\left(1 - sin\frac{\theta}{2}\right) \quad (3.6)$$

$$\sigma_3 \approx \frac{2\vartheta K_I}{\sqrt{2\pi r}}cos\frac{\theta}{2} \qquad (plane\ strain) \quad (3.7)$$

$$\sigma_3 = 0 \qquad (plane\ stress) \quad (3.8)$$

- Mode II

In the sliding mode and in Cartesian coordinates the stress at the vicinity of the crack tip (i.e the crack tip stress field) is given by the following equations:

$$\sigma_{xx} \approx \frac{K_{II}}{\sqrt{2\pi r}}sin\frac{\theta}{2}\left(2 + cos\frac{\theta}{2}cos\frac{3\theta}{2}\right)$$

$$\sigma_{yy} \approx \frac{K_{II}}{\sqrt{2\pi r}}sin\frac{\theta}{2}cos\frac{\theta}{2}cos\frac{3\theta}{2} \quad (3.9)$$

$$\tau_{xy} \approx \frac{K_{II}}{\sqrt{2\pi r}}cos\frac{\theta}{2}\left(1 - sin\frac{\theta}{2}sin\frac{3\theta}{2}\right)$$

as $r \to 0$, where

$$K_{II} = \tau\sqrt{\pi a} \quad \textit{for an infinite plate with a central crack} \quad (3.10)$$

and where K_{II} is the mode II stress intensity factor.

The crack tip displacement field is

$$u \approx \frac{K_{II}}{2\mu}\sqrt{\frac{r}{2\pi}}sin\frac{\theta}{2}(2+\kappa+cos\theta)$$

$$v \approx \frac{K_{II}}{2\mu}\sqrt{\frac{r}{2\pi}}cos\frac{\theta}{2}(2-\kappa-cos\theta) \quad (3.11)$$

as $r \to 0$.

- Mode III

Similarly, in the tearing mode the stress (i.e the crack tip stress field) is given by the following equations:

$$\tau_{xz} \approx -\frac{K_{III}}{\sqrt{2\pi r}}sin\frac{\theta}{2}$$

$$\tau_{yz} \approx \frac{K_{III}}{\sqrt{2\pi r}}cos\frac{\theta}{2} \quad (3.12)$$

as $r \to 0$, where

$$K_{III} = \tau\sqrt{\pi a} \quad \textit{for an infinite plate with a central crack} \quad (3.13)$$

and where K_{III} is the mode III stress intensity factor.

The crack tip displacement field is

$$w \approx \frac{K_{III}}{\mu}\sqrt{\frac{r}{2\pi}}sin\frac{\theta}{2} \quad (3.14)$$

as $r \to 0$.

For the three fracture modes, it is clear that there is a stress and strain singularity at the crack tip of the order of an inverse square root.

3.2 Crack tip plasticity

3.2.1 Plastic zone shapes [45]

The stress field from linear elastic fracture mechanics (equations presented above) is unbounded at the crack tip, i.e., as the distance from the crack tip (r) approaches zero there is no bound on the values attained by these stresses. However, infinite stresses do not occur in nature, and in reality, the material deforms plastically, so limiting the magnitude of the stress levels attained. In the region local to the crack tip, stress is constrained by a yield criterion appropriate to the material undergoing loading. If the size of this plastic region is very small compared to the crack length and the other dimensions, i.e. $r \ll a$ (small scale yielding), then LEFM still can be applied. But if the size of the plastic zone is large $r \gg a$ (large scale yielding), LEFM is no longer applicable and the EPFM should be applied. The size and the shape of the plastic zone can be derived by applying the singular principal stresses from Eqs (3.5) to (3.8) in one of the yielding criteria. Fig. 3.3 shows the plastic zone shape and size for mode I plane stress and plane strain.

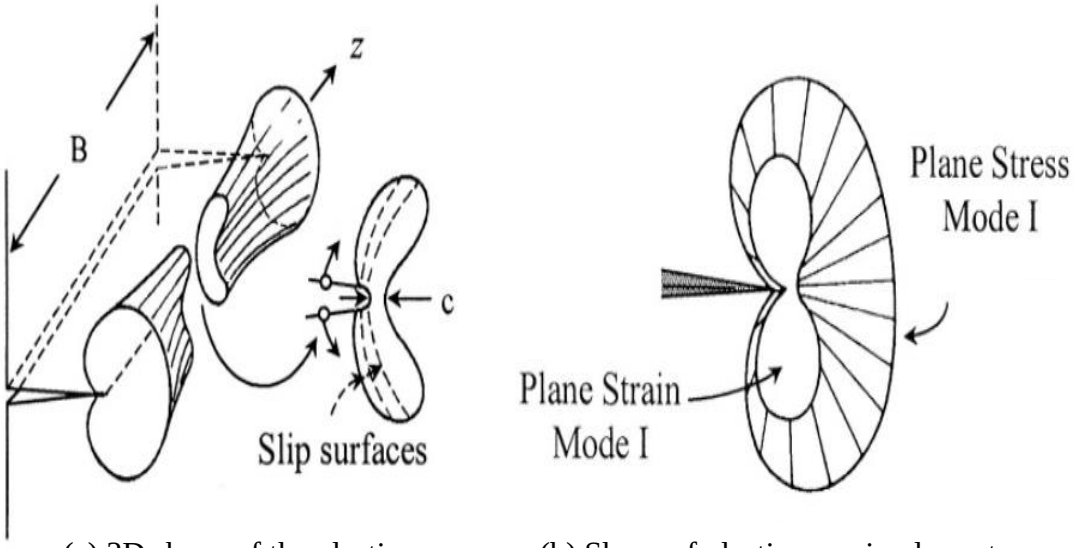

(a) 3D shape of the plastic *zone.*

(b) Shape of plastic zone in plane stress and plane strain for mode I.

Fig. 3.3. Plastic zone shape [45].

3.2.1.1 Von Mises yielding criterion

This theory is derived from the maximum distortion energy theory. In this theory, the stresses at yield in the mechanical part are represented by the principal stresses as it is defined in the following mathematical formula:

$$(\sigma_1 - \sigma_2)^2 + (\sigma_1 - \sigma_3)^2 + (\sigma_3 - \sigma_1)^2 = 2\sigma_Y^2 \tag{3.15}$$

where, $\sigma_1, \sigma_2, \sigma_3$ are the principal stresses and σ_Y is the material yield stress.

By substituting Eq. (3.5) through (3.8) into (3.15) the von Mises yielding criterion can be expressed for mode I as

$$\frac{K_I^2}{2\pi r}\left(\frac{3}{2}sin^2\theta + h(1 + cos\theta)\right) \approx 2\sigma_Y^2 \tag{3.16}$$

From Eq. (3.16) the size of the plastic zone r_p as it shown in Fig. 3.3(b) can be easily found:

$$r_p \approx \frac{1}{4\pi}\left(\frac{K_I}{\sigma_Y}\right)^2\left(\frac{3}{2}sin^2\theta + h(1 + cos\theta)\right) \tag{3.17}$$

where $h = 1$ for plane stress and $h = (1 - 2\vartheta)^2$ for plane strain.

Setting $\theta = 0$ gives the size of the plastic zone along the x-axis, which can be expressed as

$$r_p \approx \frac{h}{2\pi}\left(\frac{K_I}{\sigma_Y}\right)^2 \tag{3.18}$$

3.2.2 Dugdale's approximation [45, 91]

A strip yield model in the plane stress condition was suggested by Dugdale [7] to estimate the plastic zone size. In this model, the plastic zone ahead of the crack tip is assumed to be a narrow strip of a length r. In the strip, the stress is assumed constant and has a value equal to the yield stress σ_Y as shown in Fig. 3.4. The length of the plastic zone according to this assumption can be found by

$$r = \frac{\pi}{8}\left(\frac{K_I}{\sigma_Y}\right)^2 \tag{3.19}$$

with

$$a_e = a + r \tag{3.20}$$

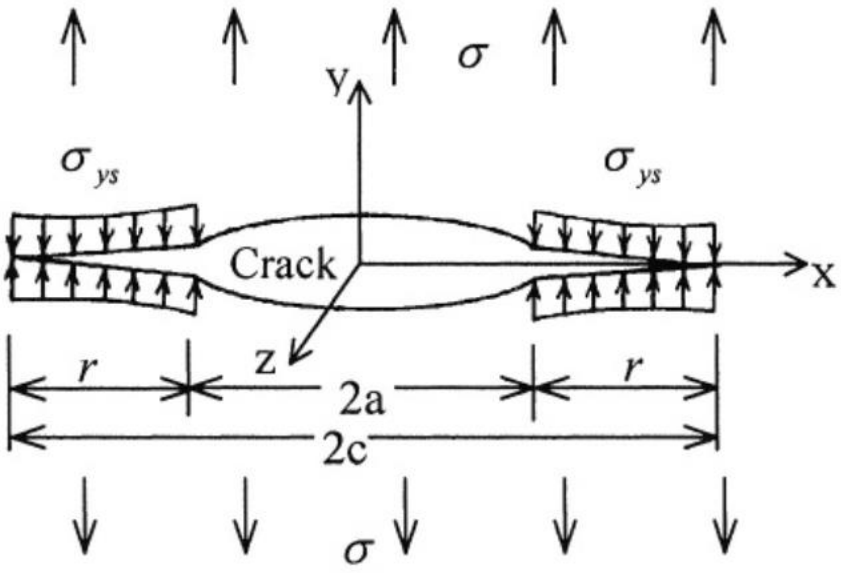

Fig. 3.4. Dugdale plastic zone approximation [45].

3.2.3 Crack tip opening displacement [45]

If the size of the plastic zone is relatively large, then the use of linear elastic fracture mechanics is invalid, and a single material parameter K_{IC} is insufficient to describe the fracture process. Nonlinear fracture mechanics is required, and one approach is the crack tip opening displacement (CTOD) model. This approach makes use of the CTOD δ_t along with the concept of a critical CTOD δ_c, (a material parameter) which is relatable to fracture toughness.

It is shown above that one possible way to reflect the effect of plasticity on a crack is by means of the effective-crack length a_e. This approach is also applicable to a CTOD model in the form illustrated in Fig. 3.5. The elastic crack opening displacement δ is related to the displacement of the upper and lower face of the crack and can be approximated by

$$\delta = \frac{4\sigma}{E}\sqrt{a^2 - x^2} \qquad (uncorrected) \tag{3.21}$$

or more correctly

$$\delta = \frac{4\sigma}{E}\sqrt{(a+r)^2 - x^2} \qquad (corrected) \tag{3.22}$$

where δ is the crack tip opening displacement, σ is the normal stress, E is the elastic modulus. Finally, a, x and r are the crack length, the distance between the loading point and the centre of the crack, and the plastic zone length respectively.

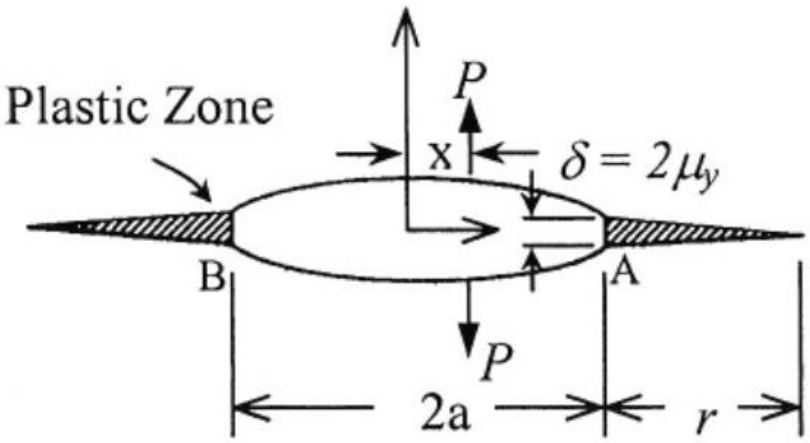

Fig. 3.5. CTOD according to the virtual crack length criterion [45].

At the crack tip ($x = a$) the CTOD δ_t is defined and on setting $\delta = \delta_t$ in Eq. (3.22) gives

$$\delta_t = \frac{4\sigma}{E}\sqrt{(a+r)^2 - a^2} \approx \frac{4\sigma}{E}\sqrt{2ar} \tag{3.23}$$

By applying the value of r from Eqs. (3.19) in Eq. (3.23) the CTOD defined for plane stress is

$$\delta_t = \frac{2K_I^2}{E\sigma_Y} \qquad (Dugdale's\ model) \tag{3.24}$$

Alternative mathematical models for δ_t exist (see [45]) and two popular models founded on Dugdale's theory are

$$\delta_t = \frac{K_I^2}{E\sigma_Y} \qquad (Burdekin) \tag{3.25}$$

and

$$\delta_t = \frac{(\kappa+1)(1+\vartheta)K_I^2}{4\pi E\sigma_Y} \qquad (Rice) \tag{3.26}$$

CTOD models gained traction in recent times because to a certain extent they overcame some of the limitations of the single parameter K_I approach. Moreover, as mentioned above, δ_t (δ_c in the case of the cohesive model) can be related to the fracture toughness and plays a significant role in cohesive models, which are discussed in the following chapter.

3.3 Dynamic fracture

It has been indicated by the elastodynamic fracture analysis that the stresses and displacements in a material loaded dynamically can differ greatly from the stresses and displacements when the material loaded statically. Dynamic loading results in higher stress levels in the vicinity of cracks and fracture can take place quickly providing insufficient time for yielding to develop. In most material, with dynamic loading the mechanical properties of the material such as the yield stress and the ultimate tensile strength increase with increasing the loading rate [91].

3.3.1 Effect of strain rate [92]

As the mechanical properties for some materials are highly affected by the loading rate, the stress-strain curve is significantly influenced by applied strain rate (see Fig. 3.6). From the figure it is apparent that with increasing rate some materials like mild steel become stronger since the flow stress is increasing. However the rupture strain decreases reducing the ductility of the material. Strain rate sensitivity is an important mechanical property to be determined, since it influences the dynamic behaviour of the material. The effect of strain rate on the material parameters that defines the stress-strain curve have been widely investigated; this includes the yield and tensile strength, rupture strain, energy dissipation and also the work hardening strength and coefficient. According to Larour [93] the true stress and not the engineering stress should be used to define the stress sensitivity and because of that only the yield stress can be directly used. However there are many attempts to investigate the strain rate sensitivity of the tensile strength for many materials, for example by using the concept of a dynamic increase factor (DIF) which represents the ratio between the dynamic and the quasi-static values of both the yield stress and the tensile strength [94].

The dependence of the flow stress on strain rate for some materials can be represented by [92]

$$\sigma_{(\dot{\varepsilon})} = C\dot{\varepsilon}^{m} \tag{3.27}$$

where $\sigma_{(\dot{\varepsilon})}$ is the rate dependent flow stress, C is the coefficient of strain hardening and m is strain rate sensitivity, which is typically a function of temperature in metals.

The rate of strain is defined as the derivative of the strain with respect to time, and it is measured in s^{-1}. The flow stress of the material increases with increasing the strain rate. It is observed that at lower plastic strains the tensile strength is less affected by rate than flow stress and yield stress. The strain rate can be expressed in terms of the crosshead velocity.

Then the engineering strain rate can be expressed as

$$\dot{e} = \frac{de}{dt} = \frac{d}{dt}\frac{(l-l_o)}{l_o} = \frac{1}{l_o}\frac{dl}{dt} = \frac{v}{l_o} \tag{3.28}$$

where $\dot{e}$ is the engineering strain rate, e is the engineering strain, l is the true length, l_o is the original length and v is the crosshead velocity.

The true strain rate is

$$\dot{\varepsilon} = \frac{d\varepsilon}{dt} = \frac{v}{l} \tag{3.29}$$

The crosshead velocity is defined as

$$v = \frac{dl}{dt} \tag{3.30}$$

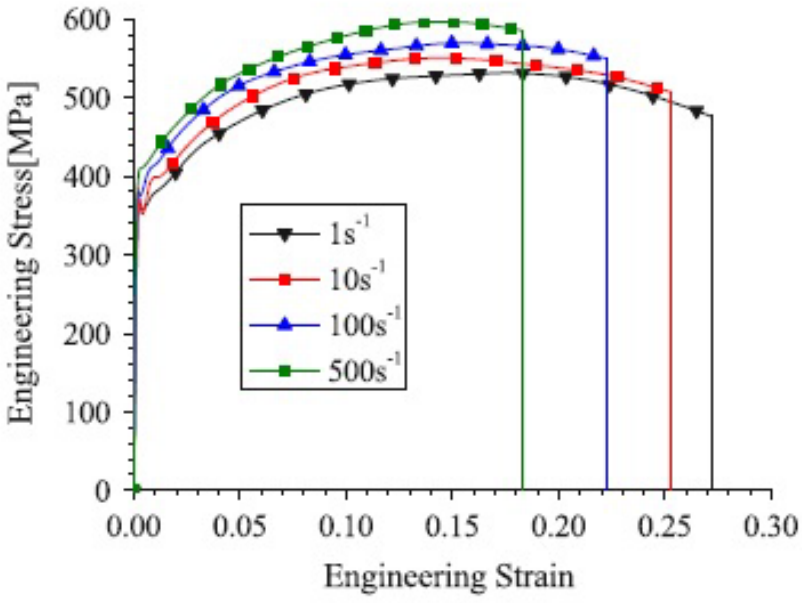

Fig. 3.6. Effect of strain rate on engineering stress-strain curve of mild steel [113].

3.3.2 Material constitutive relationships at high strain rate

The relations between stress and strain is described by constitutive equations in terms of the instantaneous values of strain, strain rate and temperature[92]. A mathematical equation is usually used to describe the flow behaviour; this equation has a number of material parameters that are required to be fed to the finite element solver to numerically simulate the material behaviour under a high loading rate [95]. There are two types of constitutive equations used in the literature to describe the flow behaviour of the materials under different applied strain rate and temperatures; the first one is based on the physical behaviour of the material. Although this method is more accurate, it requires the determination of a large number of material constants which is quite complicated. The second method is a phenomenological one which is based on experience and the experimental observations of the material behaviour. The phenomenologically based constitutive equations require fewer constants and is widely used in commercial finite element solvers [96], [97]. They are less flexible however because their constants are specific to the particular material and boundary conditions (applied strain rate and temperature ranges).

In the literature, there are many constitutive models that have been used to simulate the loading rate effect on a wide range of materials and their results acceptably fit the experimental data. A review of the most common model will be illustrated here:

The Cowper-Symonds [98] constitutive model can be considered among the simplest model that addressing the strain rate sensitivity in metallic alloys. However, it does not account for strain hardening and temperature effects. This model is represented mathematically as

$$\frac{\sigma_{dyn}}{\sigma_{stat}} = 1 + \left(\frac{\dot{\varepsilon}}{D}\right)^{\frac{1}{q}} \qquad (3.31)$$

where σ_{dyn} and σ_{stat} are the dynamic and static yield stress, respectively; $\dot{\varepsilon}$ is the strain rate, D and q are material parameters obtained from tuning with experimental result.

Second is the empirical model introduced by Johnson Cook [99] that relates the dynamic stress to the strain hardening, strain rate hardening and thermal softening, which is widely used in finite element solvers due to its simplicity. The model is represented mathematically as

$$\sigma = (A + B\varepsilon_p^n)(1 + C \ln \dot{\varepsilon}^*)(1 - T^{*m}) \quad (3.32)$$

$$\dot{\varepsilon}^* = \frac{\dot{\varepsilon}_p}{\dot{\varepsilon}_o} \quad (3.33)$$

$$T^* = \frac{T - T_{room}}{T_{melt} - T_{room}} \quad (3.34)$$

where A is the yield stress at a reference strain rate, B, C, n and m are the strain hardening constant, the strain rate strengthening coefficient, the strain hardening coefficient and the temperature softening coefficient, ε_p is the accumulated plastic strain, $\dot{\varepsilon}^*$ is a dimensionless strain rate, $\dot{\varepsilon}_o$ is a reference strain rate and T, T_{room} and T_{melt} are the working , room and melting temperatures, respectively.

The Zerilli-Armstrong model [100, 101] is an example of a Physical model that is based on dislocation mechanics. This model has two forms depending on the material structure, one for the metals with a face centered cubic (fcc) structure and the other is for the metals with the body centered cubic (bcc) structure.

The model for fcc metals is present as

$$\sigma = C_o + C_2\varepsilon^{1/2}\exp(-C_3T + C_4T \ln \dot{\varepsilon}) \quad (3.35)$$

While the relationship for the bcc metals is given as

$$\sigma = C_o + C_1 \exp(-C_3T + C_4T \ln \dot{\varepsilon}) + C_5\varepsilon^n \quad (3.36)$$

where ε, $\dot{\varepsilon}$, T, are equivalent plastic strain, equivalent strain rate, absolute temperature respectively. C_o, C_1, C_2, C_3, C_4, C_5 and n are material constants.

Some limitations on applying the previously mentioned equations (physical and phenomenological) to dynamic crack growth have been reported in the literature see [97, 102–105].

3.4 Energy balance at the crack propagation [45, 91]

Crack growth can be represented thermodynamically by investigating the energy balance of a crack growing at a slow rate. Consider a body containing an embedded crack subjected to external loading, which does a work on the body. As a result the change of this work will cause a change in the internal, kinetic and fracture energies of the body. The energy balance of such a body can be indicated from the energy conservation law as:

$$\dot{W} = \dot{E} + \dot{K} + \dot{\Gamma} \tag{3.37}$$

where $\dot{W}$ is the rate of change in the work done by the applied forces with the change in the crack's area, $\dot{E}$, $\dot{K}$ and $\dot{\Gamma}$ are the rates of change in the internal, kinetic and fracture energies respectively, with the change in the crack's area.

In a ductile material, the internal energy can be divided into elastic stored energy U^e and the dissipated energy as a result of plastic deformation U^p. So

$$E = U^e + U^p \rightarrow \dot{E} = \dot{U^e} + \dot{U^p} \tag{3.38}$$

where $\dot{U^e}$ and $\dot{U^p}$ are the rate of change in the elastic energy and the dissipated energy in the plastic deformation, respectively.

By substituting Eq. (3.38) in (3.37) we get

$$\dot{W} = \dot{U^e} + \dot{K} + \dot{U^p} + \dot{\Gamma} \tag{3.39}$$

Eq. (3.39**)** indicates that the supplied work rate to the body is equal to the rate of change of stored elastic strain energy plus the change in kinetic energy plus the change in dissipated energy in plasticity and the formation of new surfaces. For slow crack propagation, the rate of change in the kinetic energy could be neglected so Eq. (3.39) takes the following form

$$\dot{W} - \dot{U^e} = \dot{U^p} + \dot{\Gamma} \tag{3.40}$$

The right-hand side of Eq. (3.40) represent the rate of dissipated energy in the fracture process or it can be found in the literature as the fracture resistance G_{ic}, while the left-hand side depicts the energy release rate G_i (where i reffere to the loading mode *I, II, III*).

$$G_i = \dot{W} - \dot{U^e} \tag{3.41}$$

Griffith has found that the energy release rate G_i that is required to form two sides of the crack surface in an elastic material is equal to material resistance to fracture G_{ic}, mathematically speaking:

$$G_{ic} = \dot{\Gamma} = 2\gamma \tag{3.42}$$

In this case, the crack propagates when the energy release rate reaches this critical value G_{ic}, the condition for crack propagation is

$$G_i \geq G_{ic} \tag{3.43}$$

Eq. (3.42) represent the material resistance to fracture, which is a material property. The relation between the global strain energy release rate G_i and the local stress intensity factor K_i, is significantly important. This relation for mode I crack growth can be formed as:

$$G_I = \frac{K_I^2}{E} \qquad (plane\ stress) \tag{3.44}$$

$$G_I = \frac{(1-\vartheta^2)K_I^2}{E} \qquad (plane\ strain) \tag{3.45}$$

Where: G_I and K_I are the mode I strain energy release rate and stress intensity factor respectively, E is the modulus of elasticity, and ϑ is Poisson's ratio.

3.5 Cohesive-zone model (CZM)

The cohesive model was proposed in an idealized form to overcome the unrealistic stress singularity at the crack tip and to simplify the process of complex crack growth. A CZM can be used to simulate damage and fracture in different types of material such as: metals, concrete, polymers and a lot of other materials [10, 106]. Simply, this model suggests that there is a cohesive-zone ahead of the crack tip, which is controlled by a cohesive force. The crack is simulated by means of two adjoined surfaces and a cohesive traction whose magnitude is controlled by a displacement discontinuity (i.e. a separation) through a traction separation law. When an external tensile load is applied to a body it will attempt to separate these surfaces and once the traction in the cohesive-zone reaches the value of the critical cohesive traction σ_c, damage begins and a complete failure of the element happens when the separation between the two surfaces reaches a critical value δ_c.

The idea of the cohesive-zone dates back to the 1960s when Dugdale [7] introduced his strip-yield model as shown on the left side of Fig. 3.7. In this model, the stresses at the cohesive-zone were assumed constant and equal to the material yield strength σ_Y and the material behaviour is assumed to be elastic-perfectly plastic. However, in reality, most materials used in industry have an elasto-plastic behaviour and the stresses at the cohesive-zone are much larger than the yield strength. Two years later, Barenblatt [8] studied the crack behaviour in brittle fracture, he used a cohesive law, which acts in a process zone, to represent the cohesive traction rather than a constant yield stress. In this cohesive law, the traction is related to the distance from the physical crack tip as shown

on the right side of Fig. 3.7. Cohesive laws subsequent to Barenblatt's work relate traction to separation between the cohesive surfaces rather than the distance from the crack tip. In both previous models the critical traction in the process zone along the crack direction is a material property and is not dependent on the shape of the body or the type of the applied loads [10].

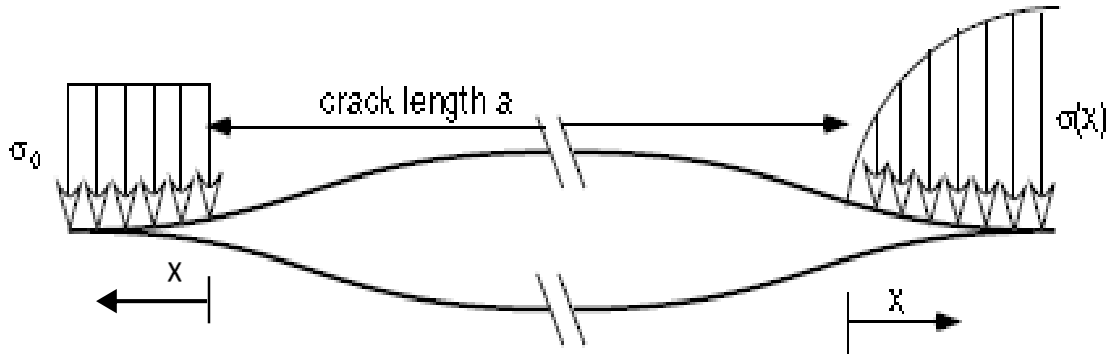

Fig. 3.7. Cohesive representation of crack: left hand side is Dugdale model, right hand side is Barenblatt model [6].

The first application of the cohesive model as an embedded element in a finite element model was carried out by Hillerborg et al.[9] in his brittle fracture study. He proposed traction separation law in which the stress at the process zone is a function of separation, which formed the genesis of different type of TSLs that followed.

3.6 Traction separation law (TSL)

Many different types of TSLs can be found in the literature, examples of which are the polynomial, exponential, bilinear, and trapezoidal laws depicted in Fig. 3.8. The cohesive model is not a physical material model, but it is a phenomenological law that tries to capture the physics of the fracture process. Therefore, there is no physical evidence of the typical shape of the function that relates the traction to the separation. Generally, in all the traction separation laws the traction increases from zero with increasing displacement until it reaches the critical cohesive traction beyond which permanent material separation takes place. Separation increases up to final failure, which occurs at a prescribed critical separation value.

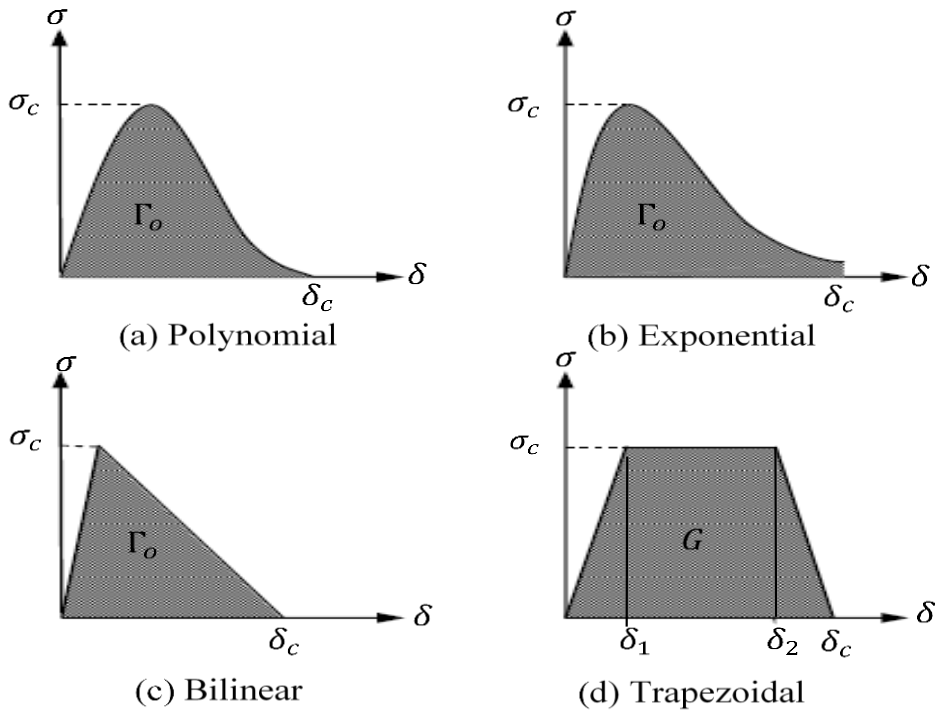

Fig. 3.8. The widely used traction separation laws.

The trapezoidal cohesive-zone model (TCZM) that is illustrated in Fig. 3.9 is adopted for this study because it provides reasonable flexibility arising from the extended parameter set $\{\delta_1, \delta_2, \delta_c, \sigma_c\}$. This can be used for example to arrive at the linear cohesive-zone model (LCZM) on setting $\delta_1 = \delta_2 = 0$ or the bilinear cohesive-zone model (BCZM) with $\delta_1 = \delta_2 \neq 0$ and thus facilitates investigations into the influences of different traction separation curves.

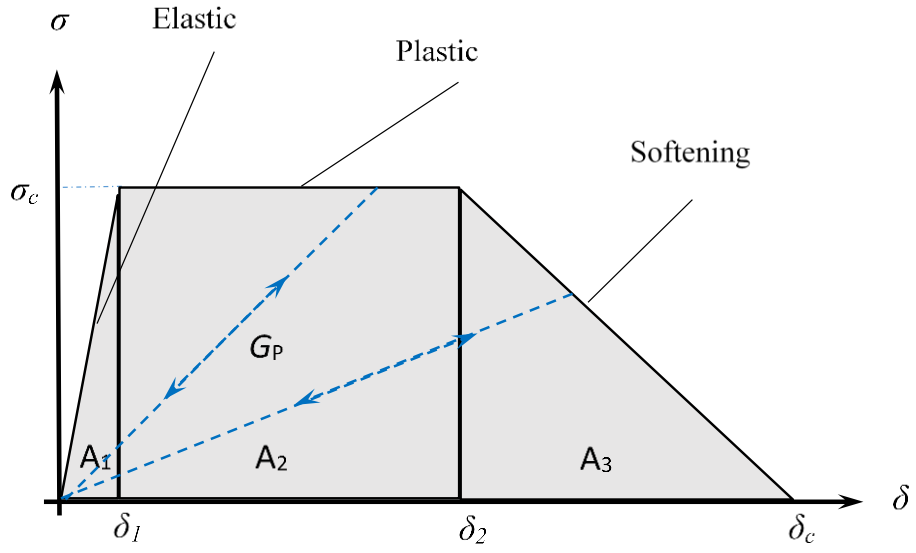

Fig. 3.9. Standard trapezoidal traction-separation law.

For a pre-defined traction separation law (TSL), two cohesive parameters are usually sufficient to simulate the fracture process. The most frequently used parameters in the literature are the cohesive-energy or toughness G_c and critical cohesive traction σ_c. The critical separation δ_c can be used in place of G_c but does suffer the disadvantage of not being directly measurable. It is important to appreciate that the cohesive approach is an approach that represents damage as a single-tearing crack, so δ_c is generally not physically observable. The area under the traction separation curve represents the total dissipated energy (per unit area) and typically accounts for energy dissipated due to local plasticity and the energy that is required to form new surface. The ability of the cohesive-zone element to represent the local dissipation mechanism of plasticity is a particular advantage of the approach. It provides for example elasto-plastic fracture-mechanics analysis for an elastic-bulk material with the assumption that plasticity is localised at the crack tip. The extent of the plasticity is accounted in the TCZM by the two parameters δ_1 and δ_2. The toughness (fracture energy) G_c is represented by the area under the traction separation curve and is represented mathematically as

$$G_c = \int_0^{\delta_c} \sigma(\delta) d\delta \tag{3-46}$$

which for the trapezoidal traction-separation law shown in Fig. 3.9 gives

$$G_c = \left(\int_0^{\delta_1} \sigma(\delta) d\delta + \int_{\delta_2}^{\delta_c} \sigma(\delta) d\delta \right) + \int_{\delta_1}^{\delta_2} \sigma(\delta) d\delta = (A_1 + A_3) + A_2 = \Gamma_o + G^{\mathrm{p}} =$$

$$\left(\frac{\sigma_c}{2} \delta_1 + \frac{\sigma_c}{2} (\delta_c - \delta_2) \right) + \sigma_c (\delta_2 - \delta_1) = \frac{\sigma_c}{2} (\delta_2 - \delta_1 + \delta_c) \tag{3-47}$$

where toughness G_c is the total dissipated energy (i.e. energy dissipated per unit area), G^{p} is the plastic dissipated energy (accounting for local plasticity), Γ_o is the critical cohesive energy (accounting for surface formation), σ is the cohesive traction, σ_c is the critical cohesive traction, δ_1 is the separation at which σ first reaches σ_c, δ_2 is the displacement at which damage is formally assumed to start, and finally δ_c is the critical cohesive separation, at which separation occurs.

It is important to appreciate that although this relationship provides the fracture-energy (per unit area)

$$\Gamma_o = \frac{\sigma_c}{2} (\delta_1 - \delta_2 + \delta_c) \tag{3-48}$$

and the plastic-energy (per unit area)

$$G^{\mathrm{p}} = \sigma_c(\delta_2 - \delta_1) \tag{3-49}$$

Identified with particular areas under the traction separation curve (see Fig. 3.9), this association is essentially a matter of choice. The association of particular dissipation mechanisms with particular features of the traction separation curve is nothing more than a contrivance. Note also that the region $[0,\ \delta_1]$ is primarily included to avoid an abrupt change in behaviour which can be problematic for some numerical solvers, however, this region is not strictly necessary and does not affect the analysis results. If the model undergoes unloading before reaching the critical stress, then the unloading-path taken is identical to the loading path. Beyond the cohesive critical stress however damage is permanent and consequently the element stiffness decreases. The new stiffness value is $K = \sigma_{max}/\delta_{max}$, where σ_{max} and δ_{max} are the stress and separation at the onset of unloading, respectively. The stress at unloading and reloading is evaluated from $\sigma(\delta) = K\delta$ as depicted in Fig. 3.9.

The traction separation law depicted in Fig. 3.9is represented mathematically as

$$\sigma_{(\delta)} = K_{coh}\,\delta \begin{cases} 1 & if\ \ 0 < \delta < \delta_1 \\ \left(1 - D_{(\delta)}\right) & if\ \ \delta_1 < \delta < \delta_c \\ 0 & if\ \ \delta \geq \delta_c \end{cases} \tag{3-50}$$

where $\sigma_{(\delta)}$ is the cohesive traction, K_{coh} represents the cohesive stiffness, the value of δ_1 should be very small and δ_2 should be close to δ_c as advised by Scheider et al. [56] and they set as.

$$\delta_1 = \frac{\sigma_c}{K_{coh}} \tag{3.51}$$

$$\delta_2 = 0.75 \times \delta_c \tag{3.52}$$

In the cohesive model, the mechanism of crack propagation in ductile material as the one used in this work is void nucleation, growth and coalescence. The damage variable $D_{(\delta)}$ is a damage parameter that represent the ratio between the damage area A_d to the original reference area A_e [71]. In the present configuration damage can be represented by the relationship

$$D(\delta) = \frac{A_d}{A_e} = \begin{cases} 1 - \frac{\delta_1}{\delta} & if\ \ \delta_1 \leq \delta < \delta_2 \\ 1 - \frac{\delta_1(\delta_c - \delta)}{\delta(\delta_c - \delta_2)} & if\ \ \delta_2 \leq \delta \leq \delta_c \end{cases} \tag{3.53}$$

If $\delta_1 = \delta_2 = \delta_o$ we will get the bilinear cohesive model, Hence

$$\Gamma_0 = \frac{1}{2}\sigma_c\delta_c \tag{3.54}$$

$$D(\delta) = \frac{A_d}{A_e} = 1 - \frac{\delta_o(\delta_c - \delta)}{\delta(\delta_c - \delta_o)} \tag{3.55}$$

3.7 Fatigue mechanism

3.7.1 Introduction

Fatigue is the phenomenon of accumulated damage, which is caused by repeated cyclic loading. When mechanical parts are subjected to a cyclic loading, an accumulation of material dislocations will occur at the surface that leads to the initiation of micro cracks. One of these micro cracks will propagate to a macro crack which will propagate to reach a critical length, then the final fracture happens. It is well known that a fatigue crack grows only in a plastically deformed region. A deep understanding of the fatigue crack process is required to identify the material parameters that affect the fatigue life. In general, fatigue crack processes could be divided into three parts: crack initiation, crack propagation (short and long crack propagation) and final fracture.

3.7.2 Fatigue crack initiation

Fatigue cracks generally initiate at the surface or at the grain boundaries along the localised maximum shear direction. Fatigue cracks initiate when the material is subjected to cyclic loads as a result of dislocation movement. For instance, if slip occurs in the loading part of the load cycle, this slip will lead to strain hardening in the slip band with increasing the load as a result, when the material goes under the unloading part of the load cycle this slip band will face a greater shear stress but in the opposite direction. A similar process will happen in the next load cycles, and the accumulation of these slip bands will lead to a stress concentration point (initial crack that could propagate later on) as shown in Fig. 3.10(a to d). This is the ideal process since the material is not always homogeneous and in fact, could include defects such as voids and/or notches which lead

to stress concentrations. In addition, the material surface roughness could play a similar role and lead to crack initiation [106, 107].

3.7.3 Fatigue crack propagation

Once a micro-crack initiates, and with continuous cyclic loading, the crack starts to propagate through a grain boundary and in the maximum shear plane. As shown in Fig. 3.10 the crack growth period can be divided into two stages. The first stage is the propagation of the micro-cracks (short crack), in this stage, the cracks propagate in the local shear stress direction for a specific short length approximately two grains. The slip characteristics, the grain size, the direction and the load level have a significant effect on the crack tip plasticity at this stage because the crack length is relatively small compared to the microstructure of the material. In general, when a crack tip reaches a grain boundary the growth rate decreases, however, it will speed up again as soon as the crack passes through the boundary as shown in Fig. 3.11. The second stage is the propagation of the macro-cracks (long crack), in this stage, the crack tends to propagate in a direction normal to the global tensile stress direction as shown in Fig. 3.10. At this stage, the plastic zone ahead of the crack tip is much larger than the material grain size, which makes the crack growth at this stage less sensitive to the material microstructure than the first stage [106, 107].

In many engineering structures, fatigue crack growth in both the first and second stage represents the largest part of the total material life. Fig. 3.12 shows a diagram for the crack length versus the number of cycles, the crack propagation stages are represented by the useful life of the mechanical part, which is about 70% of the total life. Therefore, it is important to accurately predict the fatigue crack growth rate in these stages to get a good estimation of the total fatigue life. In the diagram a_i denotes a very small crack that is difficult to find experimentally, but it is large enough to apply fracture-mechanics methods. Cracks with this magnitude of length (a_i) usually exists in mechanical parts as a result of surface roughness or defects during the production process, while a_1 denotes the minimum length that can be detected experimentally

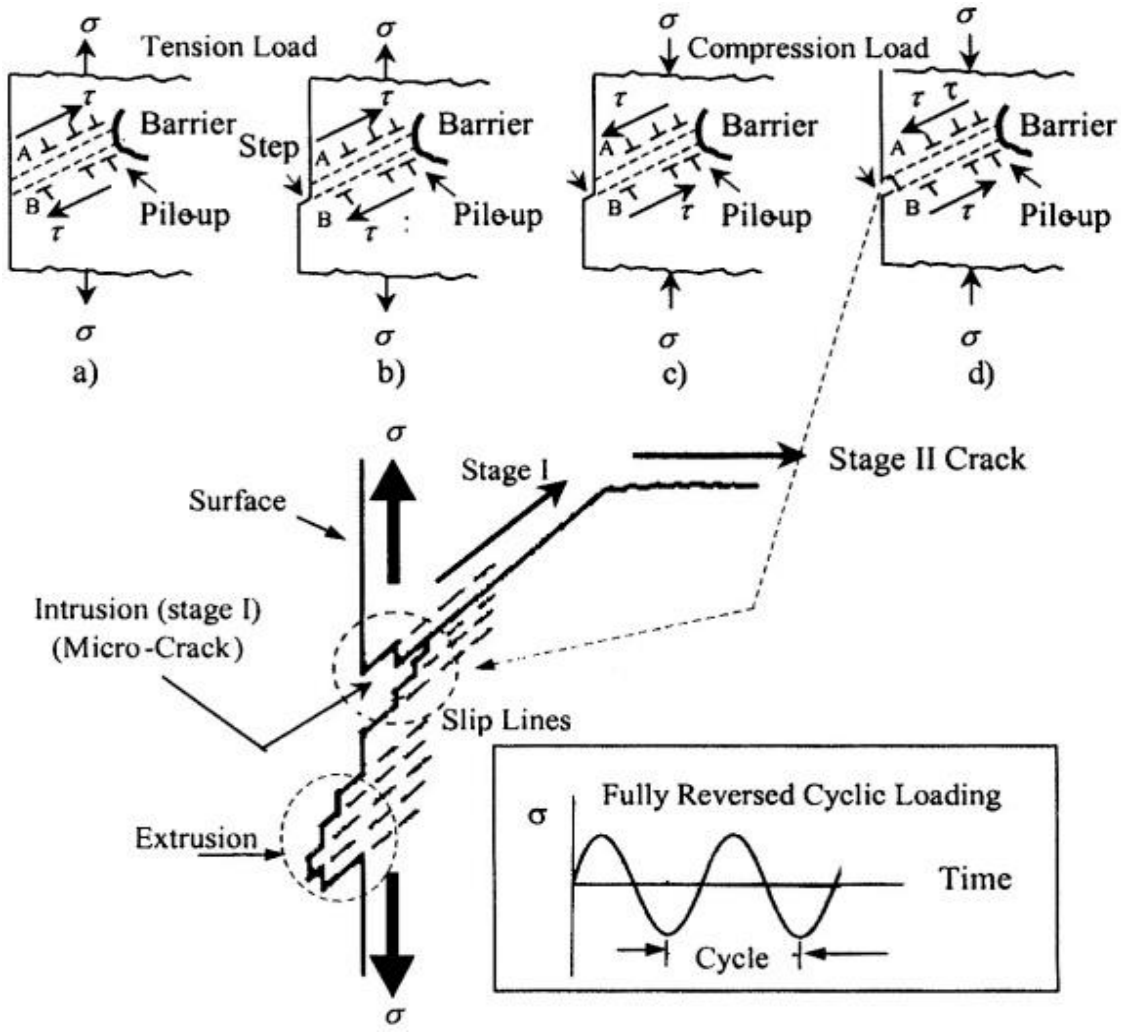

Fig. 3.10. Fatigue crack initiation and propagation process [45].

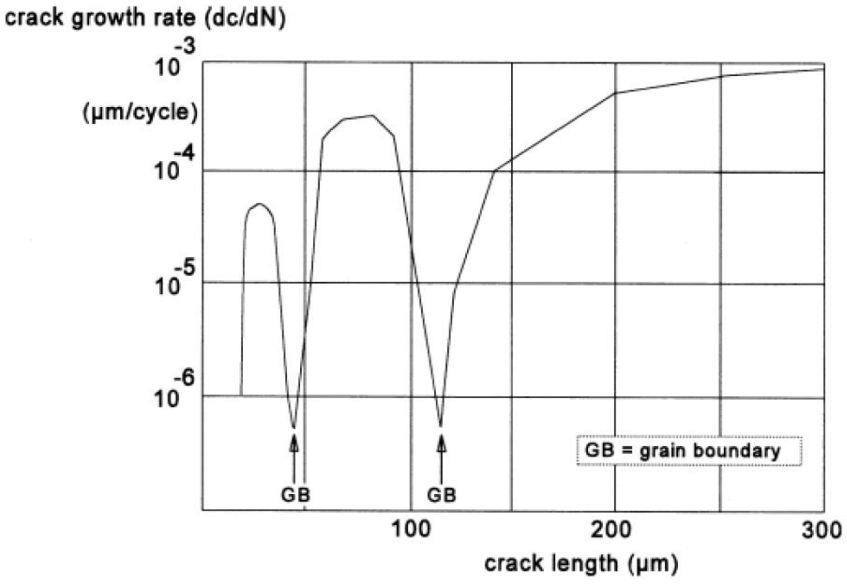

Fig. 3.11. The effect of grain boundary on crack growth rate

.

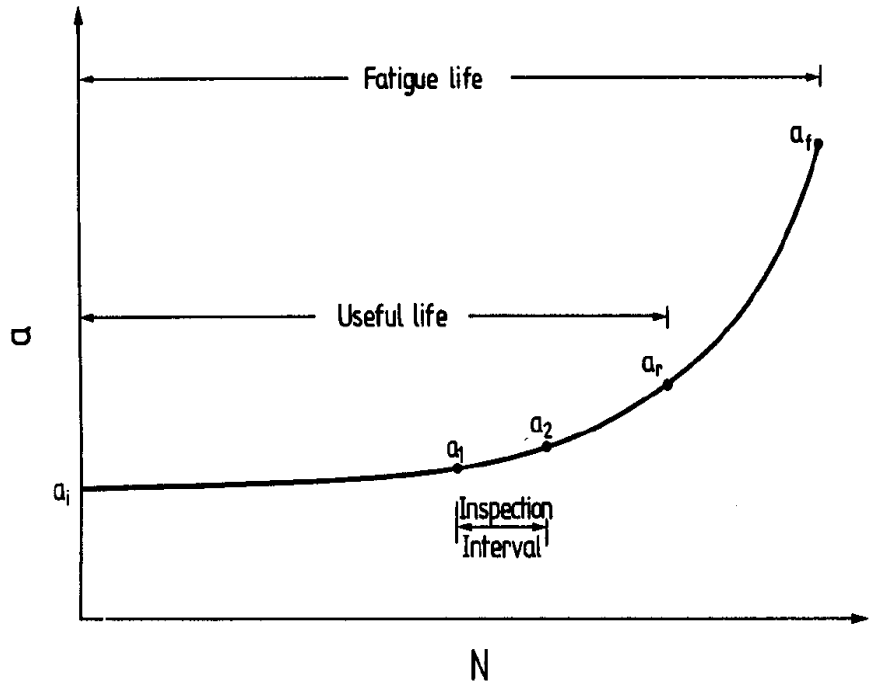

Fig. 3.12. Ideal $a - N$ curve for constant amplitude loading [91].

A large effort has been done to understand the behaviour of fatigue crack growth involving a remarkably large number of fatigue experiments to study fatigue crack growth of pre-cracked standard test specimens. From the results of these experiments, a relationship between the crack extension and the number of loading cycles required for this extension is obtained. In this relation, the change in the number of cycles is related to change in crack length through the change in the stress intensity factor (ΔK). Usually from the experimental results a diagram between the natural log of the crack growth rate (da/dN) and the natural log of ΔK is plotted. A typical $(da/dN) - \Delta K$ diagram is shown in Fig. 3.13, where the curve can be divided into three parts. Region I represents the near threshold region for long cracks, in this region the crack growth rate decreases sharply with reducing ΔK to reach a threshold value ΔK_{th} below which no crack propagation is observed.

Region II is the steady crack growth region, or so-called Paris region, in which a linear relation between log (da/dN) and $log(\Delta K)$ is observed. Reference [4] suggested a formula to represent the crack growth rate in this region, i.e.

$$\frac{da}{dN} = A(\Delta K)^n \tag{3.56}$$

where A is a constant that is obtained experimentally and assumed to be a material property, n is a constant representing the slope of the curve.

Finally region III, is an unstable crack growth region. In this region the microstructure, mean stress and the thickness have a large influence on the crack growth. The dominant fracture mode in this region is ductile tearing and is essentially governed by the maximum stress intensity factor which should be equal to the critical stress intensity factor K_c. A transition curve was introduced by Forman et al. [36] to account for the material behaviour in this region:

$$\frac{da}{dN} = \frac{B\Delta K^m}{[(1-R)K_c - \Delta K]}$$

where B *and* m *are* constants that are obtained experimentally.

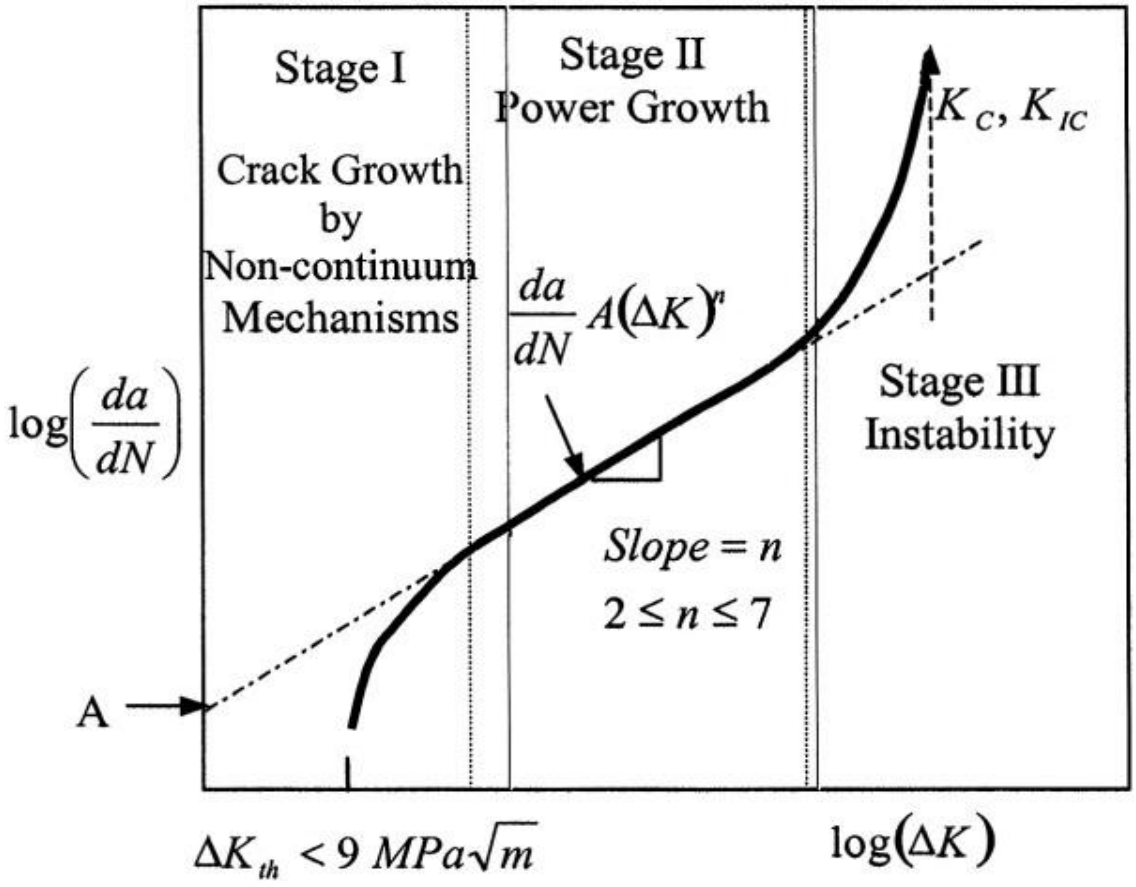

Fig. 3.13. Log-log scale for da/dN -ΔK curve [45].

Chapter 4: Frequency-dependence of fatigue crack growth in 304 stainless-steel

4.1 Introduction

Austenitic stainless-steel 304 is widely used in many structural and mechanical applications, where toughness and resistance to corrosion are required, such as automotive industries, power plants and pressure vessels [85]. The austenite phase in this austenitic stainless-steel is unstable and easily transforms to martensite under plastic deformation. Although this feature makes this type of stainless-steel a very good candidate for many applications, engineers need to be aware that in the case of cyclic-loading applications the rate at which fatigue cracks grow can vary significantly with the applied load frequency.

The martensite content affects the strength of the austenitic stainless-steel, the formation of this martensite depends on the strain amplitude, temperature, grain size and the number of loading cycles for the case of fatigue [82, 83]. As the austenitic-martensitic phase transformation depends on the plastic deformation, which in turn is dependent on strain rate, it follows that the frequency at which the cyclic load is applied can have an effect on the martensitic content and consequentially on fatigue crack-growth rates. Although the meta-stable austenitic stainless-steel type 304 is widely used in many applications, there is limited work on the effect of frequency on the fatigue crack growth in this material. Exceptions are references [89] and [90], where the influence of temperature is discussed.

This chapter is addressing the effect of frequency on fatigue crack growth in stainless-steel type 304 in air environment at room temperature. The details about the material used for this work is presented in Section 4.2 along with the specimen preparation and the test procedure. Section 4.3 is focusing on the results and the discussion. Finally, the key point of the finding of this study is summarised in Section 4.4.

4.2 Experimental details

A meta-stable austenitic stainless-steel (AISI type 304) with the chemical composition and the mechanical properties shown in Table 4.1 and

Table 4.2 as provided from the supplier has been used for the investigation of the frequency effect on the fatigue crack growth rate.

Table 4.1 Chemical composition (wt%).

C	Si	Mn	Ni	Cr	N	S	P
0.021	0.35	1.48	8.03	18.13	0.072	0.004	0.033

Table 4.2 Mechanical properties.

Yield strength (MPa)		Tensile strength (MPa)	Elongation after fracture (%)	Hardness
Rp 0.2%	Rp 0.1%			HRB
305	340	637	58	85

The true stress-plastic strain curve done by a tension test is tabulated in Table 4.3.

Table 4.3 True stress, true strain data

N	True stress (Pa)	Plastic strain	N	True stress (Pa)	Plastic strain
1	3.4e+08	0	23	8.37367e+08	0.323344
2	3.41387e+08	0.0380824	24	8.63451e+08	0.340508
3	3.63185e+08	0.0450476	25	8.87491e+08	0.356932
4	3.90833e+08	0.056557	26	9.16494e+08	0.37553
5	4.10383e+08	0.0656893	26	9.37995e+08	0.389663
6	4.24421e+08	0.0727229	28	9.56103e+08	0.401527
7	4.44926e+08	0.0837219	29	9.833e+08	0.418983
8	4.7178e+08	0.098244	30	1.01079e+09	0.436213
9	4.91104e+08	0.109111	31	1.04513e+09	0.456581
10	5.08784e+08	0.11944	32	1.07733e+09	0.476538
11	5.27553e+08	0.130156	33	1.09613e+09	0.488773
12	5.57215e+08	0.145581	34	1.13266e+09	0.510135
13	5.83168e+08	0.160956	35	1.17747e+09	0.536967
14	6.11187e+08	0.178188	36	1.22055e+09	0.562212
15	6.30968e+08	0.190282	37	1.25305e+09	0.582094
16	6.58568e+08	0.207225	38	1.28787e+09	0.603288
17	6.79015e+08	0.219638	39	1.31635e+09	0.620892
18	7.01064e+08	0.23378	40	1.34472e+09	0.640303
19	7.33421e+08	0.254575	41	1.365e+09	0.661843
20	7.60731e+08	0.272635	42	1.32432e+09	0.679986
21	7.89419e+08	0.291441	43	1.26808e+09	0.692747
22	8.11416e+08	0.306511	44	1.18279e+09	0.697458

An electrical discharge machine (EDM) was used to cut the specimens from a stainless-steel bar (0.003×0.04×4 m). The shape and the dimensions of the specimen are shown in Fig. 4.1(a). The specimens were finished by using different wet silicon carbide papers (320, 600, 1200, 2500, and 4000) and then polished with a diamond solution (9µm). The specimens were marked with 1mm spacing marks by using a laser marker machine as shown in Fig. 4.2. After that, stress relieving process (heating to 400±5ºC for 20 minute and left to cool in the oven) has been done to remove residual stress. The specimens were then polished with a diamond solution (6µm) to remove any oxide and to achieve a very fine surface as shown in Fig. 4.1(b).

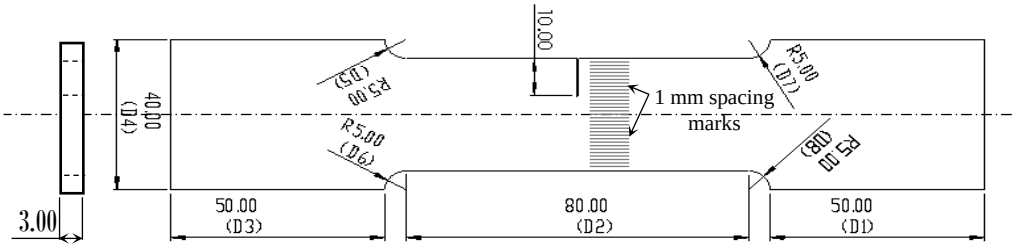

(a) Specimen dimensions (mm)

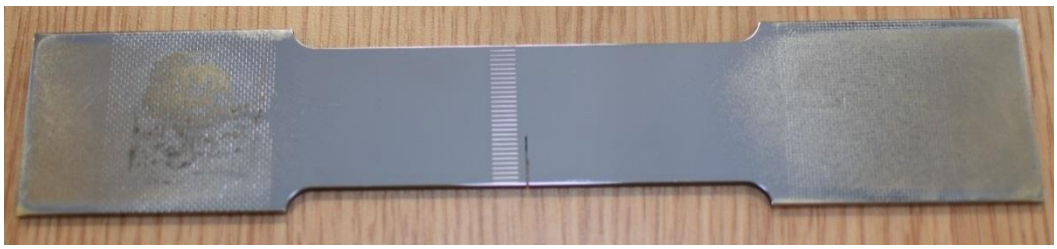

(b) Specimen after Polishing

Fig. 4.1. Fatigue test specimen.

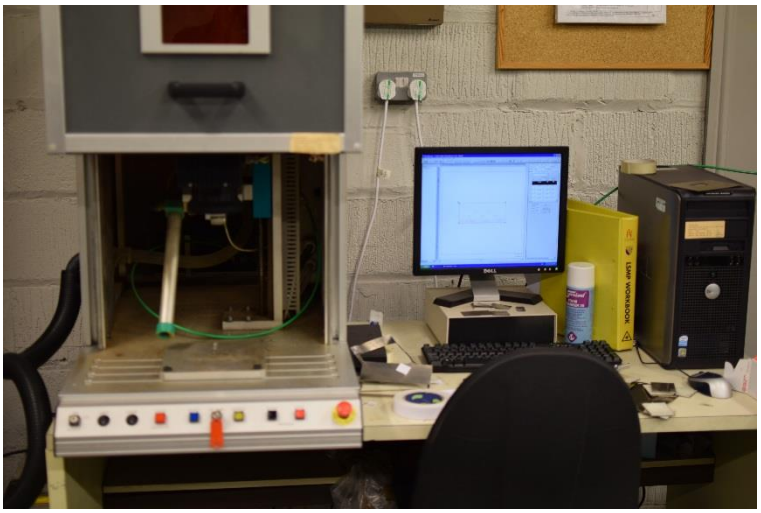

Fig. 4.2. The laser marker.

Fatigue tests were performed using an Instron 8801 servo-hydraulic fatigue testing machine rated with a maximum load capacity of 100 kN as shown in Fig. 4.3. Five loading frequencies with a loading ratio $R = 0$ {50, 30, 5, 0.1, 0.05Hz} and three with loading ratio $R = -1$ {30, 0.1, 0.05Hz} were tested with a sigmoidal cyclic load that applied with 10 kN maximum load. The fatigue specimens include an edge crack that was manufactured to ASTM standard E647. It should be mentioned that the fatigue tests have been interrupted from time to time to take a picture at each side of the specimen and write down the number of cycles associated with these pictures. To get a clear Image of the crack, a special light illuminator as shown in Fig. 4.4 was used to illuminate any reflection from the reflective surface of the specimen.

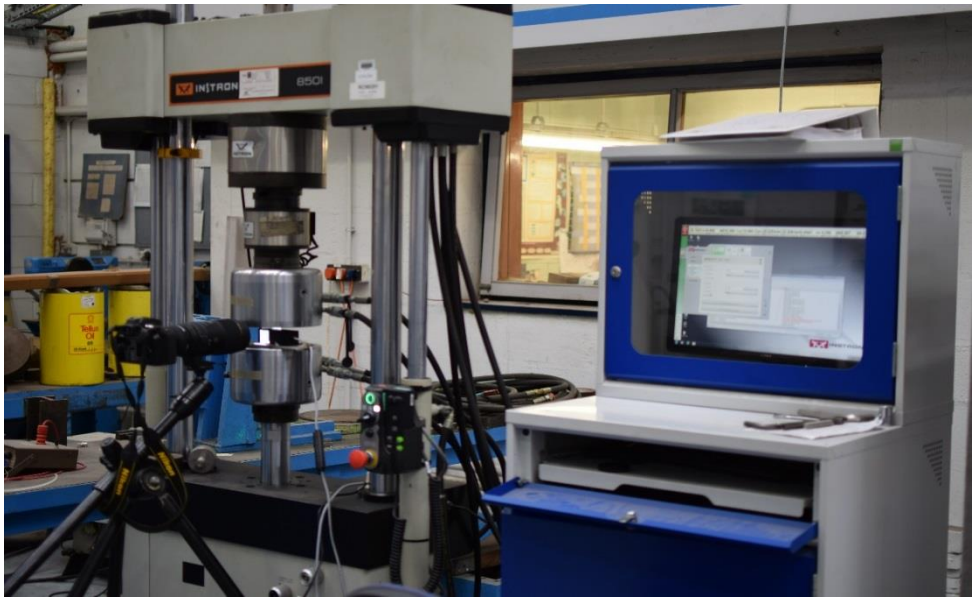

Fig. 4.3. Fatigue test machine.

Fig. 4.4. The light illuminator.

The crack length was measured using a high-resolution camera (see Fig. 4.5) and analysed using an image processing program. By correlating the number of pixels in the fatigue crack with the number of pixels in the 1mm spacing marks as shown in Fig. 4.6, the crack length was measured at each side of the specimen, and the average was used.

Fig. 4.5. High resolution camera.

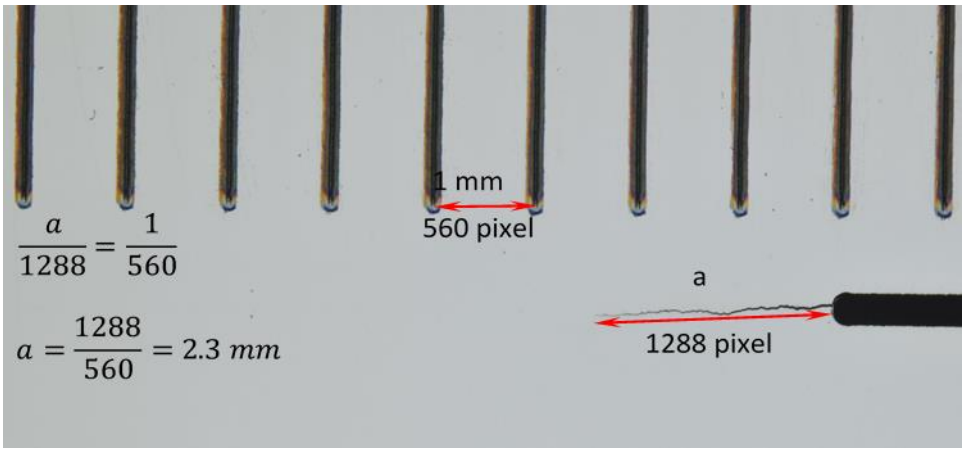

Fig. 4.6. Crack length measurement.

4.3 Results and discussion

The results of testing 20 specimens (14 at $R = 0$ three specimens at loading frequencies of (0.05, 0.1, 5, 30Hz) and one specimen at (0.5 and 50Hz) in addition to 6 at $R = -1$ two at each loading frequency) demonstrate that the loading frequency has an effect on the crack-growth rate of the austenitic stainless-steel 304 at room temperature. It is clear from Fig. 4.7 and 4.8 that the crack growth rate decreases and the fatigue life increases with increasing the frequency. This effect is only observed at frequencies lower than around 5Hz. Although it is recognised that cracks can grow faster at lower frequencies

due to microstructural effects or other damage mechanisms such as creep or corrosion [89, 90], creep and corrosion are unlikely to occur in air at room temperature for the material under consideration. It is conjectured therefore that the phase transformation from austenite to martensite could be the key factor influencing this behaviour. For the stainless steel 304, the Austenite is unstable and easily undergoes a phase transformation to martensite with plastic deformation (strain induced martensite). This transformation depends not only on the plastic strain but also on the temperature, see Fig. 4.9. Furthermore, it can be concluded from the figure that the lower the temperature, the higher the transformation is. It is known that for each temperature there is a specific critical plastic strain, below which no phase transformation occurs [84].

Fig. 4.8 and Table 4.4 to 4.17 shows the crack length-number of cycle curves and data for different loading frequencies at $R = 0$. From the result one can see that at lower frequency the crack grows faster and with increasing the frequency the crack growth slows down, this behaviour has been noticed up to a frequency of 5Hz after which the effect of the frequency on the crack growth rate will be almost constant. This behaviour can be explained as with the very low frequency there is no phase transformation to martensite or it is very small. But with increasing the frequency the applied strain rate increases, which lead to an increase in the plastic deformation and as a result an increase in the martensite percentage, hence an increase in the material strength and a greater resistance to the crack growth. The reason why the frequency effect is not seen above 5Hz is down to the martensitic content reaching its saturation limit for the specific temperature despite plastic strain increasing (e.g. from Fig. 4.9). One can see that the maximum percentage of martensite at 23 °C is about 30% so after this point increasing the frequency will not cause any change or a negligible change in the martensite percentage even if the plastic strain is increasing. In this study, the temperature at the tip area (measured by using the Fluke 53 Series II contact thermometers) was 25-28°C for the steady crack growth period when the load applied at $R = 0$ (see Fig. 4.10)

The result of this study is in agreement with the result in reference [87], where no noticeable difference was observed in the fatigue behaviour between a frequency of 90Hz and 20KHz. However, it is not completely in agreement with the result of reference [90], since they contend the crack growth decreases with increasing the frequency only if an isothermal process is applied because otherwise, the self-heating inhibit the phase transformation process.

This study shows that the crack growth decreases with increasing the loading frequency as a result of the increase in the martensitic content. It is clear from Fig. 4.10 that for the case of loading at $R = 0$ and $R = -0.33$ the increase in temperature is negligible for a crack length up to 8 mm and after this length the temperature starts to increase slightly. Although, at $R = -1$ the temperature is higher and increased gradually up to a length of 5mm followed by a large increase in temperature up to 160°C at the point of failure, the crack still grows at a faster rate at a lower frequency as shown in Fig. 4.11 and Table 4.18 to 4.23. The self-heating process will not lead to a faster crack growth at a higher frequency since even if the martensitic content is constant, the crack will grow slower at a higher frequency because of the strain rate effect. The result of this study has proven that the self-heating of the specimen happens only in the case of a reversed loading leading to an increase in the temperature, which is not significant but it could inhibit the martensitic transformation as mentioned in [90]. However, this process will not lead to a faster crack growth at a higher frequency, since even if the martensite content is constant, the crack will grow slower at a higher frequency as a result of the strain rate effect.

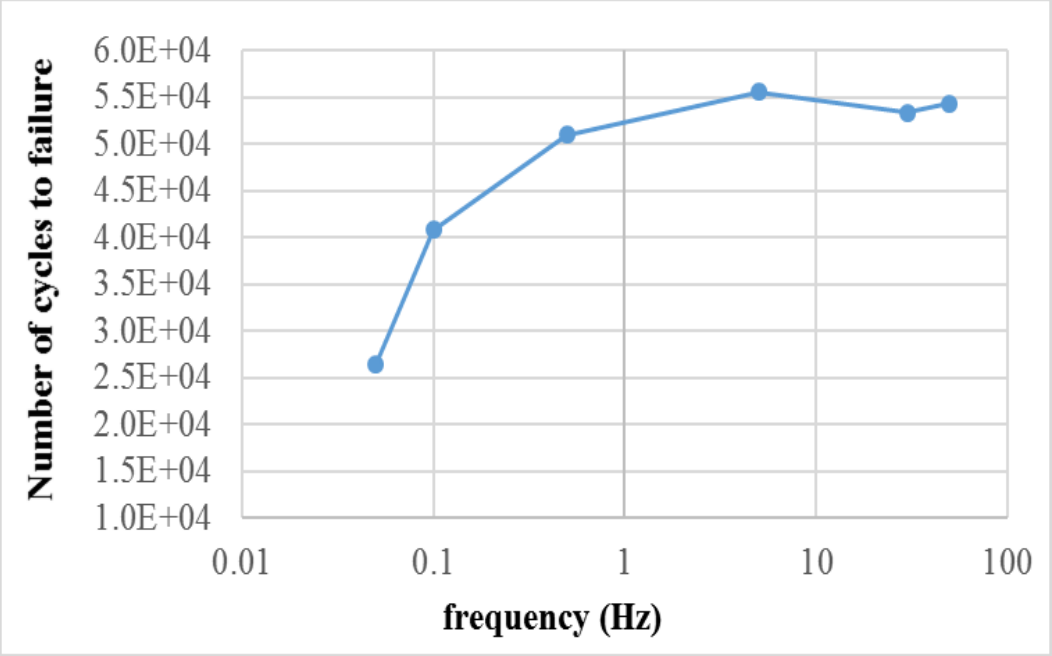

Fig. 4.7. Frequency effect on the fatigue life.

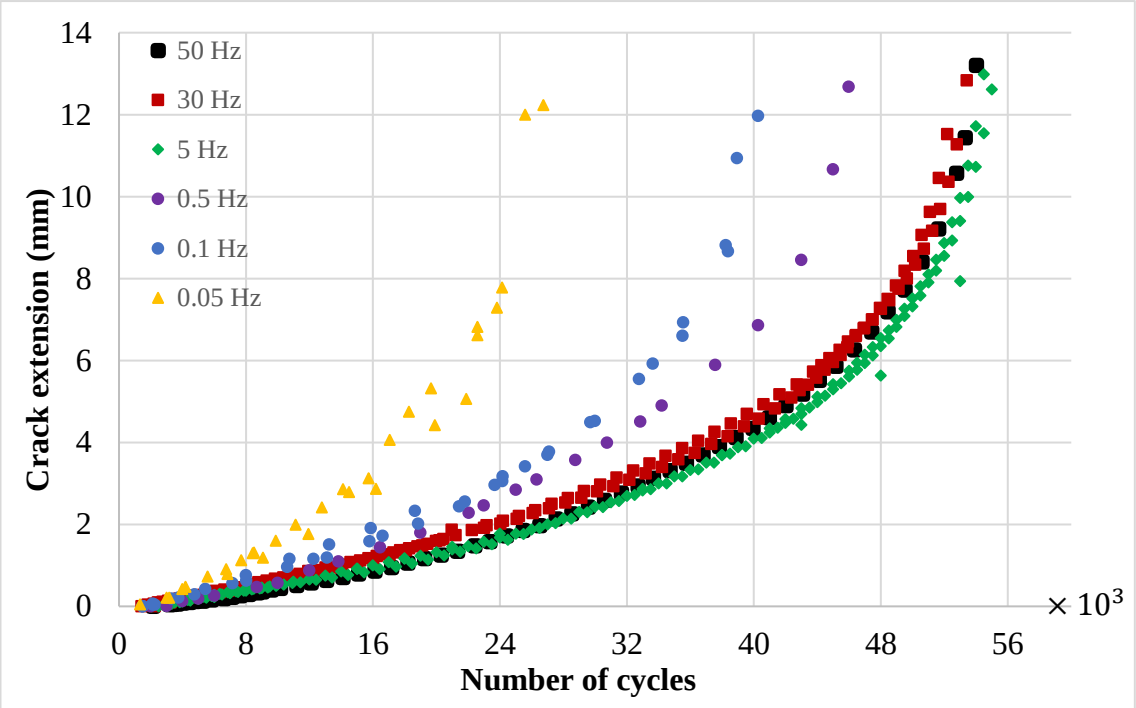

Fig. 4.8. Crack length-number of cycle curve as a function of frequency at $R = 0$.

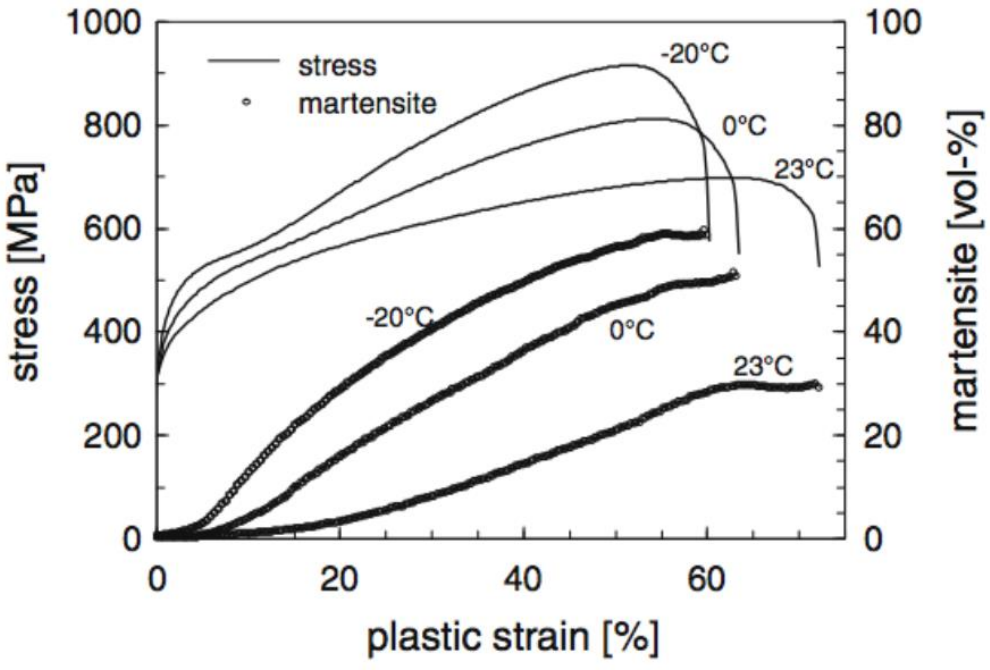

Fig. 4.9. Martensite percentage as a function of temperature and plastic strain [87].

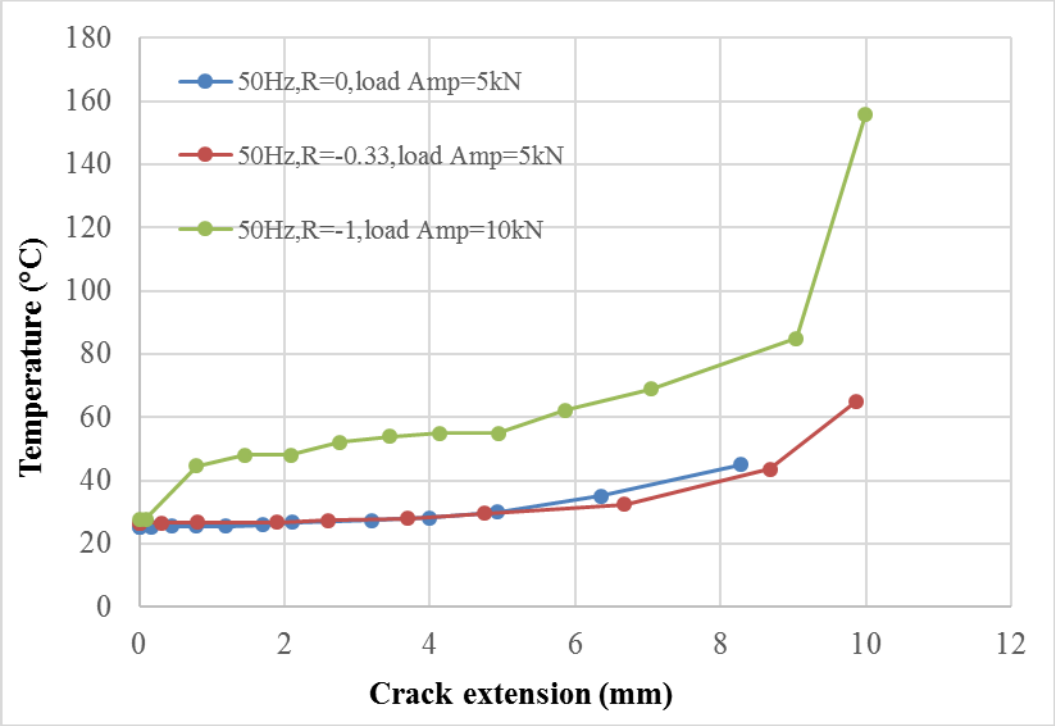

Fig. 4.10. The crack tip temperature as a function of the crack length.

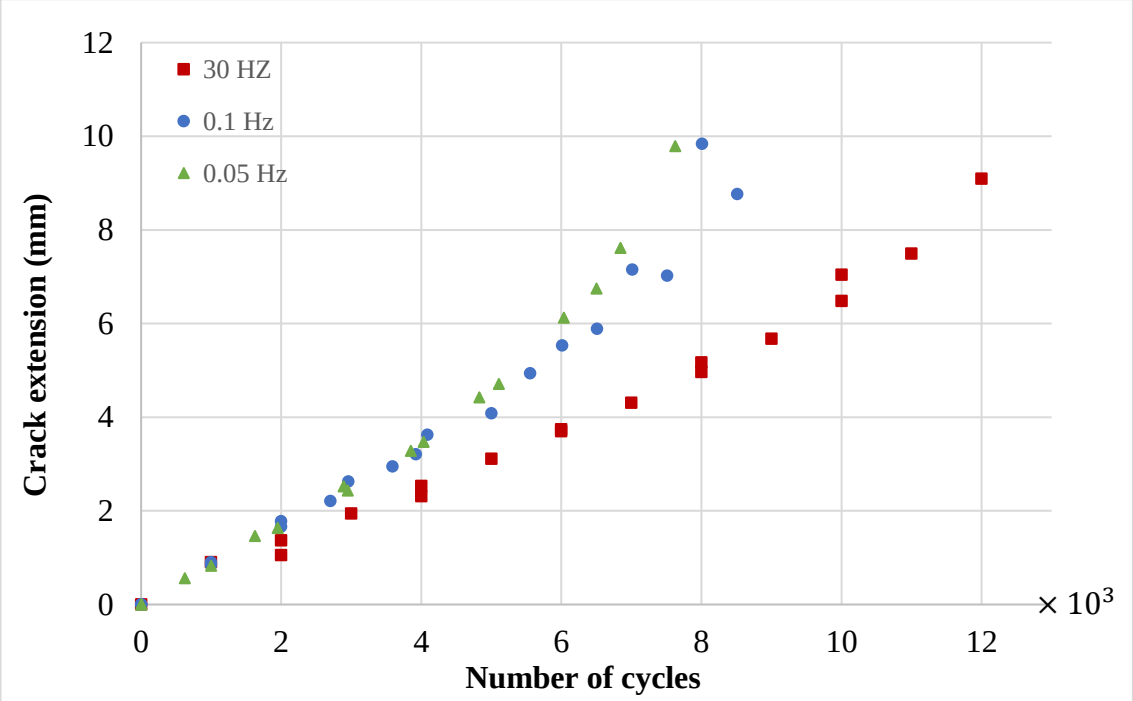

Fig. 4.11. Crack length - number of cycles curve at $R = -1$.

Table 4.4 Experimental data at $R = 0$ and frequency 0.05Hz for specimen A.

Number of cycles	Crack extension (mm)	Displacement Amp. (mm)
3000	0.2092	0.0565
4000	0.42157	0.056
6752	0.90695	0.0565
7706	1.11941	0.0588
8430	1.294	0.059
11133	1.9884	0.0604
14508	2.78534	0.062
15735	3.12243	0.064
26030	failed	

Table 4.5 Experimental data at $R = 0$ and frequency 0.05Hz for specimen B.

Number of cycles	Crack extension (mm)	Displacement Amp. (mm)
1329	0.04366	0.056
4194	0.47185	
5584	0.72645	0.0565
8503	1.309835	0.0589
9881	1.60325	0.0592
12781	2.410357	0.0605
14124	2.85778	0.0615
17068	4.064168	0.0648
18272	4.74512	0.065
19672	5.31893	0.0665
22583	6.618	0.07
24139	7.7795	0.075
26743	12.2319	0.082
27142	failed	

Table 4.6 Experimental data at $R = 0$ and frequency 0.05Hz for specimen C.

Number of cycles	Crack extension (mm)	Displacement Amp. (mm)
3165	0.04366	0.0565
6830	0.47185	0.0565
9080	0.72645	0.0589
11942	1.309835	0.0604
16188	1.60325	0.643
19915	2.410357	0.067
21878	2.85778	0.069
23815	4.064168	0.075
25600	4.74512	0.079
26367	failed	

Table 4.7 Experimental data at $R = 0$ and frequency 0.1Hz for specimen A.

Number of cycles	Crack extension (mm)	Displacement Amp. (mm)
2138	0.0372	0.0565
3309	0.18724	0.0565
5449	0.41764	0.056
8000	0.75769	0.0565
10750	1.15784	0.0568
13260	1.5044	0.057
15875	1.901525	0.0586
18650	2.32902	0.059
24175	3.1676	0.062
27106	3.77452	0.0643
29700	4.4889	0.066
35515	6.6006	0.0774
38250	8.8097	0.081
40766	failed	

Table 4.8 Experimental data at $R = 0$ and frequency 0.1Hz for specimen B.

Number of cycles	Crack extension (mm)	Displacement Amp. (mm)
2255	0.03422	0.0565
4760	0.2898	0.056
7165	0.5602	0.0566
13110	1.18776	0.0569
15800	1.5805	0.0583
21810	2.5564	0.060
24162	3.051	0.0623
27000	3.69015	0.065
32775	5.5463	0.07
35550	6.9287	0.077
38382	8.6583	0.0805
40870	11.9626	0.09
41539	failed	

Table 4.9 Experimental data at $R = 0$ and frequency 0.1Hz for *specimen C.*

Number of cycles	Crack extension (mm)	Displacement Amp. (mm)
2145	0	0.056
3747	0.17394	0.0565
8025	0.5635	0.0565
10612	0.89108	
12255	1.0684	0.0568
16610	1.61475	0.058
18865	1.90198	0.0588
21440	2.32596	0.059
23675	2.83581	0.062
25600	3.2985	0.0645
29990	4.39026	0.066
33650	5.7854	0.075
38945	10.8735	0.085
40129	failed	

Table 4.10 Experimental data at $R = 0$ and frequency 0.5Hz for specimen B.

Number of cycles	Crack extension (mm)	Displacement Amp. (mm)
3000	0.07134	0.0565
4000	0.1247	0.056
5000	0.1841	0.0345
6000	0.25724	0.0565
8700	0.465	0.0576
10000	0.5661	0.0577
12002	0.87263	0.0588
13842	1.0933	0.0365
16465	1.4384	0.0595
19000	1.7989	0.06
22056	2.2798	0.0604
23000	2.45903	0.0619
25000	2.8453	0.0628
26320	3.0935	0.0634
28770	3.5655	0.064
30750	3.9877	0.0643
32850	4.50913	0.065
34210	4.8931	0.0658
37580	5.88915	0.07
40280	6.8598	0.074
43000	8.451	0.0776
45000	10.6607	0.09
45989	12.6759	0.104
46789	failed	

Table 4.11 Experimental data at $R = 0$ and frequency 5Hz for specimen A.

Number of cycles	Crack extension (mm)	Displacement Amp. (mm)
3329	0.0598	0.056
6361	0.30583	0.0565
9383	0.4613	0.0569
12434	0.64735	0.0573
17465	0.9668	0.058
20500	1.2369	0.0588
24500	1.6252	0.0592
28500	2.1383	0.0605
32500	2.71557	0.0619
36500	3.3448	0.0623
40500	4.1092	0.065
42500	4.57207	0.0666
44000	4.9858	0.0675
45500	5.44015	0.0685
47000	5.9332	0.07
48500	6.5395	0.0723
49500	7.0833	0.0728
50500	7.5795	0.0755
51500	8.19283	0.079
52500	8.92488	0.0835
53500	9.9854	0.09
54500	11.5408	0.1
55500	14.449	0.1146
55507	failed	

Table 4.12 Experimental data at $R = 0$ and frequency 5Hz for specimen B.

Number of cycles	Crack extension (mm)	Displacement Amp. (mm)
3000	0.0539	0.0565
5000	0.17823	0.0565
7000	0.31956	0.0585
9000	0.45248	0.057
11000	0.59755	0.057
14000	0.85074	0.06
17000	1.0743	0.0585
20000	1.32173	0.0586
23000	1.57541	0.0595
26000	1.87623	0.0597
29000	2.30175	0.0605
32000	2.69462	0.062
34000	2.99497	0.0619
36000	3.32591	0.063
38000	3.6834	0.063
40000	4.09493	0.0635
42000	4.56811	0.0665
45000	5.42303	0.0687
47000	6.1398	0.069
48000	6.5404	0.07
49000	6.98793	0.072
51000	8.09685	0.0775
52000	8.86163	0.08
53000	9.96283	0.0895
54000	11.71904	0.1058
54803	Failed	

Table 4.13 Experimental data at $R = 0$ and frequency 5Hz for specimen C.

Number of cycles	Crack extension (mm)	Displacement Amp. (mm)
3000	0.08	0.0565
6000	0.2796	0.057
9000	0.45447	0.057
12000	0.655	0.0575
15000	0.9185	0.058
18000	1.1682	0.0585
21000	1.4531	0.0595
24000	1.7699	0.06
33000	2.866	0.0621
38000	3.697	0.0625
43000	4.425	0.0666
48000	5.6331	0.069
53000	7.9327	0.0885
56558	Failed	

Table 4.14 Experimental data at $R = 0$ and frequency 30Hz for specimen A.

Number of cycles	Crack extension (mm)	Displacement Amp. (mm)
1823	0.0379	0.0555
3105	0.133676	0.0565
4598	0.25525	0.056
6656	0.40233	0.0565
8794	0.5818	0.0586
10886	0.74837	0.057
13027	0.94003	0.058
15203	1.118464	0.0585
16771	1.26513	0.0584
18808	1.45702	0.0585
20978	1.6868	0.0587
24034	2.01194	0.0595
27103	2.3895	0.0595
30130	2.80326	0.06
33204	3.2393	0.0623
36274	3.74035	0.0635

39388	4.3858	0.0645
42376	5.0895	0.0667
43943	5.57483	0.069
45900	6.3186	0.07
47969	7.2779	0.0712
49521	8.18106	0.072
51116	9.625	0.085
52935	13.763	0.124
53046	failed	

Table 4.15 Experimental data at $R = 0$ and frequency 30Hz for specimen B.

Number of cycles	Crack extension (mm)	Displacement Amp. (mm)
2199	0.06377	0.0565
3464	0.16289	0.0565
5019	0.27327	0.0565
7218	0.44984	0.0566
9311	0.62155	0.0567
10357	0.7049	0.057
11405	0.7899	0.0575
12461	0.87735	0.0579
14604	1.07687	0.0582
16247	1.22128	0.0585
18283	1.41219	0.0585
20443	1.63856	0.0588
23010	1.9129	0.059
26073	2.27186	0.0595
29150	2.64886	0.0595
32179	3.08721	0.0618
37330	3.95739	0.064
41348	4.8246	0.0668
43422	5.40082	0.069
45473	6.12872	0.071
47458	7	0.0715
48981	7.8252	0.072
50582	9.0609	0.0815
52200	11.51901	0.0995
52951	failed	

Table 4.16 Experimental data at $R = 0$ and frequency 30Hz for specimen C.

Number of cycles	Crack extension (mm)	Displacement Amp. (mm)
2762	0.0511	0.056
4305	0.18129	0.056
6397	0.34497	0.0565
8515	0.524668	0.0567
11016	0.70742	0.0571
15016	1.06744	0.058
19113	1.484538	0.0585
23170	1.972566	0.059
27271	2.49484	0.0595
31370	3.13588	0.0625
35491	3.86002	0.0642
39579	4.69489	0.0655
43737	5.72191	0.0689
45943	6.45776	0.07
47498	7.00005	0.0715
49137	7.746132	0.0725
50722	8.72715	0.0795
51762	9.69082	0.082
52806	11.2682	0.093
53742	Failed	

Table 4.17 Experimental data at $R = 0$ and frequency 50Hz for specimen A.

Number of cycles	Crack extension (mm)	Displacement Amp. (mm)
3203	0.0386	0.0565
4453	0.0938	0.0545
6644	0.183	0.0565
8755	0.3298	0.0567
11216	0.5037	0.057
14123	0.70274	0.0577
17181	0.9459	0.058
21335	1.34357	0.0589
25477	1.84724	0.096
29578	2.41653	0.0597

33692	3.11952	0.0622
36803	3.6904	0.0625
39952	4.3405	0.0649
43087	5.17528	0.069
46339	6.259	0.07
49542	7.7126	0.073
52790	10.566	0.0885
54039	13.19965	0.109
54364	failed	

Table 4.18 Experimental data at $R = -1$ and frequency 0.05Hz for specimen A.

Number of cycles	Crack extension (mm)	Displacement Amp. (mm)
1000	0.828135	0.11710
1950	1.629635	0.11906
2950	2.43111	0.12073
3850	3.28342	0.12342
4827	4.418485	0.1285
6500	6.747445	0.14766
7627	9.784707	0.17625
7831	failed	

Table 4.19 Experimental data at $R = -1$ and frequency 0.05Hz for specimen B.

Number of cycles	Crack extension (mm)	Displacement Amp. (mm)
625	0.559715	0.11559
1625	1.459025	0.1200
2890	2.52184	0.12028
4035	3.47285	0.12508
5106	4.7094	0.12989
6035	6.122635	0.1376
6845	7.6163	0.14829
7883	failed	

Table 4.20 Experimental data at $R = -1$ and frequency 0.1Hz for specimen A.

Number of cycles	Crack extension (mm)	Displacement Amp. (mm)
1000	0.837165	0.11737
2000	1.657805	0.11878
2705	2.204065	0.12048
3590	2.943435	0.12249
3925	3.204615	0.1245
5000	4.081805	0.12698
6011	5.53055	0.1331
7011	7.14705	0.1353
8011	9.83814	0.1653
9011	failed	

Table 4.21 Experimental data at $R = -1$ and frequency 0.1Hz for specimen B.

Number of cycles	Crack extension (mm)	Displacement Amp. (mm)
1000	0.89893	0.11842
2000	1.77788	0.11976
2960	2.62379	0.12189
4090	3.62021	0.12536
5555	4.932815	0.12897
6510	5.881319	0.13352
7510	7.01639	0.14011
8510	8.762278	0.15923
9050	failed	

Table 4.22 Experimental data *at* $R = -1$ and frequency 30Hz for specimen A.

Number of cycles	Crack extension (mm)	Displacement Amp. (mm)
2000	1.350663	0.1157
4000	2.507538	0.11739
6000	3.73666	0.12093
8000	5.167515	0.12585
10000	7.038468	0.13517
11660	failed	

Table 4.23 Experimental data at $R = -1$ and frequency 30Hz for specimen B.

Number of cycles	Crack extension (mm)	Displacement Amp. (mm)
1000	0.692085	0.11454
2000	1.36655	0.11529
3000	1.942845	0.11603
4000	2.52971	0.117545
5000	3.109167	0.11842
6000	3.696779	0.11955
7000	4.303335	0.12177
8000	4.963045	0.12376
9000	5.6716	0.12597
10000	6.475985	0.13048
11000	7.48935	0.13533
12000	9.08901	0.15959
12555	failed	

Fig. 4.12 and Fig. 4.14 depict the relation between the crack growth rate and the stress intensity factor range ΔK at different loading frequencies for the tests when $R = 0$ and $R = -1$, respectively. The value of ΔK was evaluated as recomended in the ASTM E 647 - 05 [108]from

$$\Delta K = [\Delta P / B\sqrt{w}]F(a/w) \tag{4.1}$$

where ΔK and ΔP are the stress intensity factor range and the load range respectively, B, w and a are the specimen thickness, the specimen width and the crack length. $F(a/w)$ is a shape function evaluated according to ASTM E 647 - 05 [108] and is of the form

$$F(a/w) = \alpha^{1/2}[1.4 + \alpha][1 - \alpha]^{-3/2}G \tag{4.2}$$

$$G = 3.97 - 10.88\alpha + 26.25\alpha^2 - 38.9\alpha^3 + 30.15\alpha^4 - 9.27\alpha^5 \tag{4.3}$$

$$\alpha = a/w \tag{4.4}$$

For the case when $R = -1$ only the positive part of the load is used in the evaluation of ΔK as recommended in the literature.

The result shows that the loading frequency have an effect on the crack growth rate. From Fig. 4.12, it is clear that any frequency higher than 5 Hz have a very close crack growth

rate while the growth rate increases with decreasing the frequency below 5 Hz. The frequency dependent crack growth rate can be estimated through a power law such as the power law used in [89] and takes the form

$$\frac{da}{dN} = A(f) \times [\Delta K\ ]^n \tag{4.5}$$

where $A(f)$ is a function of the frequency and n is a material constant for a specific environmental and loading condition.

From the best fit power law of the crack growth data of stainless-steel 304 at $R = 0$ and room temperature between 24-26°C, the slope n can be seen to have a very close value at any frequency ($n = 0.8032$), while $A(f)$ is changing with the frequency. The function $A(f)$ can be obtained from the best fit of the result in Fig. 4.12 and is shown in Fig. 4.13 as a function of the frequency for any frequency higher than 0.05Hz.

From the result on Fig. 4.14, it is clear that for the test at $R = -1$ the fatigue crack growth cannot be captured by Eq. (4.5) possibly because the experimental data is insufficient and the specimens are subjected to low cycle fatigue and possibly all the data points are in the unstable crack growth region. This issue has not investigated further because it is outside the scope of this research.

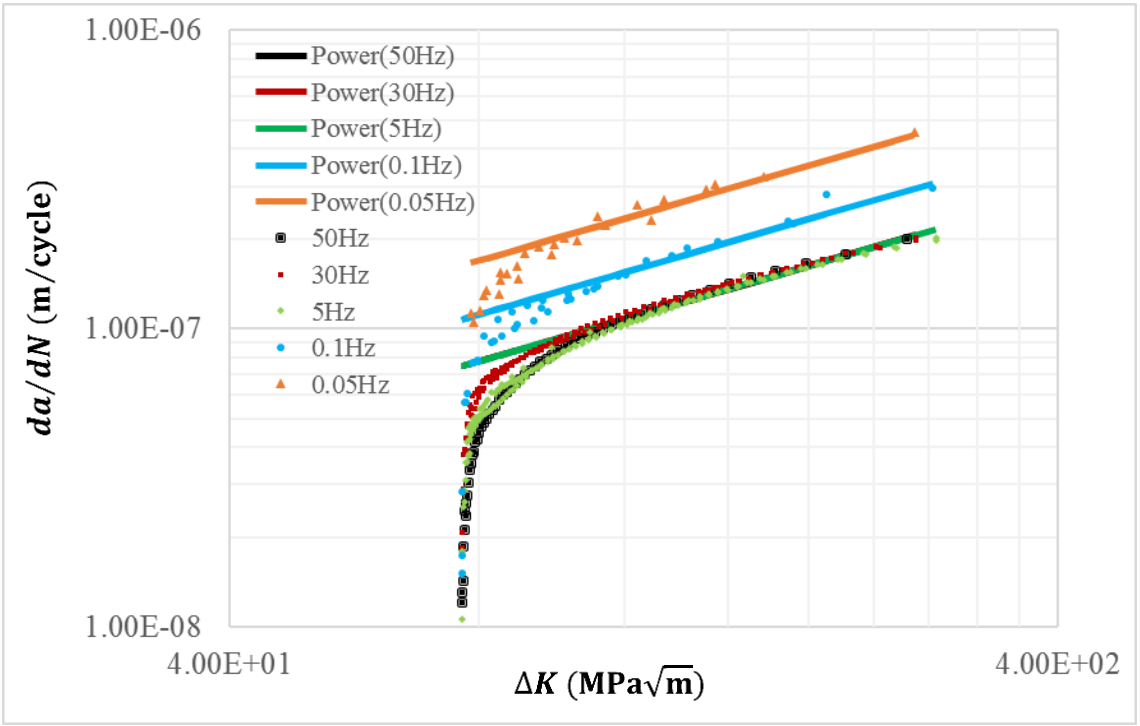

Fig. 4.12. Crack growth rate-ΔK curve as a function of the frequency at $R = 0$.

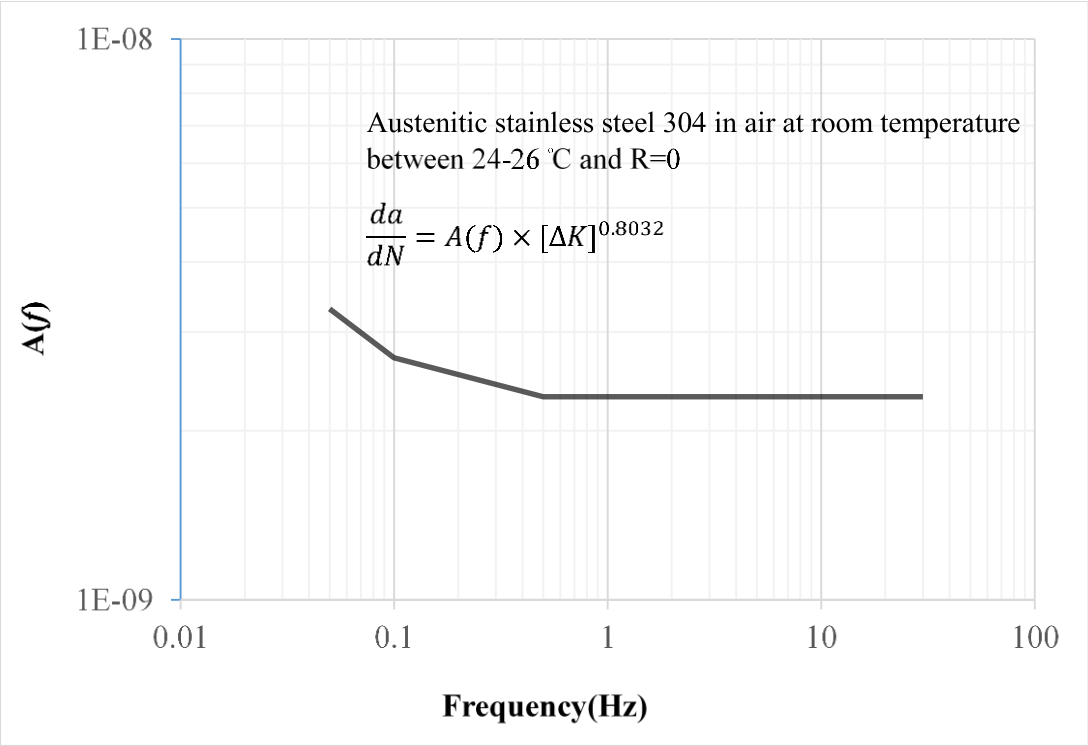

Fig. 4.13. The value of $A(f)$ as a function of the frequency.

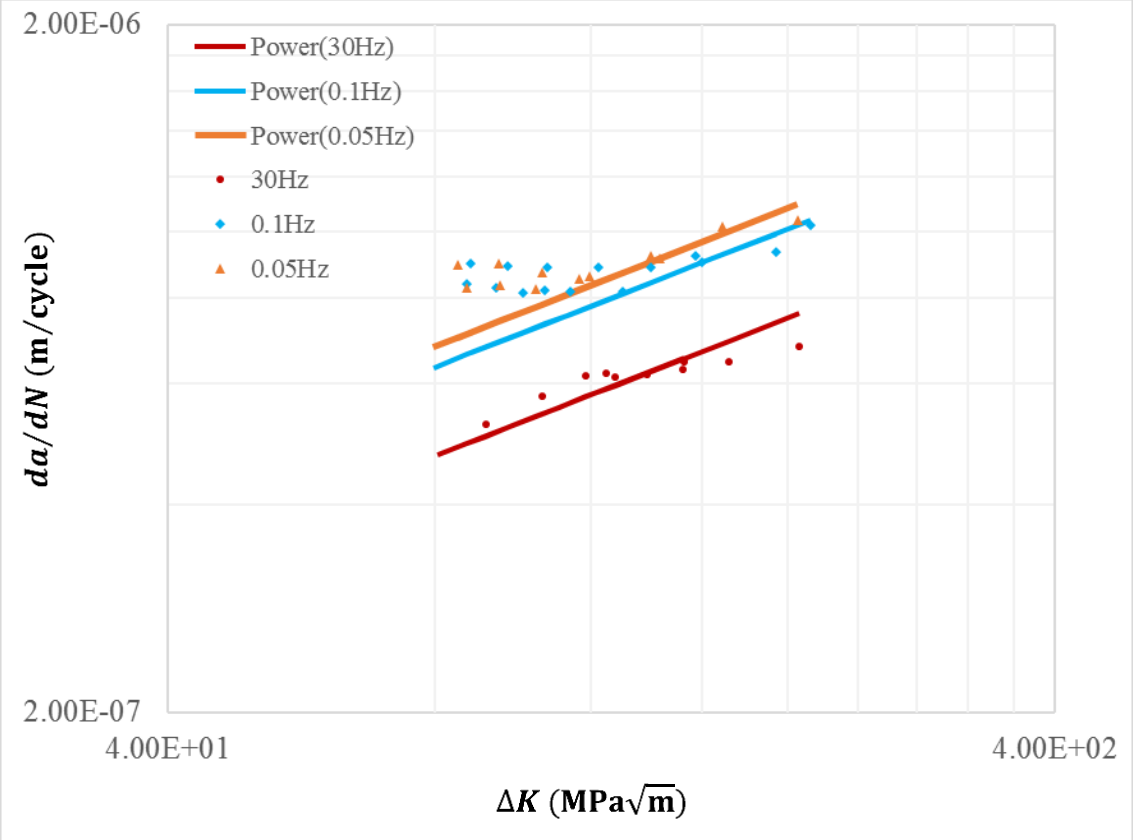

Fig. 4.14. Crack growth rate-ΔK curve as a function of the frequency at $R = -1$.

Based on the finding of this study it can be concluded that loading frequency has an effect on the crack-growth in austenitic stainless-steel 304 at room temperature. The fatigue crack grows faster at lower frequency and slower at higher frequency in the austenitic stainless-steel 304 as a result of the increase in the martensitic content. The crack will grow almost at the same rate for all frequencies above 5Hz. A frequency dependent power law has been suggested to evaluate the crack growth rate at any frequency and effective stress intensity factor.

4.4 Summary

Based on the finding of this study the following can be concluded:

- Loading frequency has an effect on the crack-growth rate in mechanical parts made of austenitic stainless-steel 304 even at room temperature especially if the load ratio R is greater than zero.
- The fatigue crack grows faster at a lower frequency and slower at a higher frequency in the austenitic stainless-steel 304 as a result of the increase in the martensitic content. So this behaviour should be considered carefully at the design stage of any mechanical part made from an austenitic stainless-steel that will be subjected to LCF at low frequency, since most of the standard-fatigue data (such as fatigue limit) is obtained at a relatively high frequency.
- After a frequency of 5Hz, the reduction in the crack growth rate will stop and the crack will grow almost at the same rate for all the higher frequencies.
- A frequency-dependent power law has been suggested to evaluate the crack growth rate at any frequency and stress intensity factor range.

Chapter 5: Rate-dependent CZM for fracture

5.1 Introduction

Monotonic and fatigue crack growth can be modelled by using a method called the Cohesive-zone model (CZM), which has become one area of the research in the field of fracture mechanics because of its ability to overcome limitations of other methods founded on linear elastic fracture mechanics (LEFM). The traditional use of the rate-independent CZM gives inaccurate results for dynamic fracture analysis because it assumes that all the energy is dissipated in a single main crack and that predicts unrealistic crack propagation speed [17]. To achieve a better representation of the physics, it is necessary to incorporate rate dependency either in the CZM or the bulk material or possibly both. Using a rate-independent CZM with a rate-dependent bulk material failed to represent the experimental evidence in many cases (see for example [22, 24–26]). Therefore the use of a rate-dependent CZM is recommended, where the cohesive traction σ is related not just to the crack separation δ, but also to separation rate $\dot{\delta}$, i.e. $\sigma = f(\delta, \dot{\delta})$; a relationship first pioneered by Glennie [27]. Glennie concluded that the reason behind the observed reduction in crack speed with increase in strain rate is an increase in stress levels in the vicinity of the crack tip. Further developments to Glennie's work has been done by Freund et al. [62], Costanzo & Walton [24, 25] and Xu et al. [63]. A negative feature of these approaches however is unrealistically large values for the stress in the cohesive-zone and associated crack arrest. A related but alternative approach is adopted by Valoroso et al. [17] and Zhou et al. [22] who employed a CZM with critical traction independent of rate but involving temporal changes in fracture energy along with critical separation. It is demonstrated from the present work however that this approach can lead to unrealistic separation values and crack tearing ahead of the crack tip.

The model proposed in this Chapter is designed to overcome these identified limitations since it is apparent from the literature that presently no optimum CZM exists that can simulate the range of crack growth physics met in practice. The CZM used as a vehicle to investigate these issues is introduced in Section 5.2 and is the trapezoidal model as it is relatively straightforward and localised plastic behaviour is readily identified. In Section 5.3, standard rate-independent CZMs are considered along with different bulk-material models to highlight the limitations of this approach. To achieve a proper understanding of how rate effects can be incorporated into the trapezoidal CZM, relatively

benign dashpot models are incorporated into the CZMs in various configurations in Section 5.4. These models provide a relatively simple vehicle for problem visualisation and assessment of the different types of behaviours. Focus here is on Mode I fracture as this is the most prevalent failure mode in fracture mechanics. An added bonus with dashpot models is that they can facilitate analytical solutions, which can then be explored to great depth. In addition, combinations of bulk material responses with CZMs can readily be assessed. The approach accommodates different localised responses, which is necessary as the behaviour in the cohesive-zone can be expected to depart significantly from the original virgin bulk material. Arising out of the analysis in Section 5.4 is a new rate-dependent model, which is introduced in Section 5.5. The energy transfers invoked by the various dashpot models to provide greater insight into the behaviour of the cohesive-zone approach are illustrated in Section 5.6. Discussed in Section 5.7 is the implementation of the new rate-dependent model arising out of the analysis in previous sections. The new model is incorporated into the commercial software package ABAQUS (via a bespoke UMAT subroutine as illustrated in Appendix B-1) and tested on a cracked specimen subject to different loading rates. The difficulties experienced with existing approaches are shown to be overcome by the new approach. Finally, the key-point of the finding of the chapter is summarised in Section 5.8.

5.2 Standard cohesive-zone models

The cohesive concept is depicted in Fig. 5.1 which describes a cracked domain and a cohesive-zone representing the damage ahead of the crack tip. Also depicted is a tensile element in the cohesive-zone whose behaviour is dictated by the trapezoidal traction separation law highlighted in the figure. The information about the standard TCZM is illustrated in Chapter 3 Section 3.6. The standard TCZM takes no account of time or rate and possible mechanisms for introducing these aspects is discussed in Section 5.4, but before that, it is of interest to examine various bulk-material models incorporating a rate-independent CZM.

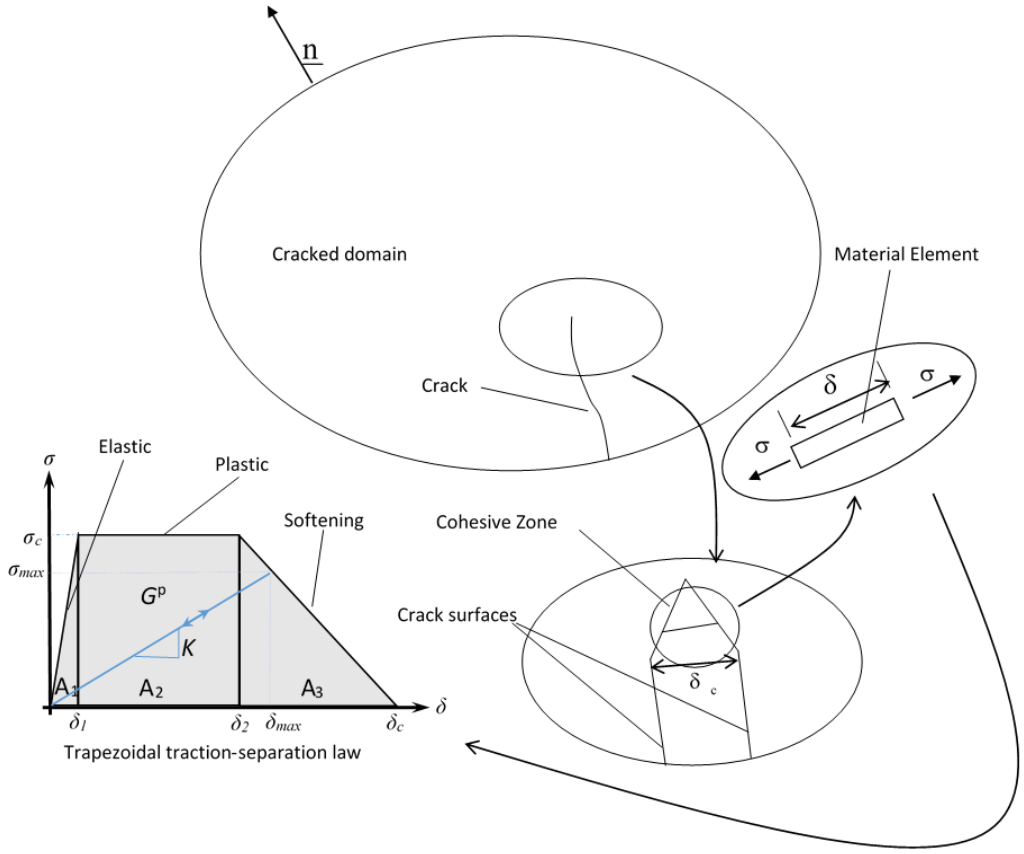

Fig. 5.1. Mode I cohesive-zone model [89].

5.3 Rate-independent CZMs

Shown in Fig. 5.1 is a depiction of how the cohesive approach is organised and a particular feature worth highlighting is the material element depicted representing damaged material in the cohesive zone. It is possible to represent the behaviour of this material element by a combination of one-dimensional springs, dashpots, sliders, and cohesive elements. A number of such arrangements of interest in this study are depicted in Fig. 5.2. These can be considered in tandem with 1-D representations of bulk-material responses using similar elements as depicted in Fig. 5.3. Organising material behaviours in this manner provides insight and a certain degree of control and in addition allows for detailed analysis, which can highlight wanted and/or unwanted responses. The cohesive elements depicted in Fig. 5.2 are all derivable from the trapezoidal traction separation law (TSL) on various settings of δ_1 and δ_2. It is of interest to explore and investigate the deficiencies in these simple models to motivate the selection of the final model. In the discussion that follows the bulk-material behaviour is identified by uppercase letters {A, B, C, D} and cohesive models by the lowercase letters {a, b, c, …, p} (see Fig. 5.2 and 5.3). For

example (A-a) refers to a linear material with a linear cohesive element (LCE) (on setting $\delta_1 = \delta_2 = 0$) and (C-f) means an elastic, rigid-plastic bulk material and a rate-dependent trapezoidal cohesive element. Analysis is restricted to subjecting a prismatic element to displacement δ_o for a range of material models and cohesive element combinations.

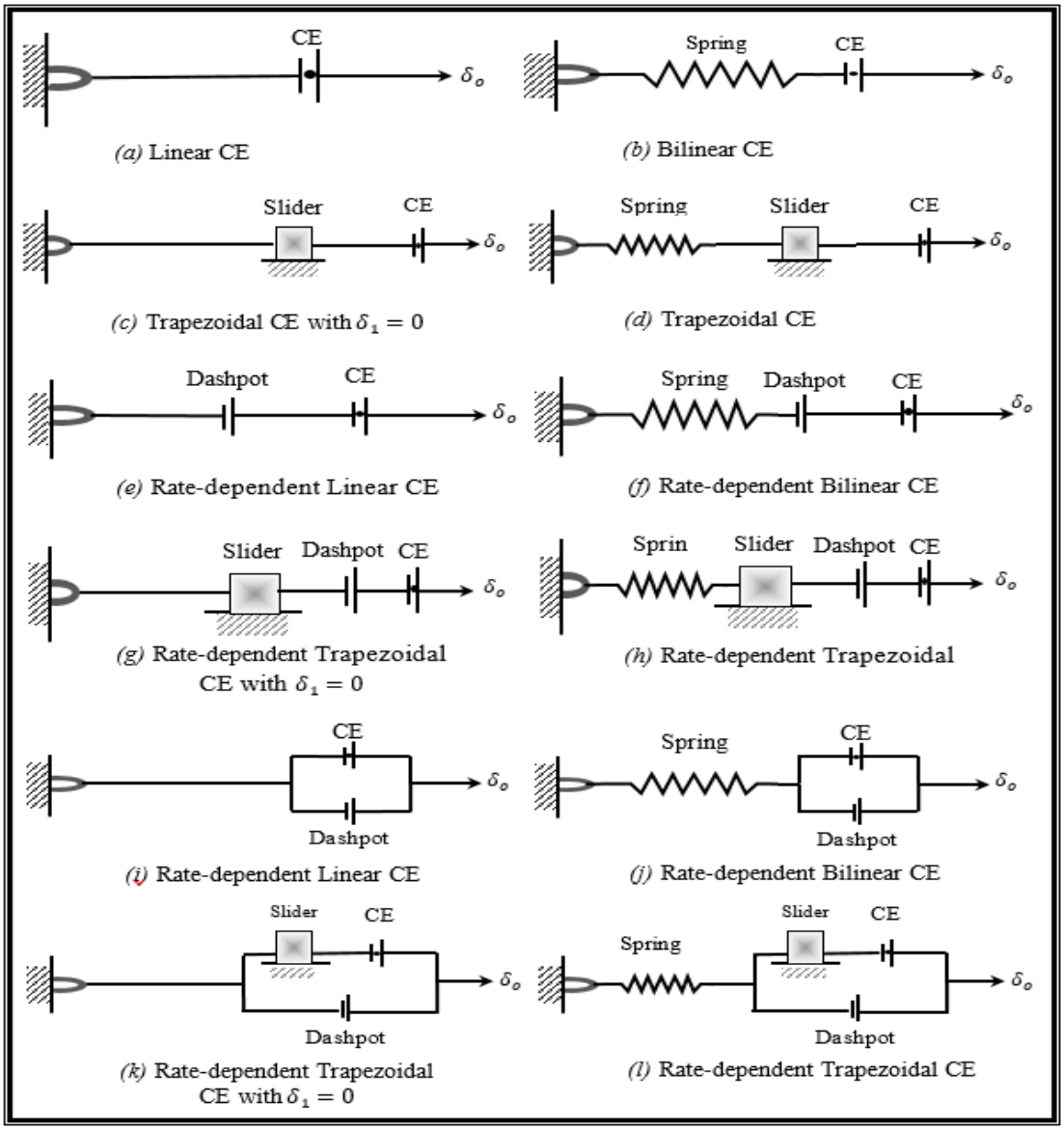

Fig. 5.2. Elementary Material Elements in the Cohesive-Zone Zone.

Although the main focus in this paper is on the inclusion of rate effects it is insightful also to explore quasi-static loading of rate-independent models to provide a base on which to construct more complex models. The cohesive elements shown in Fig. 5.2 (a, b, c, and d), are rate-independent linear, bilinear, trapezoidal (with $\delta_1 = 0$) and trapezoidal cohesive elements. Recorded in the literature is the successful application of these elements to quasi-static fracture processes for bulk-material Models (A and C) depicted

in Fig. 5.3. Limited research [19, 23, 61] has been performed on the use of rate-independent cohesive elements with rate-dependent bulk-material models of the type depicted in Fig. 5.3(B and D). However, this approach has proven insufficient to represent the experimental dynamic crack results (see references [22, 24–26]) and a rate-dependent cohesive model is a possible solution.

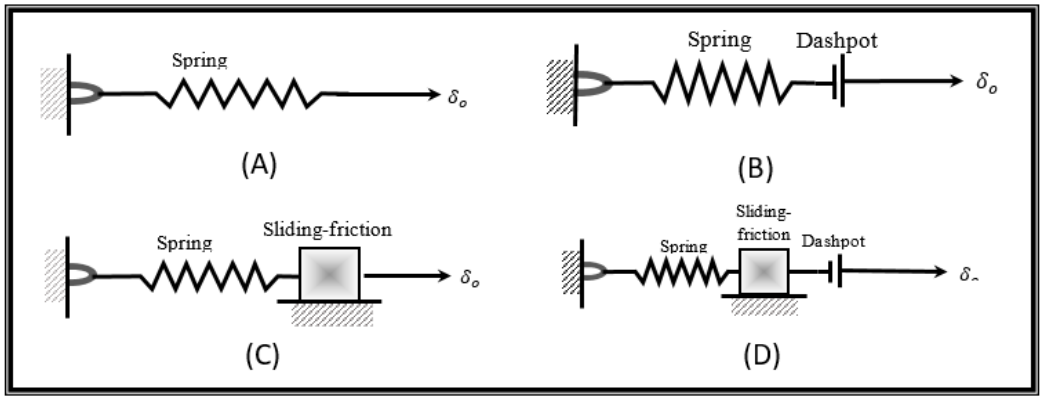

Fig. 5.3. Elementary Bulk-Material Models.

5.3.1 Model (A-a)

Combining elements from Fig. 5.3(A) and 5.2(a) provides the simplest cohesive model consisting of a linear bulk-material and a LCE. Fig. 5.4 shows the stress-displacement response. A particular feature of the model is that both the spring and the cohesive part experience the same stress, but strain is additive, i.e. $\sigma_o = \sigma^{\mathrm{e}} = \sigma^{\mathrm{coh}}$ and $\varepsilon_o = \varepsilon^{\mathrm{e}} + \varepsilon^{\mathrm{coh}}$, where ε^{e} is the elastic strain (defined as $\varepsilon^{\mathrm{e}} = \delta^{\mathrm{e}}/l_o$) and $\varepsilon^{\mathrm{coh}}$ is the strain in the cohesive part (defined as $\varepsilon^{\mathrm{coh}} = \delta^{\mathrm{coh}}/l_o$), where l_o is the initial length of a piece of identified material local to and containing an element of the CZ.

Consider an initial displacement δ_o applied to the system and let $\varepsilon_o = \delta_o/l_o$ and $\sigma_o = E\varepsilon_o$, where E is Young's Modulus of the bulk material. If $\sigma_o \leq \sigma_c$, then $\varepsilon_{\mathrm{o}} = \varepsilon^{\mathrm{e}}$, $\sigma = E\varepsilon^{\mathrm{e}}$, $\delta^{\mathrm{e}} = \delta_o = \varepsilon_o l_o$ and the material element behaves like an elastic spring. However, if $\sigma_o > \sigma_c$, then the cohesive element makes a contribution and since the total separation is additive (i.e. $\delta_o = \delta^{\mathrm{e}} + \delta^{\mathrm{coh}}$), the stress can be represented as

$$\sigma^e = \sigma_c\left(1 - \frac{\delta^{coh}}{\delta_c}\right) = E\varepsilon^e = E\frac{\delta^e}{l_o} \tag{5.1}$$

which can be solved for δ^{e} to give

$$\delta^e = \delta_c \left[\frac{\left(1-\frac{\delta_o}{\delta_c}\right)}{\left(-1+\frac{E\delta_c}{\sigma_c l_o}\right)} \right] \tag{5.2}$$

which is applicable provided $\delta_o \leq \delta_c$, otherwise the element will fail and the material will separate.

In order to better understand the crack driving force, it is insightful to explore energy transfers that take place between the bulk material, cohesive element and the surroundings. In this case $U^e = 0.5\sigma A\delta^{\mathrm{e}}$ and $W^e = U^e/A = \mathrm{A}_1 = 0.5\sigma\delta^{\mathrm{e}}$, where A is the cross-section area, A_1 is the area under the stress separation curve shown in Fig. 5.4, U^e is the elastic strain energy, W^e is the elastic strain energy (per unit area) and δ^{e} is elastic displacement. For $\sigma_o \leq \sigma_c$ the situation is trivial and the total work done by the applied load (per unit area) W^{d} is equal to W^{e},which is equal to the area A_1 shown in Fig. 5.4(a). For $\sigma_o > \sigma_c$ as the value of δ^{e} is calculated from Eq. (5.2) and σ^e from Eq. (5.1) and the elastic strain energy per unit area as shown in Fig. 5.4(b) is given by $W^e = \mathrm{A}_1 = 0.5\sigma^{\mathrm{e}}\delta^{\mathrm{e}}$ and the energy diverted to material separation is

$$W^{\Gamma} = \mathrm{A}_2 = \frac{1}{2}(\sigma_c + \sigma^e)(\delta_a - \delta_e) + \frac{1}{2}(\sigma_c + \sigma^e)(\delta_0 - \delta_a) = \frac{1}{2}\left((\sigma_c + \sigma^e)(\delta_o - \delta_e)\right)$$

$$W^{\Gamma} = \frac{1}{2}(\sigma_c + \sigma^e)\delta^{\mathrm{coh}} \tag{5.3}$$

where W^{Γ} is the cohesive energy per unit area, δ^{coh} is separation at the cohesive element and the total work done (per unit area) is $W^{\mathrm{d}} = W^{\mathrm{e}} + W^{\Gamma}$. Energy dissipation is an important aspect in cohesive models as is apparent in this simple case which features non-recoverable energy W^{Γ}.

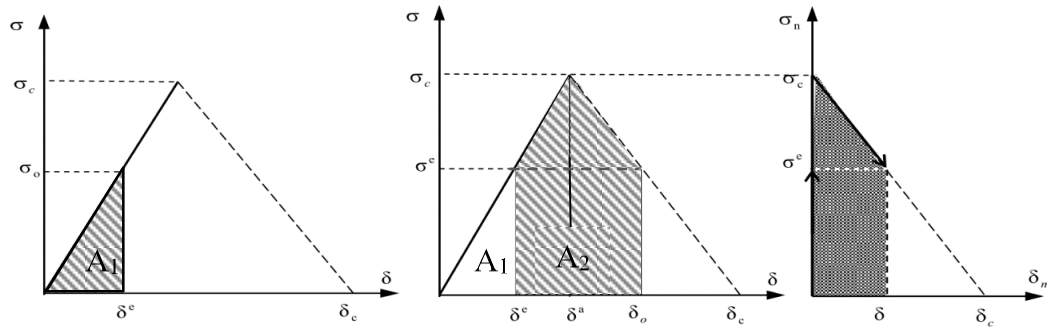

(a) Material behaviour when $\sigma_o \leq \sigma_c$ (b) Material behaviour when $\sigma_o > \sigma_c$ (c) Cohesive element

Fig. 5.4. The energy represented by the area under the stress-displacement curve

5.3.2 Model (B-a)

The addition of a dashpot to the bulk-material model above gives rise to rate-dependent fracture behaviour. In this model stress is identical in the spring, dashpot and cohesive part, but strain is additive and temporal behaviour is a feature, i.e. $\sigma_o = \sigma^{\mathrm{e}} = \sigma^{\mathrm{D}} = \sigma^{\mathrm{coh}}$ and $\varepsilon_o = \varepsilon^e(\mathrm{t}) + \varepsilon^D(\mathrm{t}) + \varepsilon^{\mathrm{coh}}$, where $\varepsilon^e(\mathrm{t})$, $\varepsilon^D(\mathrm{t})$, and $\varepsilon^{\mathrm{coh}}$ are the elastic strain ($\varepsilon^e(\mathrm{t}) = \delta^e(\mathrm{t})/l_o$), the strain in the dashpot at any time ($\varepsilon^D(\mathrm{t}) = \delta^D(\mathrm{t})/l_o$), and the strain in the cohesive element ($\varepsilon^{\mathrm{coh}} = \delta^{\mathrm{coh}}/l_o$) that is irreversible (does not change for fixed δ_o), respectively.

If an initial instantaneous displacement δ_o is applied to this system, then this will result in an initial strain $\varepsilon_o = \delta_o/l_o$ and initial stress $\sigma_o = E\varepsilon_o$. The precise subsequent response of the system depends on the magnitude of the stress σ_o. If $\sigma_o \leq \sigma_c$, then the cohesive element is not involved and $\dot{\varepsilon}_o = \dot{\varepsilon}^e + \dot{\varepsilon}^D = E^{-1}\dot{\sigma} + \eta^{-1}\sigma$, where η is a material parameter akin to viscosity. With a constant applied displacement $\dot{\varepsilon}_o = 0$ so:

$$E^{-1}\dot{\sigma} + \eta^{-1}\sigma = 0$$

$$\frac{d\sigma}{dt} = \frac{-E}{\eta}\sigma \rightarrow \int_{\sigma_o}^{\sigma} \frac{d\sigma}{\sigma} = \int_0^t \frac{-E}{\eta}dt$$

which can be solved to provide temporal stress:

$$\sigma(t) = \sigma_o exp(-E\eta^{-1}t) \tag{5.4}$$

In this case $\sigma(t)$ is always less than σ_c since $\sigma_o \leq \sigma_c$. If on the other hand $\sigma_o > \sigma_c$, then the cohesive element is involved with displacement divided initially between the spring and the cohesive element, i.e. $\delta_o = \delta^e(0) + \delta^{\mathrm{coh}}$, with the dashpot not initially involved. The subsequent response of the model is one of relaxation of stress, since $\sigma^e(t) = \sigma^e(0)exp(-E\eta^{-1}t)$ where $\sigma^e(0)$ is evaluated from Eq (5.1) by applying $\delta^e(0)$ from Eq (5.2). The dashpot displacement is obtained from $\dot{\varepsilon}^D(t) = \dot{\delta}^D(t)/l_o = \sigma^e(t)/\eta$, which gives $\delta^D(t) = \delta^e(0)\big(1 - exp(-E\eta^{-1}t)\big)$.

The energy dissipated by the dashpot is evaluated from the rate at which work is done (per unit area) by the stress field, i.e. $\dot{U}_D = \dot{W}_d^D = l_o\sigma^D\dot{\varepsilon}^D$. Substitution of $\sigma^D = \eta\dot{\varepsilon}^D$ and integration gives

$$\frac{dU_D}{dt} = Al_o\eta(\dot{\varepsilon}^D)^2$$

$$U_D = \int_0^t \eta A l_o (\dot{\varepsilon}^D)^2 \, dt$$

$$= \int_0^t \eta A l_o \left(\frac{\sigma^e_{(0)}}{\eta} exp\left(\frac{-E}{\eta} t\right)\right)^2 dt$$

$$= \frac{A l_o \sigma^e(0)^2}{\eta} \int_0^t \left(exp\left(\frac{-E}{\eta} t\right)\right)^2 dt$$

$$= \frac{A l_o \sigma^e(0)^2}{\eta} \frac{-\eta}{2E} \left(exp\left(\frac{-E}{\eta} t\right)\right)^2 \Bigg|_0^t$$

$$= \frac{1}{2} A l_o \sigma^e(0) \frac{\sigma^e(0)}{E} \left(1 - \left(exp\left(\frac{-E}{\eta} t\right)\right)^2\right) = \frac{1}{2} A l_o \sigma^e(0) \varepsilon^e(0) \left(1 - \left(exp\left(\frac{-E}{\eta} t\right)\right)^2\right)$$

$$= \frac{1}{2} A l_o \sigma^e(0) \frac{\delta^e(0)}{l_o} \left(1 - \left(exp\left(\frac{-E}{\eta} t\right)\right)^2\right)$$

$$U_D = \frac{1}{2} A \sigma^e(0) \delta^e(0) \left(1 - \left(exp\left(\frac{-E}{\eta} t\right)\right)^2\right)$$

$$W^D(t) = \frac{U_D}{A} = \frac{1}{2} \sigma^e(0) \delta^e(0) \left(1 - \left(exp\left(-\frac{E}{\eta} t\right)\right)^2\right) \quad (5.5)$$

The energy calculation of the model is as follows:

for $\sigma_o \leq \sigma_c$ the instantaneous elastic displacement $\delta^e(0) = \delta_0$ and the separation $\delta = 0$. Hence, $\delta^e(t) = \delta_0 - \delta^D(t)$.

For $\sigma_o > \sigma_c$ the instantaneous elastic displacement $\delta^e(0)$ and stress $\sigma^e(0)$ are calculated from Eqs (5.2) and (5.1) respectively. The stress at any time $\sigma^e(t)$ is calculated from Eq (5.4), while the value of $\delta^e(t)$ is evaluated as:

$$\delta^e(t) = \delta_0 - \delta - \delta^D(t)$$

$$\delta^e(t) = \delta^e(0) exp\left(\frac{-E}{\eta} t\right) \quad (5.6)$$

The cohesive element will be active for this case with cohesive separation evaluates by $\delta = \delta_o - \delta^e(0)$. The energy transfers to the system, cohesive element, dashpot and spring are readily determinable with knowledge of the stress and strain rates with total

work done (per unit area) satisfying the equation $W^{\mathrm{d}}(t) = W^{\mathrm{e}}(t) + W^{\mathrm{D}}(t) + W^{\Gamma}$. An important aspect of the relaxation process for this model is that δ^{coh} is invariant.

5.3.3 Model (C-a)

Elastic-plastic fracture mechanics is of industrial importance as plasticity provides a mechanism for energy dissipation and consequently increased toughness. One mechanism for incorporating plasticity is to assume an elastic-plastic bulk-material model like that depicted in Fig. 5.3(C). Viscous behaviour is absent in this case and localised softening is achieved with the cohesive element shown in Fig. 5.2(a). The stress-displacement curve for the elastic-plastic material, with a LCE is shown in Fig. 5.5. As with the previous serial models, stress is common to all elements, i.e. $\sigma_o = \sigma^e = \sigma^p = \sigma^{coh}$, and strain is additive, $\varepsilon_o = \varepsilon^{\mathrm{e}} + \varepsilon^p + \varepsilon^{\mathrm{coh}}$. Note also that separation at fracture δ_f has contributions from bulk-material plasticity and the cohesive element, i.e. $\delta_f = \delta^p + \delta_c$. The behaviour of this system depends on the magnitude of the stress σ_o. If $\sigma_o \leq \sigma_Y, \sigma_c$, then elastic behaviour is preponderant and the stress will be evaluated from $\sigma_o = \sigma^e$, in this case $\varepsilon^e = \varepsilon_o = \delta_o/l_o$ with $\delta^e = \delta_o$ and $\mathrm{W}^{\mathrm{e}} = 0.5\sigma_o\,\delta^e$. If however $\sigma_o > \sigma_Y$, with plastic response approximated by the linear expression $\bar{\sigma} = \sigma_Y + E_p\bar{\varepsilon}^{\mathrm{p}}$, where for uniaxial tension effective stress $\bar{\sigma} = \sigma$ and effective plastic strain $\bar{\varepsilon}^{\mathrm{p}} = \varepsilon^p$ (since at this instance it is assumed $\varepsilon^{\mathrm{coh}} = 0$), then the strain $\varepsilon_o = \varepsilon^e + \varepsilon^p$. Consequently, the applied stress σ to the element can be evaluated by solving this equation $\delta_o/l_o = \sigma_y/E + (\sigma - \sigma_y)/E^p$, which is valid when $\sigma \leq \sigma_c$, where E^p is the plastic modulus. Energy is stored elastically but plastic dissipation takes place and is equal to

$$W^p = \frac{1}{2}(\sigma_Y + \sigma)\delta^p \tag{5.7}$$

where δ^p is the extent of plastic deformation and evaluated from $\delta^p = \delta_o - \delta^e$.

Finally if $\sigma > \sigma_c$, the total strain $\varepsilon_o = \varepsilon^e + \varepsilon^p + \varepsilon^{\mathrm{coh}}$ with $\varepsilon^{\mathrm{coh}} = \delta_c(1 - \sigma^e/\sigma_c)/l_0$, $\varepsilon^p = (\sigma_c - \sigma_y)/E^p$ and $\varepsilon^e = \sigma^e/E$. From this the stress can be evaluated as

$$\frac{\delta_o}{l_o} = \frac{\sigma^e}{E} + \frac{\sigma_c - \sigma_y}{E^p} + \frac{\delta_c\left(1 - \frac{\sigma^e}{\sigma_c}\right)}{l_0} \tag{5.8}$$

where it is assumed throughout this section that $\sigma_Y < \sigma_c$ because to do otherwise would mean no plastic deformation is possible. Energy is stored elastically but dissipated in

terms of plastic dissipation, as evaluated from Eq. (5.7) with σ_c replacing σ, and energy dissipated in propagating the crack evaluated from Eq. (5.3). The total work done (per unit area) is $W^{\mathrm{d}} = W^{\mathrm{e}} + W^{\mathrm{p}} + W^{\Gamma}$. The principal feature of this model is the protection offered to the crack through plastic-energy dissipation in the bulk material.

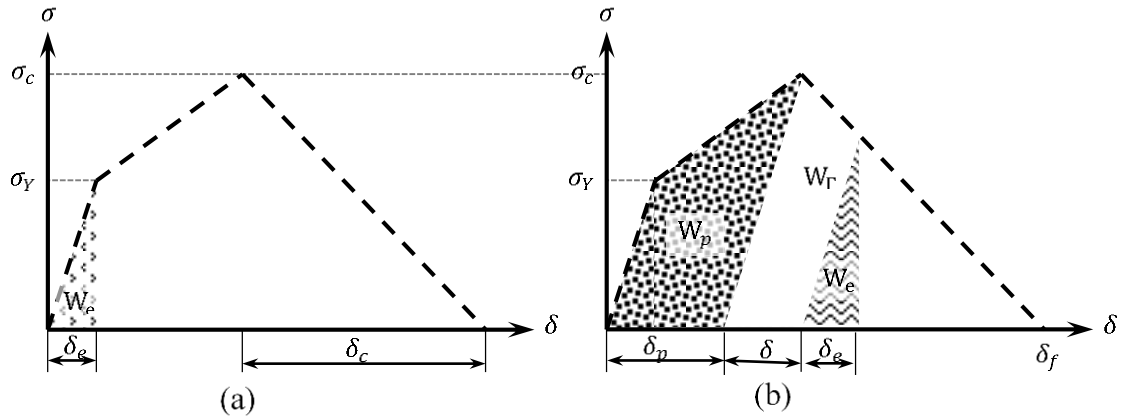

Fig. 5.5. The energy represented by the area under the stress-displacement curve.

5.4 Rate-Dependent CZMs

A useful bulk-material model is that of a linear-elastic material depicted in Fig. 5.3(A) and is particularly pertinent if other non-linear behaviours are localised to the crack tip. It is thus of interest to explore the use of a linear-elastic bulk-material model combined with rate-dependent cohesive models suggested in the literature. Combinations involving plastic behaviour in the bulk-material are also of some importance.

5.4.1 Model (A-i)

Model (A-i) provides rate dependency in the cohesive domain but linear-elastic behaviour in the bulk material. A critical feature of this particular set-up is a critical stress that is a function of the separation rate. An unwelcome aspect is the possible unboundedness of the critical stress. In the parallel part of the model (see Fig. 5.2(i)) the strain is the same and the stress is additive, but between this portion and the elastic bulk element the stress is identical, and the strain is additive. In mathematical terms $\sigma_o = \sigma^{\mathrm{e}} = \sigma^{\mathrm{s}}$, where σ^{s} is the stress applied to the parallel system and $\sigma^{\mathrm{s}} = \sigma^{\mathrm{D}} + \sigma^{\mathrm{coh}}$, $\varepsilon_o = \varepsilon^{\mathrm{s}}(\infty) + \varepsilon^{\mathrm{e}}$ and $\varepsilon^{\mathrm{coh}} = \varepsilon^{\mathrm{D}}$, where $\varepsilon^{\mathrm{s}}(\infty) = \lim_{t\to\infty} \varepsilon^{\mathrm{s}}(t)$, is the strain in the parallel system at stationary

equilibrium. Observe that for this model the strain $\varepsilon^{\mathrm{coh}}$ of the cohesive element is now a function of time.

As with previous models if an initial instantaneous displacement δ_o is applied to the system, its response depends on the magnitude of σ_o, where $\varepsilon_o = \delta_o/l_o$ and $\sigma_o = E\varepsilon_o$. If $\sigma_o \leq \sigma_c$, then $\delta^e = \delta_o$ and $W^d = W^e = 0.5\sigma^{\mathrm{e}}\delta^e$. If on the other hand $\sigma_o > \sigma_c$, then the elastic displacement δ^e is evaluated from Eq. (5.2) and material separation occurs at stationary equilibrium $\delta(\infty) = \delta_o - \delta^e$ and the stress $\sigma^e = E\delta^e/l_o$. The material separation as a function of time is

$$\delta(t) = \delta(\infty)\left(1 - exp\left(-\tfrac{E}{\eta}t\right)\right) \tag{5.9}$$

and the dissipated energy in the dashpot is obtained from

$$W^D(t) = \tfrac{1}{2}\sigma_o\delta(\infty)\left(1 - \left(exp\left(-\tfrac{E}{\eta}t\right)\right)^2\right) \tag{5.10}$$

where the total work done (per unit area) is $W^d(t) = W^e(t) + W^D(t) + \mathrm{W}^{\Gamma}(t)$.

If the rate-dependent cohesive energy is defined to be equal to the rate-independent cohesive energy plus the dissipated energy in the dashpot, then the previous equation becomes $W^d(t) = W^e(t) + W^{\Gamma_{\mathrm{rate}}}(t)$, where $W^{\Gamma_{\mathrm{rate}}}$ is the rate-dependent cohesive energy. Furthermore, critical traction can be viewed as a function of separation and separation rate, since $\sigma_{\mathrm{c}}^{\mathrm{rate}} = \sigma_c + \sigma^D$. A further common assumption is the linear relationship $\sigma^D = C\sigma_c$, where C is a parameter that is a function of separation rate. This returns an expression similar to that which has been used in reference [21], i.e. the rate-dependent stress relation can then be written as:

$$\sigma_c^{rate}\left(\dot{\delta}\right) = \sigma_c(1 + B\dot{\delta}) \tag{5.11}$$

where B is a material parameter reflecting the strength of rate dependency.

By using a similar procedure to the one used in Model (A-a) but with $\sigma_{\mathrm{c}}^{\mathrm{rate}}$ instead of σ_c for the critical cohesive stress the energy transfers in the model can be evaluated.

5.4.2 Model (A-e)

An alternative possibility for including a dashpot is to apply this in series rather that in parallel as in the model above. In the case of Model (A-e) a linear rate-independent CE (i.e. the TCZM with $\delta_1 = \delta_2 = 0$) is selected in series with a dashpot Fig. 5.2(e) to form

a rate-dependent CE and this element is connected to a linear elastic bulk-material model Fig. 5.3(A). The response of the rate-dependent cohesive element can be viewed as a function of the separation speed, since $\delta_c^{\text{rate}} = \delta_c + \delta^D$, where δ_c is the rate-independent cohesive separation and δ^D is the dashpot displacement. Setting $\delta^{\text{D}} = C\delta_c$ and on letting $C = B_1\dot{\delta}$ provides

$$\delta_c^{rate}(\dot{\delta}) = \delta_c(1 + B_1\dot{\delta}) \tag{5.12}$$

which is identical to an expression applied in reference [22] and where B_1 is a material parameter reflecting the strength of rate dependency.

The stress-displacement curve of the rate-independent and the rate-dependent cohesive element is depicted in Fig. 5.6(a). The energy calculation of this model is exactly the same as Model (A-a) apart from using δ_c^{rate} instead of δ_c to identify the critical separation of the model. An unwelcome feature of the model is the possible unboundedness of δ_c^{rate}.

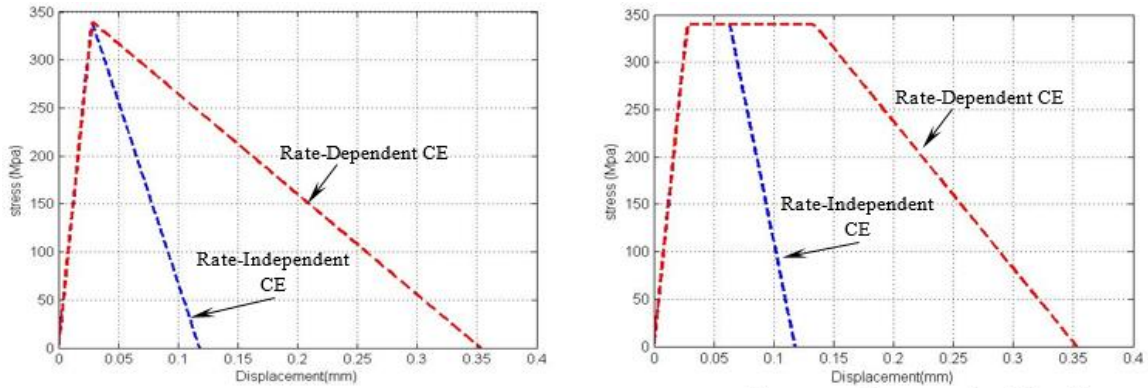

Fig. 5.6. Stress-displacement curve for the cohesive element in an elastic bulk material.

5.4.3 Model (A-g)

Combining the cohesive element shown in Fig. 5.2(g) with the material element shown in Fig. 5.3(A), provides a rate-dependent trapezoidal CE (with $\delta_1 = 0$) in an elastic bulk material. This model is similar to Model (A-e) although an important feature of this model is the incorporation of plastic energy dissipation. In this CE the process zone is separated into a plastic part (represented by the area under the traction separation curve between δ_1 and δ_2) and damage part (represented by the area under the traction separation curve

between δ_2 and δ_c^{rate}). For this model the values of δ_1 and δ_2 are selected to be zero and $0.5\delta_c^{\text{rate}}$, respectively. The critical rate-dependent separation δ_c^{rate} is assumed to satisfy Eq. (5.12), which means that when the separation speed increases, the value of the dissipated energy in plastic deformation and in the process of generating new surfaces increases. Fig. 5.6(b) shows the stress-displacement curve of the rate-independent and the rate-dependent cohesive element.

To better understand the behaviour of this model it is prudent to examine what energy transfers take place. Applying displacement δ_o provides $\sigma_o = E\varepsilon_0$ and as with the previous models the system's response depends on the magnitude of this stress. If $\sigma_o < \sigma_c$, then $\delta^e = \delta_o$ and $W^d = W^e = 0.5\sigma_0\,\delta^e$ If however $\sigma_o \geq \sigma_c$, then two possibilities arise depending on the magnitude of δ_o. If $\delta_o < \delta_2 + \delta_{max}^{e}$, with $\delta_{max}^{e} = \sigma_c/E$, then elastic energy $W^e = \frac{1}{2}\sigma_c\delta_{max}^{e}$ is constant and the local plastic dissipated energy is determined by $G^{Prate} = \sigma_c(\delta_o - \delta_{max}^{e})$ the total work done in this case evaluated as $W^d = W^e + G^{Prate}$. Finally, if $\delta_o \geq \delta_2 + \delta_{max}^{e}$, then the crack propagates giving rise to an increase in surface energy and a decrease in the stored elastic energy and no further plastic dissipation, in the case the total work satisfies the relationship $W^d = W^e + G^{Prate} + \Gamma_{rate}$.

5.4.4 Model (C-e)

The model arises from the combination of the cohesive element shown in Fig. 5.2(e) with the material element shown in Fig. 5.3(C) is similar to Model (C-a), but in this model the cohesive element is rate-dependent. In this CE the value of the critical separation δ_c is assumed to be a function of the separation speed (δ_c^{rate}), which means that as the separation speed is increased, the value of the dissipated energy in the fracture process increases. Fig. 5.7(a) shows the stress-displacement curve of the rate-independent and the rate-dependent cohesive element. The energy calculation for this model is similar to Model (C-a) but with δ_c^{rate} from Eq. (5.12) in place of δ_c.

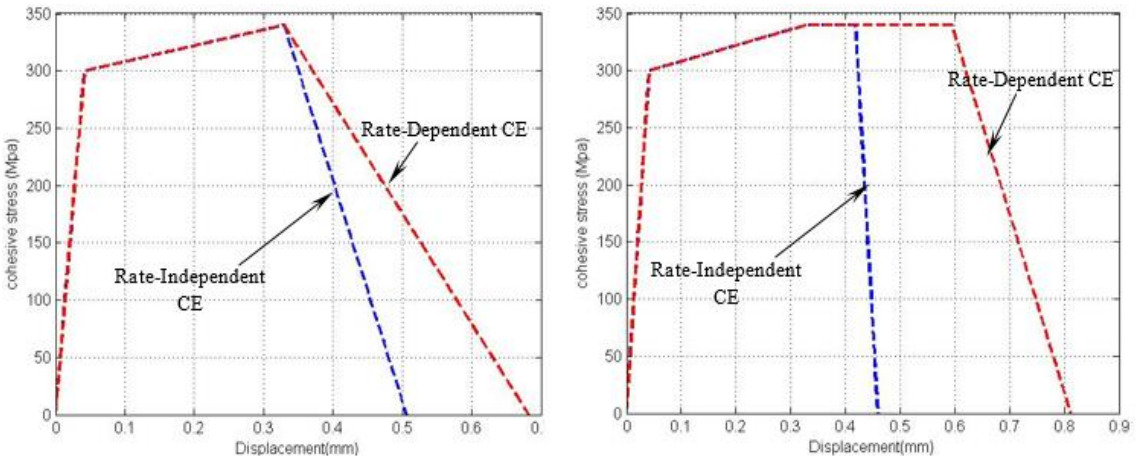

(a) LCZM (Model (C-a) & (C-e)) *(b) TCZM with $\delta_1 = 0$ (Model (C-g))*

Fig. 5.7. Stress-displacement curve for the cohesive element in an elastic-plastic bulk material

5.4.5 Model (C-g)

This model is similar to Model (C-e), but in this model a rate-dependent trapezoidal cohesive element is used as shown in Fig. 5.2(g). In this CE the value of the critical separation δ_c^{rate} is calculated from Eq. (5.12). As regards the traction separation law, δ_1 is assumed to be zero and δ_2 is set equal to $0.5\delta_c^{rate}$. A feature of this model is that with an increase in separation speed the dissipated energy increases due to plastic deformation and new surfaces formation. Shown in Fig. 5.7(b) is the stress-displacement curve of the rate-independent and the rate-dependent cohesive element.

5.5 New Rate-Dependent Cohesive Model

To overcome limitations with existing rate-dependent cohesive model a new model is introduced in this study. A systematic approach has been adopted to better understand the behaviour and limitations of said models and it is expected that any new model should not suffer unrealistic behaviour typically observed with existing approaches. To keep things reasonably simple the bilinear and the trapezoidal cohesive model are incorporated into the new model to simulate the dynamic crack growth processes. A feature of the new model is dashpots in both series and parallel to counter unrealistically high values of δ_c and σ_c observed when dashpots are applied singularly.

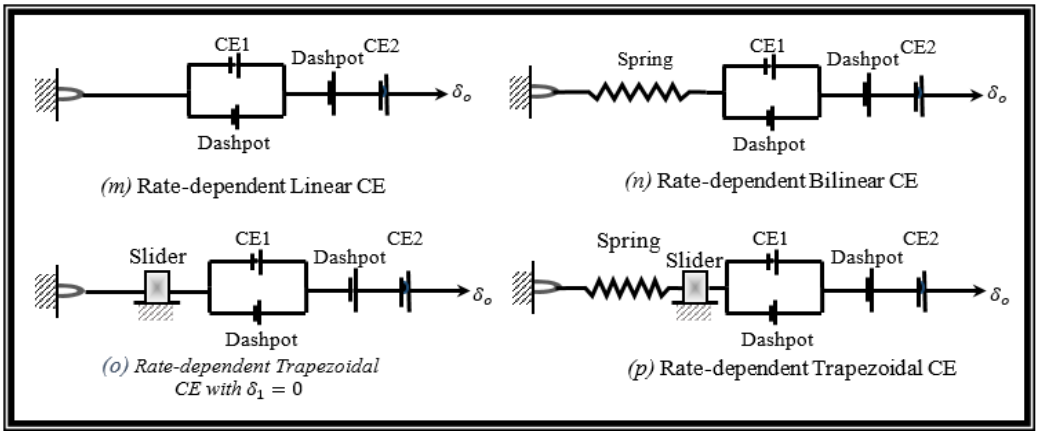

Fig. 5.8. New Elementary Rate-dependent Material Element in the Cohesive Zone.

5.5.1 Model (A-m)

The proposed new rate-dependent LCE is shown in Fig. 5.8(m). The cohesive element consists of two parts one of which is a parallel combination of a rate-independent CE in parallel with a dashpot to provide a rate-dependent critical stress. This part is active when the rate-dependent cohesive stress is less than the identified stress limit σ_{limit} thus providing a bounded critical stress. The value of σ_{limit} is set so that the area under the traction curve defined by σ_{limit} is equal to an experimentally obtained upper limit on fracture energy. Thus, for $\sigma_c^{rate} < \sigma_{limit}$, Eq. (5.11) applies and the separation is held constant at the critical separation used for the rate-independent cohesive model. At the point when σ_c^{rate} reaches its limit σ_{limit} this part of the cohesive element becomes inactive and the second part consisting of a series dashpot and rate-independent CE is activated. In this CE the critical stress is equal to σ_{limit} and the critical separation is again equal to that used in the rate-independent model. This part of the cohesive model provides a rate-dependent CE in which the critical stress is constant at σ_{limit} and a critical separation that increases with rate satisfying Eq. (5.12) with replacing B_1 by B'_1. The energetic behaviour of this model is similar to Model (A-a) but with using σ_c^{rate} instead of σ_c for $\sigma_o < \sigma_{limit}$ and if $\sigma_o \geq \sigma_{limit}$, then δ_c^{rate} is used instead of δ_c. To demonstrate this explicitly consider an initial displacement δ_o applied to this system, and set $\varepsilon_o = \delta_o / l_o$ and $\sigma_o = E\varepsilon_o$. As with previous cases the behaviour of the system depends greatly on the magnitude of σ_o. If $\sigma_o \leq \sigma_c^{\text{rate}}$ (where the inequality $\sigma_c^{\text{rate}} \leq \sigma_{limit}$ is enforced by design), then $\varepsilon_o = \varepsilon^e$, $\sigma = E\,\varepsilon^e$, $\delta^e = \delta_o = \varepsilon_o l_o$ and $W^d = W^e = 0.5\,\sigma\,\delta^e$. If on the other hand $\sigma_o > \sigma_c^{\text{rate}}$, then two possibilities arise, i.e.

$\sigma_c^{\text{rate}} \leq \sigma_{limit}$ or $\sigma_c^{\text{rate}} > \sigma_{limit}$, where in the latter case critical cohesive stress is set equal to σ_{limit} and δ_c^{rate} is used in place of δ_c for energy calculations. The work done is evaluated by $W^d = W^e + W^{\Gamma_{\text{rate}}}$, where $W^{\Gamma_{\text{rate}}} = G^{P_{rate}} + \Gamma_{rate}$.

5.6 Energy calculations

In this section, a numerical description of the energy transfers is presented to support the theoretical descriptions provided in Sections 5.3 to 5.5 and to visually highlight the important behaviours found with the different models considered. The material properties and process parameters selected for the study can be found in Table 5.1.

Table 5.1 Material properties and process parameters.

Length l_o (mm)	σ_c (MPa)	δ_c (mm)	σ_Y (MPa)	Γ_0 (N/mm)	E (MPa)	E^{p} (MPa)	δ_1 (mm)	
10	340	0.17647	300	30	72000	1390	0	
δ_2 (mm)	Viscosity (η) (Pa.s)			B (s/m)	B_1 (s/m)	B'_1 (s/m)	separation rate ($\dot{\delta}$) (m/s)	
$0.5\delta_c$	10	30	60	0.1	0.1	0.02	5	10	20

Depicted in Fig. 5.9 and 5.10 are energy-displacement diagrams for a linear rate-independent CE embedded in an elastic bulk material. From Fig. 5.10 it is evident that the stored elastic energy participates in the crack growth driving process [106]. This is reflected by a decrease in stored elastic energy originating at the point where material separates along with an increase in cohesive energy. The behaviour of this model when a dashpot is added to the bulk material (Model (B-a)) to represent the rate dependency is shown in Fig. 5.11. It is evident from this figure that the response is one of material relaxation rather than a rate-dependent fracture model. This is reflected in the relaxation of stored elastic energy as opposed to driven crack propagation. An alternative is a parallel combination of dashpots to produce a rate-dependent cohesive element as in Model (A-i). In this case however, the dashpot is built into the cohesive element, which implicitly assumes rates local to the crack feature predominantly. The local stress is dependent on the viscosity associated with the dashpot and the rate of separation. This is reflected in the value of the parameter B in Eq. (5.11), which represents the rate dependency of the local damaged material. A particular feature of this model is a critical stress which is not temporally invariant and increases with the separation speed, which

could lead to an unrealistic crack arrest. The behaviour of this model is shown in Fig. 5.12, where it can be deduced from the rise in energy that the critical stress is increasing with rate. Bearing in mind that critical stress is the damage initiation mechanism in the cohesive model an unrealistically high value can have negative connotations. With this model, the critical stress can reach levels significantly greater than the yield stress of the bulk material leading to both crack arrest and unrealistic levels of plastic deformation in any finite element model.

To avoid the possibility of a high critical stress a localised linear dashpot arrangement is an obvious possibility. Model (A-e) is one possibility consisting of a dashpot connected in series with a standard cohesive element, which leads to critical separation being a function to the separation rate of the form of Eq. (5.12). Although it is claimed in reference [22] that the model can provide more accurate results, it is demonstrated in Section 5.7 that the model has unrealistic behaviour at high strain rates. Fig. 5.13 shows the energy curves for Model (A-e), where it is apparent that the value of the critical separation is increasing with separation rate leading to high values at very high strain rates.

It is evident that a new model is necessary to overcome the limitations of both of the previous models. The proposed models considered here for localised rate-sensitive behaviour combines the elastic-bulk material element shown in Fig. 5.3(A) with a rate-dependent linear or trapezoidal cohesive element shown in Fig. 5.8.

A concern, however, is the effect of plasticity both locally and in the bulk material and therefore it is of interest also to examine models involving elasto-plastic bulk material moedel depicted in Fig. 5.3(C). There are numerous approaches for simulating the fracture process in an elasto-plastic material. An example is an elastic-bulk material and plasticity captured locally in the cohesive element as in Model (A-g) by using the trapezoidal model. This trapezoidal model could be rate-independent or rate-dependent depending on the type of problem. The energy-displacement curve for this model is shown in Fig. 5.14. Alternatively, the problem can be simulated by using the bilinear rate-dependent or rate-independent cohesive model with an elasto-plastic behaviour in the bulk material as in Models (C-a) and (C-e), which provide the results shown in Fig. 5.15 and 5.16, respectively. Contrasting the results of Model (A-g) (shown in Fig. 5.14) with the result of Model (C-e) (shown in Fig. 5.16) highlights certain distinctive

similarities. The advantage of analysis with plasticity captured locally in a CZM is a much-reduced analysis cost. However, accuracy is an issue, and the benefit of investigating the effect of the TSL and the choice of the TCZM is manifest. In the case of large-plastic deformation taking place in the bulk material, then the advantages of localised plastic analysis are diminished. However, with a view that plastic behaviour in the damaged zone is different from the virgin material then an appropriate cohesive model could be used to improve accuracy. A model of this type is Model (C-g) and the associated energy-displacement curve is depicted in Fig. 5.17.

The energy-displacement plots for the new rate-dependent cohesive element can be found in Fig. 5.18. Contrasting the results in Fig. 5.12, 5.13 and 5.18 demonstrates how the new model eliminates the unrealistic behaviour in existing rate-dependent cohesive models. To better demonstrate further the benefits of the new approach the three competing approaches are tested in fracture simulations applied to a compact tension (CT) specimen in the following section.

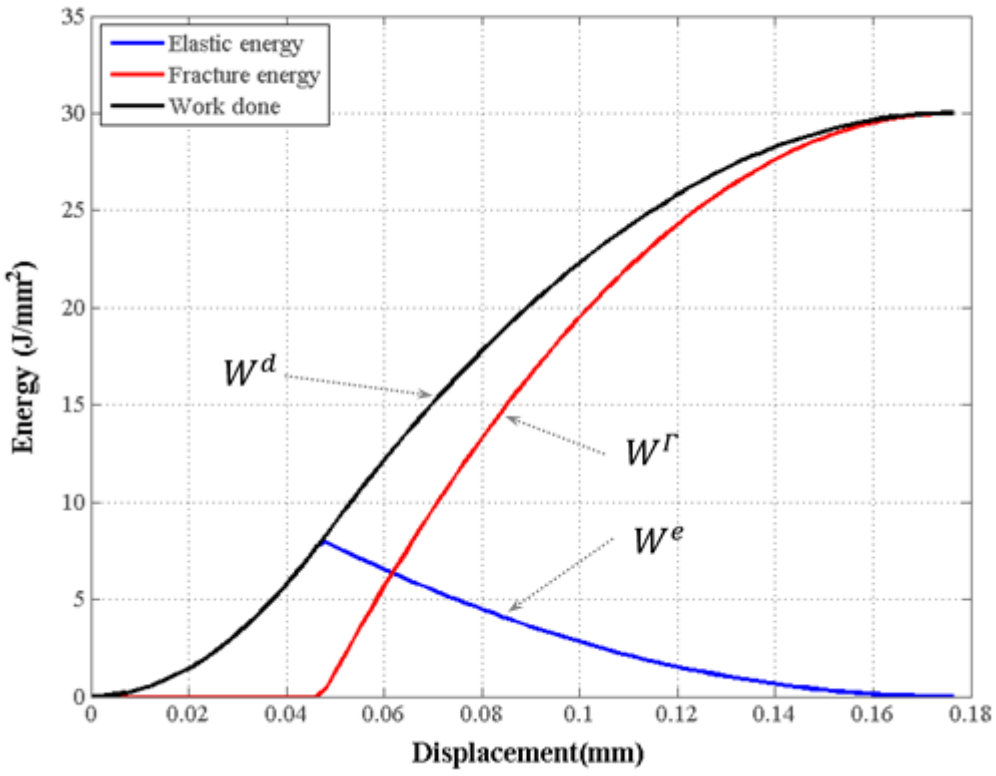

Fig. 5.9. Model (A-a) energy-displacement curve of a rate-independent CE in an elastic bulk material.

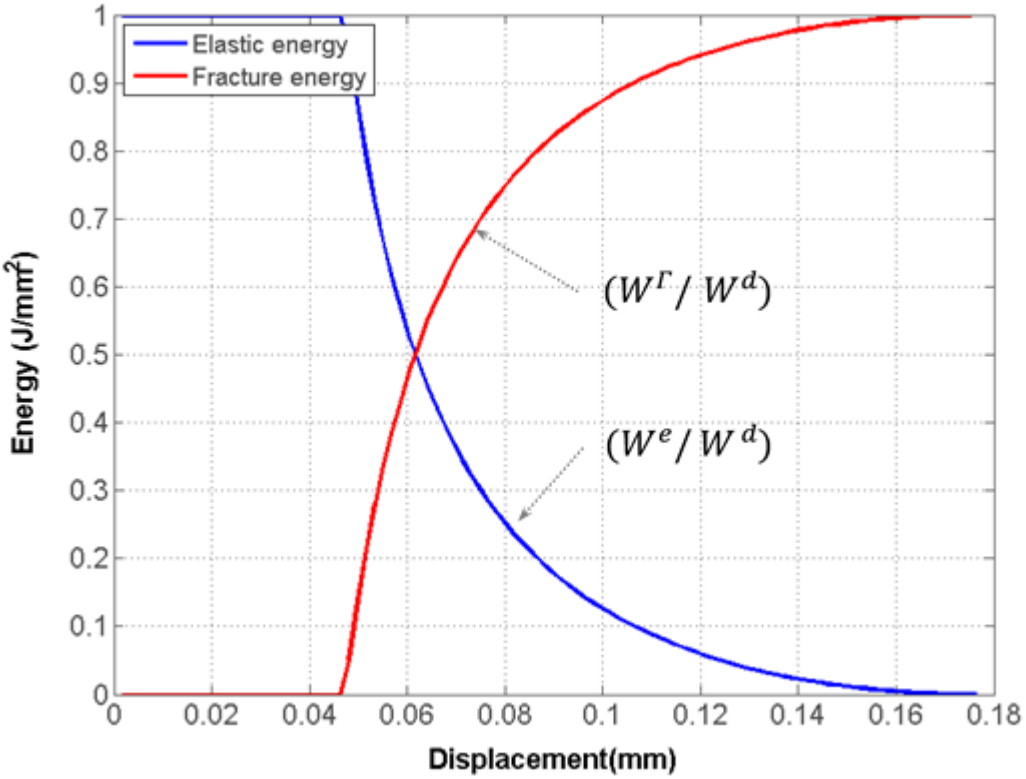

Fig. 5.10. Model (A-a) normalized elastic and fracture energy diagram.

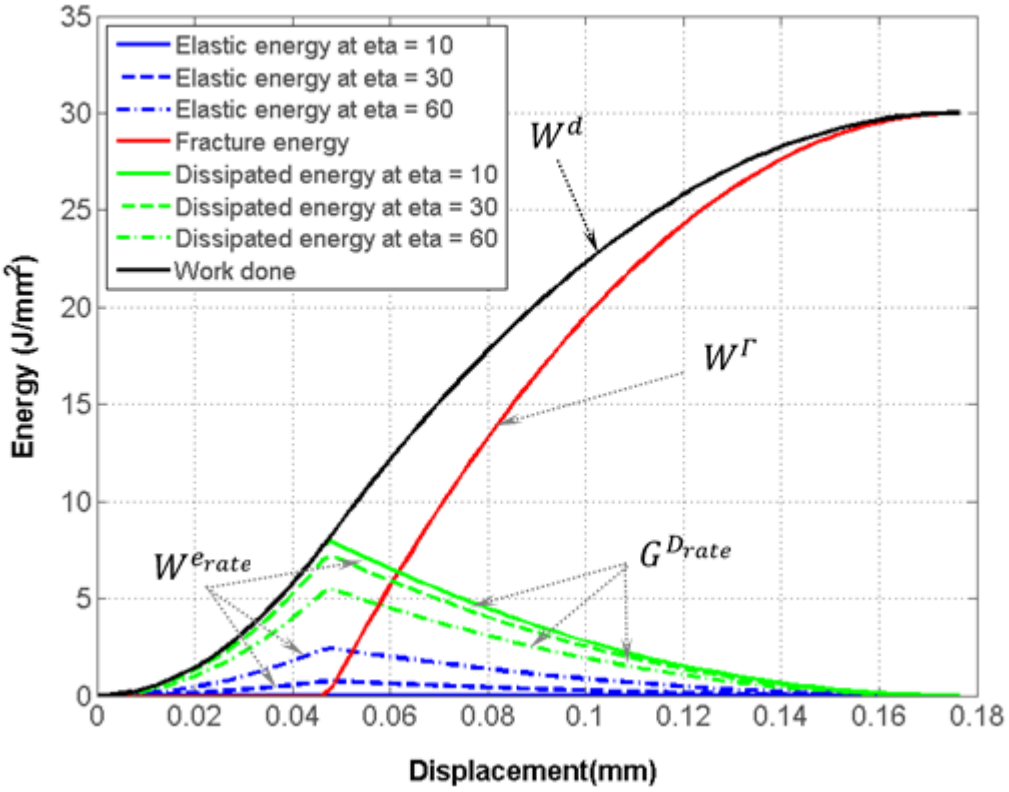

Fig. 5.11. Model (B-a) material relaxation response.

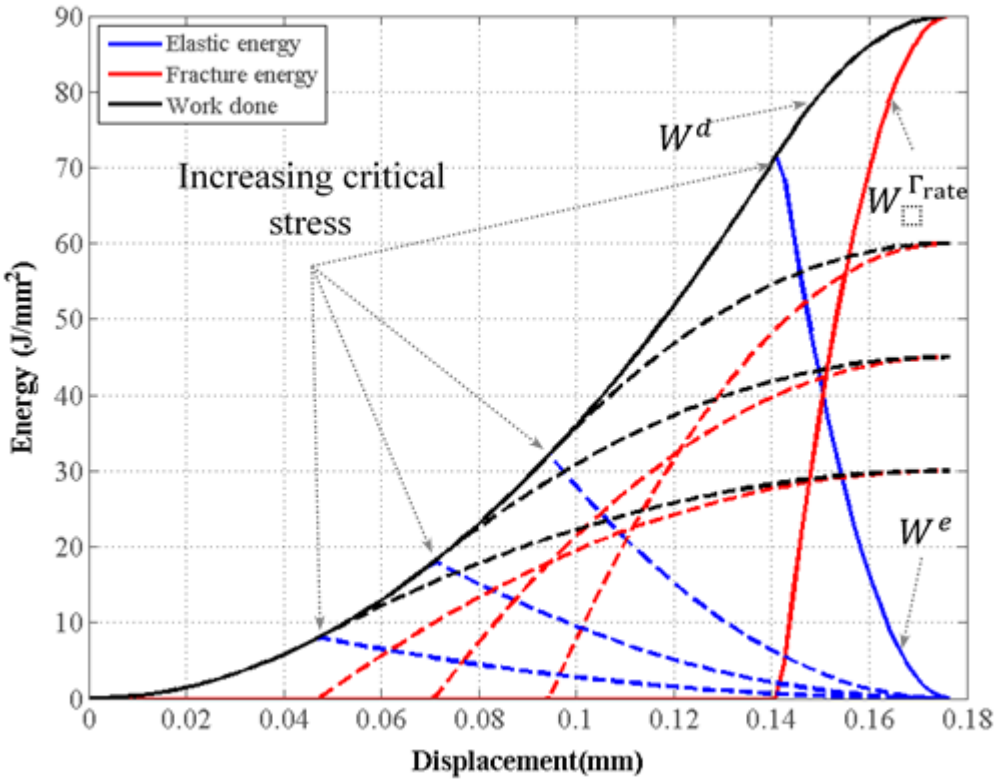

Fig. 5.12. The increase in the value of energy at critical stress because of the unrealistic increasing critical cohesive stress in Model (A-i).

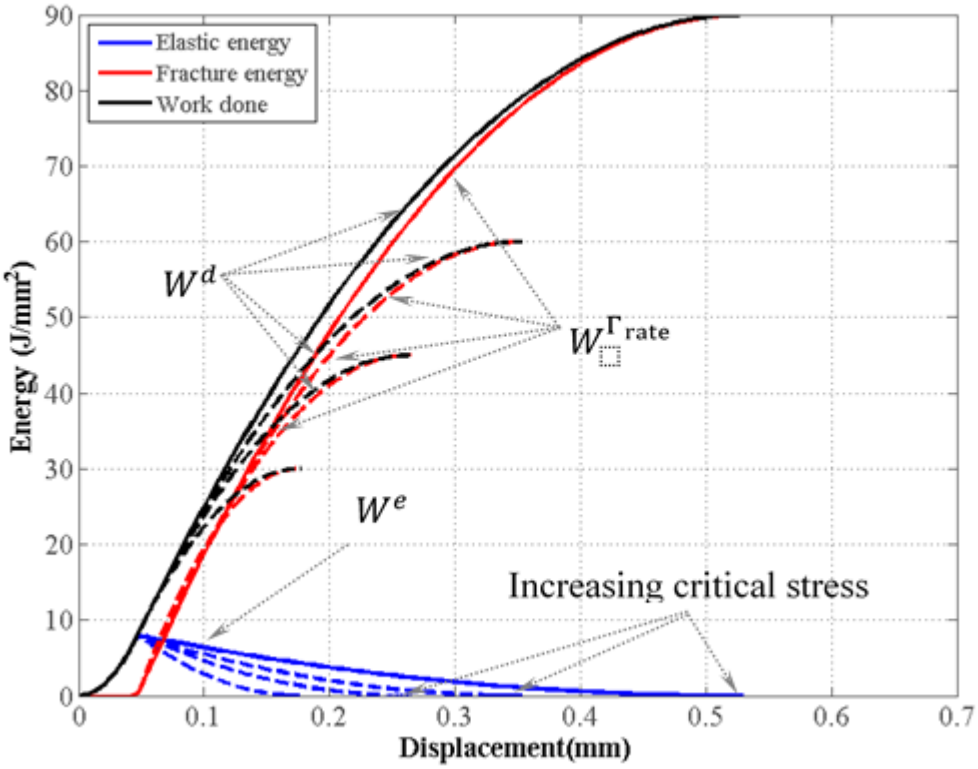

Fig. 5.13. The unrealistic increasing critical cohesive separation in Model (A-e).

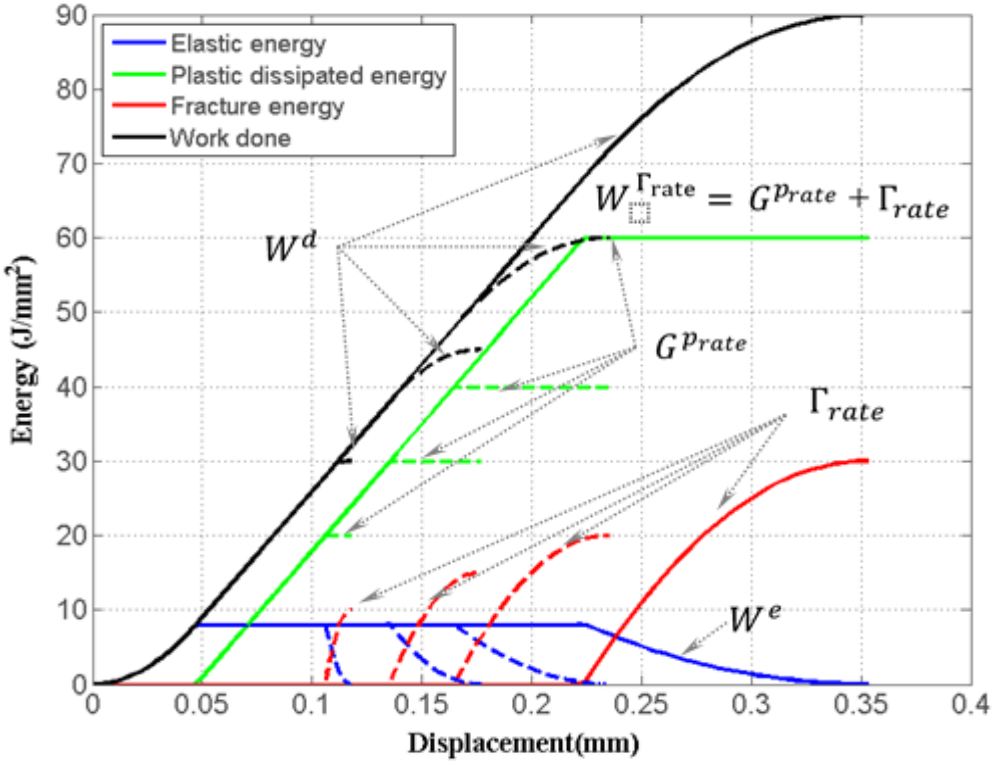

Fig. 5.14. Model (A-g) plasticity capture locally by using the trapezoidal rate-dependent CE.

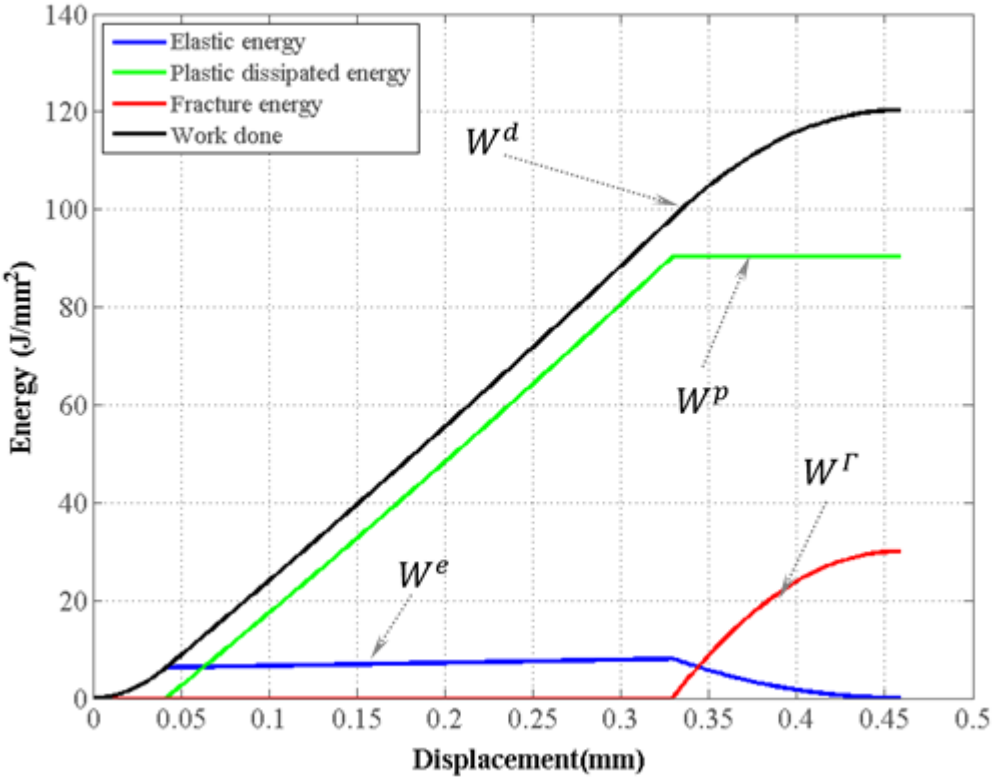

Fig. 5.15. Model (C-a) energy-displacement curve of a rate-independent CE in an elasto-plastic bulk material.

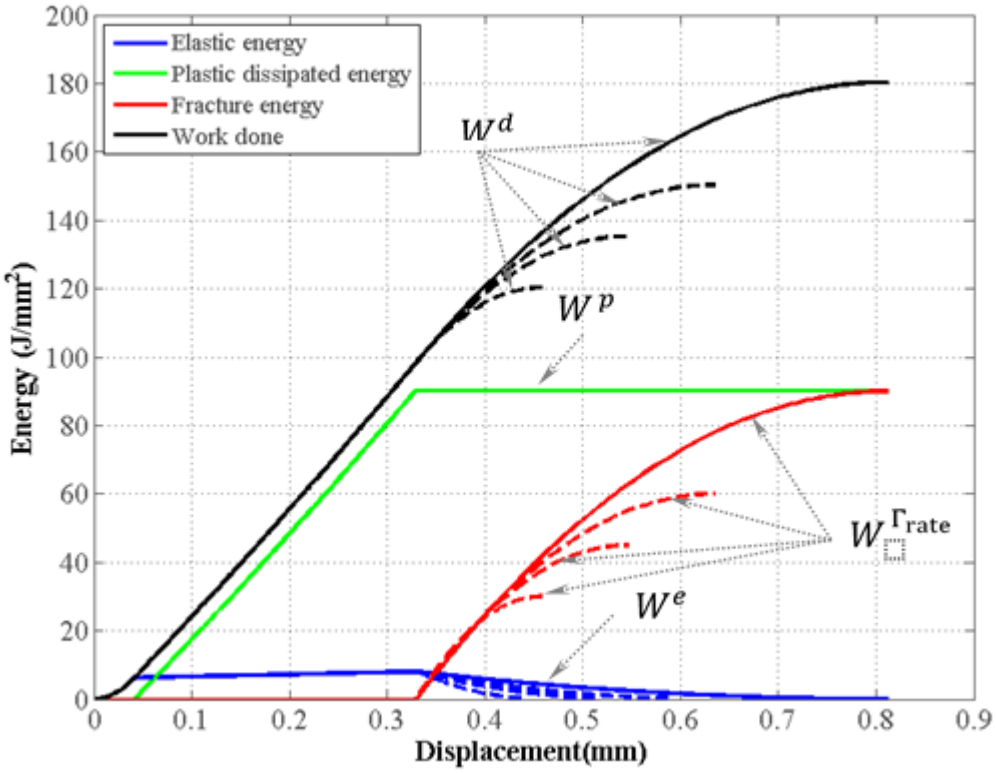

Fig. 5.16. Model (C-e) linear rate-dependent CE in an elasto-plastic material.

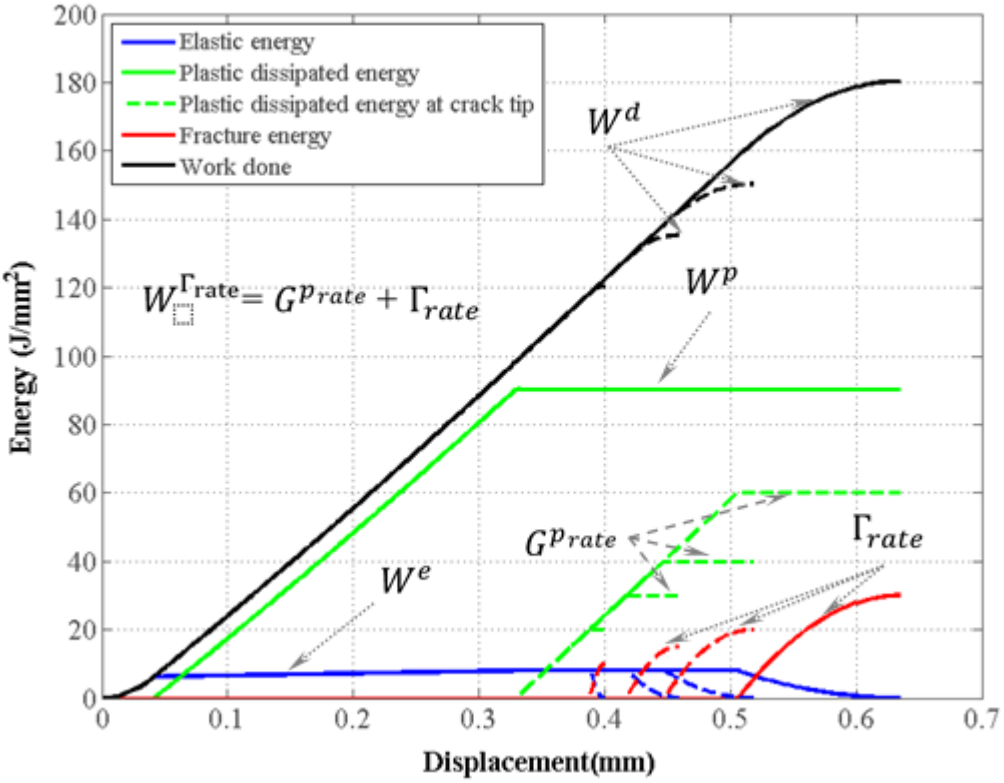

Fig. 5.17. Model (C-g) trapezoidal rate-dependent CE in an elasto-plastic material.

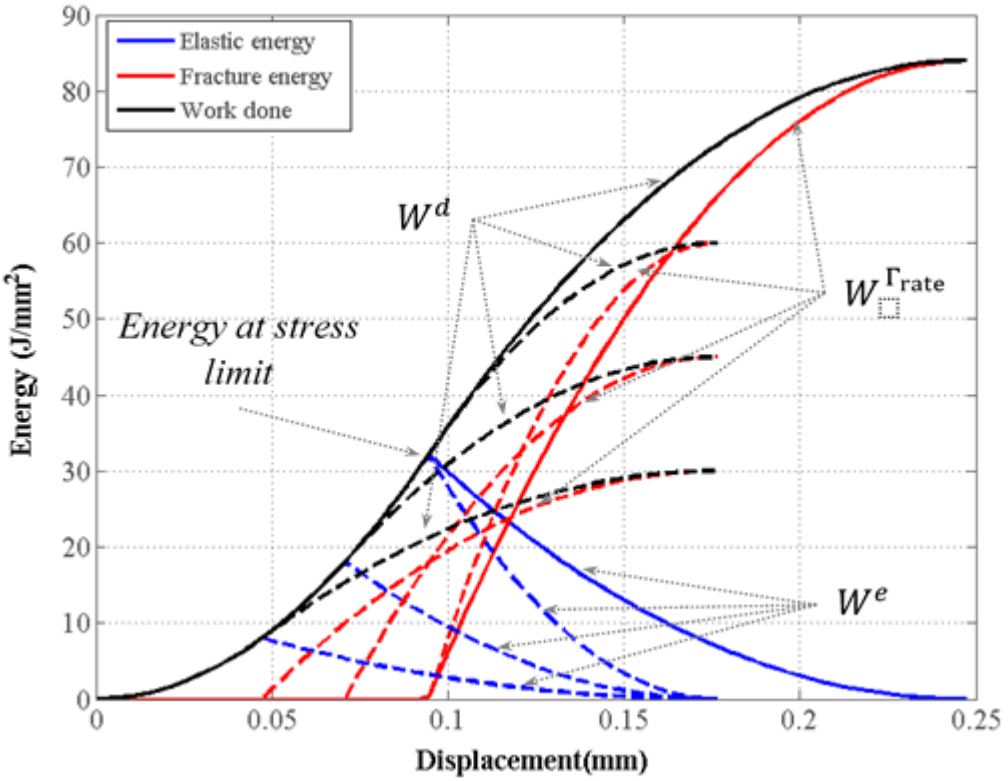

Fig. 5.18. Model (A-m) effect of stress limit in the new linear rate-dependent CE in an elastic bulk material.

5.7 Monotonic fracture simulation in ABAQUS

There are two methods for identifying cohesive behaviour in the commercial finite element solver ABAQUS; the first method is by specifying a cohesive traction between two adjacent surfaces; the main advantage of this approach is that ABAQUS will duplicate the nodes at the adjacent surfaces and connect them through cohesive forces. Hence, the thickness of the cohesive-zone is approximately zero. The second method is by inserting cohesive elements along the crack path between the bulk material elements, by default the separation width of the cohesive element defaults as unity in ABAQUS making the strain at the cohesive element equal to the separation. The cohesive behaviour in the second type is defined through a cohesive material. This facilitates a user-defined material subroutine, which can be used to specify new non-standard cohesive behaviour of the type considered here.

The types of simulation performed in this study are shown in Table 5.2. Nine quasi-static simulations are performed on a CT specimen (see Fig. 5.19) to check the effect of the TSL and the effect of plasticity. Of the nine, two make use of the BCZM and seven utilise

the TCZM with associated responses presented in Fig. 5.20 to 5.22. This is followed by an investigation into the behaviour and the limitations of methods (existing and new) used to capture rate-dependent behaviour. Numerous transient-dynamic simulations have been performed (see Table 5.2) and details are provided in Section 5.7.2.

Table 5.2 Type of simulations applied to a standard CT specimen.

Model	Analysis type	Bulk material response	Cohesive-zone response	TSL	No. of An.
QS-B	Quasi-static	Rate-independent	Standard	BCZM	2
QS-T	Quasi-static	Rate-independent	Standard	TCZM	7
DYN -B	Transient dynamic	Rate-independent	Standard	BCZM	4
DYN -T	Transient dynamic	Rate-independent	Standard	TCZM	4
DYN-σ_c^{rate}-B	Transient dynamic	Rate-independent	Rate-dependent	BCZM	7
DYN-σ_c^{rate}-T	Transient dynamic	Rate-independent	Rate-dependent	TCZM	5
DYN-δ_c^{rate}-B	Transient dynamic	Rate-independent	Rate-dependent	BCZM	4
DYN-New-B	Transient dynamic	Rate-independent	Rate-dependent	BCZM	5
DYN-New-T	Transient dynamic	Rate-independent	Rate-dependent	TCZM	5

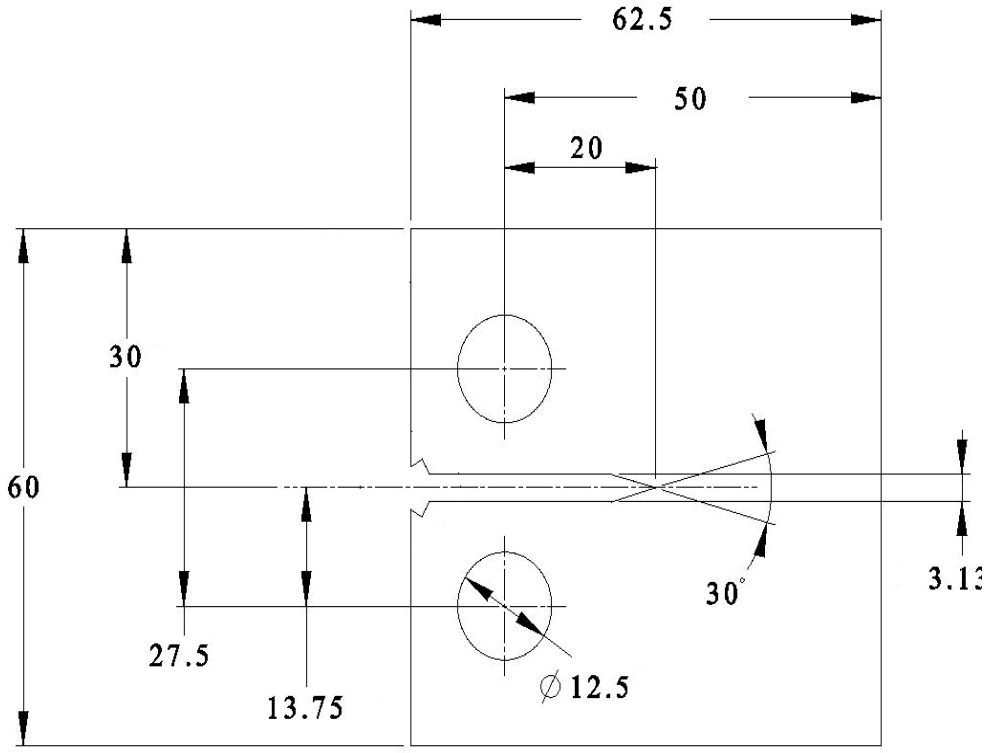

Fig. 5.19. CT specimen dimensions (mm).

5.7.1 Plasticity effects

Fracture simulations of a CT specimen with dimensions shown in Fig. 5.19 have been performed in ABAQUS by using the BCZM and repeated using the TCZM; first with an elasto-plastic bulk material and second with an elastic-bulk material. The reason for using these two models is to study the effect of the TSL and to show the benefit of using a CZM to capture plasticity locally. The numerical model consists of 7823 plane-strain elements (type CPE4R) and 100 cohesive elements (type COH2D4) [109]. A mesh sensitivity analysis has been performed which confirms that converged results are attained. Involving a full-integration plane-strain element (CPE4) or increasing the number of elements in the bulk material or the cohesive-zone, has little impact on the simulation results presented. The material properties used for the bulk material in the numerical simulations are $\{\sigma_y = 280\ \text{MPa}, E = 193\ \text{GPa}, \vartheta = 0.29$ and the plastic behaviour is set through the true stress-plastic strain shown in (Table 4.3 presented in Chapter 4)$\}$ with cohesive parameters shown in Table 5.3.

Table 5.3 Cohesive model parameters.

Cohesive parameter set	Cohesive law	Γo (N/m)	E^{coh} (GPa)	σ_c (MPa)	δ_c (m)	δ_1 (m)	δ_2 (m)
1	BCZM	189000	15000	600	0.00063	0.00004	0.00004
	TCZM	189000	15000	600	0.00038286	0.00004	0.000287145
2	BCZM	189000	15000	600	0.00063	0.00004	0.00004
	TCZM	189000	15000	350	0.00063	0.000023	0.0004725
3	BCZM	189000	15000	600	0.00063	0.00004	0.00004
	TCZM	246500	15000	460	0.00063	0.0000307	0.0004725
4	TCZM	222000	15000	310	0.00083	0.0000207	0.0006225

Shown in Fig. 5.20 and 5.21 are the plots relating load to load-line displacement (i.e. the reaction force as a function of the applied displacement measured at the loading point represented by the two circular holes shown in Fig. 5.19) for the first two cohesive parameter sets contained in Table 5.3. It is clear from these plots that the shape of the traction separation curve has a noticeable effect on the load-line curves. This emphasises the importance and influence of the type of TSL and associated cohesive parameters on responses measured remotely from the cohesive-zone. The results obtained are for the

same specimen using either the BCZM or the TCZM with invariant fracture energy and either critical traction fixed or critical separation fixed. This result is in agreement with the results obtained from many other authors [14–16]. Although the results confirm that the TSL can influence fracture behaviour the extent of this influence depends on the geometry and material of the test specimen. If the specimen has high stiffness, then greater sensitivity to the shape of the TSL can be anticipated [16]. This point is made explicit in Fig. 5.22, where load-line displacement curves can be found for fracture simulations by using the cohesive parameter set number 3 and 4 (see Table 5.3) contrasting TSLs in an elasto-plastic bulk material against a purely elastic bulk material. From these curves, it is clear that the TCZM displays a clear elasto-plastic response making it more appropriate than the BCZM for simulating fracture for an elasto-plastic bulk material yet adopting only an elastic material for the analysis. It is apparent from Fig. 5.22 that the TCZM gives a broad range of responses depending on the cohesive parameters used.

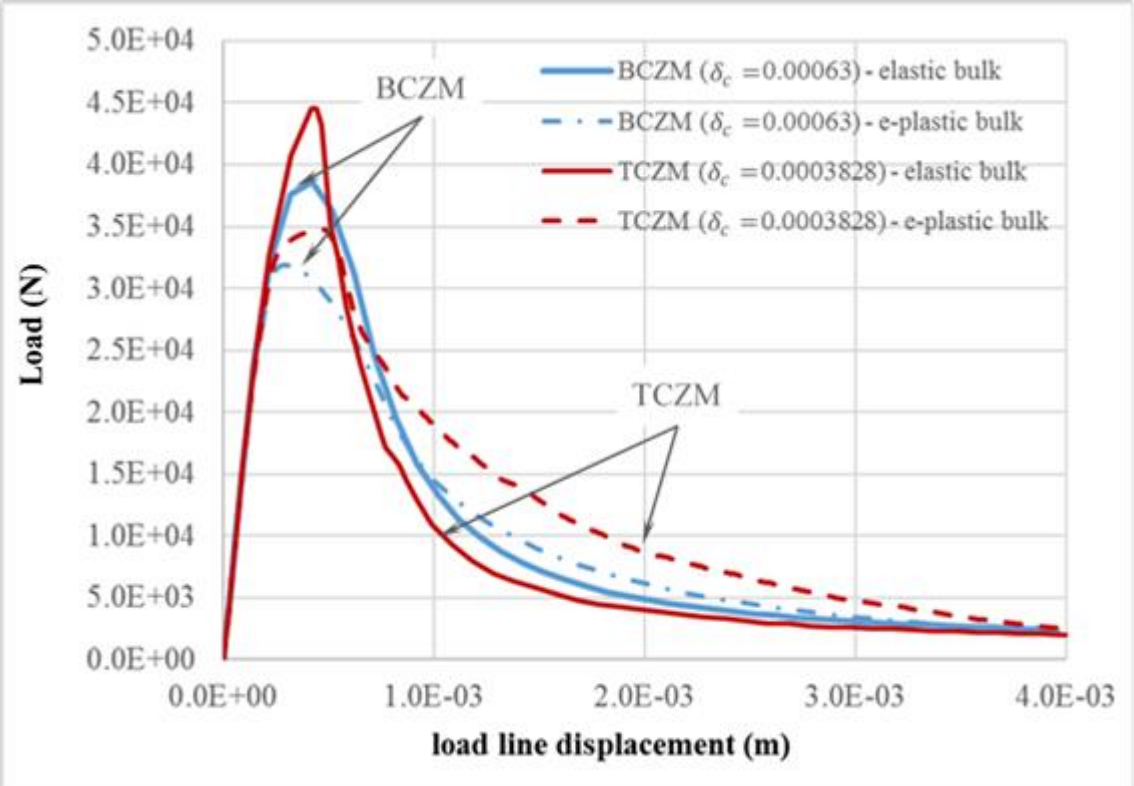

Fig. 5.20. Load versus load line displacement for the BCZM & TCZM with equal fracture energy (189 N/mm) and critical stress (600MPa).

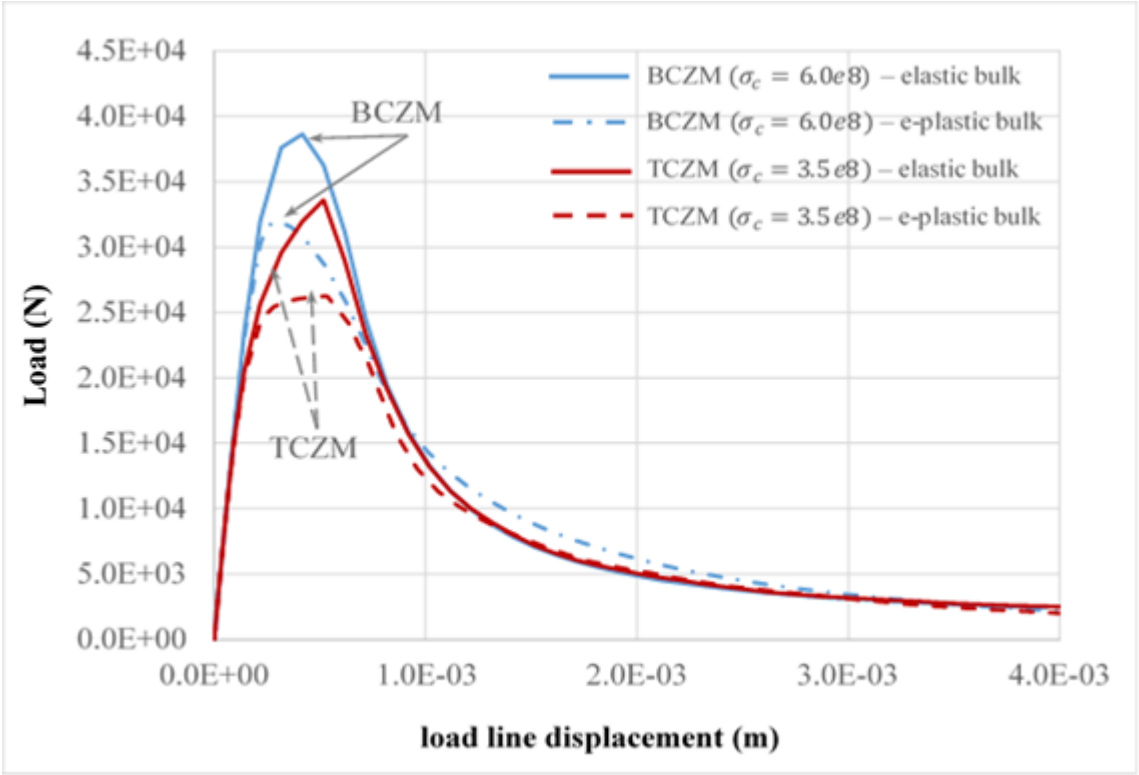

Fig. 5.21. Load versus load line displacement for the BCZM & TCZM with equal critical fracture energy (189 N/mm) and critical separation (0.00063m).

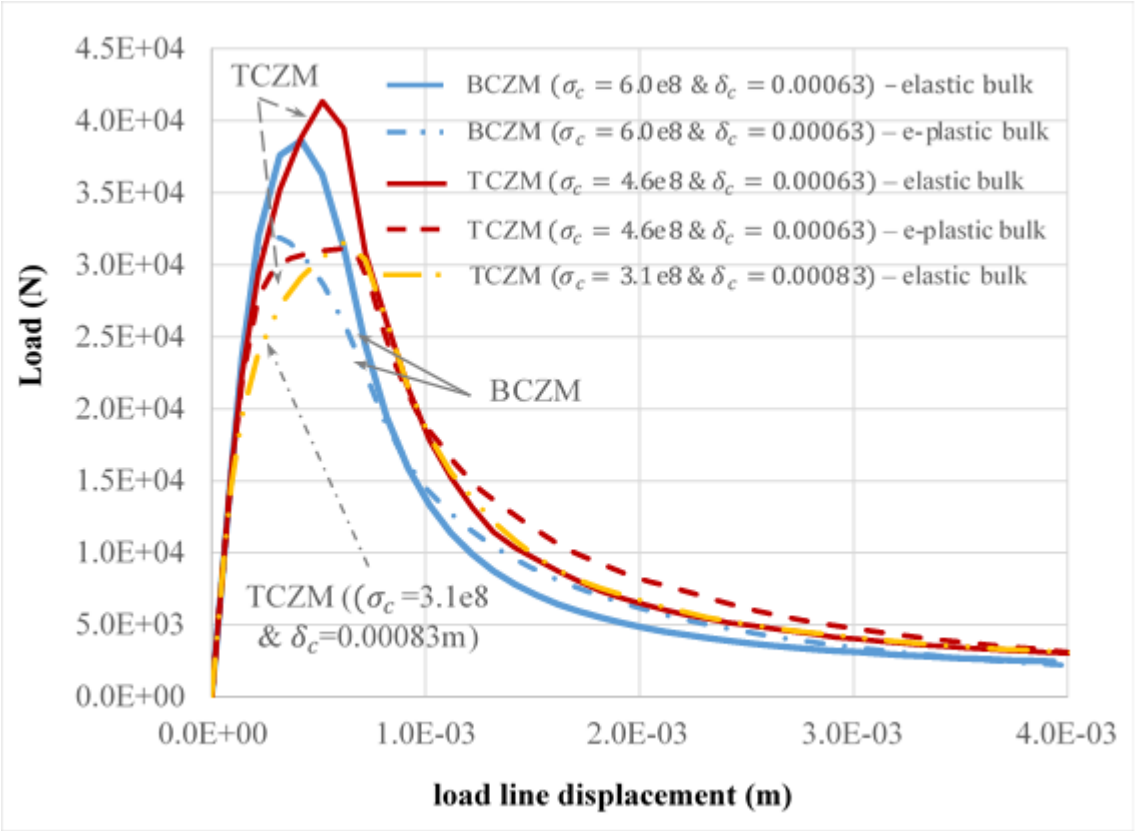

Fig. 5.22. Load versus load-line displacement for the BCZM & TCZM.

5.7.2 Strain rate effect

In this section, the rate-dependent CZM is used to simulate the fracture behaviour of a CT specimen (see Fig. 5.19) subjected to different applied loading speeds by using the cohesive parameter set 1 from Table 5.3. For each loading speed, a number of simulations are performed which are:

(i) Rate-independent BCZM and TCZM.
(ii) Stress rate-dependent BCZM and TCZM (i.e. critical stress is function of separation rate).
(iii) Separation rate-dependent BCZM (i.e. critical separation is function of separation rate) and finally.
(iv) The new rate-dependent BCZM and TCZM (i.e. new approach proposed in this study).

The crack length measurement has been done manually by evaluating the displacement jump between all the adjacent nodes in the cohesive-zone at each time step. The crack tip will be at the nodes where the displacement jump is equal to the critical cohesive separation. Shown in Fig. 5.23 to 5.26 are plots revealing the temporal response of crack length for the existing rate-dependent approaches with the BCZM at four loading speeds i.e. 0.1, 1.0, 10 and 100 m/s, respectively. At the lowest rate, it is apparent on examination of Fig. 5.23 that there is little difference between the rate-independent and rate-dependent models. Increasing the loading rate however reveals a decreasing rate of crack growth (see Fig. 5.24 to 5.26). Examination of Fig. 5.25 and 5.26 at respective loading speeds of 10 m/s and 100 m/s reveals unexpected and somewhat unrealistic behaviour with crack initiating not at the crack tip but at a point inside the specimen and subsequently propagating in two directions (see Fig. 5.27 and 5.28). This behaviour is as a consequence of the strain rate at elements in the location of the crack tip being much higher than elsewhere and consequently giving rise to a very high critical separation. A feature of the highest loading rate of 100 m/s, for the separation rate-dependent CZM is a delay in the initiation of the crack subsequently followed by rapid growth (see Fig. 5.26). This behaviour can be observed in brittle materials like the Polymethyl Methacrylate; see reference [22] for example. However both existing rate models lead to unrealistic crack stop at high loading rates and the separation rate-dependent model suffers greatest in this regard.

A feature of the new rate model described in Section 5.5 is a bounded critical stress which if correctly set should prevent unrealistic crack arrest (in this study this value was set to 4 times the yield stress). Moreover, following the reaching of this upper bound any further increase in fracture energy is as a consequence of increases in critical separation. The behaviour of the new rate-dependent model is outlined schematically in Fig. 5.29. Although there is insufficient experimental data in the literature to allow a direct comparison there is however evidence for an increase in the fracture energy with rate; see for example the experimentally-obtained curve for G_{ic} from reference [65] and reproduced in Fig. 5.30. It is evident that fracture energy does not increase without bound which is an unrealistic feature of existing models. The upper limit for fracture energy can be determined experimentally but in the absence of this data a limit of 2.5 times the rate-independent fracture energy is applied. The results obtained from the simulation of the fracture process for the CT specimen depicted in Fig. 5.19 with the new model in comparison with existing models are shown in Fig. 5.31 and 5.32. It is evident from these figures that the new model provides results close to the results obtained with the stress rate-dependent model but without a high critical-stress value. The critical stress at the first element in the stress rate-dependent model reaches 2600 MPa at a 10 m/s loading speed as shown in Fig. 5.33 and 3000 MPa at 100 m/s as shown in Fig. 5.34. Although these incredibly high values are avoided with use of the separation rate-dependent cohesive model other problems occur as observed in Fig. 5.27 and 5.28. These unrealistic responses observed in both the stress and separation rate-dependent models are eliminated by the new model as shown in Fig. 5.35. The result of the simulation using the TCZM is different from the BCZM and provides further evidence that the type of TSL has an effect (see Fig. 5.31 and 5.32). Note that the same fracture energy and critical stress were used in the simulation.

For all the rate-dependent models, the rate dependency is a function of the rate of separation and a constant parameter (B *or* B_1) (and the parameter B'_1 in addition to B for the new model only) that affects the strength of rate dependency in the material. In practice, these parameters would be determined by curve fitting experimentally-obtained results. Fig. 5.36 shows the effect of the parameter B on the crack growth speed for the stress rate-dependent and the new rate-dependent model for both BCZM and TCZM, since with increasing its value the crack growth speed is decreasing. The value of the parameter B'_1 is observed to have a minor effect on the crack growth speed for reasonable

values of σ_{limit}. Investigations for B'_1 equated to any one of the values {0.126, 0.166, 0.206, 0.246} reveals little effect at loading speeds of 10 m/s and 100 m/s. This is not too unexpected since increasing the value of σ_{limit} for an invariant fracture energy has the effect of diminishing the influence of δ_c^{rate}. A parametric study has been carried out to check the sensitivity of the model to small changes in material properties, σ_{limit} and the upper bound on fracture energy, i.e. $W_{limit}^{\Gamma_{\text{rate}}}$. A range of values between 190 to 200GPa for elastic modulus and 0.29 to 0.33 for the Poisson's ratio has negligible impact on the simulation results. Although a value for $W_{limit}^{\Gamma_{\text{rate}}}$ can be obtained experimentally and used to set σ_{limit}, it is of interest to explore the decoupling of this relationship. The response obtained for the situation where σ_{limit} is relatively high compared to the value obtained from $W_{limit}^{\Gamma_{\text{rate}}}$ is shown in Fig. 5.37. In this case the model reduces to the behaviour observed in a rate-independent cohesive model with σ_c set by $W_{limit}^{\Gamma_{\text{rate}}}$ and rate-independent δ_c applied to all the cohesive elements. Shown in Fig. 5.38 however is the behaviour, where σ_{limit} is much less than the value obtained from $W_{limit}^{\Gamma_{\text{rate}}}$, which is similar to that observed with the displacement rate-dependent cohesive model. It is evident that coupling σ_{limit} to $W_{limit}^{\Gamma_{\text{rate}}}$ provides for a stable cohesive-zone model.

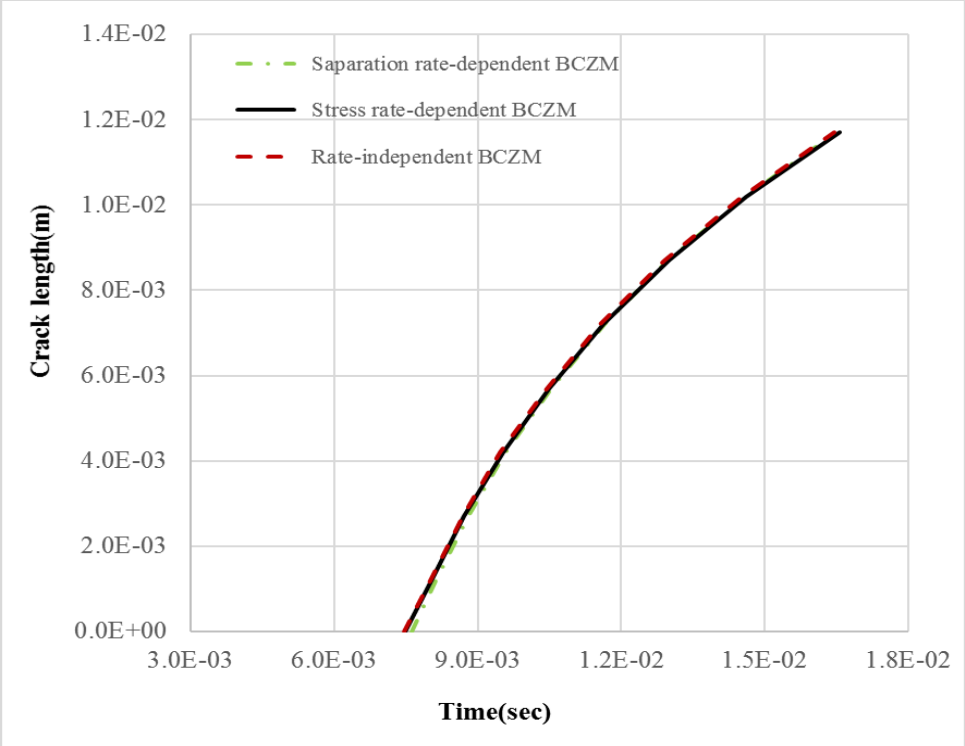

Fig. 5.23. Crack length-time curve for the 0.1 m/s loading speed under displacement control at ($B = B_1 = 0.7$).

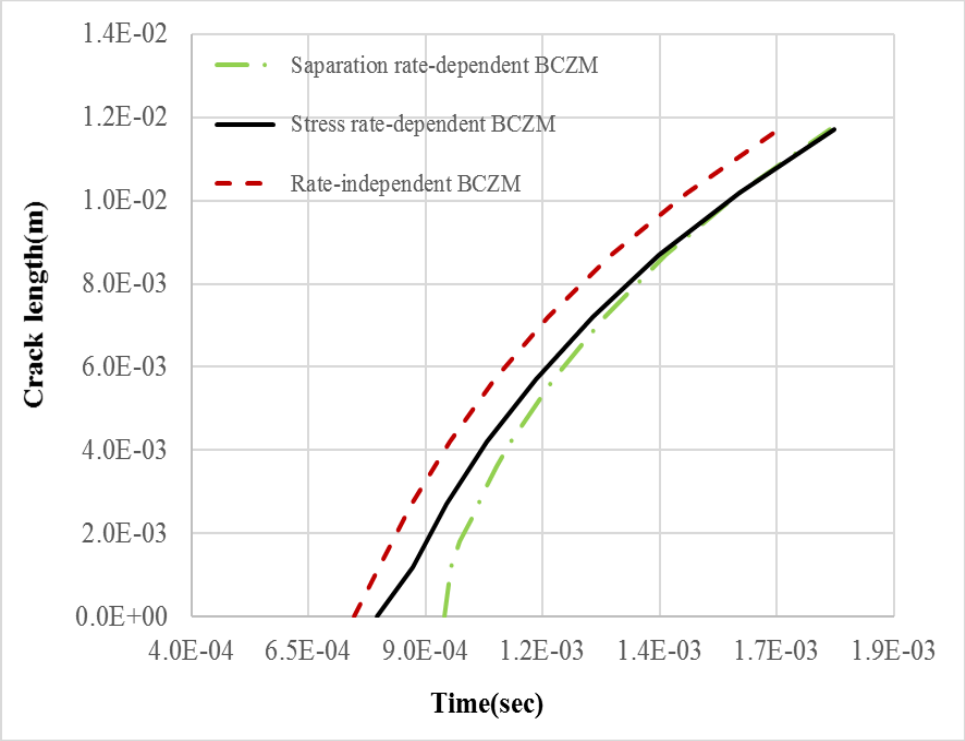

Fig. 5.24. Crack length-time curve for the 1 m/s loading speed under displacement control at ($B = B_1 = 0.7$).

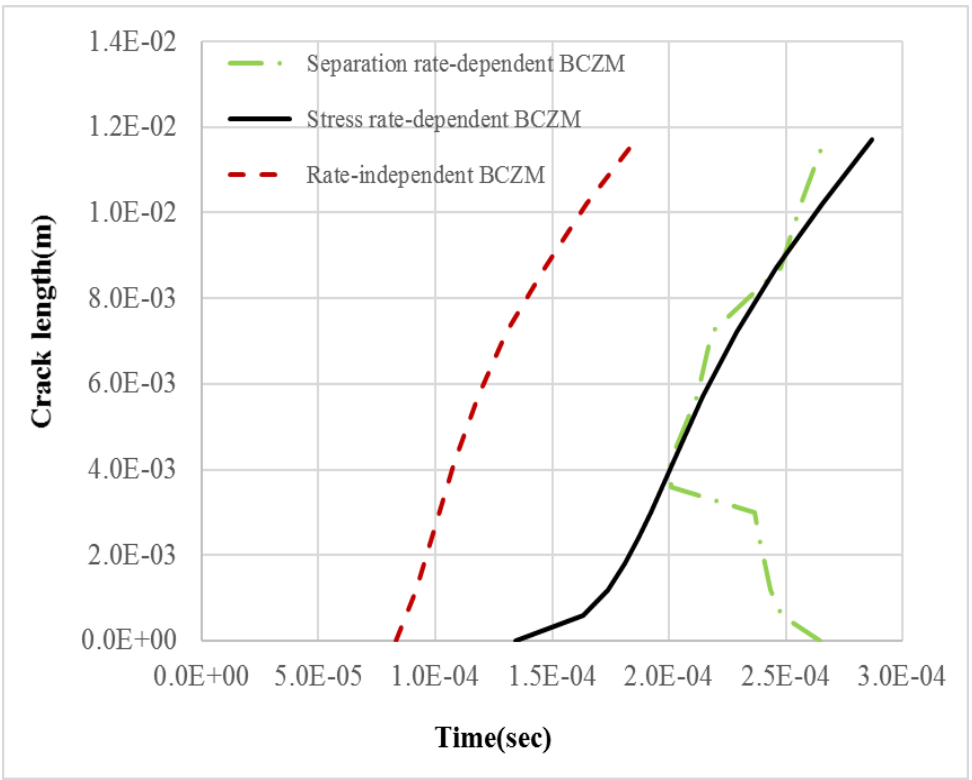

Fig. 5.25. Crack length-time curve for the 10 m/s loading speed under displacement control at ($B = B_1 = 0.7$).

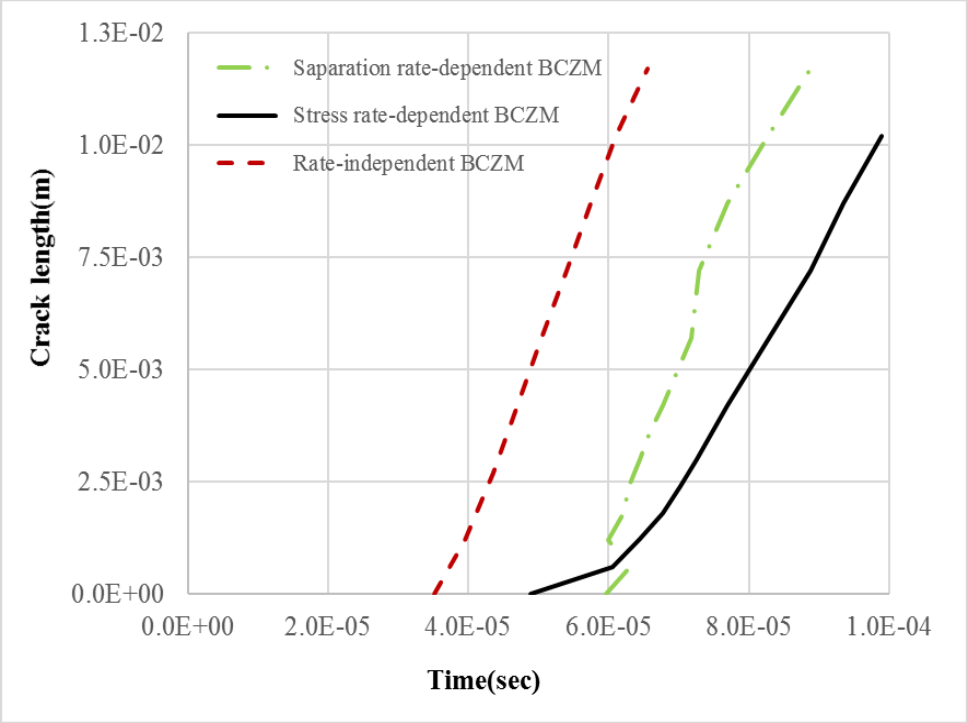

Fig. 5.26. Crack length-time curve for the 100 m/s loading speed under displacement control at $(B = B_1 = 0.7)$.

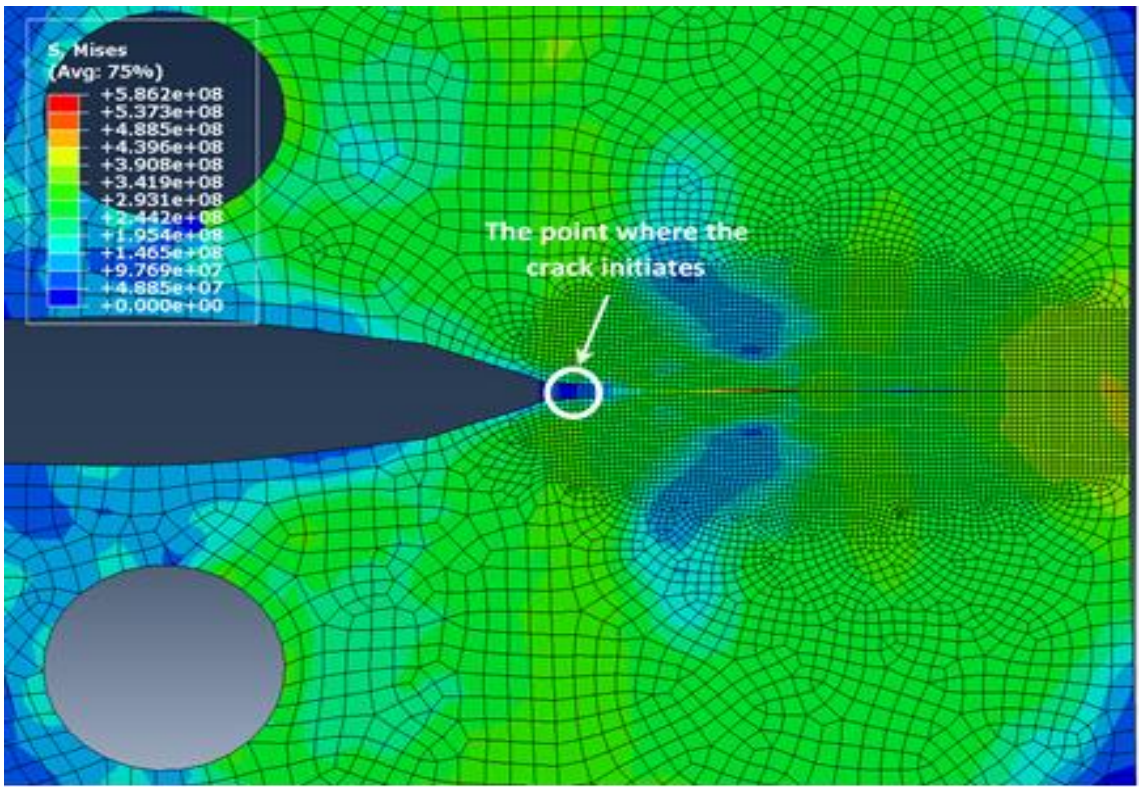

Fig. 5.27. The crack initiation point of the separation rate-dependent model at 100 m/s loading speed.

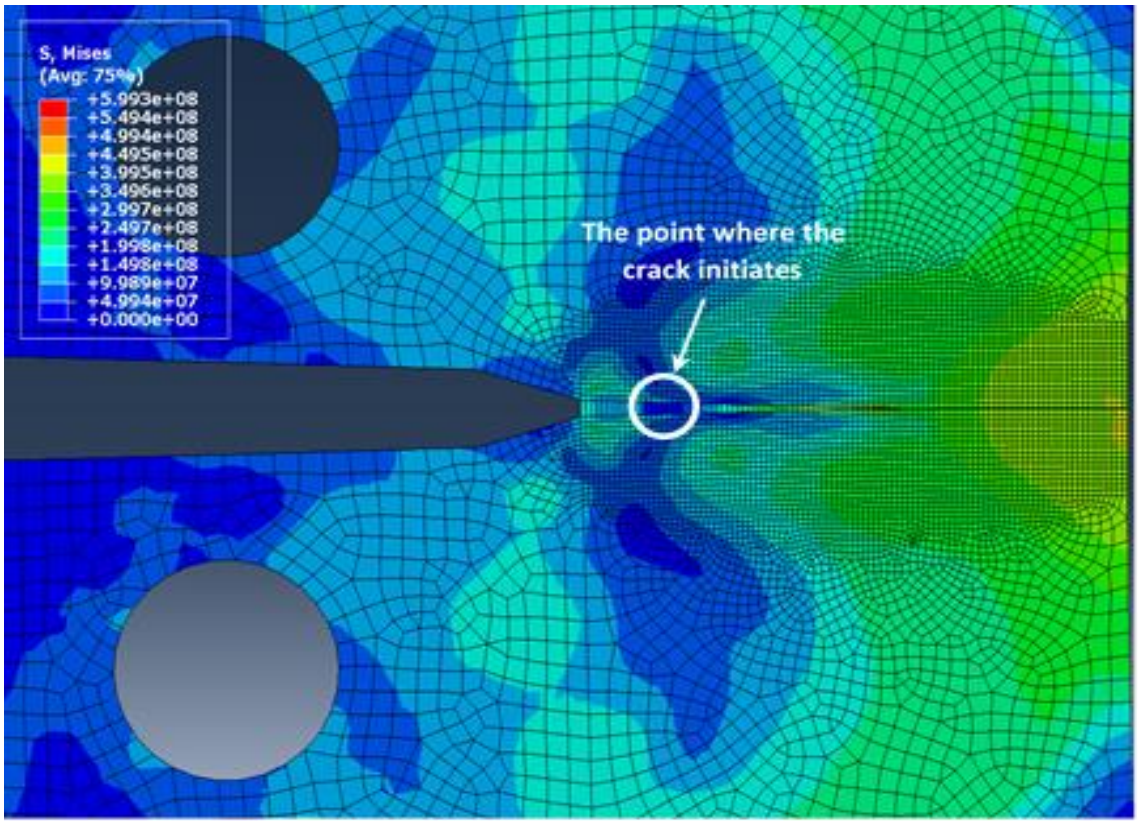

Fig. 5.28. The crack initiation point of the separation rate-dependent model at 10 m/s loading speed.

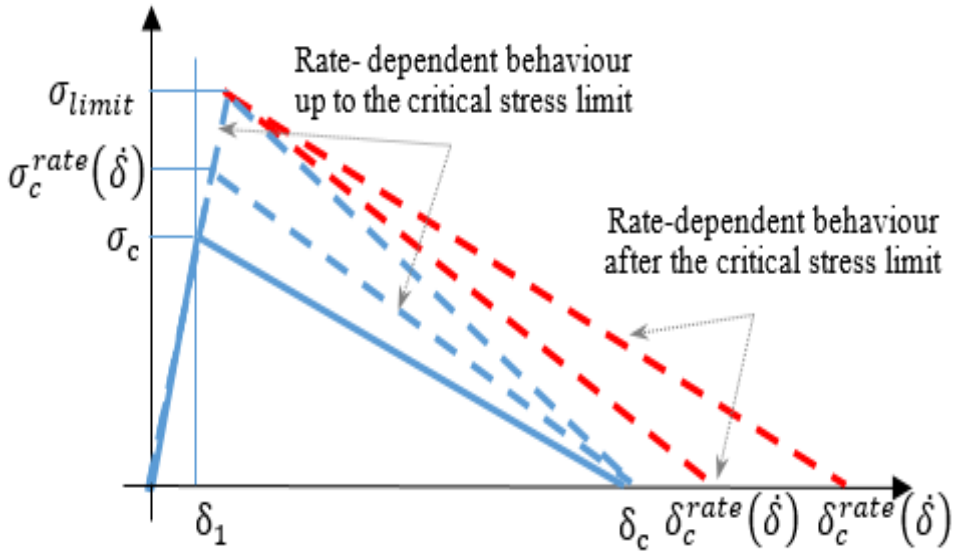

Fig. 5.29. Stress-displacement curve of the new rate-dependent BCZM.

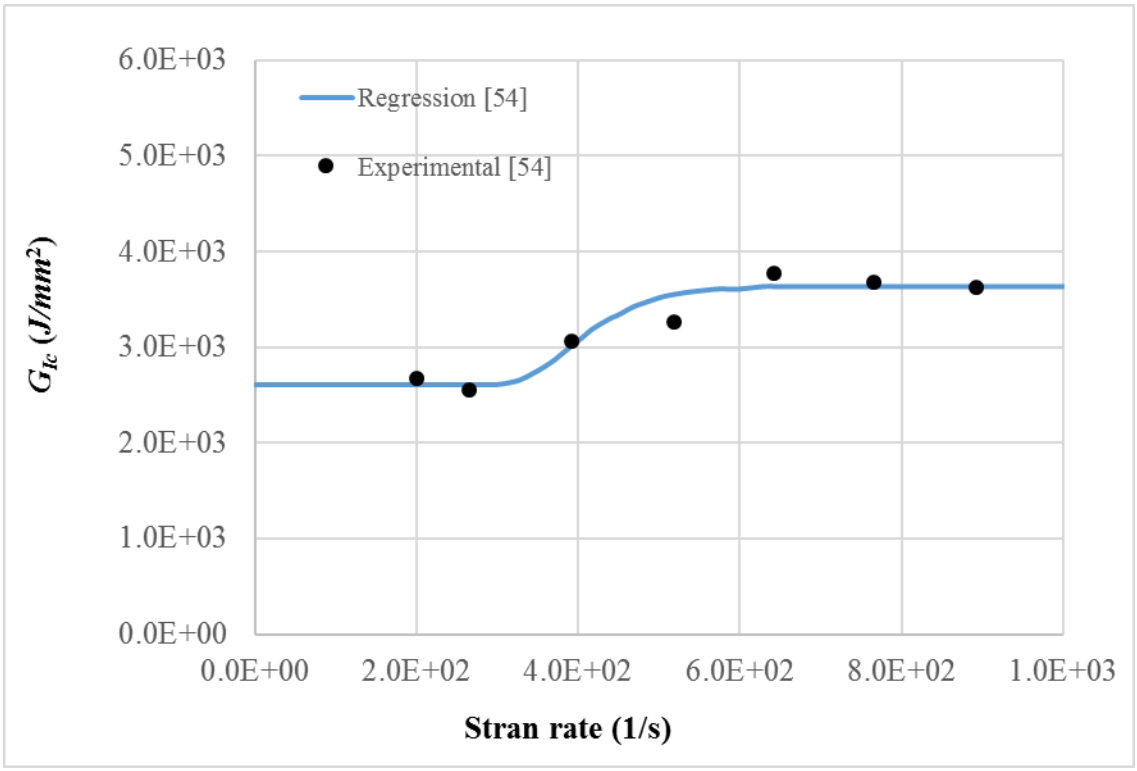

Fig. 5.30. Experimental energy-strain rate curve[65].

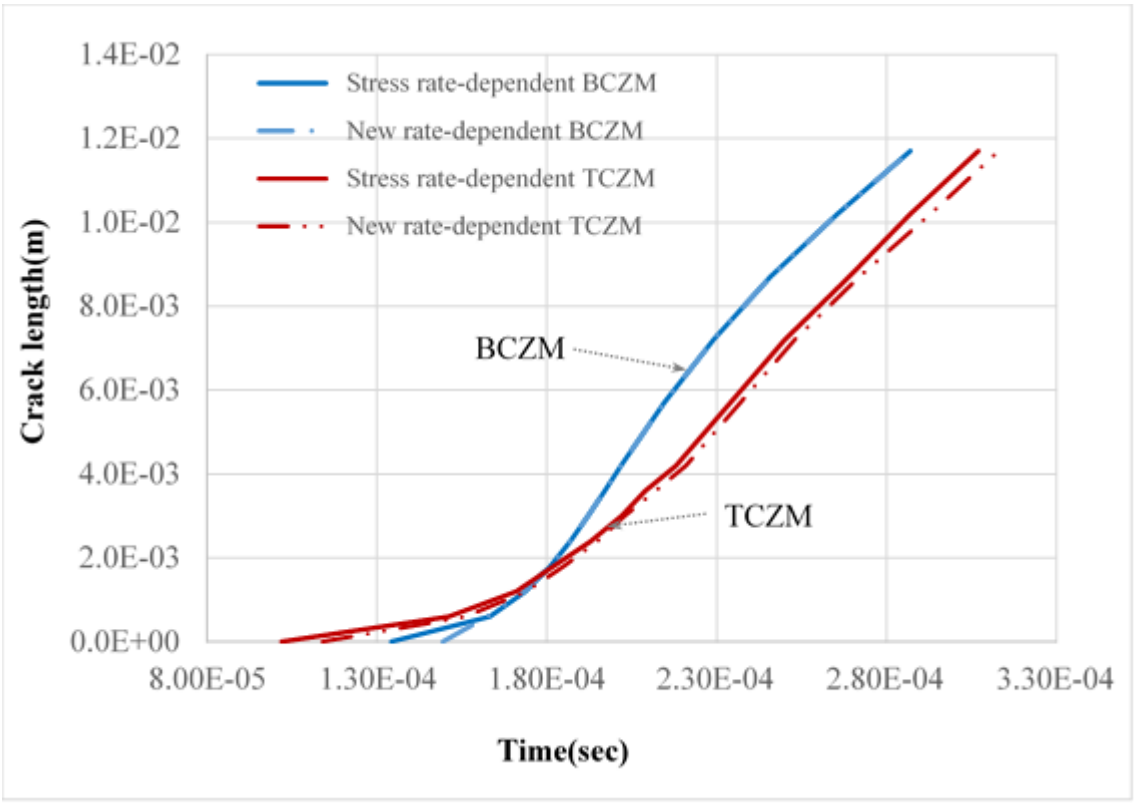

Fig. 5.31. Crack length as a function of the time (B = 0.7 and B'_1 = 0.126) at 10m/s loading speed.

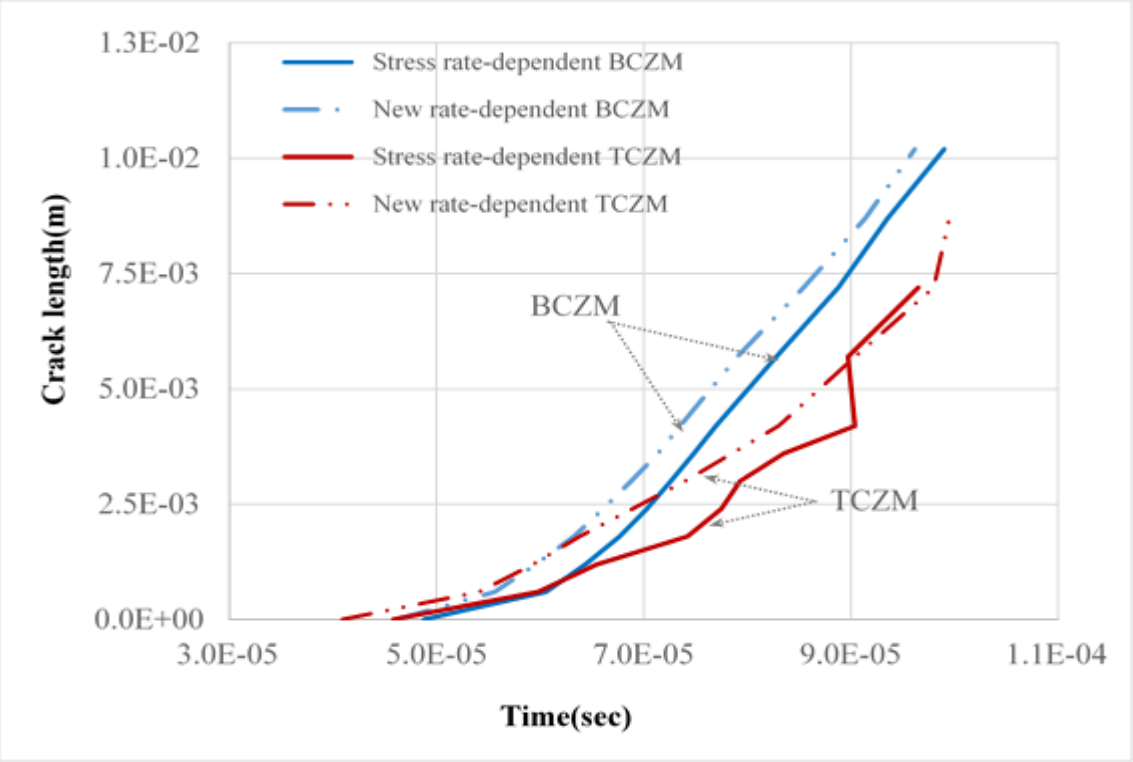

Fig. 5.32. Crack length as a function of the time at (B = 0.7 and B'_1 = 0.126) at 100m/s loading speed.

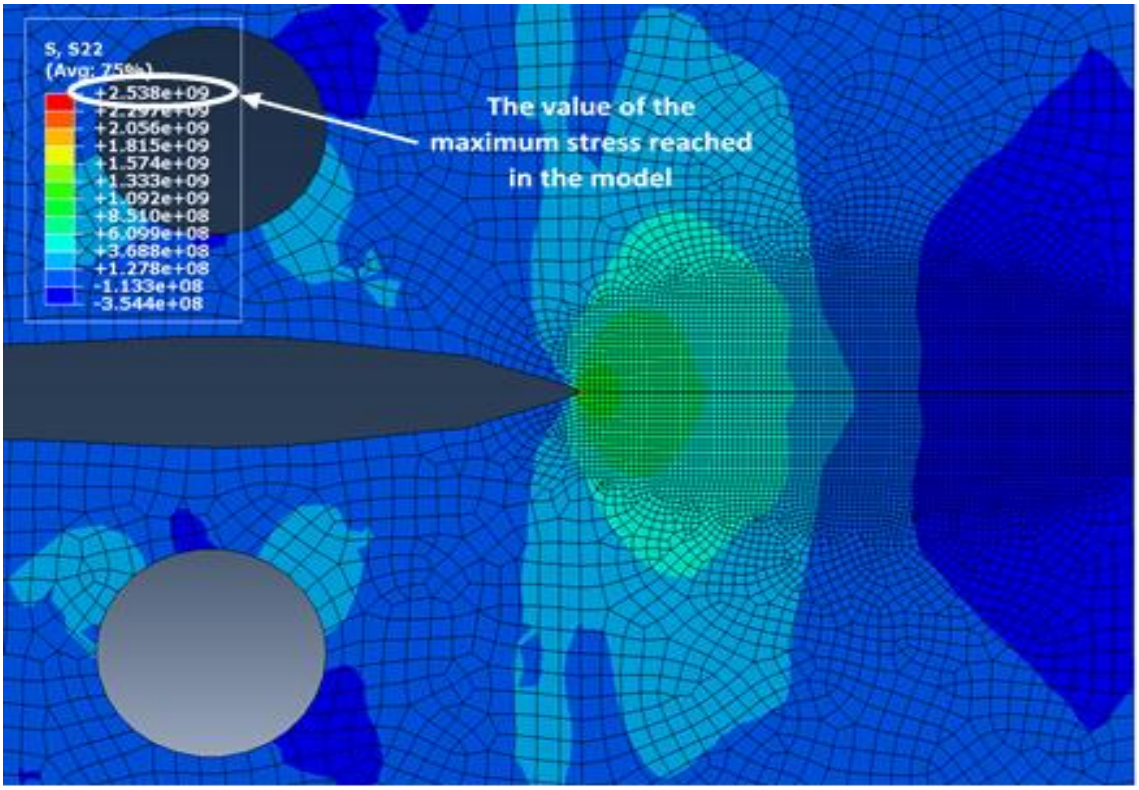

Fig. 5.33. The maximum stress reached by using the stress rate-dependent model at 10 m/s loading speed.

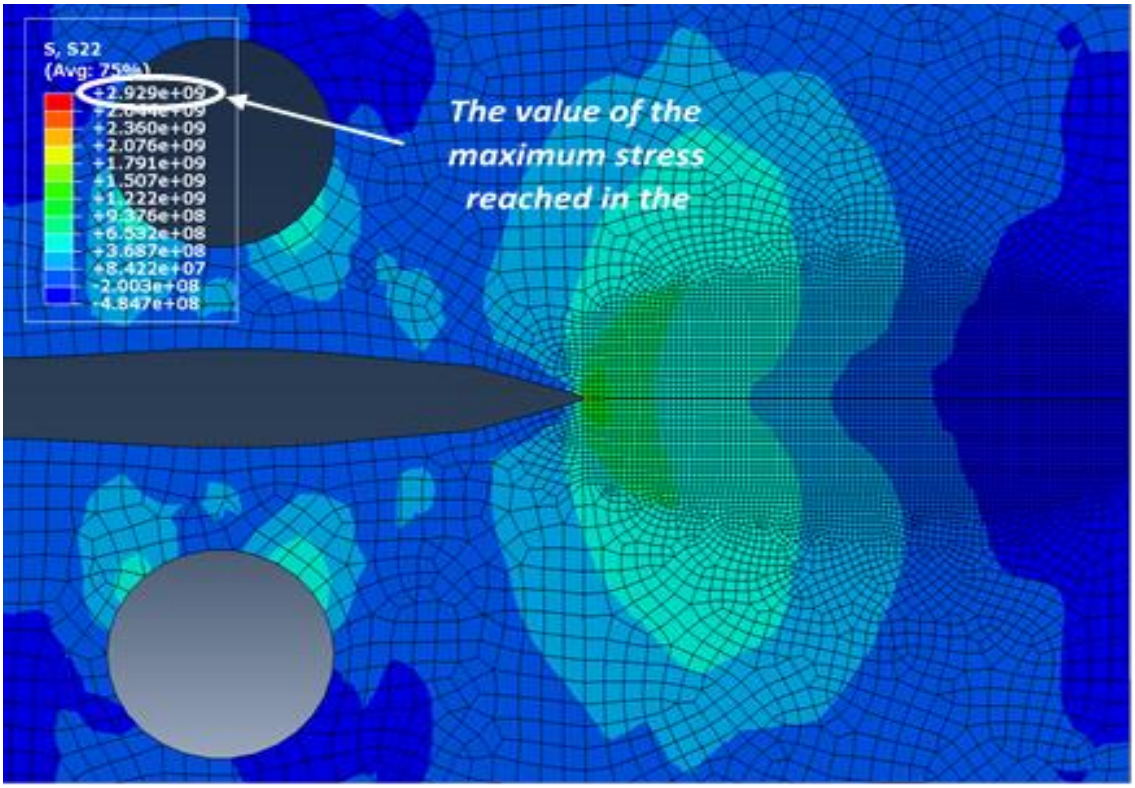

Fig. 5.34. The maximum stress reached by using the stress rate-dependent model at 100 m/s loading speed.

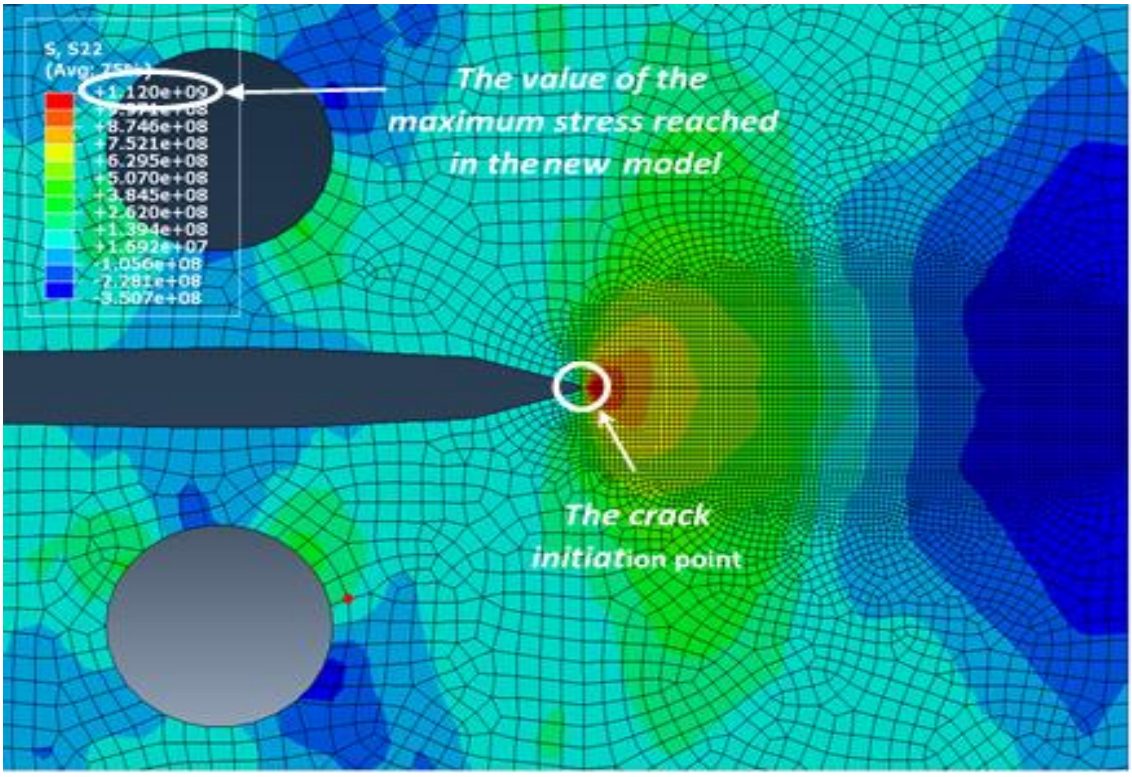

Fig. 5.35. The maximum stress and the point of crack initiation by using the new rate-dependent model under at 100 m/s loading speed.

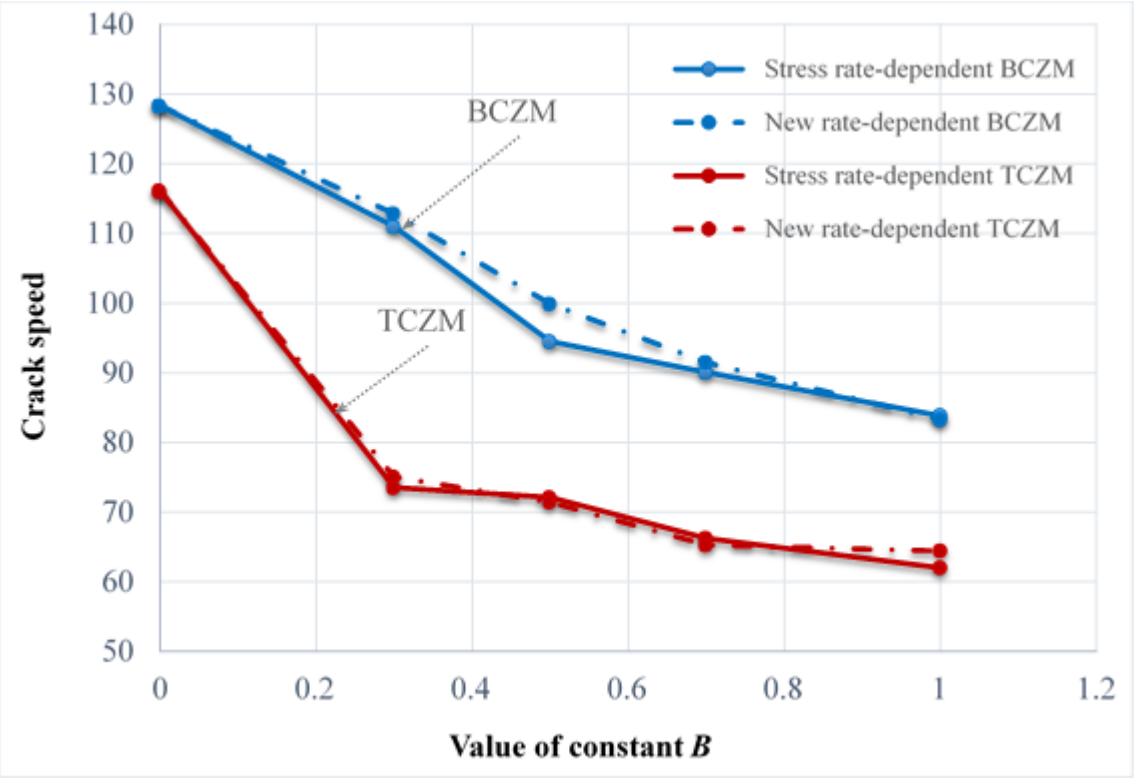

Fig. 5.36. Crack speed as a function of the parameter B at 10m/s loading speed.

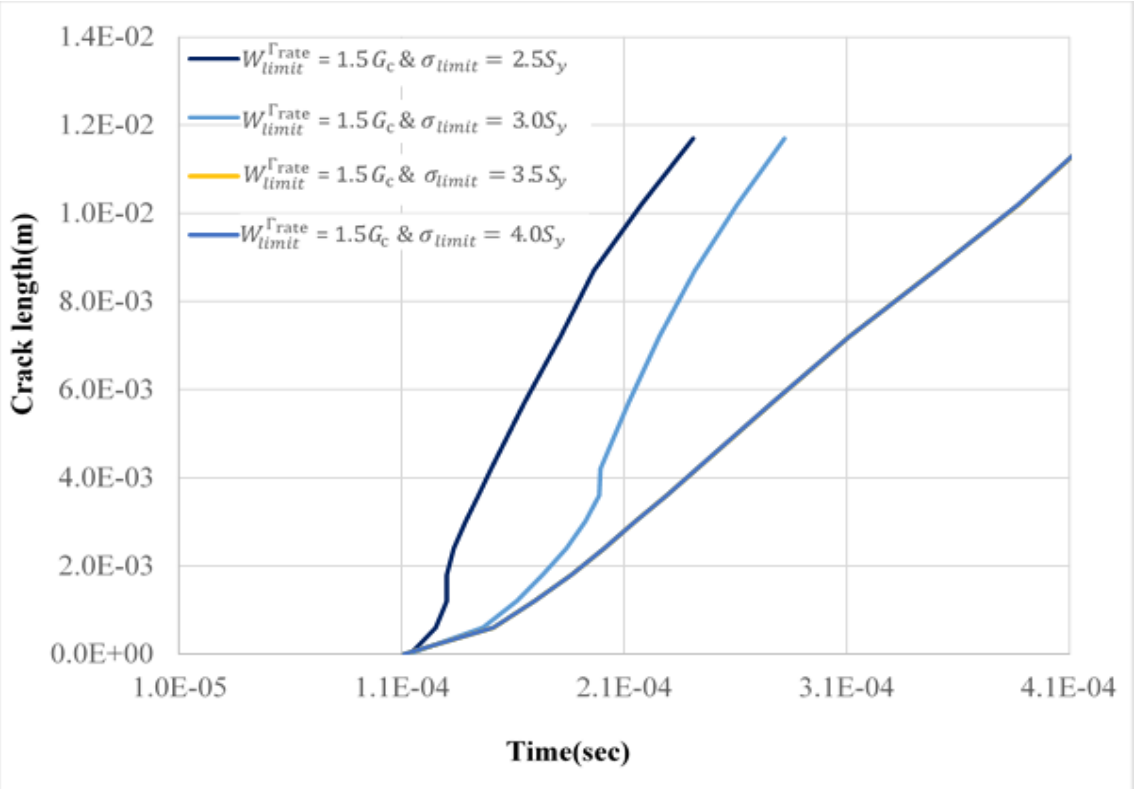

Fig. 5.37. The effect of applying a high value for σ_{limit} compared with the value evaluated from $W_{limit}^{\Gamma rate}$.

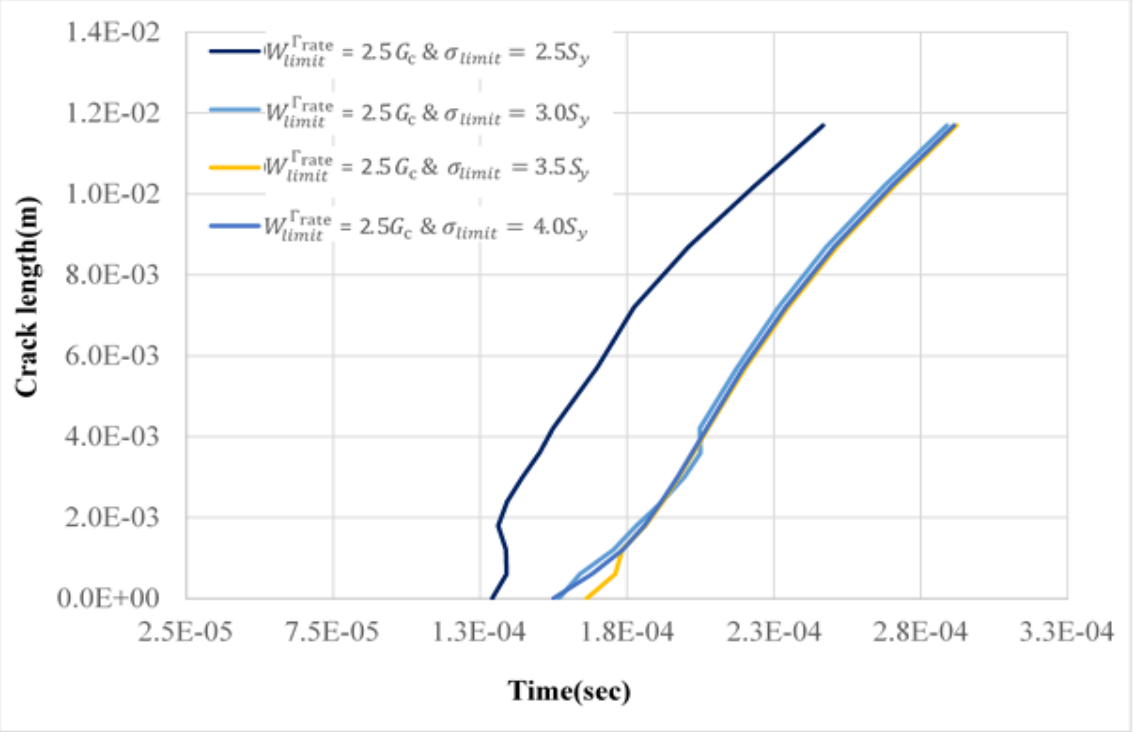

Fig. 5.38. The effect of applying a value for σ_{limit} close to the value evaluated from $W_{limit}^{\Gamma rate}$.

5.8 Summary

- The type of TSL can have a measurable effect on the results of any fracture simulation.
- The TCZM is able to capture the effects of plasticity local to the CZ and can be used with an elastic or elasto-plastic bulk material.
- Existing methods employed to account for rate-sensitivity in fracture processes have been shown to suffer from certain deficiencies including unrepresentative values of critical stress and separation.
- To overcome these limitations a new rate-dependent CZM has been trialled, which connects the rate-dependent fracture energy to critical stress and separation in a manner that ensures critical cohesive stress remains bounded and critical separation attains lower values than with competing methods.
- The new rate-dependent CZM model has been shown to provide acceptable results and provides for enhanced stability when contrasted against competing methodologies.
- The rate-dependent behaviour of the new model is dependent on two parameters $\{B, B_1\}$. It was found that an increase in B decreases crack-growth speed with B_1 having

only a minor influence on crack growth behaviour for typical values of bounds on critical cohesive stress.

Chapter 6: A computationally efficient CZM for fatigue

6.1 Introduction

Engineering structures such as bridges, power plants, aeroplanes, trains, cars and others have played a major role in human life since the beginning of the industrial revolution. However, these structures can suffer from mechanical failures caused by crack propagation leading potentially to catastrophic events, loss of human life and significant financial cost. Fatigue phenomena have been the subject of research for more than 150 years. However, complete solutions for this issue have not yet been discovered [1]. Great effort has been made to understand and evaluate the crack growth behaviour under cyclic loading. However, fatigue remains an area of active research with the development of new materials and physical models. All current models used in the description of fatigue behaviour suffer from limitations, and none are able to capture the extensive experimental evidence available in the literature.

It is apparent from the academic literature that the cohesive-zone model (CZM) is presently considered to be an attractive approach when combined with the finite element method to simulate fracture and fatigue problems. Nevertheless, an optimum CZM able to simulate any form of crack growth problem remains elusive. For the case of fatigue crack-growth simulation, an irreversible and history-dependent cohesive law is required. There are two formats for identifying the irreversibility and the cyclic history dependence in the literature, i.e. the envelope load-damage model and the loading-unloading hysteresis damage model.

In the envelope load damage method only the maximum load of the loading cycle is applied and a damage rate (dD/dN) relationship is required to be formulated. The current damage state is evaluated from the previous damage state and the integration of the damage rate equation, which can be a source of error in this method. Different formulations for the cyclic-damage rate, found in the literature, are reviewed in reference [76]. A particular concern with the appliction of a damage rate equation can be the number of material parameters involved; each requiring experimentation for their determination and for each loading mode (see references [68] and [69] for example). To reduce the cost required for calibrating parameters, the damage evolution can be linked to a Paris-like model as in references [70–75]. Unfortunately, with this approach, predictive accuracy is affected since growth is confined by the particular growth law

assumed to apply. Accuracy is also influenced by the integration scheme employed to integrate the damage rate equation. In addition, damage evolution is directly related to the cohesive-zone length (or at least to the fatigue part of the cohesive-zone length). in references [70–75] for instance, the cohesive-zone length is evaluated using

$$a_{cz} = \frac{9\pi E_3 \mathcal{G}_c}{32(\tau^o)^2} \tag{6.1}$$

or a modified version of this equation, where $\mathcal{G}_c$ is the critical energy release rate, E_3 is Young's modulus of the bulk material in the direction perpendicular to the crack plane and τ^o is the cohesive strength. The linking to cohesive-zone length in this way is essentially non-physical and consequentially cannot be measured or quantified experimentally.

Alternatively, in loading-unloading hysteresis damage models the entire cyclic loading is considered and represented. This feature permits the modelling of advanced behaviour (such as friction and plasticity) at the crack surface and surroundings [76]. Reduction of the interfacial stiffness is the base of loading-unloading hysteresis models, which is captured by means of an evolving cyclic-damage variable or a growing internal variable. The traction rate $\dot{T}$ is assumed to be a function of incremental stiffness that evolves according to the evolving damage or internal variable (see references [31] and [78] for example). A farther development to the model can be found in reference [79] by adding two additional parameters σ_f and δ_Σ to account for the fatigue stress limit. This followed by the work in references [28, 29] which have adopted a similar approaches. Although, the loading-unloading hysteresis damage model replicates to an extent fatigue behaviour over each and every time increment, it is rather costly in terms of computational time and from a practical viewpoint it is unfeasible for high-cycle fatigue simulation, where analysis can typically involve extremely large numbers of loading cycles. Although, to overcome the cost associated with hysteresis damage models, De-Andrés [77] introduced an extrapolation scheme to estimate the damage state after a specific number of cycles, his model required a step-by-step computation for a specific number of cycles to formulate a damage rate equation. A source of error in this model is assuming a constant damage behaviour for the entire propagation period.

In general, the modelling of fatigue crack growth using the CZM looks very promising but is still in its infancy with no mature CZMs yet available for use in industrial

applications [76]. However, in an attempt to advance the approach, this Chapter introduces a loading-unloading hysteresis damage model containing a fast-track feature. The new CZM is introduced in Section 6.2 along with the fast-track feature and a mechanism for capturing irreversibility. The implementation of the new CZM model in the commercial software package ABAQUS (via a bespoke UMAT subroutine) is discussed in Section 6.3. In addition, the analysis model properties (geometry, material properties, and boundary conditions) along with the mesh sensitivity analysis are considered. Section 6.4 focuses on the validation of the new model by presenting, discussing and comparing results with experimental fatigue data. Finally, summary are presented in Section 6.5.

6.2 Cohesive-zone model for fatigue

The fracture process can be simplified as shown in Fig. 6.1, where the behaviour of the material element at the crack tip can be assumed to follow a predefined traction separation law (TSL). For a pre-defined TSL, two of the cohesive parameters ($\Gamma_o, \sigma_c,$ and δ_c) are usually sufficient for simulating the fracture process, where Γ_o is the energy dissipated in the formation of new surfaces, σ_c is the critical cohesive traction and δ_c is the critical cohesive separation, at which the cohesive element fails. The trapezoidal cohesive-zone model (TCZM) on the other hand involves two additional shape parameters (δ_1 and δ_2), which are required to be specified to simulate the complete fracture process. The addition of these two parameters is to account for local plasticity at the crack tip, so avoiding the need for a global elasto-plastic analysis in a situation where only localised plasticity is involved. This feature is advantageous computationally as it permits an elastic-bulk material to be assumed. In the case of cyclic loading, the application of the standard TCZM described in Chapter 3 Section 3.6 results in an infinite life. Therefore, it is necessary to use an irreversible and history dependent TCZM to capture a finite life. This can be done by identifying a cyclic damage mechanism, which is illustrated in the next section.

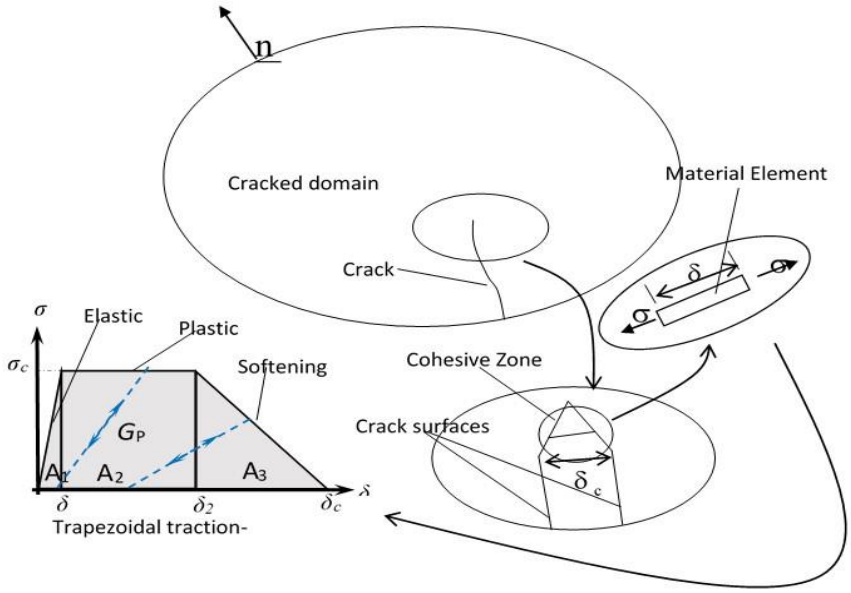

Fig. 6.1. Mode I cohesive-zone model

6.2.1 Fatigue cohesive model

The damage mechanism used for the new TCZM consists of two parts. First is the cyclic damage D^c, which itself is associated with two distinct effects: (i) an increase in local cyclic plasticity δ^p when $\delta \leq \delta_2$ and; (ii) for $\delta > \delta_2$, a further increase in δ^p as consequence of void growth and coalescence. Second is monotonic damage D^s that results from material deterioration not attributed to cyclic loading in the CZM. These two features are shown to be sufficient for the TCZM to capture fatigue crack growth.

A schematic outline of the behaviour of the proposed model is presented in Fig. 6.2 with traction represented mathematically by

$$\sigma_{(\delta)} = \begin{cases} K_{coh}\delta & if \quad \delta < 0 \\ \left(\frac{\sigma_{max}}{\delta_{max} - \delta^p_{(N+\Delta N)}}\right)(\delta - \delta^p_{(N+\Delta N)})H\left(\delta - \delta^p_{(N+\Delta N)}\right) & if \quad 0 \leq \delta \leq \delta_{max} \\ \left(1 - D_{(\delta)}\right)K_{coh}\delta & if \quad \delta_{max} < \delta < \delta_c \\ 0 & if \quad \delta \geq \delta_c \end{cases} \tag{6.2}$$

where K_{coh} represents the cohesive stiffness, δ_{max} and σ_{max} are the separation and the stress at the point of unloading, respectively (see Fig. 6.2); In the figure, $\sigma_{\max(1)}$ and $\delta_{\max(1)}$ are the value of the maximum stress and separation after the first loading cycle and $\sigma_{\max(2)}$ and $\delta_{\max(2)}$ after the second loading cycle. To ensure that the first part of the second relationship of Eq. (6.2) $\left(\text{i.e. } \sigma_{max}/\left(\delta_{max} - \delta^p_{(N+\Delta N)}\right)\right)$ returns the cohesive

stiffness K_{coh} when there is no damage at $\delta \leq \delta_1$ *and* $\delta^p_{(N+\Delta N)} = 0$ the value of σ_{max} and δ_{max} are set to be equal to σ_c and δ_1, respectively. N is the number of cycles, ΔN is the number of cycles between updates in the damage state which equals 1 for the cycle by cycle analysis. The Heaviside function $H\left(\delta - \delta^p_{(N+\Delta N)}\right)$ is defined to zero when δ is smaller than $\delta^p_{(N+\Delta N)}$ and one in other cases. Finally, $D_{(\delta)}$ is the monotonic damage variable evaluated from

$$D_{(\delta)} = \begin{cases} 1 - \frac{\delta_1}{\delta} & if \ \ \delta_1 \leq \delta < \delta_2 \\ 1 - \frac{\delta_1(\delta_c - \delta)}{\delta(\delta_c - \delta_2)} & if \ \ \delta_2 \leq \delta \leq \delta_c \end{cases} \tag{6.3}$$

As advised by Scheider et al. [56] the value of δ_1 should be very small and the value of δ_2 should be close to δ_c. Therefore, in this study these values are set to

$$\delta_1 = \frac{\sigma_c}{K_{coh}} \tag{6.4}$$

$$\delta_2 = 0.75 \times \delta_c \tag{6.5}$$

The applied separation δ is determined by adding the applied cyclic displacement δ^{cyc} to the remnant separation $\delta^p_{(N+1)}$, i.e.

$$\delta = \delta^p_{(N+1)} + \delta^{cyc} \tag{6.6}$$

where δ^{cyc} is the cyclic displacement as a result of the applied load at any time increment, with plastic damage δ^p updated by means of integration of a rate relationship, i.e.

$$\delta^p_{(N+1)} = \delta^p_{(N)} + \int_N^{N+1} \left(d\delta^p_{(N)}/dN\right) dN' \tag{6.7}$$

where $\delta^p_{(N)}$ is the stored plastic damage from the previous loading cycle, and $d\delta^p_{(N)}/dN$ is the plastic damage rate (represented here in the form of a derivative for convenience), i.e. the increase in the plastic separation δ^p per cycle.

The integral in Eq. (6.7) can be approximated using the mean value theorem for integration. If $d\delta^p_{(N)}/dN$ is assumed to be defined and smooth on the interval (N, N+1), then

$$\int_N^{N+1} \left(d\delta^p_{(N)}/dN\right) dN' = (N + 1 - N) \times \left(d\delta^p_{(N)}/dN\right) = \left(d\delta^p_{(N)}/dN\right)_{(\alpha)} \tag{6.8}$$

where α belongs to the interval [N, N+1], $\left(d\delta^{p}_{(N)}/dN\right)_{(\alpha)}$ is an intermediate value of the rate $d\delta^{p}_{(N)}/dN$ and a convenient approximation for this is

$$\left(d\delta^{p}_{(N)}/dN\right)_{(\alpha)} \approx \frac{\delta^{cyc(max)}_{(N)}}{C} \tag{6.9}$$

where C is a positive material parameter greater than unity and $\delta^{cyc(max)}_{(N)}$ is the maximum displacement reached at the end of a loading cycle.

The approximation adopted in Eq. (6.9) is expedient since $\delta^{cyc(max)}_{(N)}$ is dependent on the loading conditions with any material cyclic damage being readily captured by the material parameter C, which can be tuned to accommodate particular material behaviour on comparing analysis results with experimental data. Substitution of Eq. (6.9) into Eq. (6.7) yields an extraordinarily simple increment rule for cyclic damage, i.e.

$$\delta^{p}_{(N+1)} \approx \delta^{p}_{(N)} + \frac{\delta^{cyc(max)}_{(N)}}{C} \tag{6.10}$$

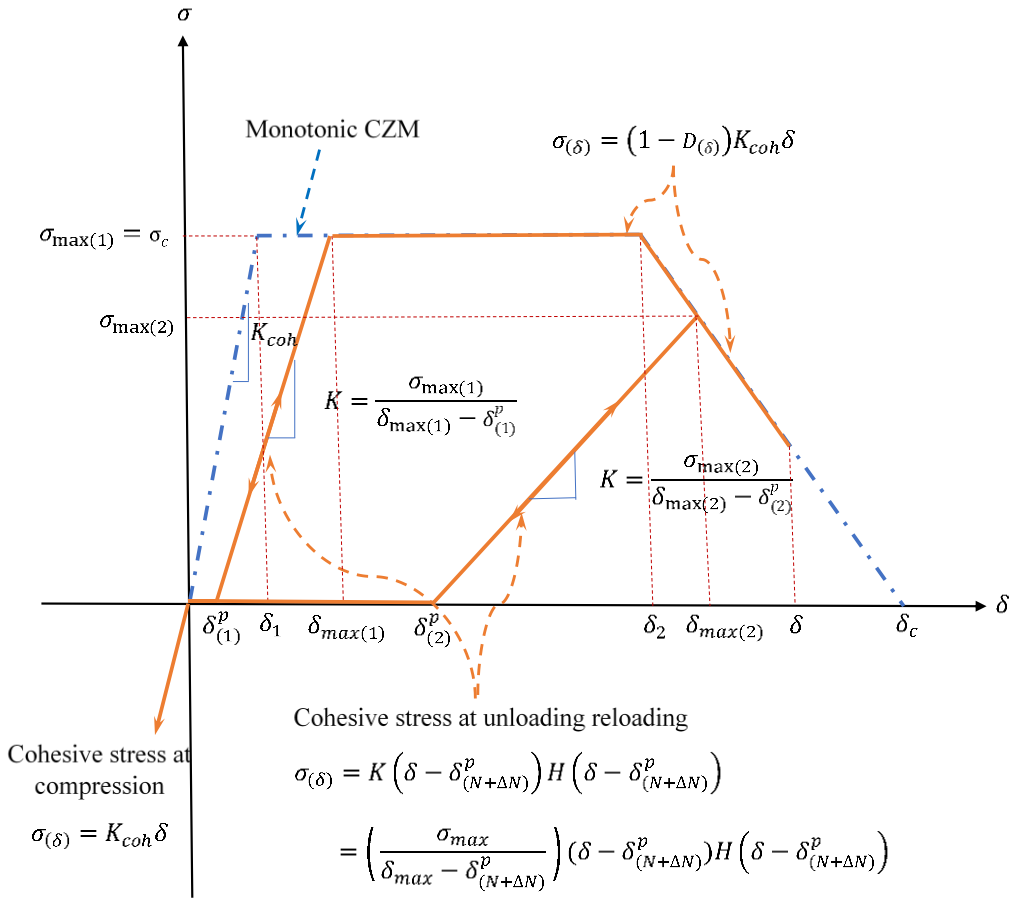

Fig. 6.2. New loading-unloading hysteresis model.

Fig. 6.3(a) shows the behaviour of the cohesive model under cyclic loading, and the accumulated dissipated energy ΔG is readily shown to be

$$\Delta G = \begin{cases} \frac{1}{2}\sigma_c\left(\delta_{max} + \delta^p_{(N+1)} - \delta_1\right) & if \quad \delta_{max} \le \delta_2 \\ \frac{1}{2}\left[\sigma_c(\delta_{max} + \delta_2 - \delta_1) - \sigma_{max}\left(\delta_2 - \delta^p_{(N+1)}\right)\right] & if \quad \delta_{max} > \delta_2 \end{cases} \tag{6.11}$$

represented by the area under the traction-separation curve in Fig. 6.3.

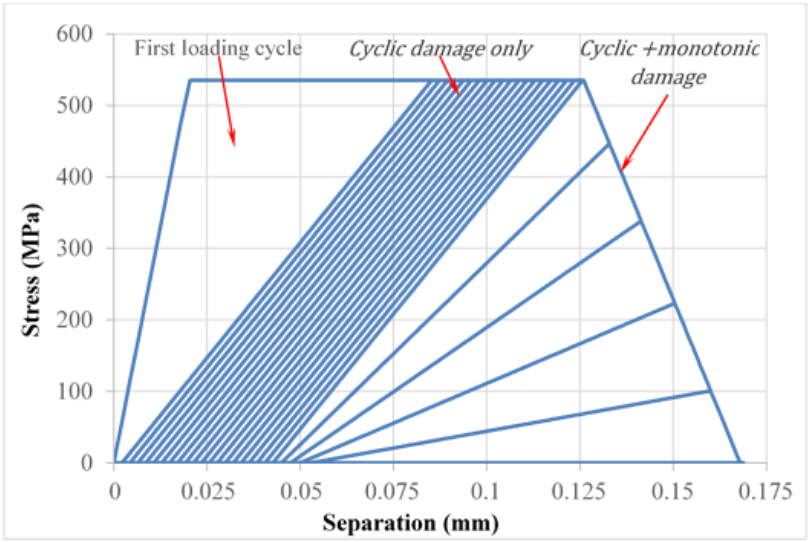

(a) Cycle by cycle

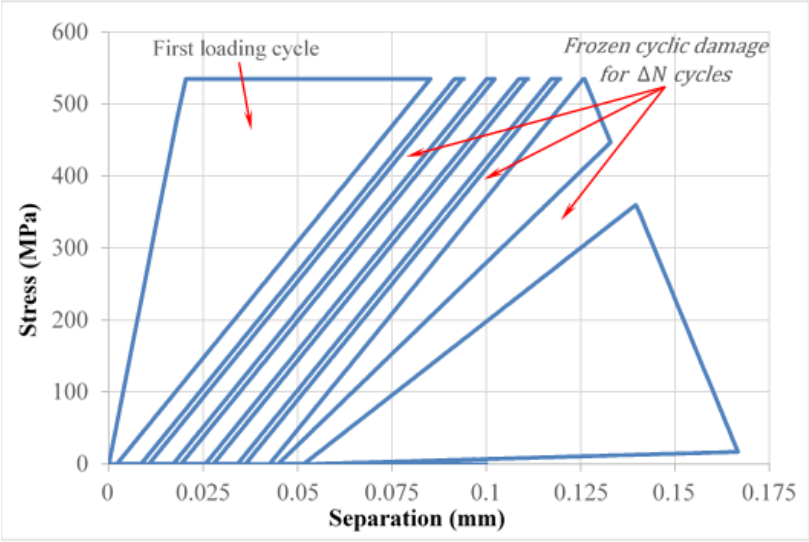

(b) Fast-track procedure with $\Delta N = 4$

Fig. 6.3. Cyclic stress-displacement curve.

6.2.2 Fast-track feature

The model described in Section 6.2.1 can be shown to represent fatigue behaviour but suffers from a particular limitation. In its present form (similar to the loading-unloading hysteresis damage model) it is practically unfeasible and computationally costly requiring excessively long computational time as a consequence of the large numbers of cycles typically involved in any realistic industrial application. In order to overcome this particular limitation, it is necessary to find an approach that limits the extent of the computational requirements. An observation of the behaviour of the existing model however, is that deviation in the cyclic behaviour tends to evolve extremely slowly. Cyclic damage is considered here to be a combination of cyclic plasticity and material deterioration and it is the cyclic plasticity that is observed to suffer low cyclic deviation. This suggests that a reasonable approximation is a linear growth rule for cyclic plasticity with constant plastic increment over a specific load envelope containing ΔN cycles. This simple observation provides the founding idea for the new fast-track procedure.

Consider then the possibility that plastic damage evaluated in a loading cycle will remain constant for a specific load envelope containing ΔN number of cycles, the value of ΔN should not be set at too a high value to allow damage to be updated to maintain accuracy. The cyclic plastic damage after $(N + \Delta N)$ is evaluated in the usual way as

$$\delta^{p}_{(N+\Delta N)} = \delta^{p}_{(N)} + \int_{N}^{N+\Delta N} \left(d\delta^{p}_{(N)}/dN\right) dN' \tag{6.12}$$

Similar to Eq. (6.7), the mean value theorem for integration is used to approximated the integral in Eq. (6.12) and with applying the approximation in Eq. (6.9) the plastic damage after $(N + \Delta N)$ cyclies is aproximated as

$$\delta^{p}_{(N+\Delta N)} \approx \delta^{p}_{(N)} + \frac{\delta^{cyc_{(max)}}_{(N)}}{C} \Delta N \tag{6.13}$$

where Eq. (6.10) is returned on setting $\Delta N = 1$.

The increment ΔN for computational expediency can be an integer value significantly greater than one but accuracy is a limiting consideration. It is important therefore to have some understanding about the effect ΔN has on the accuracy of the fast-track procedure. A simple procedure is adopted to provide a reasonable estimate for the value of ΔN, which involves first the analysis of one cycle. From this cycle information is recovered at the integration point (IP) at the crack tip, with ΔN being set by the relationship,

$$\Delta N = int\left(\frac{\delta_c - \delta_{(1)}^{cyc_{(max)}}}{N_u \times \delta_{(1)}^{p}}\right) \tag{6.14}$$

where int is a function that returns the nearest integer to the argument, N_u is a parameter that represents the number of required updates of the cyclic damage, $\delta_{(1)}^{p}$ is the cyclic plastic separation after the first loading cycle, and $\delta_{(1)}^{cyc_{(max)}}$ and δ_c are the maximum cyclic displacement reached at the first loading cycle and the critical cohesive separation, respectively. The numerator $\delta_c - \delta_{(1)}^{cyc_{(max)}}$ in Eq. (6.14) is a relatively crude approximation of the cyclic plastic separation to the point of failure. The ratio of $\delta_c - \delta_{(1)}^{cyc_{(max)}}$ and $\delta_{(1)}^{p}$ gives an indication of the number of cycles that leads to the separation of the IP at the crack tip. The value for ΔN employed as a cyclic load envelope is obtained on dividing $\left(\delta_c - \delta_{(1)}^{cyc_{(max)}}\right)/\delta_{(1)}^{p}$ with the integer N_u (representing the number of cyclic updates deemed necessary for accuracy) and returning the nearest integer. The greater the value of N_u the lower the value of ΔN (with $\Delta N \geq 1$) but consequently the greater the computational cost.

The predicted value of ΔN by Eq. (6.14) is applied as an input to the analysis along with $(\sigma_c,\ \delta_c, and\ C)$ for all cohesive elements. The value of ΔN (with N_u fixed) will automatically be higher if the problem under consideration involves high-cycle fatigue since both the maximum cyclic displacement and the cyclic plastic increment will be smaller. A detailed investigation on the effect of ΔN on the simulation results is provided in Section 6.3.3.

The separation δ_{max} and the stress σ_{max} at the end of the $N + \Delta N$ cycles are determined with

$$\delta_{max} = \delta_{(N+\Delta N)}^{p} + \delta_{(N)}^{cyc_{(max)}} \tag{6.15}$$

and

$$\sigma_{max} = \begin{cases} \sigma_c & if\ \delta_1 < \delta_{max} \leq \delta_2 \\ \left(1 - D_{(\delta_{max})}\right) \times \sigma_c & if\ \delta_2 < \delta_{max} \leq \delta_c \end{cases} \tag{6.16}$$

Thus, after $N + \Delta N$ cycles Eq. (6.16) returns the maximum stress, which is equal to the cohesive critical stress if δ_{max} from Eq. (6.15) is less than δ_2. If however, δ_{max} is larger than δ_2, then the maximum stress σ_{max} is evaluated in a similar fashion to Eq. (6.2) by

using the monotonic damage variable $D_{(\delta_{max})}$ of Eq. (6.3) with δ replaced by δ_{max}. The evaluated values from Eq. (6.15) and (6.16) are provided to the next loading cycle along with the new value of δ at $N + \Delta N$, with δ determined using Eq. (6.6) and applied in Eq. (6.2).

To keep things reasonably simple ΔN is assumed to remain invariant for the total process and at the end of a loading cycle the number of cycles satisfies the relationship $N_{i+1} = N_i + \Delta N$. To evaluate the exact number of cycles at which the cohesive element fails, it is necessary to compare the value of δ_{max} (evaluated by using Eq. (6.15)) with δ_c and if larger, then the number of cycles at which the element failed satisfies the relationship

$$N_f = N_{i+1} - int\left(\frac{(\delta_{max}-\delta_c)}{\left(\delta_{(N)}^{cyc(max)}/c\right)}\right) \tag{6.17}$$

The second term on the right-hand side of Eq. (6.17) represents the unwanted number of cycles that do not contribute to the failure of the cohesive element. The numerator $\delta_{max} - \delta_c$ represents the cyclic damage as a result of this unwanted number of cycles, with the denominator $\delta_{(N)}^{cyc(max)}/C$ being cyclic damage increment. The ratio of $\delta_{max} - \delta_c$ and $\delta_{(N)}^{cyc(max)}/C$ therefore provides an estimation the overshoot in the prediction of the number of cycles to failure and hence must be removed as shown in Eq. (6.17).

6.3 Implementation of the new cohesive-zone model in ABAQUS

The commercial finite element solver ABAQUS is used as a vehicle for the numerical analysis in this study. In ABAQUS, the fracture process using the cohesive model can be identified either by a cohesive surface or by cohesive elements that are situated along the crack path. In this study, cohesive elements are used, although existing elements in ABAQUS are somewhat constrained by TSLs that are history independent and not applicable for the simulation of fatigue crack growth. However, the TSL can be defined through their material behaviour and ABAQUS provides a facility to specify new material behaviour (as the new cohesive model introduced in this study) through a user-defined material subroutine. The UMAT subroutine for the new cohesive model can be found in Appendix B-2.

6.3.1 UMAT implementation and testing

To test the UMAT subroutine, a three-element model (two material elements and one cohesive element connecting them) is used as shown in Fig. 6.4. The material properties in the bulk material and the cohesive element are shown in Table 6.1The parameter C is set to have a small value (i.e. 40) to artificially reduce the number of cycles required for failure of the cohesive element. The load is applied as a cyclic displacement with fixed maximum amplitude of 11.6×10^{-5} m and $R = 0$. The analysis is performed initially on a cycle by cycle basis (i.e. $\Delta N = 1$) and then with the new fast-track technique on setting $\Delta N = 4$. The cyclic stress of the new fatigue model (in a cycle by cycle manner first and by using the new technique with $\Delta N = 4$) are shown with respect to the separation and time in Fig. 6.3 and 6.5, respectively. Note that the reason for the large amount of dissipated energy at the first cycle (as apparent in Fig. 6.3) is because the applied load is set relatively high to mimic the load used in the experimental fatigue test. Fig. 6.3 also shows the growth of the plastic separation with the number of cycles until the separation δ reaches δ_2. At which point the cohesive stiffness decreases with increasing number of cycles because of material deterioration leading to failure of the cohesive element. Fig. 6.5 shows the required analysis time for a typical element to fail using the cycle-by-cycle model (dashed curve) and the fast-track model (solid curve). It reveals that the fast-track procedure provides a reduced number of cycles and hence computational effort, which of the order of ΔN^{-1} of that required without its implementation. The figure shows that for an analysis involving 26 loading cycles the fast-track procedure takes some 140 s whilst the cycle-by-cycle analysis takes 560 s.

Table 6.1 Material and cohesive element properties for the three-element model.

Bulk material	σ_y (MPa)	E (GPa)	ϑ				
	340	193	0.29				
Cohesive elements	Γo (N/m)	K_{coh} (GPa/m)	σ_c (MPa)	δ_c (mm)	δ_1 (mm)	δ_2 (mm)	C
	68500	19700	511	0.168	0.02594	0.126	40

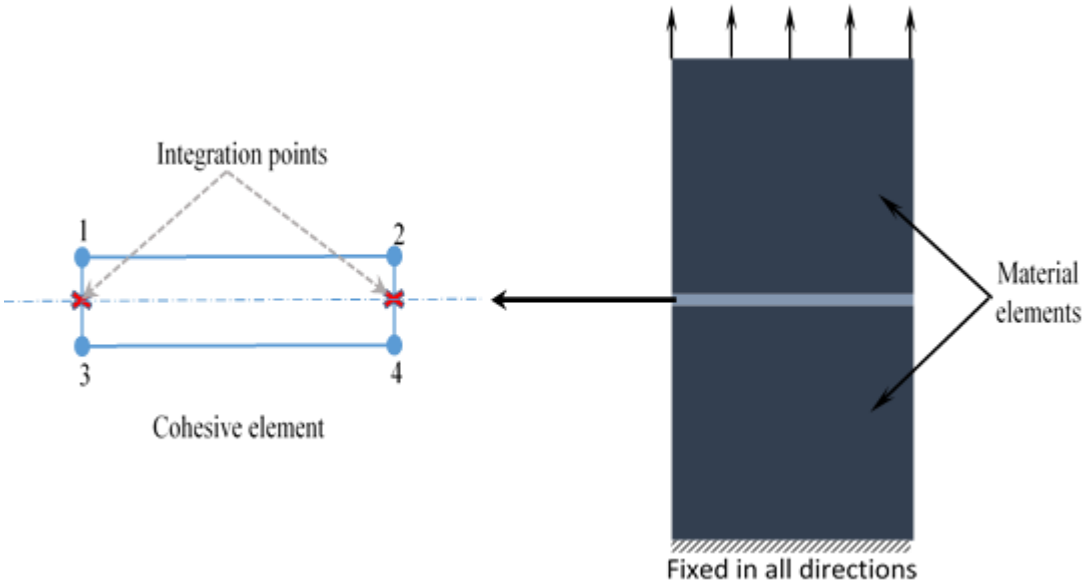

Fig. 6.4. Implementation of the CE in the FE model.

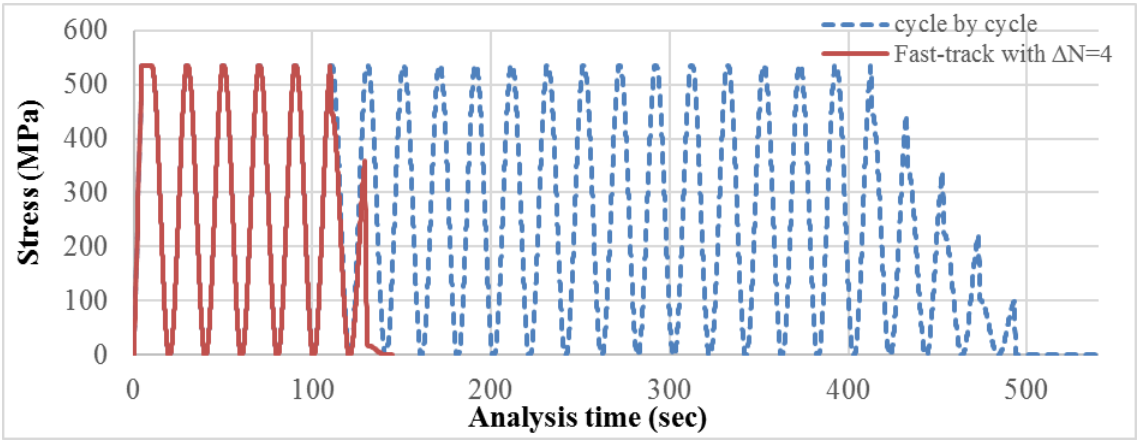

Fig. 6.5. Cyclic stress as function of time.

6.3.2 Analysis model: geometry and boundary conditions

conforms to the shape of the specimens used in the fatigue experimental trials. The numerical model consists of 23618 plane-stress elements of which 22988 (type CPS4), 390 (type CPS3), and 240 cohesive elements (type COH2D4) [109]. The material properties for the bulk material element and the cohesive element are found in Table 6.2. The initial values of the cohesive parameters were set as follows: δ_c equals the crack tip opening displacement (CTOD) as measured experimentally in a CT specimen and equals 0.000168 m; the value of the critical cohesive stress σ_c was set to equal the material yield stress and its value is 340 MPa. The analysis was run first using these initial values and subsequently adjusted by means of curve fitting analysis results and contrasting with

experimental fatigue data; the parameter set in Table 2 was found to give the best fit. The boundary conditions applied to the analysis model are shown in Fig. 6.6. Loading is in the form of a uniform cyclic displacement in the y-direction applied at the top surface and fixed in all direction at the bottom surface.

During the fatigue test the number of cycles is recorded along with the applied displacement at this number of cycles as presented in Chapter 4. However, these displacements do not represent the actual displacements in the fatigue specimen and when used in the finite element analysis these result in a loading level higher than 10 kN. To find the correct boundary condition that should be applied to the finite element analysis to ensure a loading condition similar to that applied during the fatigue test, a correction factor was applied to the measured displacement in Chapter 4. The value of the correction factor is 0.646 which is found by dividing the maximum displacement required to return a reaction force at the loading edge of 10 kN in a one cycle analysis (which is 0.073 mm), over the maximum applied displacement at the first cycle from the experimental data in Chapter 4 which is 0.113 mm. With this correction factor, the load is applied to the numerical analysis in eight steps: first a ramp load that increases from zero to 3.65×10^{-5}m followed by nineteen stage with sinusoidal load at $R = 0$ and Maximum displacement of $(7.3, 7.6, 7.8, 8, 8.2, 8.4, 8.5, 8.6, 8.7, 9, 9.2, 9.6, 10, 10.2, 10.4, 11.2, 12, 15.2, 20.6) \times 10^{-5}$m, respectively as shown in Fig. 6.7. The number of cycles in each stage is 6400, 3200, 2400, 1600, 1600, 1600, 1600, 1600, 1600, 800, 800, 800, 800, 800, 800, 800, 800, 800, (the last step is run until failure), respectively. The number of cycles at each stage is set to ensure that the loading conditions match to those of the fatigue experiment. The reaction force as a function of time is shown in Fig. 6.8.

Table 6.2 Material and cohesive element properties for full model.

Bulk material	σ_y (MPa)	E (GPa)	ϑ				
	340	193	0.29				
Cohesive elements	Γo (N/m)	K_{coh} (GPa/m)	σ_c (MPa)	δ_c (mm)	δ_1 (mm)	δ_2 (mm)	C
	47039	19700	340	0.168	0.01726	0.126	775

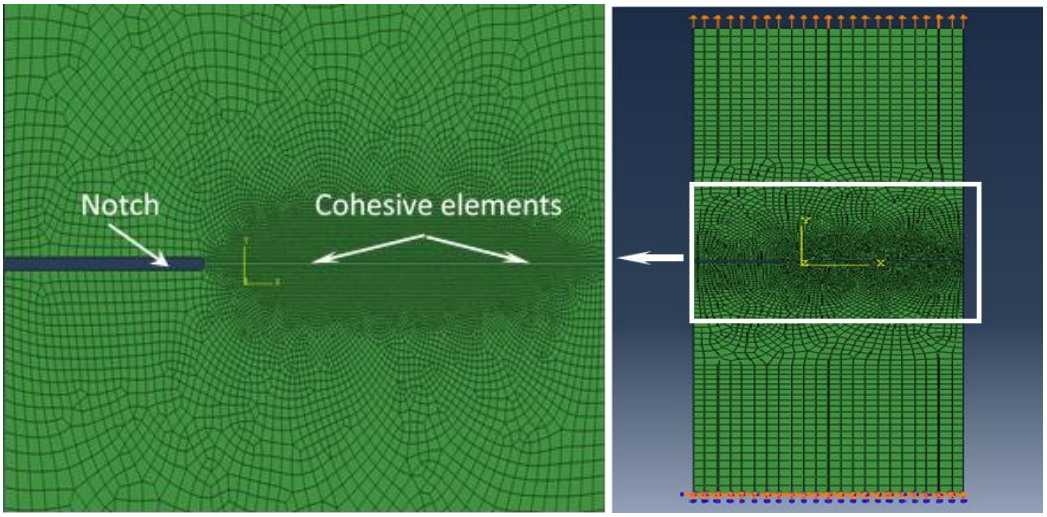

Fig. 6.6. Boundary conditions and loading for FE model.

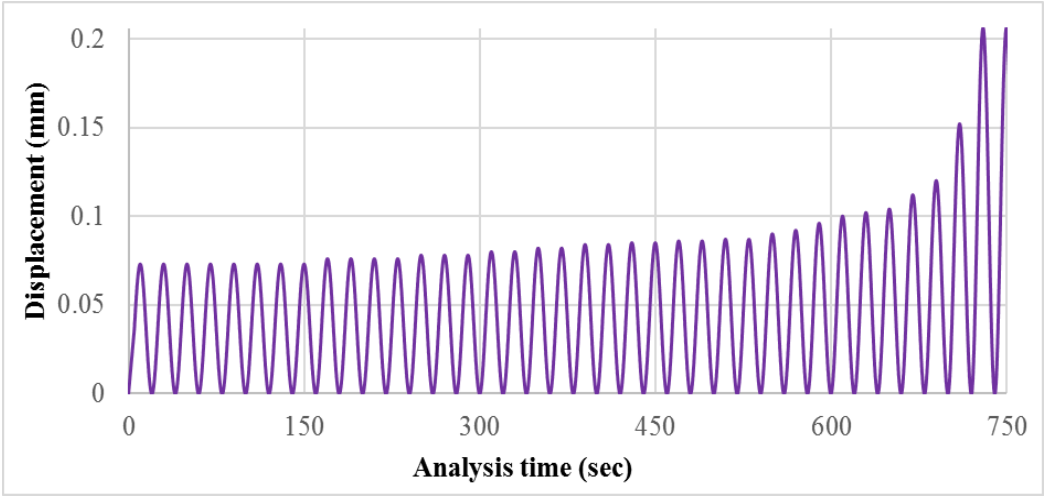

Fig. 6.7. Displacement as function of time.

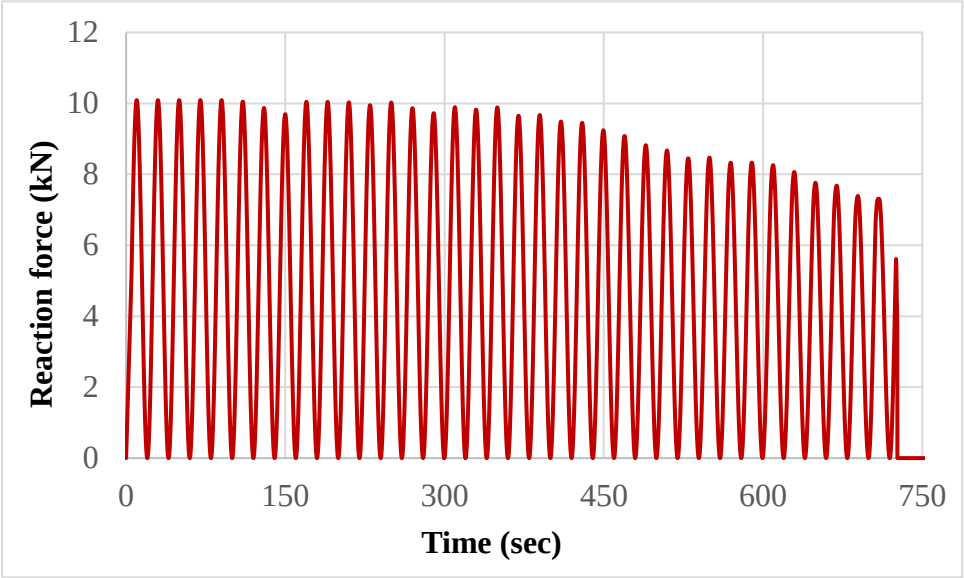

Fig. 6.8. Reaction force as function of time.

6.3.3 Fast-track effect on accuracy of the result

The effect of the updates-parameter N_u (and consequently ΔN) found in Eq. (6.14), on the dissipated energy as tested on the three-element model is shown in Table 6.3, Fig. 6.9 and 6.10 and its effect on the crack growth on full model is shown in Fig. 6.11 and 6.12. In general, a decrease in the value of N_u (increasing the value of ΔN) gives rise to a predicted slower crack growth. From Table 6.3, the error in the estimated number of cycles at failure is found to be dependent on the value of N_u, since for $\Delta N = 2$ $(i.e\ N_u = 12)$ the error is 0% while for $\Delta N = 3$ $(i.e\ N_u = 8)$ the error in the predicted result is 4%. The error in the simulation result become significant when N_u set to a small value, for examble the error in the case when $\Delta N = 10$ $(i.e\ N_u = 2)$ is 24%. The results indicate the expected behaviour that the greater the value of N_u (and hence lower value of ΔN) the reduction in observable differences. From Table 6.3, Fig. 6.9 and 6.10 it is observable that there is little dependence of the results on the value of ΔN in the virtual-plastic region (i.e. when $\delta_{max} \leq \delta_2$). However, differences become more noticeable in the region of material deterioration (i.e. $\delta_{max} > \delta_2$). However, revealed in Fig. 6.10 is that acceptable results are achievable if ΔN is such that the damage is updated reasonably regularly (i.e. N_u is not too low).

From the results of the full model analysis shown in Fig. 6.11 and 6.12, it can be concluded that any value higher than 6 for the updates-parameter N_u provides satisfactory results with a significant reduction in computational cost. It is evident in Fig. 6.11, that the predicted results are reasonably close to each other for values of N_u set to (56, 28, 14, 7), which correspond to $\Delta N \approx (100, 200, 400, 800)$, respectively. Differences are more noticeable however for values of N_u lower than 6, where $N_u = 3$ corresponds to $\Delta N \approx 2000$ and $N_u = 1$ corresponding to $\Delta N \approx 5600$, as shown in Fig. 6.12. In this study, a value of $N_u = 7$ corresponding to $\Delta N \approx 800$, was found to be sufficient for good accuracy and a significant reduction in numerical analysis time. The motivation for a higher value of ΔN is clear, where for example a process taking 7 months in a cycle by cycle basis is reducible to around 6.3 hours with $\Delta N = 800$. The reduction in computational time (i.e. the ratio of CPU-time with the fast-track procedure over the CPU-time with the cycle by cycle analysis) is of the order of ΔN^{-1}.

Table 6.3 Local effect of ΔN on the dissipated energy ΔG.

N	$\Delta N = 1$		$\Delta N = 2$		$\Delta N = 3$		$\Delta N = 6$		$\Delta N = 10$	
	δ_{max} *(mm)*	ΔG *(KN/m)*	δ_{max} *(mm)*	ΔG *(KN/m)*	δ_{max} *(mm)*	ΔG *(KN/m)*	δ_{max} *(mm)*	ΔG *(KN/m)*	δ_{max} *(mm)*	ΔG *(KN/m)*
1	0.0852	16.8	0.0852	16.8	0.0852	16.8	0.0852	16.8	0.0852	16.8
3	0.0895	18.9			0.0895	18.9				
6	0.0959	22.1	0.0959	22.1	0.0959	22.1	0.0959	22.1		
9	0.102	25.3			0.102	25.3				
10	0.104	26.4	0.104	26.4					0.104	26.4
12	0.109	28.5	0.109	28.5	0.109	28.5	0.109	28.5		
15	0.115	31.7			0.115	31.7				
18	0.121	34.9	0.121	34.9	0.121	34.9	0.121	34.9		
20	0.126	37.0	0.126	37.0					0.126	37.0
24	0.160	63.0	0.160	57.7	0.146	53.1	0.134	45.0		
25	Failed	68.5	Failed	68.5						
26					Failed	68.5				
27							Failed	68.5		
30									0.153	59.4
31									Failed	68.5

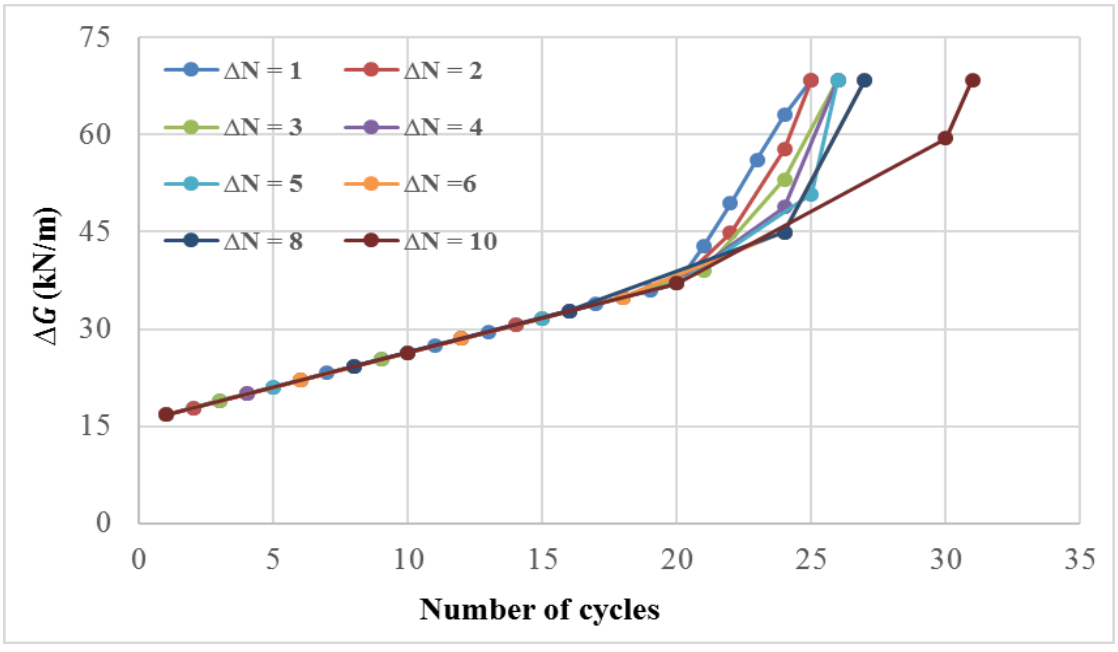

Fig. 6.9. Dissipated energy with the number of cycles as a function of ΔN.

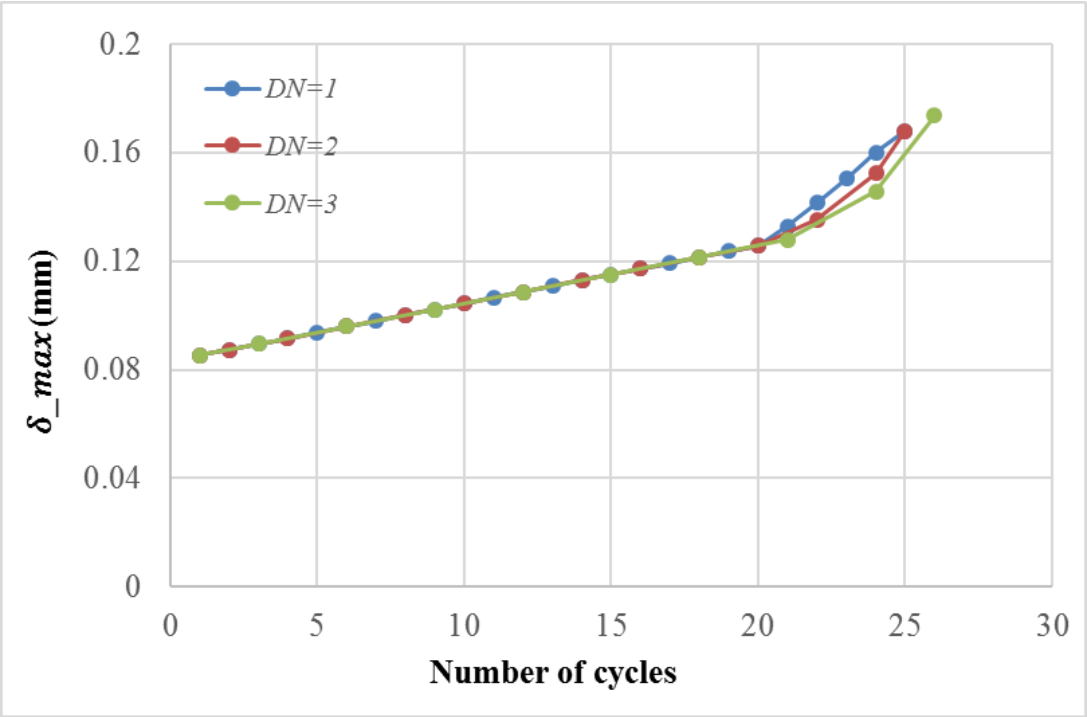

Fig. 6.10. The value of δ_{max} with the number of cycles as a function of ΔN.

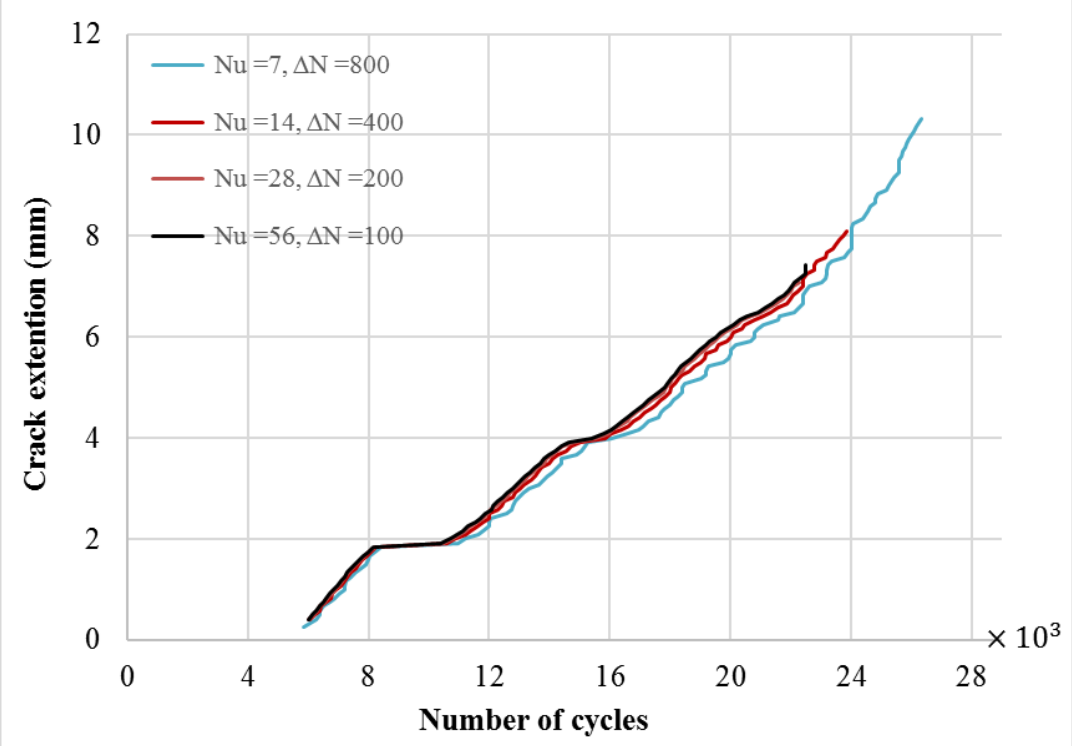

Fig. 6.11. Comparison of the model prediction with N_u values higher than 6 at R = 0 and a frequency of 0.05Hz.

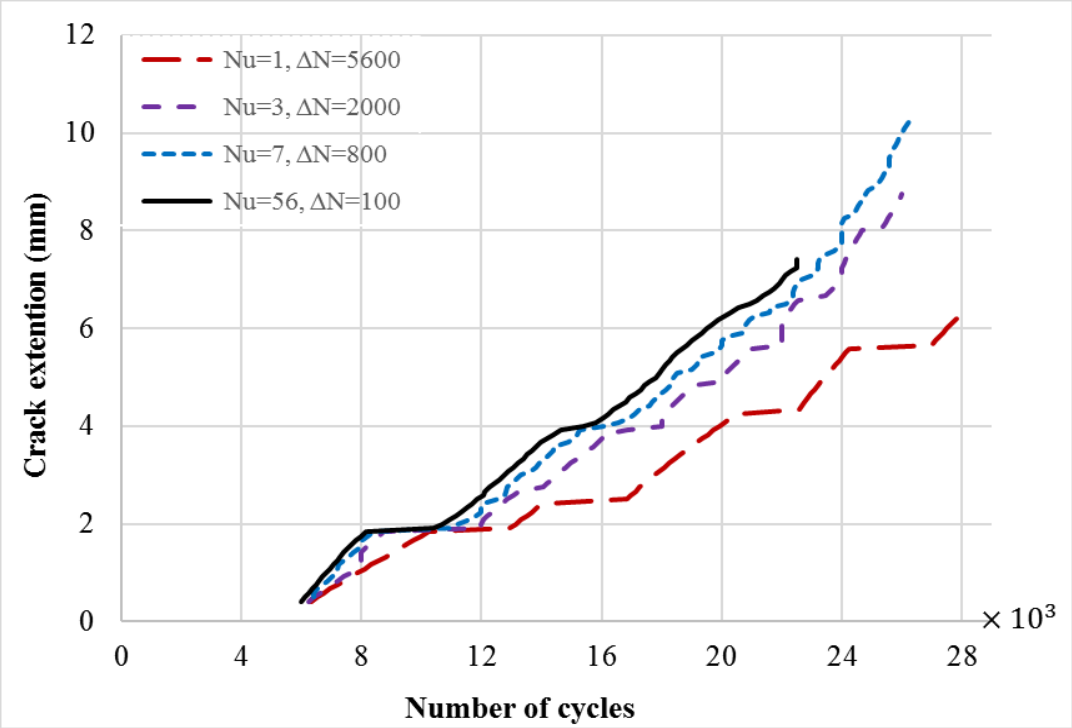

Fig. 6.12. Comparison of the model prediction with different N_u values at R = 0 and a frequency of 0.05Hz.

6.3.4 Mesh sensitivity analysis

Converged results have been confirmed by running a mesh sensitivity analysis. Increasing the overall number of bulk-material elements or the cohesive-zone elements has been found to have little impact on the results presented. However, it might well be anticipated that the number of elements in the cohesive-zone will be critical to a good outcome. The length of the cohesive-zone can be estimated through a similar formulation to the plastic zone estimated by von Mises yield criterion as

$$l_{coh} = \frac{E}{2\pi}\frac{G_{Ic}}{\sigma_c^2} \tag{6.18}$$

For the problem under consideration the length of the cohesive-zone is 12.5 mm, whereas the length of the ligament is 20 mm. It is possible to deduce from the plots shown in Fig. 6.13 that the number of cohesive elements in the cohesive zone only has a minor influence on the crack growth and fatigue life. However, the number of element in the cohesive zone could affect the accuracy of the stress field at the crack tip as shown in Fig. 6.14 to 6.19. According to these results if the focus is to accurately represent the stress field at the crack tip, the cohesive elements are required to share the same nodes with the bulk material elements (see Fig. 6.19). In this study, 150 elements are employed the cohesive-

zone to ensure that the cohesive element share the same nodes with the bulk material elements and to ensure high accuracy and precise description of the crack growth behaviour local to the crack.

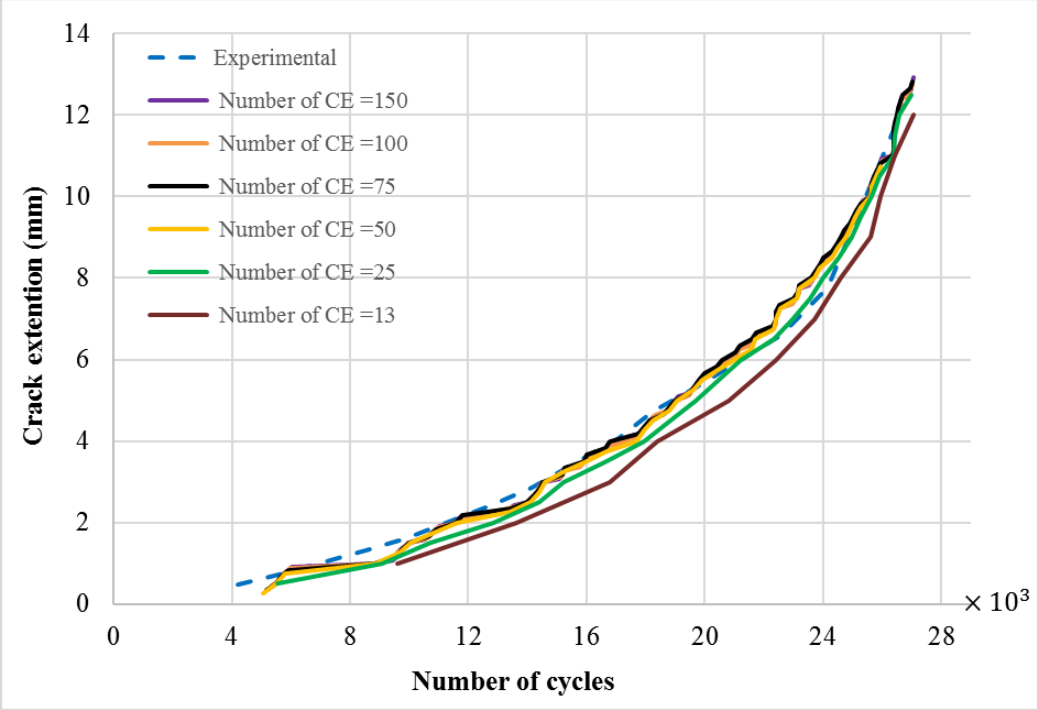

Fig. 6.13. Importance of the number of cohesive element in the cohesive-zone (at $\Delta N = 800$).

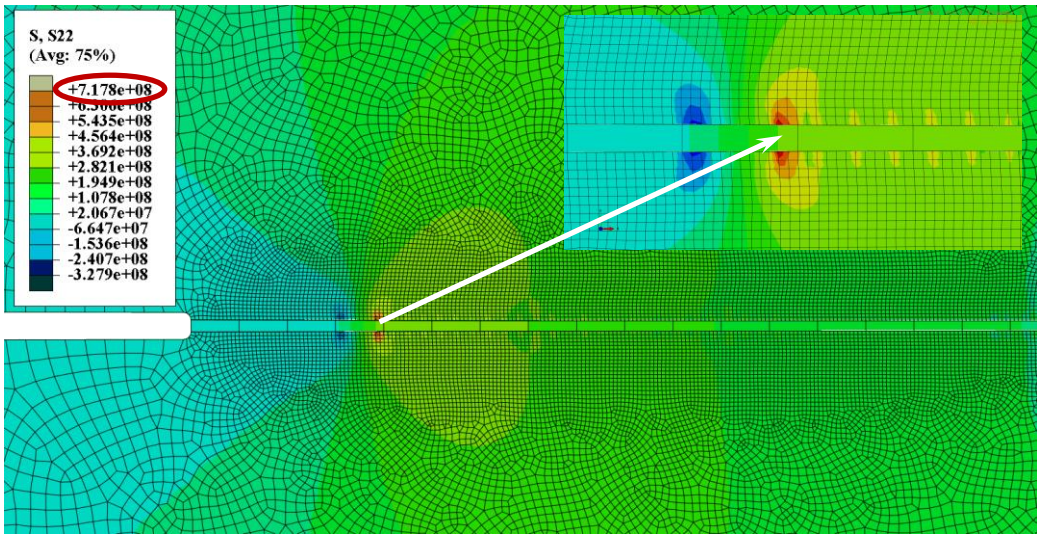

Fig. 6.14. The stress field when 13 cohesive elements used.

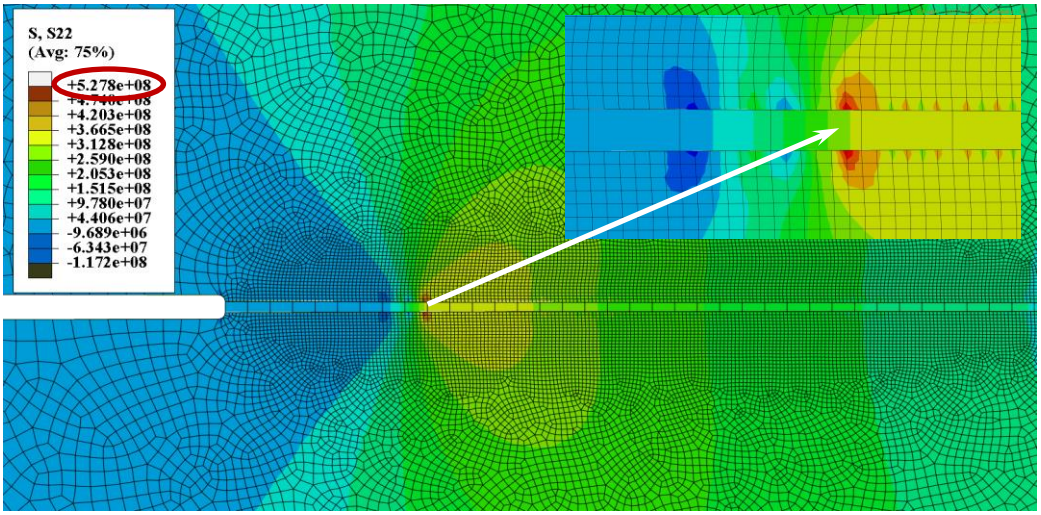

Fig. 6.15. The stress field when 25 cohesive elements used.

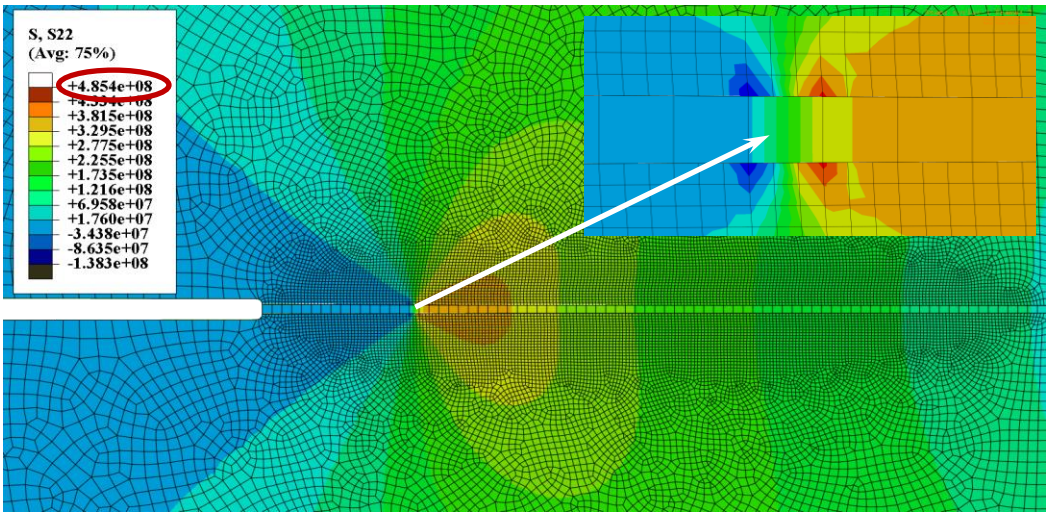

Fig. 6.16. The stress field when 50 cohesive elements used.

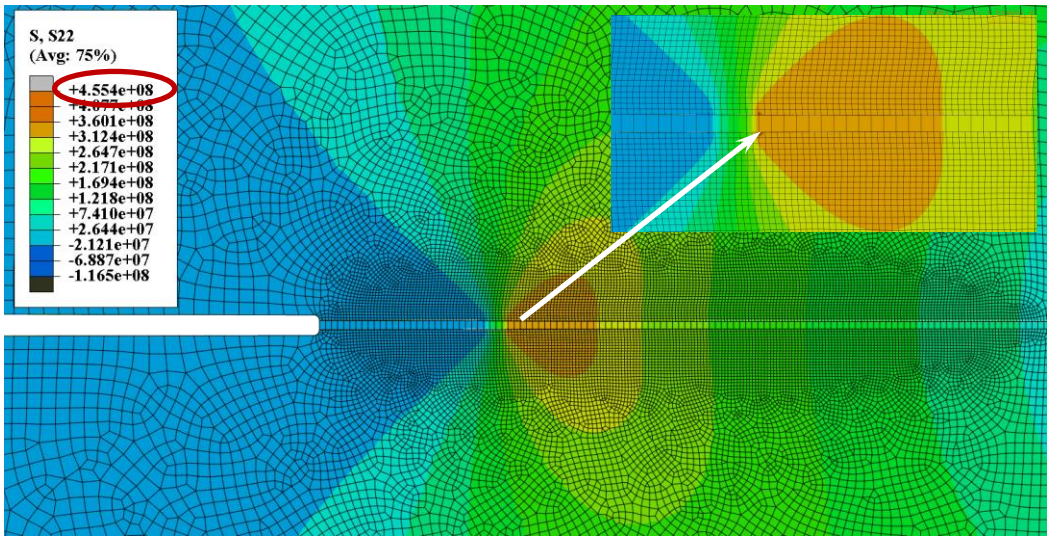

Fig. 6.17. The stress field when 75 cohesive elements used.

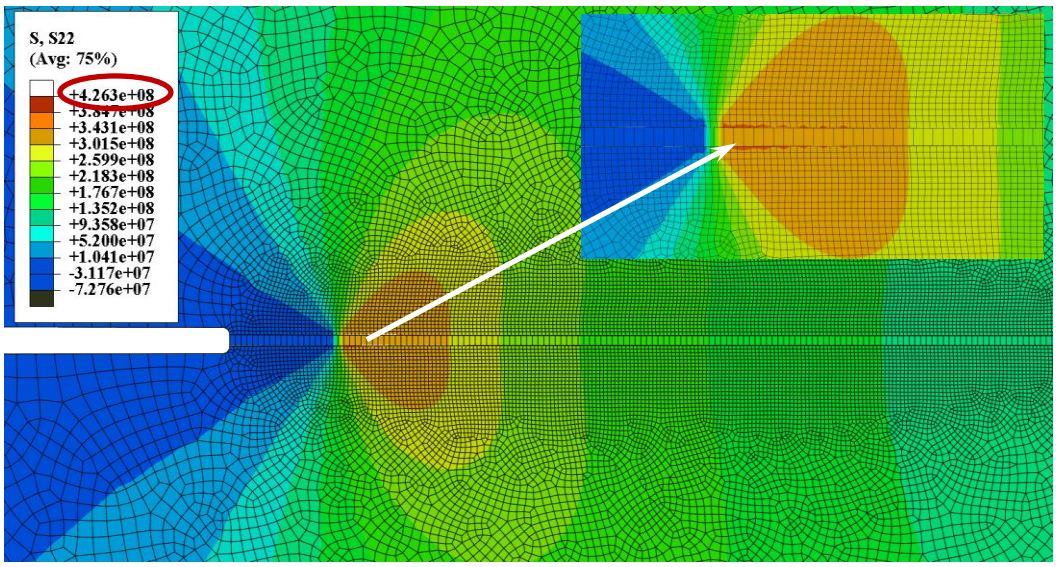

Fig. 6.18. The stress field when 100 cohesive elements used.

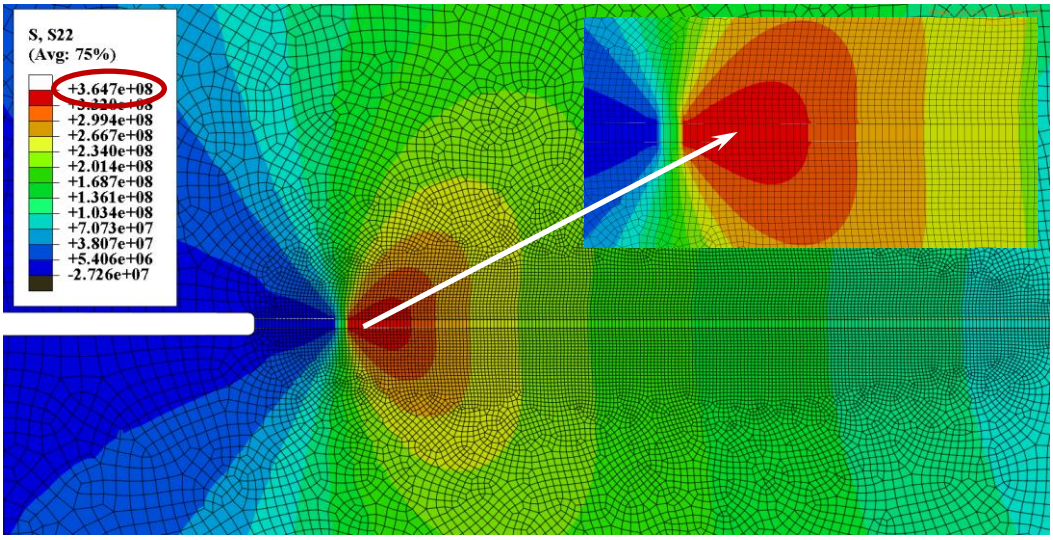

Fig. 6.19. The stress field when 150 cohesive elements used.

6.4 Results and discussion

To overcome the inherent limitations of the loading-unloading hysteresis damage model, a new cohesive-zone model with fast track facility has been introduced. This model is founded on the basis of loading-unloading hysteresis but with the facility to "freeze in" damage for a loading cycle over a predefined number of cycles. The damage is updated in the next loading cycle to comply with the conditions at the new state at $N + \Delta N$ cycles. The approach has been proven to be efficient in terms of time and computational cost

reduction. Analysis that can require months or possibly years to be solved (depending of the computational platform) using a cycle by cycle approach can be resolved in just a few hours or a few days to a good accuracy with the fast-track feature. Shown in Fig. 6.20 is experimental (from the result of the test performed in Chapter 4) and predicted crack extension versus the number of cycles; the predicted crack growth by the new approach with $\Delta N \approx 800$ is in good agreement with the experimental data.

One advantage of the new model over the previous models proposed in the literature [77, 80, 81, 110] is its simplicity. The model does not require the establishment of a relationship that links the damage to the number of cycles as in previous work. The damage in this case is calculated for one cycle and applied over ΔN cycles and then updated automatically for the next loading cycle. Another advantage of the model is that ΔN is automatically set according to the problem (low cycle fatigue or high cycle fatigue) and incorporates a technique to evaluate the accurate number of cycles at failure rather than simply assuming it is a multiple of ΔN.

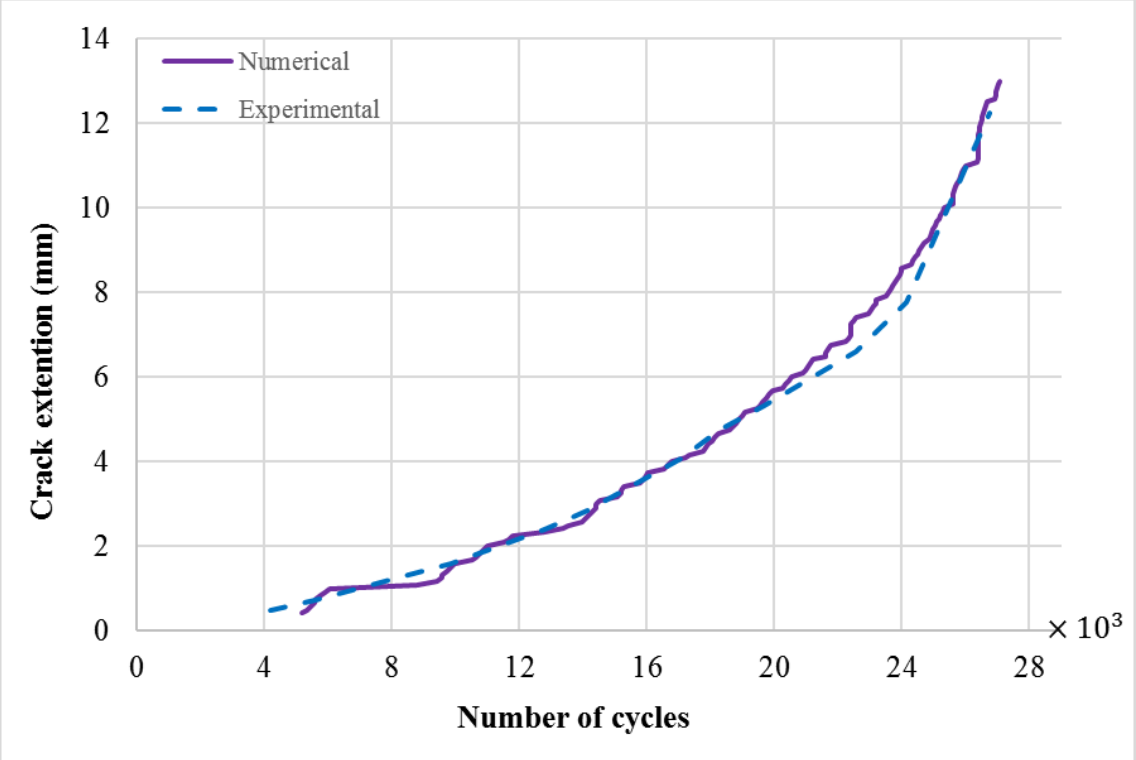

Fig. 6.20. Numerical prediction at ($\sigma_c = 340\ MPa,\ C = 775,\ N_u = 7\ (\Delta N = 800)$, $R = 0\ \&\ f = 0.05Hz$) versus experiment at ($R = 0\ \&\ f = 0.05Hz$).

6.5 Summary

- A new trapezoidal cohesive-zone model for fatigue that can be applied to high and low-cycle fatigue simulations has been introduced.
- Decreasing the value of N_u is observed to lower crack growth. If however, N_u is set so that the damage variable is sufficiently updated (after 800 cycles proved sufficient in the tests), then the results can be expected to be in good agreement with the experimental data with significant reduction in computational costs.
- The new CZM model has been shown to provide acceptable results with a significant reduction in the cost in term of the computational time of the order of ΔN^{-1}.
- Although the number of elements in the cohesive-zone has an effect on the stress field at the crack tip, it has a minor effect on the crack growth prediction.
- It is observed that the model tends to underestimate the crack extension for crack growth less than 1.2 mm but subsequently the predicted crack growth is in line with experimental data.

Chapter 7: Frequency-dependent CZM for fatigue

7.1 Introduction

The process of fatigue failure can be divided into three parts: crack initiation, crack propagation, and then fast fracture, which leads to the final failure [2, 106]. The fatigue behaviour of a part can be significantly affected by different factors such as mechanical, microstructural and environmental. As fatigue failure can result when the applied stress is much smaller than the yield stress of the material, it has become a point of interest for many researchers. A significant number of experimental studies have been done to estimate the life of mechanical parts, but these can be costly and extremely time-consuming giving rise to an urgent need for fatigue models with an ability to predict crack growth rates and fatigue life [106].

The academic literature reveals that the cohesive-zone model (CZM) is an attractive candidate for the modelling and simulation of fatigue problems. The CZM is founded on a traction-separation law (TSL), where traction is related to material separation through a constitutive equation. When the traction reaches its critical value σ_c, material damage initiates and material softening occurs. Following damage initiation, traction decreases until it finally reaches zero which is the point of material separation. This point is also identified when the separation between the surfaces of the cracked-material reaches a critical value δ_c, at which point the crack propagates with all cohesive energy Γ_o dissipated. The advantage of using the cohesive models over other models is its ability to predict the initiation and the propagation of the crack. Furthermore, it can also be applied to both monotonic and cyclic loads. The focus in this chapter is on frequency-dependent cohesive-zone models, which are designed to capture the frequency effect on the fatigue crack propagation at any frequency dependent material such as the austenitic stainless-steel 304.

A summary of the available cohesive model for fatigue along with a new model produced in this work was illustrated in Chapter 6. However, all of these models are rate-independent and do not capture the frequency effect. In this work, the new rate-dependent trapezoidal CZM that introduced in Chapter 5 is modified and implemented in the new cohesive-zone for fatigue that introduced in Chapter 6 to produce a frequency-dependent CZM that can be used to capture the loading frequency effect on fatigue crack growth. In this fatigue model the fatigue crack growth is set to be controlled by the cohesive strength

which set to be equal to yield stress of the material at a proof strain equal to 0.1% and because the model under consideration is a trapezoidal model it captures local plastic deformation at the crack tip.

7.2 Cohesive-zone model for fatigue

Rate dependency can be introduced into a monotonic cohesive-zone model by means of a dashpot as shown in Chapter 5. The traction-separation curve for a frequency Dependent TCZM is shown in Fig. 7.1. It is of interest to observe that as loading frequency increases how the cohesive critical traction also increases until it reaches a specified limit and then subsequently takes on a constant value.

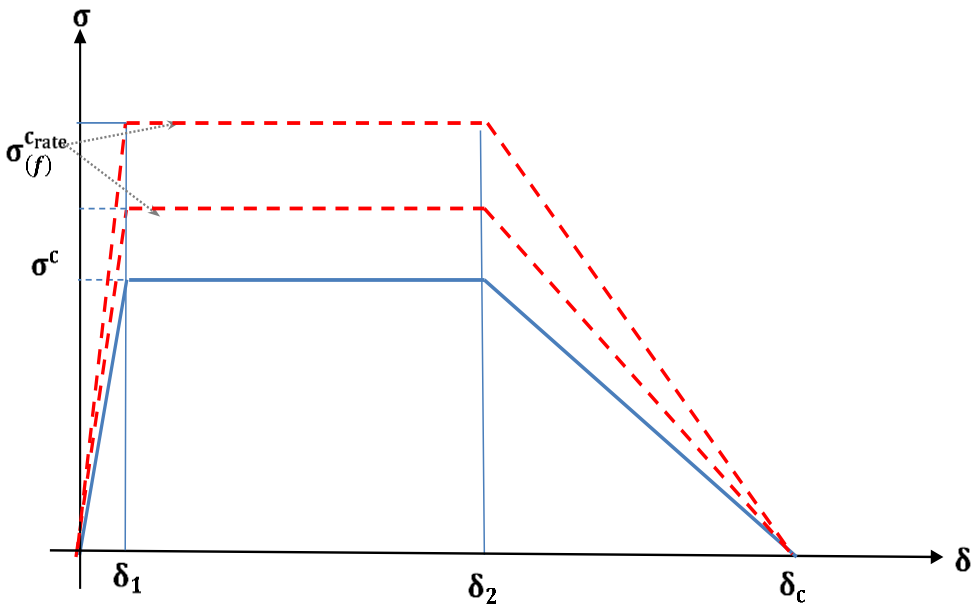

Fig. 7.1. Mode I trapezoidal rate-dependent CZM.

The area under the traction separation curve represents the fracture energy G_c, which is defined mathematically to be

$$G_c = \int_0^{\delta_c} \sigma_{(\delta)}\, d\delta \tag{7.1}$$

In the case of a trapezoidal CZM the fracture energy can be considered to be formed in two parts, i.e. plastic G_p and cohesive Γ_o components to give

$$G_c = G_p + \Gamma_o \tag{7.2}$$

The area under the curve(s) in Fig. 7.1 is equal to

$$G_c = \frac{1}{2}\sigma_{(f)}^{c_{rate}}\left((\delta_2 - \delta_1) + \delta_c\right) \tag{7.3}$$

The variable $\sigma_{(f)}^{c_{rate}}$ is termed the frequency-dependent critical cohesive stress, its behaviour derived from the rate-dependent models presented in Chapter 5. The frequency-dependent critical stress $\sigma_{(f)}^{c_{rate}}$ increases with the frequency up to a specific limit $\sigma_{(limit)}^{c}$and is assumed to behave exponentially and is represented mathematically by

$$\sigma_{(f)}^{c_{rate}} = \sigma_{(limit)}^{c} \times exp(-\frac{f_o}{f}) \tag{7.4}$$

where $\sigma_{(limit)}^{c}$ is the maximum value for the increase in the frequency-dependent critical stress, its value evaluated from tuning with the experimental data at loading frequency of 50 Hz.

The value of the base frequency f_o is set to ensure that at 0.05Hz the frequency-dependent critical stress equals the yield stress at a proof strain equal to 0.1%. Note also that Eq. (7.4) arises out of a rheological model satisfying the differential equation $d\sigma_{(f)}^{c_{rate}}/d\tau = -\sigma_{(f)}^{c_{rate}}$, where τ represents a dimensionless time and for frequency loading is related to frequency by $\tau = f_0/f$. Although the particular form of Eq. (7.4) is not unique it provides a relatively simple model for the desired response of $\sigma_{(f)}^{c_{rate}}$. Note that as $f \to \infty$ the function $\sigma_{(f)}^{c_{rate}}$ asymptotically approaches the constant value $\sigma_{(limit)}^{c}$, which is an effect observed experimentally as discussed in reference [111]. This behaviour arises from the saturation of fracture energy with rate and for austenitic stainless-steel 304 it can be linked to the saturation of the austenitic-martensitic phase transformation. In essence the frequency-dependent fatigue model consists of the model outlined in Chapter 6 apart from $\sigma_{(f)}^{c_{rate}}$ replacing σ_c. The model is illustrated graphically in Fig. 7.2 and described mathematically as

$$\sigma_{(\delta)} = \begin{cases} K_{coh}\delta & if \quad \delta < 0 \\ \left(\frac{\sigma_{max}}{\delta_{max}-\delta^{p}_{(N+\Delta N)}}\right)(\delta - \delta^{p}_{(N+\Delta N)})H\left(\delta - \delta^{p}_{(N+\Delta N)}\right) & if \quad 0 \le \delta \le \delta_{max} \\ \left(1 - D_{(\delta)}\right)K_{coh}\delta & if \quad \delta_{max} < \delta < \delta_c \\ 0 & if \quad \delta \ge \delta_c \end{cases} \tag{7.5}$$

where K_{coh} represents the cohesive stiffness, $\sigma_{(\delta)}$, σ_{max} and δ_{max} are the cohesive traction, the stress and the separation at the point of unloading, respectively (see Fig. 7.2).

These parameters take the values of δ_1 and σ_c, respectively to insure that when there is no unloading or at the first cycle the first part of the second equation in Eq. (6.2)returns the cohesive stiffness K_{coh}. Here δ_c, δ_1, δ_2, δ and δ^p are the critical cohesive separation, the separation at which the permanent damage starts, the separation at which the material deterioration starts, the applied separation and the remnant separation after unloading, respectively. The Heaviside function $H\left(\delta - \delta^{p}_{(N+\Delta N)}\right)$ in Eq. (7.4) is defined to equal zero if δ is smaller than δ^p and one in any other condition. N is the number of cycles, ΔN is the number of cycles between updates in the damage state. Finally, $D_{(\delta)}$ is a monotonic damage variable evaluated from

$$D_{(\delta)} = \begin{cases} 1 - \frac{\delta_1}{\delta} & if \quad \delta_1 \le \delta < \delta_2 \\ 1 - \frac{\delta_1(\delta_c - \delta)}{\delta(\delta_c - \delta_2)} & if \quad \delta_2 \le \delta \le \delta_c \end{cases} \tag{7.6}$$

The choice of δ_1 and δ_2 is arbitrary (since there are no evidence of the right shape of the traction-separation law). The value of δ_1 is set to a relatively small value to ensure a very stiff connection in the undamaged cohesive elements, while δ_2 is set to be close to δ_c to capture the local dissipated energy at the crack tip as a result of local plastic deformation, since the focus of the model is crack propagation in ductile materials. These choices is similar to what is advised in reference[56], for definiteness δ_1 and δ_2 are set as

$$\delta_1 = \frac{\sigma^{crate}_{(f)}}{K_{coh}} \tag{7.7}$$

$$\delta_2 = 0.75 \times \delta_c \tag{7.8}$$

The applied separation δ is determined by adding the applied cyclic displacement δ^{cyc} to the remnant separation $\delta^{p}_{(N+\Delta N)}$, i.e.

$$\delta = \delta^{p}_{(N+\Delta N)} + \delta^{\mathrm{cyc}} \tag{7.9}$$

For a detailed information about the evaluation of $\delta^{p}_{(N+\Delta N)}$ and the fast-track feature see Chapter 6 Section 6.2.2.

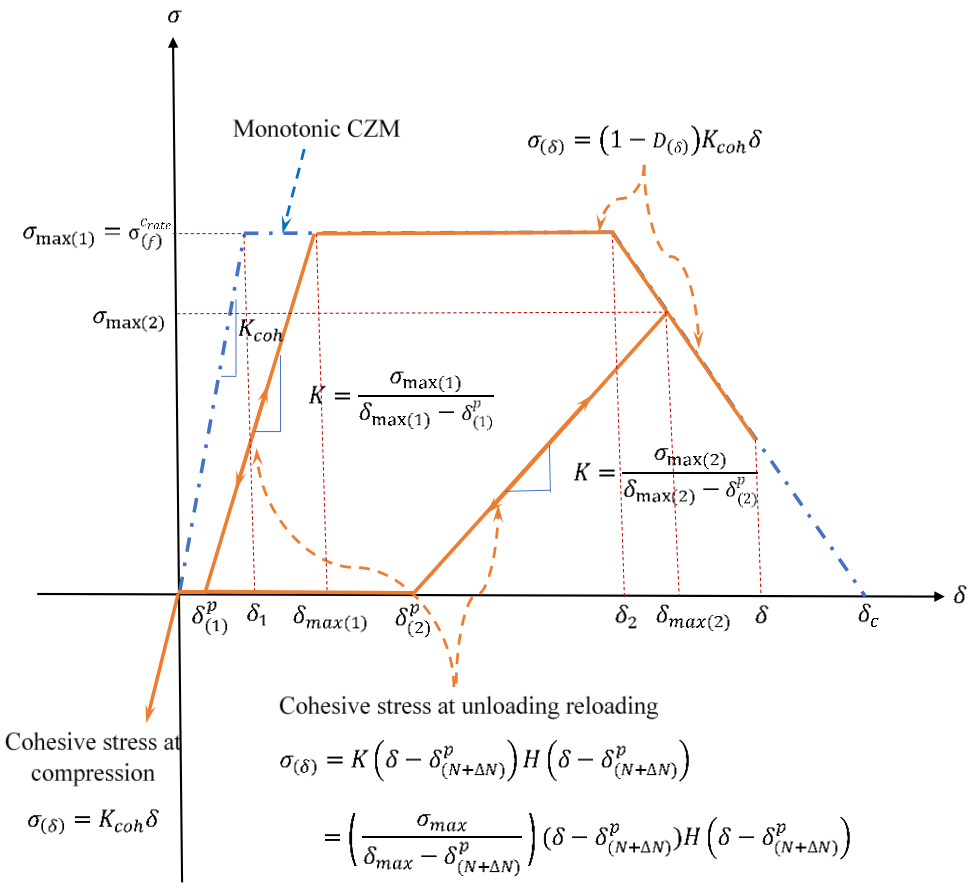

Fig. 7.2. New frequency-dependent loading-unloading hysteresis model.

7.3 Implementation of the cohesive-zone model in ABAQUS

In this study, the commercial finite element solver ABAQUS [109] is chosen to be the vehicle for performing the numerical analysis. In ABAQUS, the cohesive model can be identified either in the form of cohesive surface or by implementing cohesive elements in the numerical model along the crack path. Introducing a new cohesive model (such as the CZM described in Section 7.2) to ABAQUS is achieved with the cohesive element through a user-defined material (UMAT) subroutine. The UMAT subroutine for the new frequency-dependent CZM can be found in Appendix B-3.

7.3.1 Implementing and testing the UMAT

The new frequency-dependent CZM is implemented in ABAQUS by using a UMAT subroutine. To test the subroutine and to demonstrate the benefit of using the fast-track

feature, a three-element model (3-EM) (two material elements linked through a cohesive element) is initially used as shown in Fig. 7.3. Shown in Table 7.1 are the properties of the bulk material element and the cohesive element. The boundary conditions are displacement fixed in all directions at the bottom edge and a constant cyclic displacement applied at three loading frequencies (0.05, 0.1 and 30Hz) with $R = 0$ and 7.3 mm maximum amplitude at the top edge (see Fig. 7.3). Fig. 7.4 to 7.6 shows the cyclic stress with the analysis time at different loading frequencies. From these curves, the behaviour of the new frequency-dependent model is illustrated. Increasing the frequency increases the critical stress of the cohesive model and at the same time the advantage of the fast-track feature is illustrated by comparing the number of cycles required to finish the analysis. Application of the fast-track feature provides a reduction in CPU-time of the order of ΔN^{-1}.

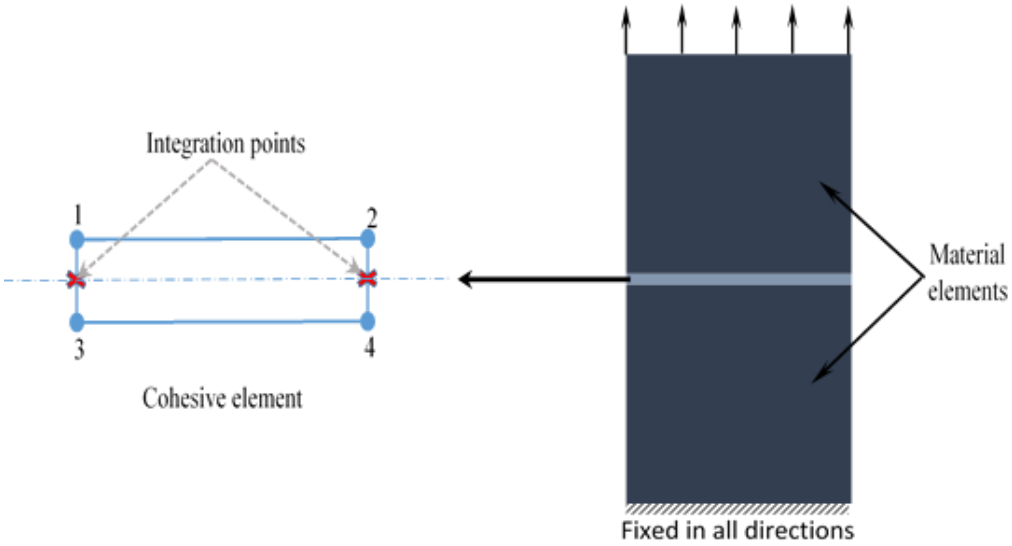

Fig. 7.3. Implementation of the cohesive element in the finite element model.

Table 7.1 Material and cohesive element properties for stainless steel 304.

Bulk material	Young's modulus (E) (GPa)			Poisson's ratio (ϑ)		
	193			0.29		
Cohesive elements	G_c (N/m)	K_{coh} (GPa/m)	σ_c (MPa)	δ_c (m)	δ_1 (m)	δ_2 (m)
	47039	19700	340	0.000168	0.0000173	0.000126
	ΔN		$\sigma^c_{(limit)}$ (MPa)	f_o (Hz)	C 3-EM	C *Full-model*
	1	4	400	0.008	40	775

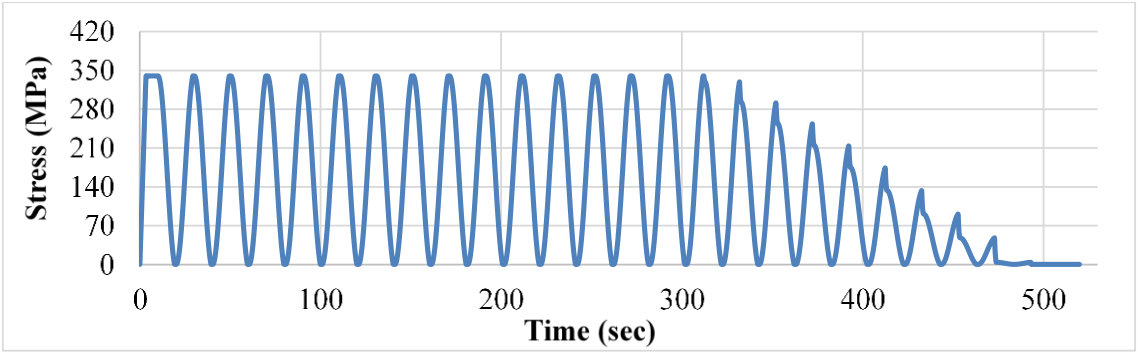

(a) cycle by cycle analysis

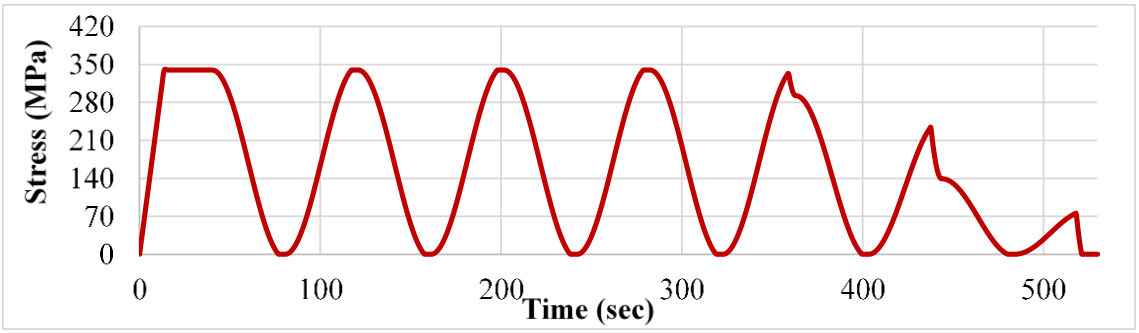

(b) fast-track procedure with $\Delta N = 4$

Fig. 7.4. Cyclic stress levels in the cohesive element with the time (real-time) at $f = 0.05Hz$.

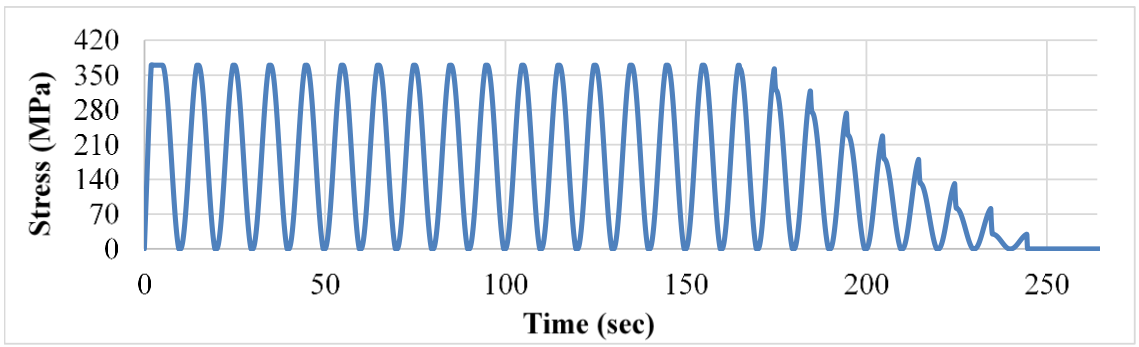

(a) cycle by cycle analysis

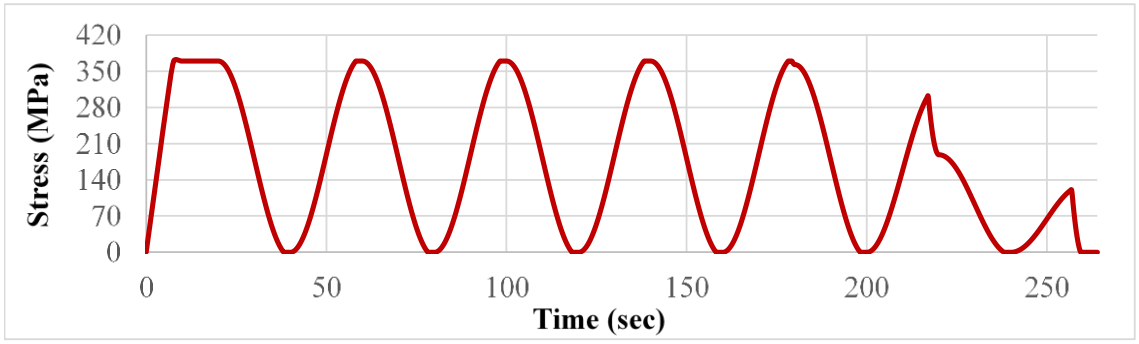

(b) fast-track procedure with $\Delta N = 4$

Fig. 7.5. Cyclic stress levels in the cohesive element with the time (real-time) at $f = 0.1Hz$.

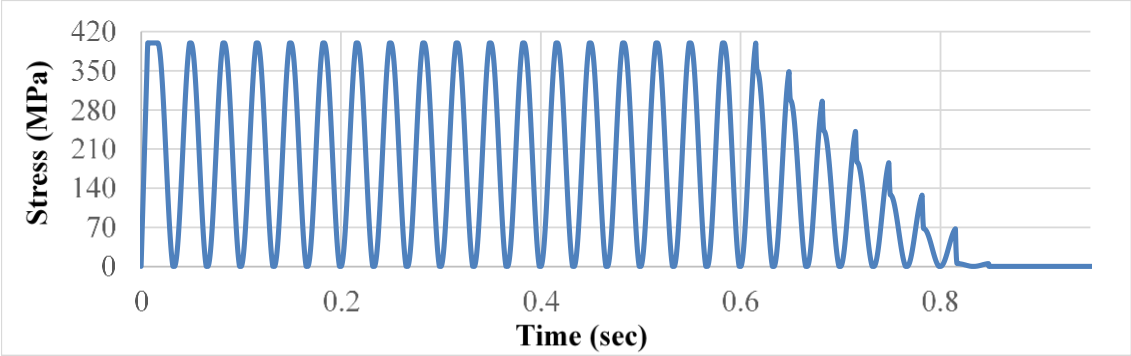

(a) cycle by cycle analysis

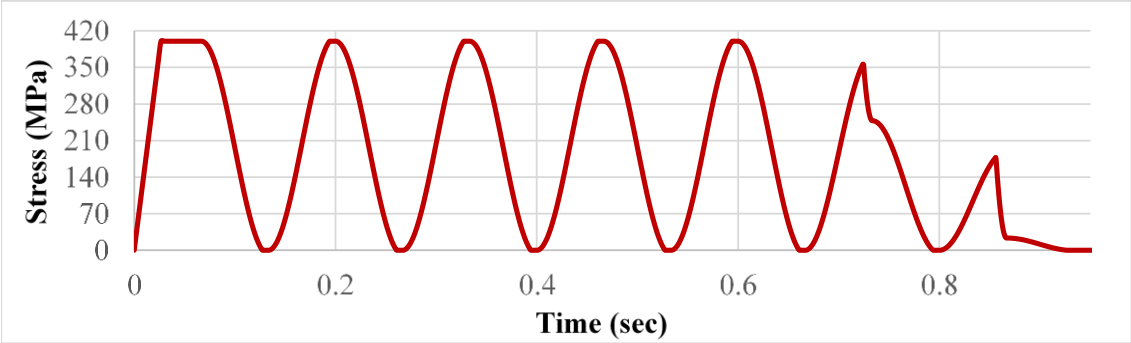

(b) fast-track procedure with $\Delta N = 4$

Fig. 7.6. Cyclic stress levels in the cohesive element with the time (real-time) at $f = 30Hz$.

7.3.2 Analysis model: geometry and boundary conditions

Shown in Fig. 7.7 is a finite element model for fatigue specimens used in the experimental trials. The model consists of 23618 plane-stress elements of which 22988 (type CPS4), 390 (type CPS3), and 240 cohesive elements (type COH2D4). Details on material properties for both the cohesive element and the bulk material elements are presented in Table 7.1, the numerical analysis was done at six loading frequencies (0.05, 0.1, 0.5, 5, 30, 50). The critical cohesive stress σ_c for tests performed at the loading frequency 0.05Hz is set to be equal to the yield stress of the material. Likewise the value of the parameter C is set by tuning the model with the experimental results at the same loading frequency of 0.05 Hz. This value is applied for all the analysis performed at different frequencies yielding good agreement with experimental results and thus provides good supporting evidence for the validity of the approximation in Eq. (7.4).

Fig. 7.7 shows the applied boundary conditions for the model, which consists of a uniform cyclic displacement in the y-direction applied at the top surface with the bottom surface fixed in all directions. A number of stages are involved (see Table 7.2) in

incrementing the applied displacement in order to accurately capture the experimental loading conditions. The first stage involves the application of a ramp function to increase the displacement from zero to 3.65×10^{-5}m. This is followed by stages with a sinusoidal cyclic displacement at $R = 0$, where the number of cycles at each stage is set to ensure a match with the loading conditions incurred in the fatigue experiment. A maximum load of 10 kN is set for the loading equipment during the experimental trial. The loading conditions are tabulated in Table 7.2 and presented for each frequency in Fig. 7.8 to 7.11. The number of cycles at each stage is directly recorded from the fatigue experiment performed in Chapter 4, While the displacement amplitude is determined from the fatigue experiment performed in Chapter 4 but after it multiplied with a 0.646 correction factor. The reason for the correction factor is that the measured displacement amplitude from the machine does not represent the applied displacement to the specimen and represent a reference displacement that result in a 10 kN force at the specimen. From the test in Chapter 4 it is clear that the maximum displacement when there is no crack propagation is 0.113mm and from the FE analysis it was found to be 0.073 from these data the correction factor is evaluated by dividing the maximum displacement from FE analysis by the maximum displacement form the fatigue test, then this factor is applied on all the experimental data. Fig. 7.12 to 7.15 shows the reaction force at the loading edge at loading frequency of 0.05, 0.1, 0.5 and 30Hz, respectively.

For the effect of the fast-track facility and the mesh sensitivity analysis check Chapter 6 Sections 6.3.3 and 6.3.4 respectively.

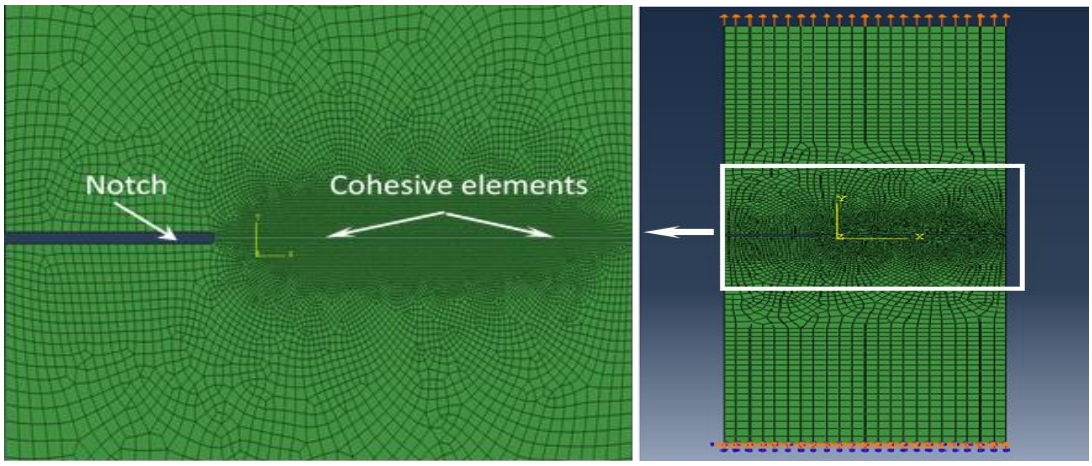

Fig. 7.7. Boundary conditions and loading for FE model.

Table 7.2 Cyclic amplitude with the number of cycles at that amplitude

	$f = 0.05\ Hz$		$f = 0.1\ Hz$		$f = 0.5\ Hz$		$f = 5, 30\ and\ 50\ Hz$	
	Max δ (mm)	N (cycles)	Max δ (mm)	N (cycles)	Max δ (mm)	N (cycles)	Max δ (mm)	N (cycles)
Stage 2	0.073	6400	0.073	8000	0.073	5600	0.073	8000
Stage 3	0.076	3200	0.0735	6400	0.0745	4800	0.0735	2400
Stage 4	0.078	2400	0.076	4800	0.076	4800	0.074	4800
Stage 5	0.08	1600	0.0795	3200	0.077	4000	0.075	4000
Stage 6	0.082	1600	0.08	2400	0.078	3200	0.076	3200
Stage 7	0.084	1600	0.083	2400	0.08	3200	0.0765	3200
Stage 8	0.085	1600	0.085	2400	0.082	2400	0.078	2400
Stage 9	0.86	1600	0.09	2400	0.083	2400	0.079	2400
Stage 11	0.087	1600	0.096	1600	0.085	2400	0.08	2400
Stage 12	0.09	800	0.10	1600	0.089	2400	0.081	2400
Stage 13	0.092	800	0.102	1600	0.092	2400	0.083	2400
Stage 14	0.096	800	0.104	800	0.096	2400	0.086	2400
Stage 15	0.10	800	0.106	800	0.10	2400	0.088	2400
Stage 16	0.102	800	0.108	800	0.108	2400	0.092	2400
Stage 17	0.104	800	0.112	800	0.116	2400	0.094	2400
Stage 18	0.112	800	0.116	800	0.132	800	0.098	1600
Stage 19	0.12	800	0.12	800	0.144	800	0.102	1600
Stage 14	0.152	800	0.124	800	0.176	800	0.108	1600
Stage 16	0.206	until failure	0.13	800	0.206	until failure	0.12	1600
			0.206	until failure			0.132	800
							0.148	800
							0.206	until failure

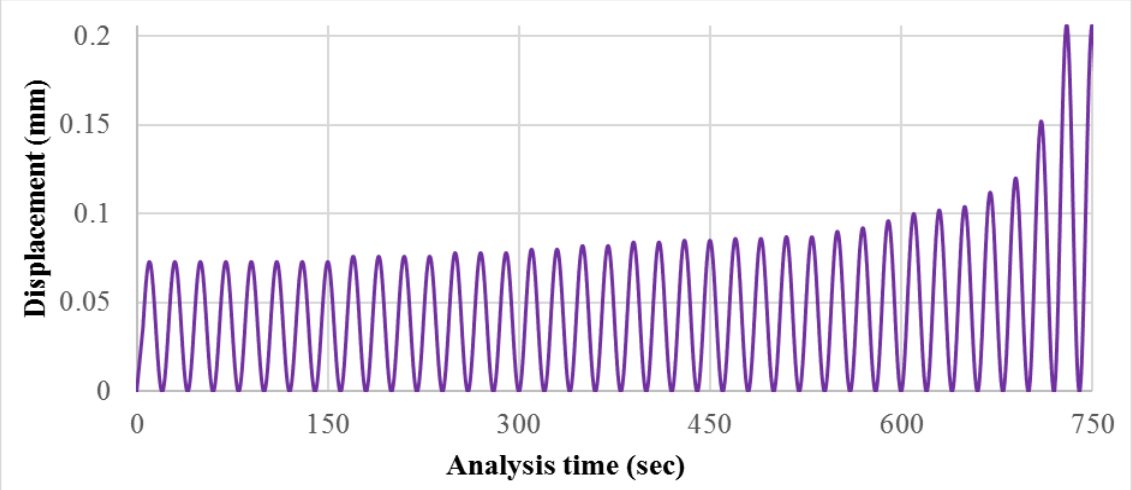

Fig. 7.8. Displacement as function of time at $f = 0.05$Hz.

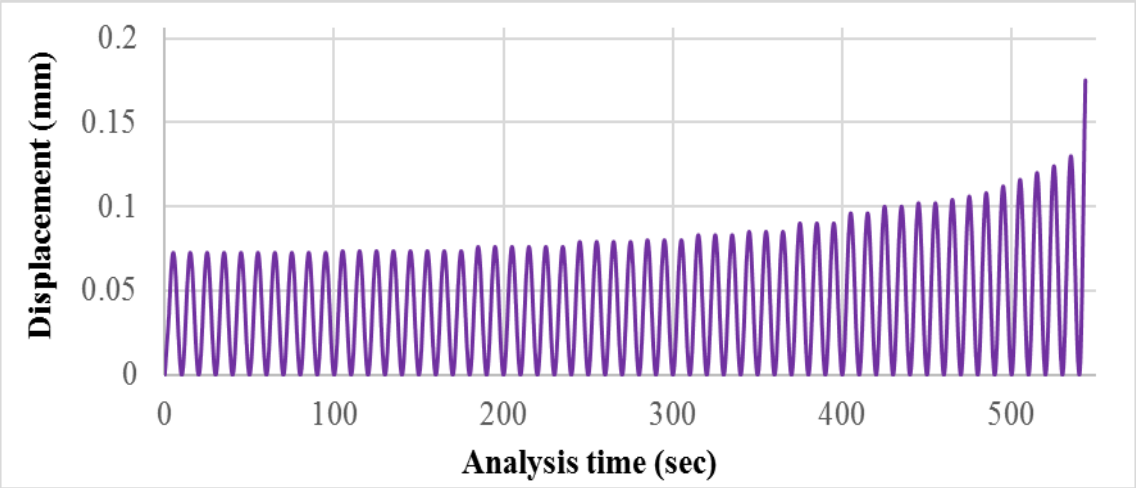

Fig. 7.9. Displacement as function of time at $f = 0.1$Hz.

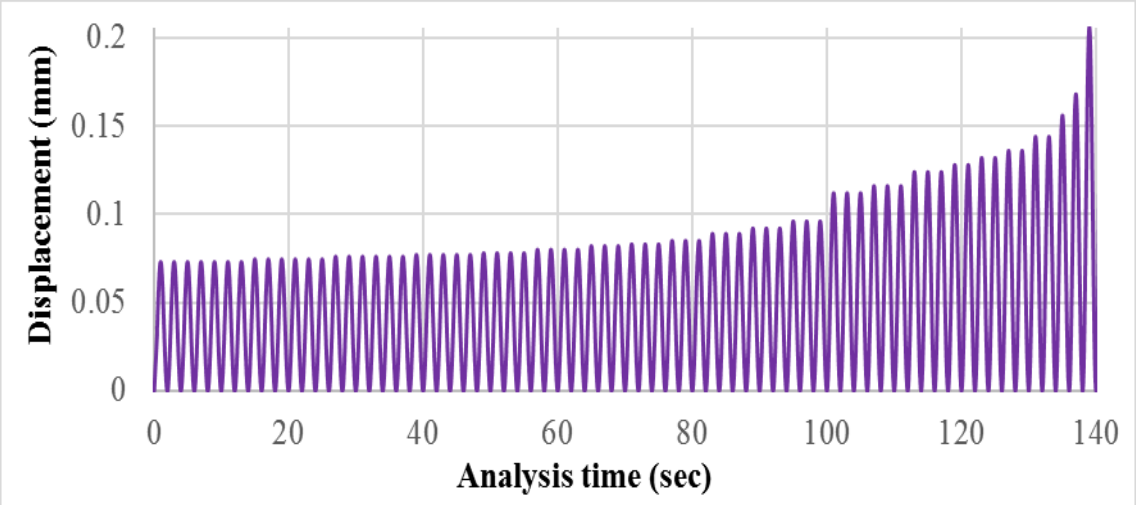

Fig. 7.10. Displacement as function of time at $f = 0.5$Hz.

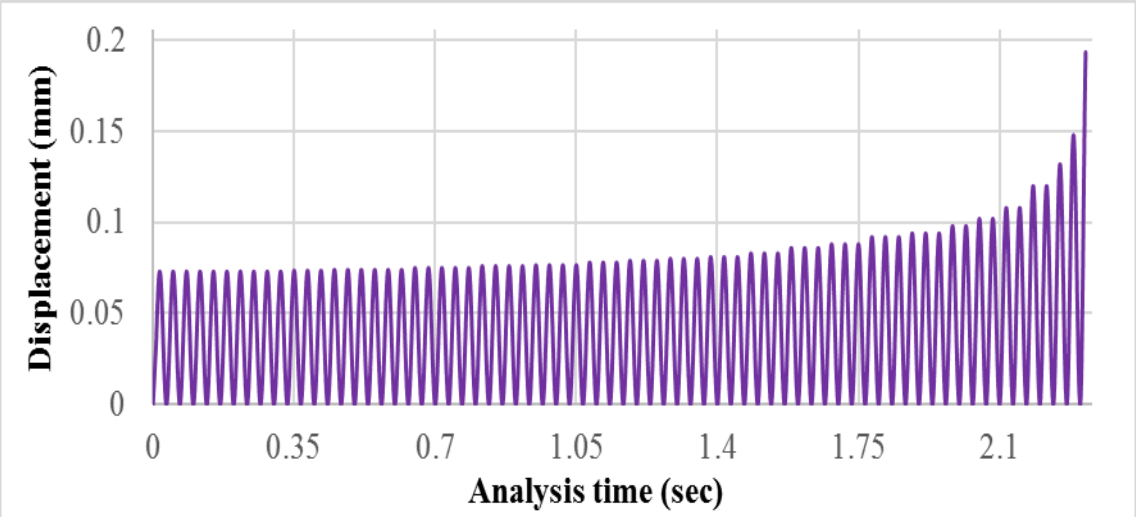

Fig. 7.11. Displacement as function of time at $f = 5{,}30\ and\ 50$Hz.

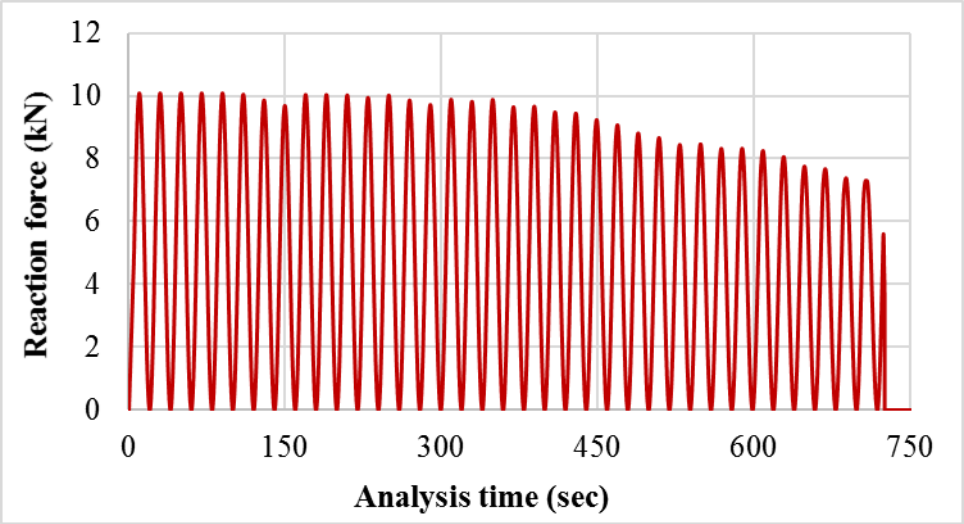

Fig. 7.12. Reaction force as function of time at $f = 0.05$Hz.

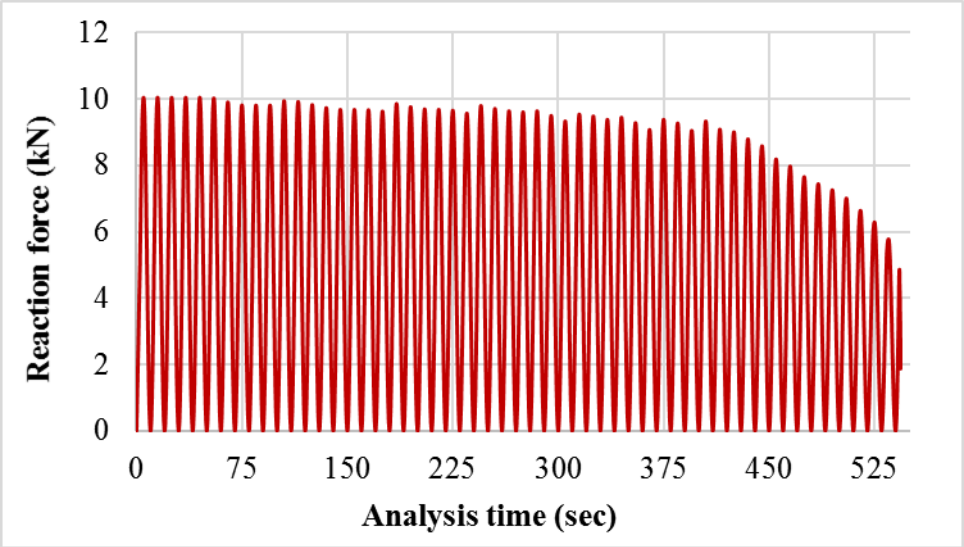

Fig. 7.13. Reaction force as function of time at $f = 0.1$Hz.

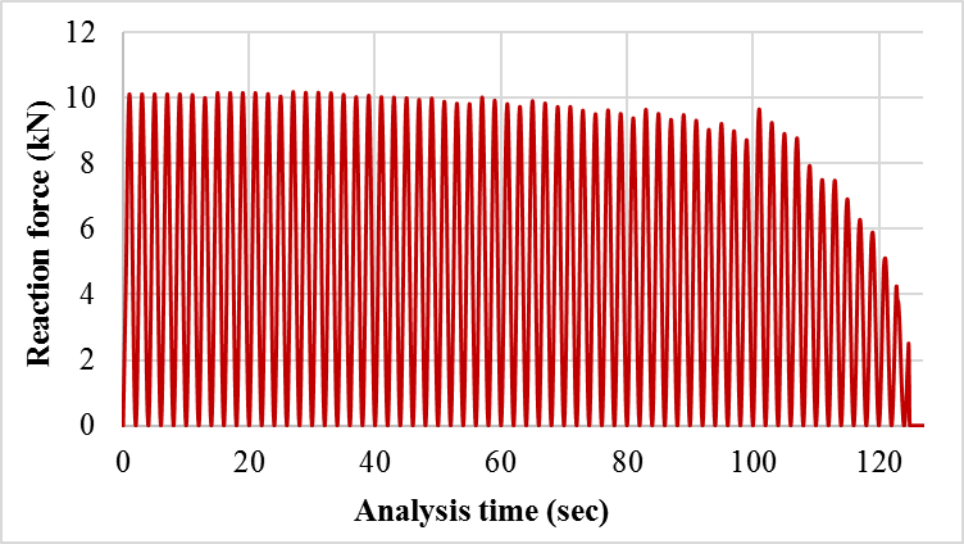

Fig. 7.14. Reaction force as function of time at $f = 0.5$Hz.

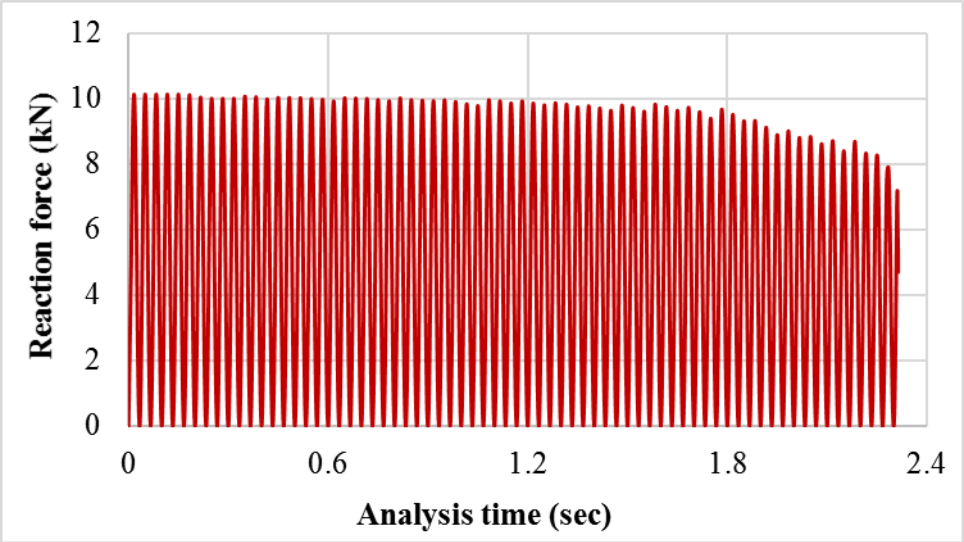

Fig. 7.15. Reaction force as function of time at $f = 30$Hz.

7.4 Results and discussion

The cohesive-zone model introduced in Section 7.2 is used to simulate the fatigue tests performed in Chapter 4 and the numerical results show that the new cohesive model can predict the crack growth behaviour at different loading frequencies with good accuracy and a significant reduction in the required CPU-time. A fast-track facility has been introduced to the new cohesive-zone model (see Chapter 6 Section 6.2.2) to overcome the essential limitations of the loading-unloading hysteresis damage model. The fast-track facility has the ability to "freeze in" the damage for a specific loading cycle over a predefined number of cycles ΔN. In the next loading cycle the damage updates to fulfil the new state at $N + \Delta N$ cycles. The new fast-track approach has been proven to be effective in term of accuracy and time reduction.

The advantages of the new frequency-dependent CZM over the available models in the literature (e.g. [77, 80, 81, 110]) are the ability to capture the frequency effect and its simplicity. It does not require the formation of a relationship to link the damage to the number of cycles as in previous work. Another advantage of the model is that it can be applied to both low and high-cycle fatigue analysis, since the number of cycles in the load envelope ΔN that used for the fast-track procedure is automatically set according to the problem under consideration.

The numerical predicted curves for crack growth with the number of cycles along with experimental curves for different loading frequencies are shown in Fig. 7.16 to 7.13. Fig.

7.16 presents the result at loading frequency $f = 0.05$ Hz which is used to tune the cohesive parameters (i.e. f_o *and* C) for the new model since $\sigma_{(f)}^{crate}$ for this loading frequency set to be equal to the material yield stress at 0.1% strain and δ_c set to be equal to the crack tip opening displacement measured on a CT specimen. By using these cohesive properties, the fixed parameter C was determined first by tuning the analysis result with the experimental data at 0.05 Hz. The value of critical stress limit $\sigma_{(limit)}^{c}$ is evaluated by tuning with the experimental result at loading frequency (50 Hz). Finally, the value of the base frequency f_o was found using Eq. (7.4) by applying the value of $\sigma_{(limit)}^{c}$ and the cohesive parameters at 0.05Hz. Predictions obtained with these settings when compared with data at other frequencies (i.e. 0.1, 0.5, 5 and 30Hz) provide good support for the form of Eq. (7.4) and the new model. The predicted and experimentally obtained crack growth at loading frequencies of 0.1Hz and 0.5Hz are shown in Fig. 7.17 and 7.12 respectively, with the results at 5, 30, and 50Hz are shown in Fig. 7.19. It is clear from the results that the predicted growth rate by the new model at different loading frequencies is in good agreement with the experimental results. The percentage of error in the estimated crack length [(estimated length-measured length)/measured length) *100%] is shown in Table 7.3, where the minus sign signifies that the model is under estimating the crack length. From the results in Table 7.3. it is clear that the predicted crack length is in an acceptable level of accuracy.

Table 7.3 Percentage difference in predicted and experimentally measured crack lengths.

N	$f = 0.05\ Hz$		$f = 0.1\ Hz$		$f = 0.5\ Hz$		$f = 50\ Hz$	
(cycles)	a (mm)	Error %	a (mm)	Error %	a (mm)	Error %	a (mm)	Error %
8000	0.98	-19.30	0.50	-19.80	0.38	-6.62	0.30	7.64
12000	2.18	-0.40	1.04	-7.60	0.79	-10.00	0.56	-2.15
17000	3.96	-1.94	1.77	0.09	1.36	-10.00	0.89	-4.40
20000	5.586	2.20	2.25	-6.25	1.75	-10.00	1.15	-5.66
24000	7.75	0.96	3.10	2.10	2.42	-8.80	1.50	-9.58
28000			4.19	4.24	3.25	-4.40	2.00	-8.51
32000			5.60	-5.86	4.25	-1.16	2.60	-7.80
36000			8.17	0.27	5.50	-1.44	3.29	-7.00
40000					7.40	8.82	4.22	-3.00
44000							5.50	0.60
48000							7.25	4.10
52000							9.50	-1.32

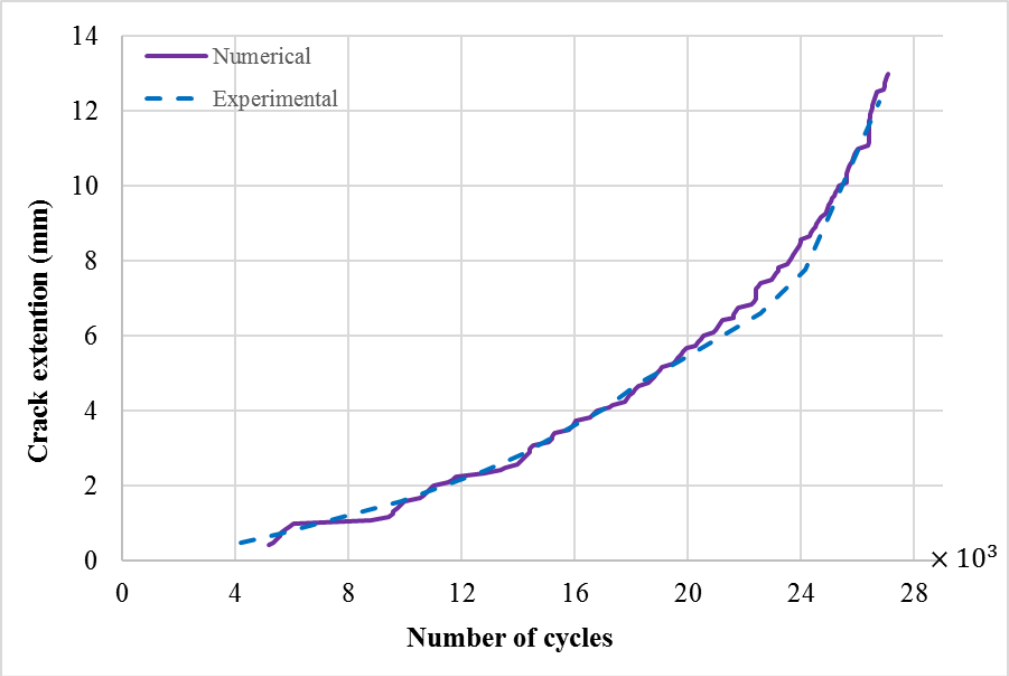

Fig. 7.16. Crack length as function of loading cycles at $R = 0,\ f = 0.05Hz$ & $\Delta N = 800$.

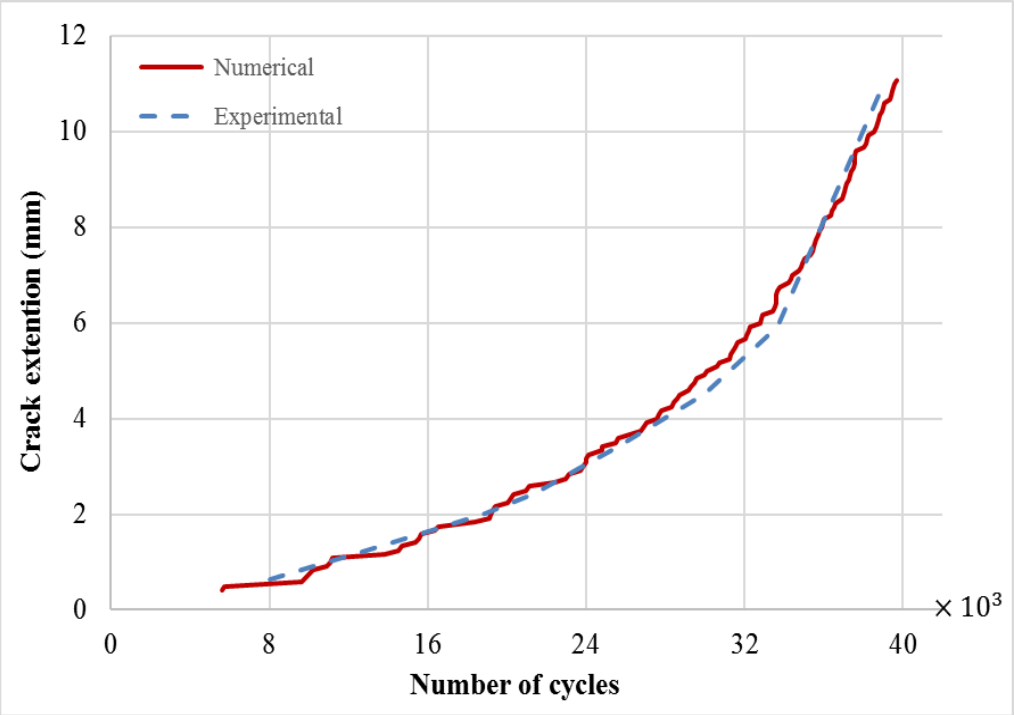

Fig. 7.17. Crack length as function of loading cycles at $R = 0,\ f = 0.1Hz$ & $\Delta N = 800$.

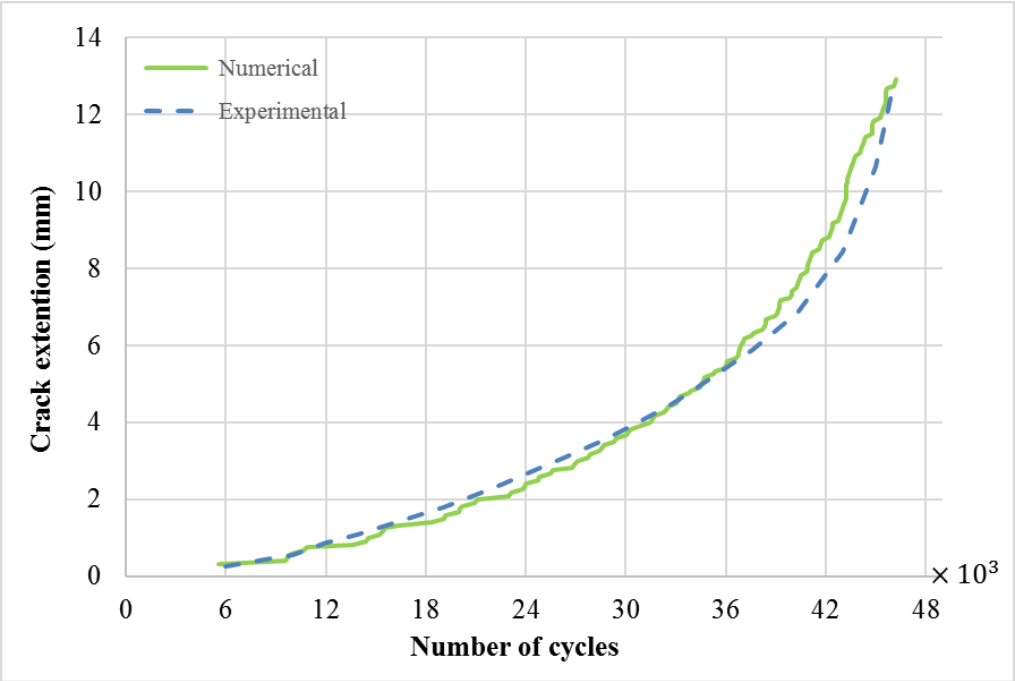

Fig. 7.18. Crack length as function of loading cycles at $R = 0,\ f = 0.5Hz$ & $\Delta N = 800$.

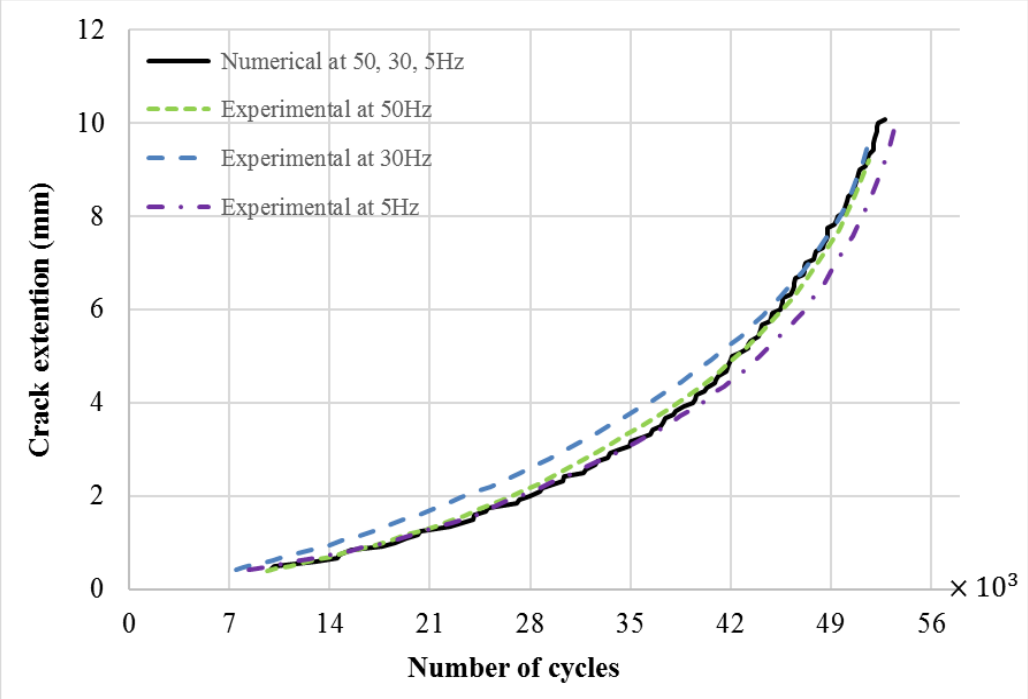

Fig. 7.19. Crack length as function of loading cycles at $R = 0,\ f = 50, 30, and\ 5Hz$ & $\Delta N = 800$.

7.5 Summary

Based on the finding of this study the following can be concluded:

- A new frequency-dependent trapezoidal cohesive-zone model with fast-track facility for fatigue that can be used for low and high-cycle fatigue simulation has been developed.
- The new rate-dependent CZM has been implemented in the finite element solver ABAQUS (via a bespoke UMAT subroutine) and has been tested at different applied frequencies (0.05, 0.1, 0.5, 5, 30, and 50 Hz).
- The rate-dependent critical stress is increasing with the loading frequency up to 5 Hz and turn to be nearly constant at frequencies higher than 5 Hz.
- The new frequency-dependent CZM model has been shown to give an acceptable prediction with a significant reduction in the computational time of the order of ΔN^{-1}.

Chapter 8: Conclusions and future work

The main aim of this PhD thesis is to improve the cohesive-zone model for both fatigue and fracture modelling. Searching the academic literature revealed that the effect of strain rate on fatigue and fracture is not fully covered by the cohesive-zone modelling approach. The process of developing the frequency-dependent TCZM can be divided into Three steps.

8.1 Monotonic rate-dependent model

First, because the modelling of monotonic fracture tends to be relatively easier than fatigue, the initial focus of the research was on the development of a monotonic rate-dependent CZM along with testing the implantation of such a model in the finite element solver ABAQUS. The development of the rate-dependent model was achieved by means of an analysis of different combinations of springs, dashpots, sliders, and cohesive elements in an one-dimensional model. The existing rate-dependent methodologies in the literature were discussed and tested, which led to a new model that overcame their limitations. From the findings of the investigation in Chapter 5 the following conclusions can be drawn:

1- Conclusions:

- The ABAQUS finite element solver has shwon itself to be an ideal vehicle for all the numerical analysis, and all the new models have been implemented in the solver through a user material UMAT subroutine.
- The choice of the TSL should be made according to the material under consideration. In this regards, it has been found that the TCZM adequately captures elasto-plastic material behaviour.
- Existing rate-dependent methodologies currently employed for dynamic fracture analysis have been demonstrated to suffer unrealistic behaviour such as unbounded critical stress and separation.
- A new rate-dependent TCZM, which overcomes the limitation of the previous models, has been trialled. A feature of this model is a bounded rate-dependent critical stress and control of the increase in fracture energy as a consequence of strain-rate.

2- Future works recommendations:

- The rate-dependent CZM is presently limited to Mode I and 2D fracture analysis, so it would be beneficial to develop the model to be applicable for mixed mode and 3D fracture analysis.
- An experimental investigation of the fracture energy limit and its relationship to the limiting value of the critical stress is necessary.
- A comprehensive experimental study of the strain-rate effect on crack growth is required to further validate the new model.

8.2 A computationally efficient cohesive-zone model for fatigue

The second step of the research involved the development of a new CZM for fatigue that overcame the cost associated with the loading-unloading hysteresis model. A feature of the new model is a damage mechanism that combines cyclic plasticity with material deterioration. Although the accumulation of the damage is based on the concept of loading-unloading hysteresis, the model has the benefit of incorporating a fast-track feature. The observation that fatigue cracks tend to grow extremely slowly with a near invariant cyclic response raised the possibility of applying a linear growth rule to approximate cyclic damage. This approximation involves "freezing in" the damage state for one loading cycle over a predefined load envelope of ΔN cycles. From testing the new fatigue model presented in Chapter 6, the following conclusions can be outlined:

1- Conclusions:

- A feature of the new fatigue model is that it can be directly applied for high and low-cycle fatigue analysis.
- The predicted crack growth by the new model is affected by the value of the damage update parameter N_u, however a good agreement with the experimental results can be achieved if N_u is set so that the cyclic damage is allowed to be adequately updated.
- The application of the fast-track feature has been proven to return satisfactory results with a significant reduction in the computational cost in the order of ΔN^{-1}.

2- Future works recommendations:

- An experimental fatigue investigation at different loading conditions and different specimen type is required to standardise the cohesive parameters $\{\sigma_c,\ \delta_c,\ \delta_1,\ \delta_2,\ C\}$ of the new model.
- Investigate the sensitivity of the model to the loading ratio R.
- Extended the model to 3D analysis and different loading conditions.

8.3 Frequency-dependent CZM for fatigue

The third step in the research was the combining of the new cohesive-zone model with a rate mechanism to capture the frequency effect associated with fatigue for some materials. In order to test and validate the new model an experimental fatigue test at different frequencies was performed on austenitic stainless-steel 304. The test results confirmed that crack growth in this material is sensitive to the loading frequency with the crack growing faster at a lower frequency. However, this sensitivity to the loading frequency dissappeared above a frequency of 5Hz. The new frequency-dependent model was used to simulate the fatigue tests, and the following conclusions can be outlined from the investigation presented in in Chapter 7:

1- Conclusions:

- The new frequency-dependent TCZM can be applied for high and low-cycle fatigue.
- The new frequency-dependent CZM has been implemented in ABAQUS by means of a UMAT subroutine and has proven to give satisfactory results when tested at different loading frequencies, i.e. {0.05, 0.1, 5, 30, and 50 Hz}.
- With increasing loading frequency, the frequency-dependent cohesive stress $\sigma_{(f)}^{C_{rate}}$ increases. This behaviour is noticeable up to a frequency of 5 Hz and then is nearly constant at higher frequencies.
- A comparison of the predicted results with the experimental ones shows that the new frequency-dependent TCZM gives a satisfactory prediction with a reduction in CPU-time of the order of ΔN^{-1}.
- The mesh sensitivity analysis shows that the number of elements occupying the cohesive-zone has a minor effect on the predicted crack growth rate even though it influences the crack tip stress field.

2- Future works recommendations:

- It is required to perform further experimentation on different specimen shapes and boundary condition to standardise the model parameters $\{a,\ b,\ d,\ n\}$.
- Since the austenitic-martensitic phase transformation depends on the strain level, it is required to investigate the frequency effect at different loading levels and different loading ratios R and validate the model with these results.
- Extend the model for application to mixed-mode and 3D fatigue analysis.

References

[1] B. Farahmand, *Virtual Testing and Predictive Modeling*. Springer Science+Business Media, 2009.

[2] J. Schijve, *Fatigue of structures and materials*. Dordrecht: Kluwer Academic Publishers, 2001.

[3] G. R. Irwin, "Analysis of Stresses and Strains near the End of a Crack Traversing a Plate," *J. Appl. Mech. ASME*, vol. E24, pp. 351–369, 1957.

[4] P. C. Paris, M. P. Gomez and W. E. Anderson, "A rational analytic theory of fatigue," *Trend Eng.*, vol. 13, pp. 9–14, 1961.

[5] J. Rice, "A path independent integral and the approximate analysis of strain concentration by notches and cracks," *J. Appl. Mech.*, vol. 35, no. 2, pp. 379–386, 1968.

[6] I. Scheider, "Cohesive model for crack propagation analyses of structures with elastic–plastic material behavior foundations and implementation," *GKSS Res. center, Geesthacht*, 2001.

[7] D. Dugdale, "Yielding of steel sheets containing slits," *J. Mech. Phys. Solids*, vol. 8, no. 2, pp. 100–104, 1960.

[8] G. I. Barenblatt, "The mathematical theory of equilibrium cracks in brittle fracture," *Adv. Appl. Mech.*, vol. 7, no. 1, pp. 55–129, 1962.

[9] A. Hillerborg, M. Modéer and P. Petersson, "Analysis of crack formation and crack growth in concrete by means of fracture mechanics and finite elements," *Cem. Concr. Res.*, vol. 6, pp. 773–782, 1976.

[10] K. Schwalbe, I. Scheider and A. Cornec, *Guidelines for Applying Cohesive Models to the Damage Behaviour of Engineering Materials and Structures*. Berlin, Heidelberg: Springer Berlin Heidelberg, 2013.

[11] A. Needleman, "An analysis of decohesion along an imperfect interface," *Int. J. Fract.*, vol. 42, no. 1, pp. 21–40, 1990.

[12] T. Siegmund and A. Needleman, "A numerical study of dynamic crack growth in

elastic-viscoplastic solids," *Int. J. Solids Struct.*, vol. 34, no. 7, pp. 769–787, Mar. 1997.

[13] V. Tvergaard and J. W. Hutchinson, "The relation between crack growth resistance and fracture process parameters in elastic-plastic solids," *J. Mech. Phys. Solids*, vol. 40, no. 6, pp. 1377–1397, Aug. 1992.

[14] M. L. Falk, A. Needleman and J. R. Rice, "A critical evaluation of cohesive zone model of dynamic fracture," in *Proceedings of the 5th, Journal de Physique IV, Proceedings 11(Pr.5)*, 2001, pp. 43–50.

[15] X. Zhang, Y.-W. Mai and R. G. Jeffrey, "A cohesive plastic and damage zone model for dynamic crack growth in rate-dependent materials," *Int. J. Solids Struct.*, vol. 40, no. 21, pp. 5819–5837, Oct. 2003.

[16] G. Alfano, S. De Barros, L. Champaney and N. Valoroso, "Comparison Between Two Cohesive-Zone Models for the Analysis of Interface Debonding," *Eur. Congr. Comput. Methods Appl. Sci. Eng.*, pp. 1–18, 2004.

[17] N. Valoroso, G. Debruyne and J. Laverne, "A cohesive zone model with rate-sensitivity for fast crack propagation," *Mech. Res. Commun.*, vol. 58, pp. 8–13, Jan. 2014.

[18] K. Ravi-Chandar, "Dynamic fracture of nominally brittle materials," *Int. J. Fract.*, vol. 90, no. 1901, pp. 83–102, 1998.

[19] F. Zhou, J.-F. Molinari and Y. Li, "Three-dimensional numerical simulations of dynamic fracture in silicon carbide reinforced aluminum," *Eng. Fract. Mech.*, vol. 71, no. 9–10, pp. 1357–1378, Jun. 2004.

[20] G. Camacho and M. Ortiz, "Computational modelling of impact damage in brittle materials," *Int. J. Solids Struct.*, vol. 33, no. 20–22, pp. 2899–2938, 1996.

[21] D. Kubair, P. Geubelle and Y. Huang, "Analysis of a rate-dependent cohesive model for dynamic crack propagation," *Eng. Fract. Mech.*, vol. 70, no. 5, pp. 685–704, 2002.

[22] F. Zhou, J.-F. Molinari and T. Shioya, "A rate-dependent cohesive model for simulating dynamic crack propagation in brittle materials," *Eng. Fract. Mech.*, vol. 72, no. 9, pp. 1383–1410, Jun. 2005.

[23] S. H. Song, G. H. Paulino and W. G. Buttlar, "A bilinear cohesive zone model tailored for fracture of asphalt concrete considering viscoelastic bulk material," *Eng. Fract. Mech.*, vol. 73, no. 18, pp. 2829–2848, Dec. 2006.

[24] F. Costanzo and J. Walton, "Numerical simulations of a dynamically propagating crack with a nonlinear cohesive zone," *Int. J. Fract.*, vol. 91, no. 4, pp. 373–389, 1998.

[25] F. Costanzo and J. R. Walton, "A study of dynamic crack growth in elastic materials using a cohesive zone model," *Int. J. Eng. Sci.*, vol. 35, no. 12–13, pp. 1085–1114, Sep. 1997.

[26] J. S. Langer and A. E. Lobkovsky, "Critical examination of cohesive-zone models in the theory of dynamic fracture," *J. Mech. Phys. Solids*, vol. 46, no. 9, pp. 1521–1556, Sep. 1998.

[27] E. Glennie, "A strain-rate dependent crack model," *J. Mech. Phys. Solids*, vol. 19, no. 5, pp. 255–272, 1971.

[28] A. Ural, V. R. Krishnan and K. D. Papoulia, "A cohesive zone model for fatigue crack growth allowing for crack retardation," *Int. J. Solids Struct.*, vol. 46, no. 11–12, pp. 2453–2462, Jun. 2009.

[29] P. Beaurepaire and G. I. Schuëller, "Modeling of the variability of fatigue crack growth using cohesive zone elements.," *Eng. Fract. Mech.*, vol. 78, no. 12, pp. 2399–2413, Aug. 2011.

[30] M. Elices, G. V. Guinea, J. Gómez and J. Planas, "The cohesive zone model: advantages, limitations and challenges," *Eng. Fract. Mech.*, vol. 69, no. 2, pp. 137–163, Jan. 2002.

[31] O. Nguyen and E. Repetto, "A cohesive model of fatigue crack growth," *Int. J. Fract.*, vol. 110, pp. 351–369, 2001.

[32] C. J. Gilbert, R. H. Dauskardt and R. O. Ritchie, "Microstructural mechanisms of cyclic fatigue-crack propagation in grain-bridging ceramics," *Ceram. Int.*, vol. 23, no. 5, pp. 413–418, 1997.

[33] O. E. Wheeler, "Spectrum loading and crack growth," *J. basic Eng.*, vol. 94, no. 1, pp. 181–186, 1972.

[34] D. C. Drucker and L. Palgen, “On stress-strain relations suitable for cyclic and other loading,” *J. Appl. Mech.*, vol. 48, no. 3, pp. 479–485, 1981.

[35] A. Needleman, “A continuum model for void nucleation by inclusion debonding,” *J. Appl. Mech.*, vol. 54, no. 3, pp. 525–531, 1987.

[36] R. G. Forman, V. E. Kearney and R. M. Engle, “Numerical analysis of crack propagation in cyclic-loaded structures,” *J. basic Eng.*, vol. 89, no. 3, pp. 459–463, 1967.

[37] H. A. Willenborg, J., Engle, R.M., Wood, “A crack growth retardation model using an effective stress concept,” *Organization*, no. January 1971, 1971.

[38] G. Xu, A. S. Argon and M. Ortiz, “Nucleation of dislocations from crack tips under mixed modes of loading: Implications for brittle against ductile behaviour of crystals,” *Philos. Mag. A Phys. Condens. Matter, Struct. Defects Mech. Prop.*, vol. 72, no. 2, pp. 415–451, 1995.

[39] J. Rice, “Mathematical analysis in the mechanics of fracture,” in *Fracture: an advanced treatise*, vol. 2, H. Liebowitz, Ed. Academic Press, 1968, pp. 191–311.

[40] D. Carka and C. M. Landis, “On the Path-Dependence of the J-Integral Near a Stationary Crack in an Elastic-Plastic Material,” *J. Appl. Mech.*, vol. 78, no. 1, 2011.

[41] F. Riemelmoser and R. Pippan, “The J-integral at Dugdale cracks perpendicular to interfaces of materials with dissimilar yield stresses,” *Int. J. Fract.*, vol. 103, no. 4, pp. 397–418, 2000.

[42] J. W. Hutchinson, “Singular behaviour at the end of a tensile crack in a hardening material,” *J. Mech. Phys. Solids*, vol. 16, no. 1, pp. 13–31, 1968.

[43] J. R. Rice and G. F. Rosengren, “Plane strain deformation near a crack tip in a power-law hardening material,” *J. Mech. Phys. Solids*, vol. 16, no. 1, pp. 1–12, 1968.

[44] M. Kikuchi, “Analysis of HRR fields of surface cracks,” *Int. J. Fract.*, vol. 58, no. 3, pp. 273–283, 1992.

[45] N. Perez, *Fracture Mechanics*. Boston: Kluwer Academic Publishers, 2004.

[46] S. Marie and S. Chapuliot, "Ductile tearing simulation based on a local energetic criterion," *Fatigue Fract. Eng. Mater. Struct.*, vol. 21, pp. 215–227, 1998.

[47] C. E. Turner, "A reassesment of ductile tearing resistance (Part I) In Fracture behavior of materials and structures," in *ECF 8 Fracture behavior of materials and structures*, 1990, vol. 8, pp. 933–949.

[48] S. Dhar, S. Marie and S. Chapuliot, "Determination of critical fracture energy, Gfr, from crack tip stretch," *Int. J. Press. Vessel. Pip.*, vol. 85, no. 5, pp. 313–321, May 2008.

[49] S. Marie and S. Chapuliot, "2D crack growth simulation with an energetic approach," *Nucl. Eng. Des.*, vol. 212, no. 1–3, pp. 31–40, Mar. 2002.

[50] C. E. Turner, "A reassesment of ductile tearing resistance (Part II) In Fracture behavior of materials and structures," in *ECF 8 Fracture behavior of materials and structures*, 1990, pp. 951–968.

[51] S. Marie and S. Chapuliot, "Ductile crack growth simulation from near crack tip dissipated energy," *Nucl. Eng. Des.*, vol. 196, no. 3, pp. 293–305, Apr. 2000.

[52] N. Klingbeil, "A total dissipated energy theory of fatigue crack growth in ductile solids," *Int. J. Fatigue*, vol. 25, no. 2, pp. 117–128, Feb. 2003.

[53] J. Daily and N. Klingbeil, "Plastic dissipation in fatigue crack growth under mixed-mode loading," *Int. J. Fatigue*, vol. 26, no. 7, pp. 727–738, Jul. 2004.

[54] J. Daily and N. Klingbeil, "Plastic dissipation in mixed-mode fatigue crack growth along plastically mismatched interfaces," *Int. J. Fatigue*, vol. 28, no. 12, pp. 1725–1738, Dec. 2006.

[55] D. Cojocaru and A. M. Karlsson, "Assessing plastically dissipated energy as a condition for fatigue crack growth," *Int. J. Fatigue*, vol. 31, no. 7, pp. 1154–1162, Jul. 2009.

[56] I. Scheider, M. Schödel, W. Brocks and W. Schönfeld, "Crack propagation analyses with CTOA and cohesive model: Comparison and experimental validation," *Eng. Fract. Mech.*, vol. 73, no. 2, pp. 252–263, Jan. 2006.

[57] A. Needleman, "A continuum model for void nucleation by inclusion debonding,"

J. Appl. Mech., vol. 54, no. September, pp. 525–531, 1987.

[58] A. Needleman, "An analysis of tensile decohesion along an interface," *J. Mech. Phys. Solids*, vol. 38, no. 3, pp. 289–324, Jan. 1990.

[59] V. Tvergaard and J. Hutchinson, "Effect of strain dependent cohesive zone model on predictions of interface crack growth," *Int. J. Solids Struct.*, vol. 33, no. 2, pp. 3297–3308, 1996.

[60] A. Turon, C. G. Dávila, P. P. Camanho and J. Costa, "An engineering solution for mesh size effects in the simulation of delamination using cohesive zone models," *Eng. Fract. Mech.*, vol. 74, no. 10, pp. 1665–1682, Jul. 2007.

[61] M. Ortiz and A. Pandolfi, "Finite-deformation irreversible cohesive elements for three-dimensional crack-propagation analysis," *Int. J. Numer. Methods Eng.*, vol. 44, pp. 1267–1282, 1999.

[62] L. B. Freund and Y. J. Lee, "Observations on high strain rate crack growth based on a strip yield model," *Int. J. Fract.*, vol. 42, no. 3, pp. 261–276, Mar. 1990.

[63] D. B. Xu, C. Y. Hui, E. J. Kramer and C. Creton, "A micromechanical model of crack growth along polymer interfaces," *Mech. Mater.*, vol. 11, no. 3, pp. 257–268, May 1991.

[64] S. Marzi and O. Hesebeck, "A rate-dependent, elasto-plastic cohesive zone mixed-mode model for crash analysis of adhesively bonded joints," in *7th European LS-DYNA Cpmferemce*, 2009.

[65] S. Marzi, O. Hesebeck, M. Brede and F. Kleiner, "A Rate-Dependent Cohesive Zone Model for Adhesively Bonded Joints Loaded in Mode I," *J. Adhes. Sci. Technol.*, vol. 23, no. 6, pp. 881–898, Jan. 2009.

[66] S. Marzi, O. Hesebeck, M. Brede and F. Kleiner, "An End-Loaded Shear Joint (ELSJ) Specimen to Measure the Critical Energy Release Rate in Mode II of Tough, Structural Adhesive Joints," *J. Adhes. Sci. Technol.*, vol. 23, no. 15, pp. 1883–1891, Jan. 2009.

[67] C. Xu, T. Siegmund and K. Ramani, "Rate-dependent crack growth in adhesives II. Experiments and analysis," *Int. J. Adhes. Adhes.*, vol. 23, no. 1, pp. 15–22, Jan. 2003.

[68] P. Robinson, U. Galvanetto, D. Tumino, G. Bellucci and D. Violeau, "Numerical simulation of fatigue-driven delamination using interface elements," *Int. J. Numer. Methods Eng.*, vol. 63, no. 13, pp. 1824–1848, 2005.

[69] D. Tumino and F. Cappello, "Simulation of Fatigue Delamination Growth in Composites with Different Mode Mixtures," *J. Compos. Mater.*, vol. 41, no. 20, pp. 2415–2441, 2007.

[70] A. Turon, J. Costa, P. Camanho and J. Mayugo, "Simulation of delamination propagation in composites under high-cycle fatigue by means of cohesive zone models," *NASA Tech. Rep.*, 2006.

[71] A. Turon, J. Costa, P. P. Camanho and C. G. Dávila, "Simulation of delamination in composites under high-cycle fatigue," *Compos. Part A Appl. Sci. Manuf.*, vol. 38, no. 11, pp. 2270–2282, 2007.

[72] A. Pirondi and F. Moroni, "A Progressive Damage Model for the Prediction of Fatigue Crack Growth in Bonded Joints," *J. Adhes.*, vol. 86, no. 5–6, pp. 501–521, 2010.

[73] P. W. Harper and S. R. Hallett, "A fatigue degradation law for cohesive interface elements - Development and application to composite materials," *Int. J. Fatigue*, vol. 32, no. 11, pp. 1774–1787, 2010.

[74] A. Pirondi and F. Moroni, "Simulation of Mixed-Mode I/II Fatigue Crack Propagation in Adhesive Joints with a Modified Cohesive Zone Model," *J. Adhes. Sci. Technol.*, vol. 25, no. 18, pp. 2483–2499, 2011.

[75] B. L. V. Bak, A. Turon, E. Lindgaard and E. Lund, "A Benchmark Study of Simulation Methods for High-Cycle Fatigue-Driven Delamination Based on Cohesive Zone Models," *Compos. Struct.*, 2016.

[76] B. L. V. Bak, C. Sarrado A. Turon and J. Costa, "Delamination Under Fatigue Loads in Composite Laminates: A Review on the Observed Phenomenology and Computational Methods," *Appl. Mech. Rev.*, vol. 66, no. 6, 2014.

[77] A. De-Andrés, J. Pérez and M. Ortiz, "Elastoplastic finite element analysis of three-dimensional fatigue crack growth in aluminum shafts subjected to axial loading," *Int. J. Solids Struct.*, vol. 36, no. 15, pp. 2231–2258, 1999.

[78] B. Yang, S. Mall and K. Ravi-Chandar, "A cohesive zone model for fatigue crack growth in quasibrittle materials," *Int. J. Solids Struct.*, vol. 38, no. 22–23, pp. 3927–3944, May 2001.

[79] K. L. Roe and T. Siegmund, "An irreversible cohesive zone model for interface fatigue crack growth simulation," *Eng. Fract. Mech.*, vol. 70, no. 2, pp. 209–232, Jan. 2003.

[80] P. Towashiraporn, G. Subbarayan and C. S. Desai, "A hybrid model for computationally efficient fatigue fracture simulations at microelectronic assembly interfaces," *Int. J. Solids Struct.*, vol. 42, no. 15, pp. 4468–4483, 2005.

[81] P. S. Koutsourelakis, K. Kuntiyawichai and G. I. Schuëller, "Effect of material uncertainties on fatigue life calculations of aircraft fuselages: A cohesive element model," *Eng. Fract. Mech.*, vol. 73, no. 9, pp. 1202–1219, 2006.

[82] S. Ganesh Sundara Ranan and K. A. Padmanabhan, "A comparison of the room-temperature behaviour of AISI 304LN stainless steel and Nimonic 90 under strain cycling," *Int. J. Fatigue*, vol. 17, no. 4, pp. 271–277, May 1995.

[83] D. Ye, S. Matsuoka, N. Nagashima and N. Suzuki, "The low-cycle fatigue, deformation and final fracture behaviour of an austenitic stainless steel," *Mater. Sci. Eng. A*, vol. 415, no. 1–2, pp. 104–117, 2006.

[84] G. Baudry and A. Pineau, "Influence of strain-induced martensitic transformation on the low-cycle fatigue behavior of a stainless steel," *Mater. Sci. Eng.*, vol. 28, no. 2, pp. 229–242, 1977.

[85] J. Colin, A. Fatemi and S. Taheri, "Fatigue Behavior of Stainless Steel 304L Including Strain Hardening, Prestraining, and Mean Stress Effects," *J. Eng. Mater. Technol.*, vol. 132, no. 2, 2010.

[86] A. A. Lebedev and V. V. Kosarchuk, "Influence of phase transformations on the mechanical properties of austenitic stainless steels," *Int. J. Plast.*, vol. 16, no. 7–8, pp. 749–767, 2000.

[87] C. Müller-Bollenhagen, M. Zimmermann, and H.-J. Christ, "Very high cycle fatigue behaviour of austenitic stainless steel and the effect of strain-induced martensite," *Int. J. Fatigue*, vol. 32, no. 6, pp. 936–942, 2010.

[88] D. Kalkhof, M. Niffenegger and H. J. Leber, "Monitoring of Fatigue Degradation in Austenitic Stainless Steels," *Fatigue Fract. Eng. Mater. Struct.*, vol. 27, no. 7, pp. 595–607, 2004.

[89] L. A. James, "The effect of frequency upon the fatigue-crack growth of Type 304 stainless steel at 1000° F," in *Stress Analysis and Growth of Cracks: Proceedings of the 1971 National Symposium on Fracture Mechanics: Part 1*, 1972, pp. 218–229.

[90] I. Nikitin and M. Besel, "Effect of low-frequency on fatigue behaviour of austenitic steel AISI 304 at room temperature and 25°C," *Int. J. Fatigue*, vol. 30, no. 10–11, pp. 2044–2049, 2008.

[91] E. Gdoutos, *Fracture mechanics: an introduction*, Second Edi. Netherlands: Springer, 2006.

[92] G. E. Dieter and D. Bacon, *Mechanical Metallurgy*, SI Metric. London: McGraw Hill Book Company, 1988.

[93] P. Larour, "Strain rate sensitivity of automotive sheet steels: influence of plastic strain, strain rate, temperature, microstructure, bake hardening and pre-strain," 2010.

[94] E. Cadoni, L. Fenu and D. Forni, "Strain rate behaviour in tension of austenitic stainless steel used for reinforcing bars," *Constr. Build. Mater.*, vol. 35, pp. 399–407, 2012.

[95] S. Mandal, V. Rakesh, P. V. Sivaprasad, S. Venugopal and K. V. Kasiviswanathan, "Constitutive equations to predict high temperature flow stress in a Ti-modified austenitic stainless steel," *Mater. Sci. Eng. A*, vol. 500, no. 1–2, pp. 114–121, 2009.

[96] A. Rusinek, J. A. Rodríguez-Martínez and A. Arias, "A thermo-viscoplastic constitutive model for FCC metals with application to OFHC copper," *Int. J. Mech. Sci.*, vol. 52, no. 2, pp. 120–135, 2010.

[97] H. Zhao, "A constitutive model for metals over a large range of strain rates - Identification for mild-steel and aluminium sheets," *Mater. Sci. Eng. A*, vol. 230, no. 1–2, pp. 95–99, 1997.

[98] G. R. Cowper and P. S. Symonds, "Strain hardening and strain-rate effects in the

impact loading of cantiliver beams," 1957.

[99] G. R. Johnson and W. H. Cook, "A constitutive model and data for metals subjected to large strains, high strain rates and high temperatures," in *Proceedings of the 7th International Symposium on Ballistics, volume 21*, 1957, pp. 541–547.

[100] F. J. Zerilli, R. W. Armstrong, F. J. Zerilli and R. W. Armstrong, "Constitutive relations for the plastic deformation of metals Effect of Strain Rate Upon Plastic Flow of Steel," vol. 989, no. 1994, 1996.

[101] F. J. Zerilli and R. W. Armstrong, "Dislocation-mechanics-based constitutive relations for materials dynamics calculations," *J. Appl. Phys.*, vol. 61, no. 5, pp. 1816–1826, 1987.

[102] A. M. Lennon and K. T. Ramesh, "The influence of crystal structure on the dynamic behavior of materials at high temperatures," *Int. J. Plast.*, vol. 20, no. 2, pp. 269–290, 2004.

[103] A. Rusinek, R. Zaera and J. R. Klepaczko, "Constitutive relations in 3-D for a wide range of strain rates and temperatures - Application to mild steels," *Int. J. Solids Struct.*, vol. 44, no. 17, pp. 5611–5634, 2007.

[104] J. Kim, E. Yim, C. Jeon, C. Jung and B. Han, "Cold performance of various biodiesel fuel blends at low temperature," *Int. J. Auto. Tech.*, vol. 13, no. 2, pp. 293–300, 2012.

[105] W. E. Luecke, T. A. Siewert and F. W. Gayle, "Contemporaneous structural steel specifications," *Nist Ncstar*, 2005.

[106] H. Dahlan, "A Fast-Track Method for Fatigue Crack Growth Prediction with a Cohesive Zone Model," University of Manchester, PhD 2013.

[107] Y.-L. Lee, J. Pan, R. B. Hathaway and M. E. Barkey, *Fatigue Testing and Analysis*. US: Elsevier Butterworth-Heinemann, 2005.

[108] ASTM, "Standard Test Method for Measurement of Fatigue Crack Growth Rates 1," no. July, 2005.

[109] ABAQUS, *ABAQUS 6.13 User Guide*. USA: Dassault Systèmes Simulia Corp, 2013.

[110] B. L. V Bak, E. Lindgaard, E. Lund and A. Turon, "Performance of cohesive zone models for fatigue driven delaminations," in *11th World Congress on Computational Mechanics*, 2014, pp. 1–2.

[111] S. Salih, K. Davey and Z. Zou, "Rate-dependent elastic and elasto-plastic cohesive zone models for dynamic crack propagation," *Int. J. Solids Struct.*, vol. 90, pp. 95–115, 2016.

[112] D. Gross and T. Seelig, *Fracture mechanics: with an introduction to micromechanics*. Netherlands: Springer Science+Business Media, 2011.

[113] K. Liu, Z. Wang, W. Tang, Y. Zhang and G. Wang, "Experimental and numerical analysis of laterally impacted stiffened plates considering the effect of strain rate," *Ocean Eng.*, vol. 99, pp. 44–54, 2015.

Appendices

Appendix A: Publications

- **Journal paper**

Published

[1] S. Salih, K. Davey and Z. Zou, "Rate-dependent elastic and elasto-plastic cohesive zone models for dynamic crack propagation," *Int. J. Solids Struct.*, vol. 90, pp. 95–115, 2016.

Submitted

[2] S. Salih, K. Davey, and Z. Zou, "A computationally efficient cohesive-zone model for fatigue," *Fatigue Fract. Eng. Mater. Struct.*, submitted in February 2018

[3] S. Salih, K. Davey, and Z. Zou, "Frequency-Dependent Cohesive-Zone Model for Fatigue," International Journal of Solids and *Structures*, submitted in August 2017

- **Conference papers**

[4] S. Salih, K. Davey, and Z. Zou, "Frequency-Dependent Cohesive-Zone Model for Fatigue," *6th International Conference on Fracture Fatigue and Wear*, 26-27 July 2017, University of Porto, Porto, Portugal

[5] S. Salih, K. Davey, and Z. Zou, "Frequency Dependence of Fatigue Crack Growth in 304 Stainless-Steel," *MACE PGR Conference 2017*, 3rd April 2017, University of Manchester, Mancheser, UK

Appendix B: UMAT subroutines

B-1 New rate-dependent TCZM for fracture

```
C**********************************************************************
C     UMAT FOR THE NEW RATE-DEPENDENT COHESIVE MODEL
C     CAN BE USED FOR MODE ONE ONLY
C     WRITEN BY SARMED A. SALIH
C======================================================================
C  HEADER OF THE SUBROUTINE
C
      SUBROUTINE UMAT(STRESS,STATEV,DDSDDE,SSE,SPD,SCD,
     1 RPL,DDSDDT,DRPLDE,DRPLDT,
     2 STRAN,DSTRAN,TIME,DTIME,TEMP,DTEMP,PREDEF,DPRED,CMNAME,
     3 NDI,NSHR,NTENS,NSTATV,PROPS,NPROPS,COORDS,DROT,PNEWDT,
     4 CELENT,DFGRD0,DFGRD1,NOEL,NPT,LAYER,KSPT,KSTEP,KINC)
C
      INCLUDE 'ABA_PARAM.INC'
C
      CHARACTER*80 CMNAME
C
      DIMENSION STRESS(NTENS),STATEV(NSTATV),
     1 DDSDDE(NTENS,NTENS),DDSDDT(NTENS),DRPLDE(NTENS),
     2 STRAN(NTENS),DSTRAN(NTENS),TIME(2),PREDEF(1),DPRED(1),
     3 PROPS(NPROPS),COORDS(3),DROT(3,3),DFGRD0(3,3),DFGRD1(3,3)
C======================================================================
C     THIS PART IS THE USER CODING TO DEFINE DDSDDE, STRESS, STATEV,
C     SSE, SPD, SCD AND,IF NECESSARY, RPL, DDSDDT, DRPLDE, DRPLDT,PNEWDT
C----------------------------------------------------------------------
      DIMENSION UPSTRAN(NTENS),UPDSTRAN(NTENS),STRANRAT(NTENS),
     1         CYCSTRAN(NTENS),UPCYCSTRAN(NTENS)
      PARAMETER(ZERO=0.D0, ONE=1.D0, TWO=2.D0, THREE=3.D0, FOUR=4.D0)
      REAL*8 Ecoh,S,Sc,Sf,dc,Scr,BETA1,BETA,d1,EG,K,Smax,dmax,de,X,XX
      INTEGER N,UNLOADING,FAILED
```

```
C
      IF (NDI.NE.1) THEN
        WRITE(7,*) 'THIS UMAT MAY ONLY BE USED WITH MODE ONE FRACTURE'
        CALL XIT
      END IF
C             ***************************************
C     PROPS(1)IS THE CRITICAL COHESIVE STRESS
C     PROPS(2)IS THE CRITICAL COHESIVE SEPARATION
C     PROPS(3)IS COHESIVE ELASTIC STEFNESS
C     PROPS(4)IS THE VALUE OF THE FIRST RATE-DEPENDETN PARAMETER
C     PROPS(5)IS THE VALUE OF THE SECOND RATE-DEPENDETN PARAMETER
C     PROPS(6)IS THE VALUE OF THE RATE-DEPENDENT CRITCAL STRESS LIMIT
C                       ******
C     STATEV(1)IS THE SEPARATION AT THE END OF THE LOADING CYCLE
C     STATEV(2)IS TEH STRESS AT THE END OF THE LOADING CYCLE
C     STATEV(3)IS A VARIABLE TO INDICATE THE FAILUR OF THE ELMENT
C     STATEV(4)IS A VARIABLE TO INDICATE THE ONSET OF UNLOADING IN THE
C           MONOTONIC LOADING CASE
C     STATEV(5)IS AN  INTERNAL CONTROL VARIABLE
C     STATEV(6)IS THE VALUE OF THE RATE-DEPENDENT CRITICAL STRESS
C     STATEV(7)IS THE VALUE OF THE RATE-DEPENDENT CRITICAL SEPARATION
C     STATEV(8)IS THE VALUE OF THE RATE-DEPENDENT CRITICAL ENERGY
C             ***************************************
C     DEFINING ELATIC CONSTANTS
      Sc=PROPS(1)
      dc=PROPS(2)
      Ecoh=PROPS(3)
      BETA=PROPS(4)
      BETA1=PROPS(5)
      Sy=PROPS(6)
      SLIMIT=FOUR*Sy
C
      IF(STATEV(6).EQ.ZERO)THEN
      Scr=Sc
```

```
      ELSE
      Scr=STATEV(6)
      ENDIF
C
      IF(STATEV(7).EQ.ZERO)THEN
      dcr=dc
      ELSE
      dcr=STATEV(7)
      ENDIF
      FAILED=STATEV(3)
      gamarate=STATEV(8)
      d1=Scr/Ecoh
C
      DO K1=1, NTENS
      UPSTRAN(K1)=STRAN(K1)+DSTRAN(K1)
C ================================================================
C               CASE ONE IF THERE IS NO UNLOADING
C ================================================================
1     IF(FAILED.EQ.ZERO)GOTO 3
      GOTO 170
C
C     CONDITION TO CHECK IF THE MODEL REACH THE SOFTING PART
C
3     IF ((K1.EQ.1).AND.(STATEV(4).EQ.ZERO).AND.(DSTRAN(K1).GT.ZERO).AND
     1 .(STRAN(K1).GE.ZERO).AND.(UPSTRAN(K1).GT.(0.15*(Sc/Ecoh))))GOTO 4
      GOTO 100
C
C     CALCULAT THE RATE DEPENDENT COHESIVE STRESS
C
4     UPTIME=TIME(1)+DTIME
      STRANRAT(K1)=UPSTRAN(K1)/UPTIME
      Srate=(ONE+BETA*STRANRAT(K1))*Sc
      IF(Srate.LE.SLIMIT)GOTO 5
      GOTO 6
```

```
5     gamarate=((0.875*Srate*dcr)-(0.5*Srate*d1))
      gama=((0.875*Sc*dc)-(0.5*Sc*Sc/Ecoh))
      Scr=Srate
      dcr=dc
      d1=Scr/Ecoh
      IF(gamarate.GE.(2.5*gama))THEN
      gamarate=(2.5*gama)
      Scr=(gamarate)/(0.875*dcr-0.5*d1)
      ENDIF
      STATEV(6)=Scr
      STATEV(7)=dcr
      GOTO 100
C
6     IF((Srate.GT.SLIMIT))GOTO 7
      GOTO 100
7     Scr=SLIMIT
      STATEV(6)=Scr
      d1=Scr/Ecoh
      dcr=(ONE+BETA1*STRANRAT(K1))*dc
      STATEV(7)=dcr
      gamarate=((0.875*SLIMIT*dcr)-(0.5*SLIMIT*d1))
      gama=((0.875*Sc*dc)-(0.5*Sc*Sc/Ecoh))
      IF(gamarate.GE.(2.5*gama))THEN
      gamarate=(2.5*gama)
      dcr=(gamarate+(0.5*d1*SLIMIT))/(0.875*SLIMIT)
      STATEV(7)=dcr
      ENDIF
      STATEV(8)=gamarate
C
100   d1=Scr/Ecoh
      d2=0.75*dcr
      S2=Ecoh*d2
C
      IF(STATEV(2).EQ.ZERO)THEN
```

```
      Smax=Scr
      ELSE
      Smax=STATEV(2)
      ENDIF
C
      IF(STATEV(1).EQ.ZERO)THEN
      dmax=d1
      ELSE
      dmax=STATEV(1)
      ENDIF
C
      K=Smax/dmax
      S=K*STRAN(K1)
      Sf=Ecoh*dcr
C              ****************************************
C                  THE CASE OF CYCLIC LOADING
C              ****************************************
C
105   IF((UPSTRAN(K1).LT.dmax).AND.(S.LE.Smax))GOTO 110
      GOTO 115
C     COMPUTE THE STIFFNESS MATRIX
110            DO K2=1, NTENS
                DDSDDE(K2, K1)=ZERO
              END DO
                DDSDDE(K1, K1)=K
C
C            UPDATE THE STRESS
C
              DO K2=1, NTENS
                 STRESS(K1)=STRESS(K1)+DDSDDE(K2,K1)*DSTRAN(K1)
              END DO
C
C            PRINT THE VALUE OF THE STRESS AND THE STRAN
      IF (K1.EQ.1)THEN
```

```
      STATEV(5)=ONE
      STATEV(9)=ONE
      STATEV(10)=ZERO
      WRITE(7,*) NOEL,'LOADING',stress(K1),UPSTRAN(K1),DSTRAN(K1),dcr
     1          ,Scr,Srate,SLIMIT,STRANRAT(K1),gamarate,gama,BETA,BETA1
        ENDIF
      GOTO 220
C     .AND.(S.GT.Scr)
115   IF((UPSTRAN(K1).GE.d1).AND.(UPSTRAN(K1).LE.d2).AND.(DSTRAN(K1)
     1   .GE.ZERO))GOTO 120
      GOTO 121
C
120       STRESS(K1)=Scr
C     COMPUTE THE STIFFNESS MATRIX
        DO K2=1, NTENS
        DDSDDE(K2, K1)=ZERO
        END DO
        DDSDDE(K1, K1)=ZERO
c
      IF (K1.EQ.1)THEN
      WRITE(7,*)  NOEL,'PLASTIC',stress(K1),UPSTRAN(K1),Scr,dcr,gamarate
     1                ,STRANRAT(K1),Srate
c      STATEV(1)=UPSTRAN(K1)
c      STATEV(2)=STRESS(K1)
      STATEV(5)=ZERO
      STATEV(9)=ZERO
      STATEV(10)=ONE
      STATEV(11)=UPSTRAN(K1)
      STATEV(12)=STRESS(K1)
      ENDIF
      GOTO 220
C
121   IF((UPSTRAN(K1).GT.d2).AND.(UPSTRAN(K1).LT.dcr).AND.(STATEV(10)
     1      .EQ.ONE).AND.(DSTRAN(K1).GE.ZERO)) GOTO 122
```

```
      GOTO 125
C
122       EG=(-Scr)/(dcr-d2)
C
C     COMPUTE THE STIFFNESS MATRIX
          DO K2=1, NTENS
          DDSDDE(K2, K1)=ZERO
          END DO
          DDSDDE(K1, K1)=EG
C     CONDITION FOR PENETRATION
C
C     UPDATE THE STRESS
          DO K2=1, NTENS
            STRESS(K1)=STRESS(K1)+DDSDDE(K2,K1)*DSTRAN(K1)
          END DO
          if(STRESS(K1).LT.ZERO)then
           STRESS(K1)=ZERO
          endif
C     PRINT THE VALUE OF THE STRESS AND THE STRAN
      IF (K1.EQ.1)THEN
C      STATEV(1)=UPSTRAN(K1)
C      STATEV(2)=STRESS(K1)
      STATEV(4)=ONE
      STATEV(5)=ZERO
      STATEV(9)=ZERO
      STATEV(11)=UPSTRAN(K1)
      STATEV(12)=STRESS(K1)
      WRITE(7,*) 'SOFTENING',stress(K1),UPSTRAN(K1),Scr,dcr,gamarate,
     1                STRANRAT(K1)
      ENDIF
      GOTO 220
C
c
125   IF(DSTRAN(K1).GT.ZERO)GOTO 130
```

```
      GOTO 190
130   IF((S.LE.Smax).AND.(UPSTRAN(K1).GT.dmax).AND.(dmax.GE.d2).AND.
     1   (DSTRAN(K1).GE.ZERO).AND.(STATEV(9).EQ.ONE))GOTO 140
      GOTO 150
C
140          STRESS(K1)=Smax
             UPDSTRAN(K1)=UPSTRAN(K1)- dmax
             EG=(-Smax)/(dcr-dmax)
C     COMPUTE THE STIFFNESS MATRIX
             DO K2=1, NTENS
             DDSDDE(K2, K1)=ZERO
             END DO
             DDSDDE(K1, K1)=EG
C     UPDATE THE STRESS
             DO K2=1, NTENS
               STRESS(K1)=STRESS(K1)+DDSDDE(K2,K1)*UPDSTRAN(K1)
             END DO
             if(STRESS(K1).LT.ONE)GOTO 142
             GOTO 143
142             STRESS(K1)=ZERO
             GOTO 220
C     PRINT THE VALUE OF THE STRESS AND THE STRAN
143   IF (K1.EQ.1)THEN
      STATEV(1)=UPSTRAN(K1)
      STATEV(2)=STRESS(K1)
      STATEV(4)=ONE
      STATEV(5)=ZERO
      STATEV(11)=UPSTRAN(K1)
      STATEV(12)=STRESS(K1)
      WRITE(7,*) NOEL,'SOFTENING1',stress(K1),UPSTRAN(K1),Smax,dmax,
     1          STRAN(K1),DSTRAN(K1),Scr,dcr
       ENDIF
      GOTO 220
C
```

```
150   IF((S.GT.Smax).AND.(UPSTRAN(K1).GT.dmax).AND.(UPSTRAN(K1).LE.dcr
     1  ).AND.(dmax.GT.d2).AND.(STATEV(9).EQ.ONE).AND.(DSTRAN(K1).GE.
     2  ZERO))GOTO 160
C
      GOTO 164
160   IF((K1.EQ.1).AND.(STRESS(K1).LT.Smax).AND.(STATEV(5).EQ.ONE))THEN
      STRESS(K1)=Smax
      UPDSTRAN(K1)=UPSTRAN(K1)- dmax
      ELSE
      UPDSTRAN(K1)=DSTRAN(K1)
      ENDIF
            EG=(-Smax)/(dcr-dmax)
C     COMPUTE THE STIFFNESS MATRIX
            DO K2=1, NTENS
            DDSDDE(K2, K1)=ZERO
            END DO
            DDSDDE(K1, K1)=EG
C     UPDATE THE STRESS
            DO K2=1, NTENS
              STRESS(K1)=STRESS(K1)+DDSDDE(K2,K1)*UPDSTRAN(K1)
            END DO
            IF(STRESS(K1).LT.ONE)GOTO 162
            GOTO 163
162               STRESS(K1)=ZERO
            GOTO 220
C     PRINT THE VALUE OF THE STRESS AND THE STRAN
163   IF (K1.EQ.1)THEN
      STATEV(1)=UPSTRAN(K1)
      STATEV(2)=STRESS(K1)
      STATEV(4)=ONE
      STATEV(5)=ZERO
      STATEV(11)=UPSTRAN(K1)
      STATEV(12)=STRESS(K1)
      WRITE(7,*) NOEL,'SOFTENING2',stress(K1),UPSTRAN(K1),Smax,dmax,
```

```
     1          STRAN(K1),DSTRAN(K1),Scr,dcr
      ENDIF
      GOTO 220
164   IF(((UPSTRAN(K1).GE.dcr)).AND.
     1   (DSTRAN(K1).GE.ZERO))GOTO 165
      GOTO 170
165            STRESS(K1)=ZERO
C     PRINT THE VALUE OF THE STRESS AND THE STRAN
        if (K1.EQ.1)THEN
         STATEV(3)= ONE
         WRITE(7,*) NOEL,'FAILED',stress(K1),UPSTRAN(K1),dcr,Scr,Srate
     1             ,STRANRAT(K1),BETA,BETA1
        ENDIF
      GOTO 220
C
C                       CONDITION FOR PENTRATION
C
================================================================
170   IF ((FAILED.EQ.ONE).AND.(STRAN(K1).GT.ZERO)) GOTO 180
      GOTO 190
180           STRESS(K1)=ZERO
        if (K1.EQ.1)THEN
         WRITE(7,*) NOEL,'FAILED1',stress(K1),UPSTRAN(K1),dcr
        ENDIF
      GOTO 220
190   IF ((FAILED.EQ.ONE).AND.(UPSTRAN(K1).LE.ZERO)) GOTO 200
      GOTO 220
C
200       DO K2=1, NTENS
         DDSDDE(K2, K1)=ZERO
         END DO
         DDSDDE(K1, K1)=Ecoh
C
C     UPDATE THE STRESS
```

```
C
      DO K2=1, NTENS
      STRESS(K1)=STRESS(K1)+DDSDDE(K2,K1)*DSTRAN(K1)
      END DO
C     PRINT THE VALUE OF THE STRESS AND THE STRAN
      IF (K1.EQ.1)THEN
      WRITE(7,*) NOEL,'COMPRESTION',stress(K1),UPSTRAN(K1),UPSTRAN
     1(K1),STRAN(K1),DSTRAN(K1),X,dmax,Smax
      ENDIF
220   END DO
C
     RETURN
     END
```

B-2 New TCZM with fast-track feature for fatigue

```
C**********************************************************************
C     UMAT FOR Fast-frack fagigue TCZM
C     CAN BE USED FOR cyclic load in MODE ONE ONLY
C     WRITEN BY SARMED A. SALIH
C ======================================================================
C     HEADER OF THE SUBROUTINE
C
      SUBROUTINE UMAT(STRESS,STATEV,DDSDDE,SSE,SPD,SCD,
     1 RPL,DDSDDT,DRPLDE,DRPLDT,
     2 STRAN,DSTRAN,TIME,DTIME,TEMP,DTEMP,PREDEF,DPRED,CMNAME,
     3 NDI,NSHR,NTENS,NSTATV,PROPS,NPROPS,COORDS,DROT,PNEWDT,
     4 CELENT,DFGRD0,DFGRD1,NOEL,NPT,LAYER,KSPT,KSTEP,KINC)
C
      INCLUDE 'ABA_PARAM.INC'
C
      CHARACTER*80 CMNAME
C
      DIMENSION STRESS(NTENS),STATEV(NSTATV),
     1 DDSDDE(NTENS,NTENS),DDSDDT(NTENS),DRPLDE(NTENS),
     2 STRAN(NTENS),DSTRAN(NTENS),TIME(2),PREDEF(1),DPRED(1),
     3 PROPS(NPROPS),COORDS(3),DROT(3,3),DFGRD0(3,3),DFGRD1(3,3)
C ======================================================================
C     THIS PART IS THE USER CODING TO DEFINE DDSDDE, STRESS, STATEV,
C     SSE, SPD, SCD AND, IF NECESSARY, RPL, DDSDDT, DRPLDE, DRPLDT,PNEWDT
C----------------------------------------------------------------------
      DIMENSION UPSTRAN(NTENS),UPDSTRAN(NTENS),STRANRAT(NTENS),
     1          CYCSTRAN(NTENS),UPCYCSTRAN(NTENS)
      PARAMETER (ZERO=0.D0, ONE=1.D0, TWO=2.D0, THREE=3.D0)
      REAL*8 Ecoh,S,Sc,Sf,dc,ETA,d1,d2,EG,Q,Smax,dmax,de,X,Z,C
      INTEGER N, UNLOADING, FAILED, NOFPT, DN, Ncycles, Nu
C
      IF (NDI.NE.1) THEN
        WRITE(7,*) 'THIS UMAT MAY ONLY BE USED WITH MODE ONE FRACTURE'
```

```
      CALL XIT
    END IF
C   ================================================================
C            **************REQUIRED INPUT***************
C   ================================================================
C    PROPS(1)IS THE CRITICAL COHESIVE STRESS
C    PROPS(2)IS THE CRITICAL COHESIVE SEPARATION
C    PROPS(3)IS THE NUMER OF CYCLES IN THE LOAD ENVELOPE
C    PROPS(4)IS THE MATERIAL PARAMETER C THAT CAOTURES THE CYCLIC
C          PLASTICITY
C   ================================================================
C            ****** STATE DEPENDENT VARIABLES *********
C   ================================================================
C    STATEV(1)IS THE DAMAGE PARAMETER
C    STATEV(2)IS THE SEPARATION AT THE END OF THE LOADING CYCLE
C    STATEV(3)IS TEH STRESS AT THE END OF THE LOADING CYCLE
C    STATEV(4)IS THE STORED PLASTIC DISPLACEMENT
C    STATEV(5)IS THE MAXIMUM CYCLIC DISPLACEMENT
C    STATEV(6)IS A VARIABLE TO INDICATE THE ONSET OF UNLOADING AND
C          CONTROLING WHEN THE PLASTIC DISPLACEMENT X STORED
C    STATEV(7)IS A VARIABLE TO INDICATE ThE FAILER OF THE ELEMENT
C    STATEV(8)IS THE NUMBER OF LOADING CYCLES
C    STATEV(9)IS THE SEPARATION AT EACH TIME INCREMENT
C    STATEV(10)IS  THE STRESS AT EACH TIME INCREMENT
C    STATEV(11)IS AN  INTERNAL CONTROL VARIABLE
C    STATEV(12)IS AN  INTERNAL CONTROL VARIABLE
C    STATEV(13)IS AN  INTERNAL CONTROL VARIABLE
C    STATEV(14)IS AN  INTERNAL CONTROL VARIABLE
C   ================================================================
C
C    DEFINING INPUTS
    Sc=PROPS(1)
    dc=PROPS(2)
    Ncycles=PROPS(3)
```

```
      C=PROPS(4)
       Ecoh=PROPS(5)
C
      D=STATEV(1)
      X=STATEV(4)
      FAILED=STATEV(7)
      N=STATEV(8)
C
      d1= Sc/Ecoh
      d2=0.75*dc
      IF(STATEV(2).EQ.ZERO)THEN
      dmax=d1
      Smax=Sc
      ELSE
      dmax=STATEV(2)
      Smax=STATEV(3)
      ENDIF
C
      DO K1=1, NTENS
C
      UPSTRAN(K1)=STRAN(K1)+DSTRAN(K1)
      CYCSTRAN(K1)=X+UPSTRAN(K1)
C
CC    EVALUTATING THE VALUE OF THE MAXIMUM UPPLIED CYCLIC LOAD
C
      If(UPSTRAN(K1).GT.STATEV(5))THEN
      STATEV(5)=UPSTRAN(K1)
      ENDIF
C
CC    CALCULATING THE VALUE OF X
C
      IF((K1.EQ.1).AND.(UPSTRAN(K1).GT.ZERO).AND.(DSTRAN(K1).LT.ZERO))
     1     THEN
           STATEV(11)=ONE
```

```
      ENDIF
C     UPDATING TEH CYCLIC STRAIN
C
      IF ((FAILED.EQ.ONE).AND.(UPSTRAN(K1).GT.ZERO).AND.(DSTRAN(K1).GT.
     1    ZERO))THEN
         STATEV(11)= ZERO
      ENDIF
      IF ((FAILED.EQ.ONE).AND.(UPSTRAN(K1).GT.ZERO).AND.(DSTRAN(K1).LT.
     1    ZERO))THEN
         STATEV(11)= ONE
      ENDIF
C     EVALUATEE THE NUMBER OF LOADING CYCLE
      IF((K1.EQ.1).AND.(STATEV(12).EQ.ZERO).AND.(UPSTRAN(K1).GT.ZERO).
     1   AND.(DSTRAN(K1).GT.ZERO).AND.(STATEV(11).EQ.ZERO))THEN
      STATEV(12)=one
      ENDIF
      IF((K1.EQ.1).AND.(STATEV(12).EQ.ONE).AND.(STATEV(11).EQ.ONE).AND.
     1  (UPSTRAN(K1).GT.ZERO).AND.(DSTRAN(K1).LT.ZERO))THEN
      STATEV(12)=ZERO
C               **********************************
C     EVALUATE THE NUMBER OF APPLYED CYCLE
      N=STATEV(8)+Ncycles
      STATEV(8)= N
      STATEV(13)=ONE
      ENDIF
C
      IF(FAILED.EQ.ZERO)GOTO 10
      GOTO 110
C     EVALUATION OF THE JACOBAIN MATRIX AND UPDATING THE STRESS
10    IF((CYCSTRAN(K1).LE.dmax))GOTO 15
      GOTO 20
C
15    IF((STATEV(13).EQ.ONE).AND.(STATEV(14).EQ.ONE).AND.(DSTRAN(K1).LT.
     1   ZERO))THEN
```

```
          X=STATEV(4)+(STATEV(5)/C)
          IF(K1.EQ.1)THEN
          STATEV(6)=ONE
          ENDIF
      ENDIF
C
      IF((K1.EQ.1).AND.(STATEV(6).EQ.ONE).AND.(DSTRAN(K1).GT.ZERO))
     1   GOTO 16
      GOTO 18
16          X=STATEV(4)+(Ncycles*(STATEV(5)/C))
          STATEV(4)=X
          STATEV(6)=ZERO
C     ****UPDATING Smax AND dmax ACORDING TO UPDATED X****
          dmax=X+STATEV(5)
          STATEV(2)=dmax
          STATEV(17)=Smax
C
        IF ((dmax.GT.d2).AND.(dmax.LT.dc))THEN
          Smax=((d1*(dc-dmax))/(dmax*(dc-d2)))*Ecoh*dmax
          STATEV(3)=Smax
        ENDIF
C
        IF ((K1.EQ.1).AND.(dmax.GT.dc))GOTO 17
        GOTO 18
17            DN=INT((dmax-dc)/(STATEV(5)/C))
            N=STATEV(8)-DN
            STRESS(K1)=ZERO
            STATEV(3)=Smax
            STATEV(7)= ONE
            WRITE(7,*) NOEL,'FAILED',N
      GOTO 200
C
C     COMPUTE THE STIFFNESS MATRIX
18             DO K2=1, NTENS
```

```
            DDSDDE(K2,K1)=ZERO
          END DO
            DDSDDE(K1,K1)=Smax/(dmax-X)
C
C          UPDATE THE STRESS
C
         IF(CYCSTRAN(K1).LT.ZERO)THEN
           DO K2=1, NTENS
             STRESS(K1)=STRESS(K1)+DDSDDE(K2,K1)*DSTRAN(K1)
           END DO
         ELSEIF((CYCSTRAN(K1).LE.X).AND.(CYCSTRAN(K1).GE.ZERO))THEN
             STRESS(K1)=ZERO
         ELSEIF((CYCSTRAN(K1).GT.X).AND.(CYCSTRAN(K1).GT.ZERO))THEN
           DO K2=1, NTENS
            STRESS(K1)=STRESS(K1)+DDSDDE(K2,K1)*DSTRAN(K1)
           IF (STRESS(K1).LT.ZERO)THEN
             STRESS(K1)=0
           ENDIF
           END DO
         ENDIF
C
C    PRINT THE VALUE OF THE STRESS AND THE STRAN
    IF (K1.EQ.1)THEN
C     WRITE(7,*) NOEL,'LOADING',STRESS(K1),CYCSTRAN(K1),DDSDDE(K1,K1)
C    1     ,DSTRAN(K1),Smax,dmax,X,N
       STATEV(9)=CYCSTRAN(K1)
       STATEV(10)=STRESS(K1)
      IF(DSTRAN(K1).GT.ZERO)THEN
       STATEV(13)=ZERO
       STATEV(11)=ZERO
      ENDIF
    ENDIF
C
    GOTO 200
```

```
C
20    IF((CYCSTRAN(K1).GE.dmax).AND.(CYCSTRAN(K1).LT.d2).AND.(DSTRAN(K1
     1   ).GT.ZERO))GOTO 30
      GOTO 50
C     EVALUATIONG THE VALUE OF TEH DAMAGE VARAIBLE
C
30      D=1-(d1/CYCSTRAN(K1))
      DO K2=1, NTENS
           DDSDDE(K2, K1)=ZERO
      END DO
           DDSDDE(K1, K1)=ZERO
      IF ((K1.EQ.1).AND.(D.GT.STATEV(1)))THEN
         STATEV(1)=D
      ENDIF
      STRESS(K1)=(1-D)*Ecoh*CYCSTRAN(K1)
C     PRINT THE VALUE OF THE STRESS AND THE STRAN
      IF (K1.EQ.1)THEN
      STATEV(2)=CYCSTRAN(K1)
      STATEV(3)=STRESS(K1)
      STATEV(9)=CYCSTRAN(K1)
      STATEV(10)=STRESS(K1)
      STATEV(11)=ZERO
      STATEV(13)=ZERO
      STATEV(14)=ONE
      WRITE(7,*) NOEL,'DAMAGE1',STATEV(3),STATEV(2),X,N
      ENDIF
      GOTO 200
C
50    IF((CYCSTRAN(K1).GT.d2).AND.(CYCSTRAN(K1).LT.dc).AND.(DSTRAN(K1
     1   ).GT.ZERO))GOTO 60
      GOTO 90
60    D=1-((d1*(dc-CYCSTRAN(K1)))/(CYCSTRAN(K1)*(dc-d2)))
      DO K2=1, NTENS
           DDSDDE(K2, K1)=ZERO
```

```
      END DO
           DDSDDE(K1, K1)=(-Sc)/(dc-d2)
      IF ((K1.EQ.1).AND.(D.GT.STATEV(1)))THEN
         STATEV(1)=D
      ENDIF
C
C     UPDATE THE STRESS
C
70    STRESS(K1)=(1-D)*Ecoh*CYCSTRAN(K1)
            IF(STRESS(K1).LE.ZERO)GOTO 80
            goto 85
80               STRESS(K1)=ZERO
            IF (K1.EQ.1)THEN
               WRITE(7,*) NOEL,'FAILEDx',N
            ENDIF
C     PRINT THE VALUE OF THE STRESS AND THE STRAN
85    IF (K1.EQ.1)THEN
      STATEV(2)=CYCSTRAN(K1)
      STATEV(3)=STRESS(K1)
      STATEV(9)=CYCSTRAN(K1)
      STATEV(10)=STRESS(K1)
      STATEV(11)=ZERO
      STATEV(13)=ZERO
      STATEV(14)=ONE
      STATEV(16)=ONE
      WRITE(7,*) NOEL,'DAMAGE2',STRESS(K1),CYCSTRAN(K1),Smax,dmax,X,N,
     1      STATEV(5)
      ENDIF
      GOTO 200
C
90    IF((((CYCSTRAN(K1).GE.dc)).OR.(D.GT.ONE)).AND.(DSTRAN(K1).GT.ZERO
     1    ))GOTO 100
      GOTO 110
100           STRESS(K1)=ZERO
```

```
C     PRINT THE VALUE OF THE STRESS AND THE STRAN
        if (K1.EQ.1)THEN
          STATEV(7)= ONE
          STATEV(9)=CYCSTRAN(K1)
          STATEV(10)=STRESS(K1)
          WRITE(7,*) NOEL,'FAILED',N
        ENDIF
      GOTO 200
C   ================================================================
C                       CONDITION FOR PENTRATION
C   ================================================================
110   IF ((FAILED.EQ.ONE).AND.(STRAN(K1).GT.ZERO)) GOTO 120
      GOTO 130
120           STRESS(K1)=ZERO
        if (K1.EQ.1)THEN
          WRITE(7,*) NOEL,'FAILED ELEMENT',N
          STATEV(9)=CYCSTRAN(K1)
          STATEV(10)=STRESS(K1)
        ENDIF
      GOTO 200
C
130   IF ((FAILED.EQ.ONE).AND.(UPSTRAN(K1).LE.ZERO)) GOTO 140
      GOTO 200
C
140       DO K2=1, NTENS
        DDSDDE(K2, K1)=ZERO
        END DO
        DDSDDE(K1, K1)=Ecoh
C
C     UPDATE THE STRESS
C
        DO K2=1, NTENS
        STRESS(K1)=STRESS(K1)+DDSDDE(K2,K1)*DSTRAN(K1)
        END DO
```

```
C     PRINT THE VALUE OF THE STRESS AND THE STRAN
        IF (K1.EQ.1)THEN
        WRITE(7,*) NOEL,'COMPRESTION'
          STATEV(9)=CYCSTRAN(K1)
          STATEV(10)=STRESS(K1)
        ENDIF
200   END DO
C
      RETURN
      END
```

B-3 New frequency-dependent TCZM for fatigue

```
C**********************************************************************
C     UMAT FOR FREQYEBCY-DEPENDENT TCZM
C     CAN BE USED FOR cyclic load in MODE ONE ONLY
C     WRITEN BY SARMED A. SALIH
C  ===================================================================
C  HEADER OF THE SUBROUTINE
C
      SUBROUTINE UMAT(STRESS,STATEV,DDSDDE,SSE,SPD,SCD,
     1 RPL,DDSDDT,DRPLDE,DRPLDT,
     2 STRAN,DSTRAN,TIME,DTIME,TEMP,DTEMP,PREDEF,DPRED,CMNAME,
     3 NDI,NSHR,NTENS,NSTATV,PROPS,NPROPS,COORDS,DROT,PNEWDT,
     4 CELENT,DFGRD0,DFGRD1,NOEL,NPT,LAYER,KSPT,KSTEP,KINC)
C
      INCLUDE 'ABA_PARAM.INC'
C
      CHARACTER*80 CMNAME
C
      DIMENSION STRESS(NTENS),STATEV(NSTATV),
     1 DDSDDE(NTENS,NTENS),DDSDDT(NTENS),DRPLDE(NTENS),
     2 STRAN(NTENS),DSTRAN(NTENS),TIME(2),PREDEF(1),DPRED(1),
     3 PROPS(NPROPS),COORDS(3),DROT(3,3),DFGRD0(3,3),DFGRD1(3,3)
C  ===================================================================
C     THIS PART IS THE USER CODING TO DEFINE DDSDDE, STRESS, STATEV,
C     SSE, SPD, SCD AND,IF NECESSARY, RPL, DDSDDT, DRPLDE, DRPLDT,PNEWDT
C----------------------------------------------------------------------
      DIMENSION UPSTRAN(NTENS),UPDSTRAN(NTENS),STRANRAT(NTENS),
     1          CYCSTRAN(NTENS),UPCYCSTRAN(NTENS)
      PARAMETER(ZERO=0.D0, ONE=1.D0, TWO=2.D0, THREE=3.D0)
      REAL*8 Ecoh,S,Sc,Scr,f,f_min,Sf,dc,ETA,d1,d2,EG,Q,Smax,dmax,de,X,Z
     1      ,C
      INTEGER N, UNLOADING, FAILED, NOFPT,DN, Ncycles, Nu
C
      IF (NDI.NE.1) THEN
```

```
      WRITE(7,*) 'THIS UMAT MAY ONLY BE USED WITH MODE ONE FRACTURE'
      CALL XIT
    END IF
C   ================================================================
C            **************REQUIRED INPUT***************
C   ================================================================
C    PROPS(1)IS THE CRITICAL COHESIVE STRESS
C    PROPS(2)IS THE CRITICAL COHESIVE SEPARATION
C    PROPS(3)IS THE NUMER OF REQUIRED DAMAGE UPDATES
C    PROPS(4)IS THE MATERIAL PARAMETER C THAT CAOTURES THE CYCLIC
C          PLASTICITY
C   ================================================================
C            ****** STATE DEPENDENT VARIABLES *********
C   ================================================================
C    STATEV(1)IS THE DAMAGE PARAMETER
C    STATEV(2)IS THE SEPARATION AT THE END OF THE LOADING CYCLE
C    STATEV(3)IS TEH STRESS AT THE END OF THE LOADING CYCLE
C    STATEV(4)IS THE STORED PLASTIC DISPLACEMENT
C    STATEV(5)IS THE MAXIMUM CYCLIC DISPLACEMENT
C    STATEV(6)IS A VARIABLE TO INDICATE THE ONSET OF UNLOADING AND
C          CONTROLING WHEN THE PLASTIC DISPLACEMENT X STORED
C    STATEV(7)IS A VARIABLE TO INDICATE ThE FAILER OF THE ELEMENT
C    STATEV(8)IS THE NUMBER OF LOADING CYCLES
C    STATEV(9)IS THE SEPARATION AT EACH TIME INCREMENT
C    STATEV(10)IS  THE STRESS AT EACH TIME INCREMENT
C    STATEV(11)IS AN  INTERNAL CONTROL VARIABLE
C    STATEV(12)IS AN  INTERNAL CONTROL VARIABLE
C    STATEV(13)IS AN  INTERNAL CONTROL VARIABLE
C    STATEV(14)IS AN  INTERNAL CONTROL VARIABLE
C   ================================================================
C
C    DEFINING INPUTS
    Sc=PROPS(1)
    dc=PROPS(2)
```

```
      Ncycles=PROPS(3)
      C=PROPS(4)
      f=PROPS(5)
      f_o=PROPS(6)
      Ecoh =PROPS(7)
      IF(STATEV(15).EQ.ZERO)THEN
      Scr=400E6*exp-(f_o/f )
      STATEV(15)=Scr
      ENDIF
C
      D=STATEV(1)
      X=STATEV(4)
      FAILED=STATEV(7)
      N=STATEV(8)
      Scr=STATEV(15)
C
      d1= Scr/ Ecoh
      d2=0.75*dc
      IF(STATEV(2).EQ.ZERO)THEN
      dmax=d1
      Smax=Scr
      ELSE
      dmax=STATEV(2)
      Smax=STATEV(3)
      ENDIF
C
      DO K1=1, NTENS
C
      UPSTRAN(K1)=STRAN(K1)+DSTRAN(K1)
      CYCSTRAN(K1)=X+UPSTRAN(K1)
C
C     EVALUTATING THE VALUE OF THE MAXIMUM APPLIED CYCLIC LOAD
C
      If(UPSTRAN(K1).GT.STATEV(5))THEN
```

```
      STATEV(5)=UPSTRAN(K1)
      ENDIF
C
C     CALCULATING THE VALUE OF X
C
      IF((K1.EQ.1).AND.(UPSTRAN(K1).GT.ZERO).AND.(DSTRAN(K1).LT.ZERO))
     1      THEN
           STATEV(11)=ONE
      ENDIF
C     UPDATING TEH CYCLIC STRAIN
C
      IF ((FAILED.EQ.ONE).AND.(UPSTRAN(K1).GT.ZERO).AND.(DSTRAN(K1).GT.
     1    ZERO))THEN
         STATEV(11)= ZERO
      ENDIF
      IF ((FAILED.EQ.ONE).AND.(UPSTRAN(K1).GT.ZERO).AND.(DSTRAN(K1).LT.
     1    ZERO))THEN
         STATEV(11)= ONE
      ENDIF
C     EVALUATEE THE NUMBER OF LOADING CYCLE
      IF((K1.EQ.1).AND.(STATEV(12).EQ.ZERO).AND.(UPSTRAN(K1).GT.ZERO).
     1   AND.(DSTRAN(K1).GT.ZERO).AND.(STATEV(11).EQ.ZERO))THEN
      STATEV(12)=one
      ENDIF
      IF((K1.EQ.1).AND.(STATEV(12).EQ.ONE).AND.(STATEV(11).EQ.ONE).AND.
     1  (UPSTRAN(K1).GT.ZERO).AND.(DSTRAN(K1).LT.ZERO))THEN
      STATEV(12)=ZERO
C               **********************************
C     EVALUATE THE NUMBER OF APPLYED CYCLE
      N=STATEV(8)+Ncycles
      STATEV(8)= N
      STATEV(13)=ONE
      ENDIF
C
```

```
      IF(FAILED.EQ.ZERO)GOTO 10
      GOTO 110
C     EVALUATION OF THE JACOBAIN MATRIX AND UPDATING THE STRESS
10    IF((CYCSTRAN(K1).LE.dmax))GOTO 15
      GOTO 20
C
15    IF((STATEV(13).EQ.ONE).AND.(STATEV(14).EQ.ONE).AND.(DSTRAN(K1).LT.
     1   ZERO))THEN
          X=STATEV(4)+(STATEV(5)/C)
          IF(K1.EQ.1)THEN
          STATEV(6)=ONE
          ENDIF
      ENDIF
C
      IF((K1.EQ.1).AND.(STATEV(6).EQ.ONE).AND.(DSTRAN(K1).GT.ZERO))
     1    GOTO 16
      GOTO 18
16          X=STATEV(4)+(Ncycles*(STATEV(5)/C))
          STATEV(4)=X
          STATEV(6)=ZERO
C     ****UPDATING Smax AND dmax ACORDING TO UPDATED X****
          dmax=X+STATEV(5)
          STATEV(2)=dmax
          STATEV(17)=Smax
C
        IF ((dmax.GT.d2).AND.(dmax.LT.dc))THEN
          Smax=((d1*(dc-dmax))/(dmax*(dc-d2)))*Ecoh*dmax
          STATEV(3)=Smax
        ENDIF
C
        IF ((K1.EQ.1).AND.(dmax.GT.dc))GOTO 17
        GOTO 18
17            DN=INT((dmax-dc)/(STATEV(5)/C))
            N=STATEV(8)-DN
```

```
          STRESS(K1)=ZERO
          STATEV(3)=Smax
          STATEV(7)= ONE
          WRITE(7,*) NOEL,'FAILED',N
      GOTO 200
C
C     COMPUTE THE STIFFNESS MATRIX
18            DO K2=1, NTENS
                DDSDDE(K2,K1)=ZERO
              END DO
                DDSDDE(K1,K1)=Smax/(dmax-X)
C
C           UPDATE THE STRESS
C
          IF(CYCSTRAN(K1).LT.ZERO)THEN
            DO K2=1, NTENS
               STRESS(K1)=STRESS(K1)+DDSDDE(K2,K1)*DSTRAN(K1)
            END DO
          ELSEIF((CYCSTRAN(K1).LE.X).AND.(CYCSTRAN(K1).GE.ZERO))THEN
               STRESS(K1)=ZERO
          ELSEIF((CYCSTRAN(K1).GT.X).AND.(CYCSTRAN(K1).GT.ZERO))THEN
            DO K2=1, NTENS
              STRESS(K1)=STRESS(K1)+DDSDDE(K2,K1)*DSTRAN(K1)
             IF (STRESS(K1).LT.ZERO)THEN
               STRESS(K1)=0
             ENDIF
            END DO
          ENDIF
C
C     PRINT THE VALUE OF THE STRESS AND THE STRAN
      IF (K1.EQ.1)THEN
C      WRITE(7,*) NOEL,'LOADING',STRESS(K1),CYCSTRAN(K1),DDSDDE(K1,K1)
C     1     ,DSTRAN(K1),Smax,dmax,X,N
         STATEV(9)=CYCSTRAN(K1)
```

```
          STATEV(10)=STRESS(K1)
        IF(DSTRAN(K1).GT.ZERO)THEN
          STATEV(13)=ZERO
          STATEV(11)=ZERO
        ENDIF
      ENDIF
C
      GOTO 200
C
20    IF((CYCSTRAN(K1).GE.dmax).AND.(CYCSTRAN(K1).LT.d2).AND.(DSTRAN(K1
     1   ).GT.ZERO))GOTO 30
      GOTO 50
C     EVALUATIONG THE VALUE OF TEH DAMAGE VARAIBLE
C
30      D=1-(d1/CYCSTRAN(K1))
      DO K2=1, NTENS
          DDSDDE(K2, K1)=ZERO
      END DO
          DDSDDE(K1, K1)=ZERO
      IF ((K1.EQ.1).AND.(D.GT.STATEV(1)))THEN
        STATEV(1)=D
      ENDIF
      STRESS(K1)=(1-D)*Ecoh*CYCSTRAN(K1)
C     PRINT THE VALUE OF THE STRESS AND THE STRAN
      IF (K1.EQ.1)THEN
      STATEV(2)=CYCSTRAN(K1)
      STATEV(3)=STRESS(K1)
      STATEV(9)=CYCSTRAN(K1)
      STATEV(10)=STRESS(K1)
      STATEV(11)=ZERO
      STATEV(13)=ZERO
      STATEV(14)=ONE
      WRITE(7,*) NOEL,'DAMAGE1',STATEV(3),STATEV(2),X,N
      ENDIF
```

```
      GOTO 200
c
50    IF((CYCSTRAN(K1).GT.d2).AND.(CYCSTRAN(K1).LT.dc).AND.(DSTRAN(K1
     1   ).GT.ZERO))GOTO 60
      GOTO 90
60    D=1-((d1*(dc-CYCSTRAN(K1)))/(CYCSTRAN(K1)*(dc-d2)))
      DO K2=1, NTENS
          DDSDDE(K2, K1)=ZERO
      END DO
          DDSDDE(K1, K1)=(-Scr)/(dc-d2)
      IF ((K1.EQ.1).AND.(D.GT.STATEV(1)))THEN
         STATEV(1)=D
      ENDIF
C
C     UPDATE THE STRESS
C
70    STRESS(K1)=(1-D)*Ecoh*CYCSTRAN(K1)
            IF(STRESS(K1).LE.ZERO)GOTO 80
            GOTO 85
80              STRESS(K1)=ZERO
            IF (K1.EQ.1)THEN
               WRITE(7,*) NOEL,'FAILEDx',N
            ENDIF
C     PRINT THE VALUE OF THE STRESS AND THE STRAN
85    IF (K1.EQ.1)THEN
      STATEV(2)=CYCSTRAN(K1)
      STATEV(3)=STRESS(K1)
      STATEV(9)=CYCSTRAN(K1)
      STATEV(10)=STRESS(K1)
      STATEV(11)=ZERO
      STATEV(13)=ZERO
      STATEV(14)=ONE
      STATEV(16)=ONE
      WRITE(7,*) NOEL,'DAMAGE2',STRESS(K1),CYCSTRAN(K1),Smax,dmax,X,N,
```

```
     1      STATEV(5)
      ENDIF
      GOTO 200
C
90    IF((((CYCSTRAN(K1).GE.dc)).OR.(D.GT.ONE)).AND.(DSTRAN(K1).GT.ZERO
     1    ))GOTO 100
      GOTO 110
100           STRESS(K1)=ZERO
C     PRINT THE VALUE OF THE STRESS AND THE STRAN
         if (K1.EQ.1)THEN
           STATEV(7)= ONE
           STATEV(9)=CYCSTRAN(K1)
           STATEV(10)=STRESS(K1)
           WRITE(7,*) NOEL,'FAILED',N
         ENDIF
      GOTO 200
C   ======================================================================
C                     CONDITION FOR PENTRATION
C   ======================================================================
110   IF ((FAILED.EQ.ONE).AND.(STRAN(K1).GT.ZERO)) GOTO 120
      GOTO 130
120          STRESS(K1)=ZERO
         if (K1.EQ.1)THEN
           WRITE(7,*) NOEL,'FAILED ELEMENT',N
           STATEV(9)=CYCSTRAN(K1)
           STATEV(10)=STRESS(K1)
         ENDIF
      GOTO 200
c     ((FAILED.EQ.ONE).OR.((UNLOADING.EQ.ONE).AND.(STRAN(K1).LE. ZERO)))
130   IF ((FAILED.EQ.ONE).AND.(UPSTRAN(K1).LE.ZERO)) GOTO 140
      GOTO 200
C
140       DO K2=1, NTENS
         DDSDDE(K2, K1)=ZERO
```

```
        END DO
        DDSDDE(K1, K1)=Ecoh
C
C     UPDATE THE STRESS
C
        DO K2=1, NTENS
        STRESS(K1)=STRESS(K1)+DDSDDE(K2,K1)*DSTRAN(K1)
        END DO
C     PRINT THE VALUE OF THE STRESS AND THE STRAN
        IF (K1.EQ.1)THEN
        WRITE(7,*) NOEL,'COMPRESTION'
          STATEV(9)=CYCSTRAN(K1)
          STATEV(10)=STRESS(K1)
        ENDIF
200   END DO
C
     RETURN
     END
```